INVESTIGATION OF CHARGE TRANSPORTS THROUGH FERROCENE-CONTAINING POLYMER BRUSHES

GAN LU

NATIONAL UNIVERSITY OF SINGAPORE

2015

NVESTIGATION OF CHARGE TRANSPORTS THROUGH FERROCENE-CONTAINING POLYMER BRUSHES

GAN LU

(B.Sc., *SICHUAN UNIVERSITY*)

A THESIS SUBMITTED

FOR THE DEGREE OF DOCTOR OF PHILOSOPHY

DEPARTMENT OF CHEMISTRY

NATIONAL UNIVERSITY OF SINGAPORE

2015

Thesis Declaration

I hereby declare that this thesis is my original work and it has been written by me in its entirety, under the supervision of Assistant Professor Christian A. Nijhuis, Department of Chemistry, National University of Singapore. I have duly acknowledged all the sources of information which have been used in the thesis.

This thesis has also not been submitted for any degree in any university previously.

Gan Lu		16/04/2016
Name	Signature	Date

Acknowledgements

I would like to express my sincere appreciations to all the people who help and support me during the research and their contributions to the work presented here.

First of all, I wish to express my deep and sincere gratitude to my supervisor, Dr Christian A. Nijhuis for his continuous professional guidance and inspiration, as well as unreserved support throughout my Ph.D. study. His wide knowledge, constructive criticisms and insightful comments have provided a fundamental and significant basis for the present thesis. More importantly, his rigorous research methodology, objectivity and enthusiasm in scientific discovery will deeply impact on my life and future career.

This work would have not been completed without the help and collaborations of different people. With sincere thanks, I want to thank Dr Dominik Jańczewski and Dr Jing Song for their constant supports and co-supervision, suggestions and encouragements during the five years and I gratefully appreciate his and her kind help and concern.

I am deeply grateful to all the past/current lab mates and collaborators in both groups, especially Dr Suchand Sangeeth and Yuan Li, Dr Xiaoying Zhu, Dr Shifeng Guo and Dr Tao He. Without their help and encouragements, this work could not have been completed on time.

I wish to express sincere appreciations to all my colleagues and friends, for being such good colleagues and friends over the years during the good and bad moments.

Thank you for your help, willing to discuss all kinds of issues and making such a nice atmosphere in the lab.

I would like to express my thanks to National University of Singapore for the supply of the research scholarship.

Finally, I would like to express my loving thanks to my parents. Their love and encouragements ignited my passion for the accomplishment documented in this thesis.

Table of Contents

Thesis Declaration i

Acknowledgement iii

Table of Contents v

Summary x

Lists of Tables xii

Lists of Schemes xiv

Lists of Figures xvi

Lists of Abbreviations xxviii

Lists of Symbols xxxii

Chapter 1: General Introduction 1

1.1 Introduction 1

1.2 Reference 3

Chapter 2 Applications of Functional Polymers/Polymer Brushes in Molecular Electronic Field 7

2.1 Introduction 8

2.2 Synthesis of polymer brush by controlled methods 9

2.2.1 Living radical/controlled polymerization (CRP) 9

2.2.2 Surface-initiated atom transport radical polymerization (SI-ATRP) 11

2.2.3 Properties of functional polymer brushes 15

2.3 Development of organic electronic devices 16

2.3.1 Molecular junctions 16

2.3.1.1 Single-molecule based junctions 18

2.3.1.2 SAMs based junctions 19

2.3.1.3 Molecular wires/oligomers based molecular junctions 24

2.3.2 Polymer brush application in organic electronic devices 32

2.3.2.1 Applications in field-effect transistor (FET) devices 33

2.3.2.2 Applications in memory effect devices 37

2.3.2.3 Enhancement of the charge transport characteristics by polymer brush 41
2.3.3 Electrodes applied to molecular junctions 42
2.3.3.1 Top electrodes: hard contact 43
2.3.3.2 Top electrodes: soft contact 43
2.3.3.3 Bottom electrodes: metal surface 45
2.3.3.4 Bottom electrodes: non-metal surface 45
2.3.4 Molecular electronic devices: EGaIn based device 46
2.4 Limitations and gaps in previous work 46
2.5 Purpose, significance and scope for our work 47
2.6 Summary 48
2.7 References 48

Chapter 3 Side Chain Effects in the Packing structure and Stiffness of Redox-Responsive Ferrocene-Containing Polymer Brushes 55
3.1 Introduction 55
3.2 Results and discussion 61
3.2.1 Selections of catalyst and solvent for ATRP reactions 61
3.2.2 Reaction recipe for ATRP reactions 63
3.2.3 Polymerization kinetics studies: a “living” growth 65
3.2.4 SI-ATRP for Fc-containing polymer brushes 67
3.2.5 Polymer brush surface characterizations 68
3.2.5.1 Water contact angle measurements 69
3.2.5.2 AFM measurements 70
3.2.5.3 UV/Vis spectroscopy measurements 72
3.2.5.4 FT-IRRAS measurements 73
3.2.5.5 XPS measurements 75
3.2.6 Wet electrochemistry: cyclic voltammetry (CV) 76
3.2.7 Ideal packing model 81
3.2.7.1 Estimations of side chain length by software 81
3.2.7.2 Tacticity in polymer brush — the most stable conformations 82
3.2.7.3 Calculations for model parameters 83

3.2.7.4 Packing model for polymer brushes 85
3.2.8 Thickness correlations 86
3.2.9 Nanomechanical response of polymer brushes measured by colloidal probe AFM 89
3.2.10 Thermal properties of Fc-containing bulk polymers 92
3.3 Conclusions 93
3.4 Experimental section 94
3.4.1 Chemical and materials 94
3.4.2 Determination of monomer conversion and molecular weight 95
3.4.3 Activation and modification for substrates 95
3.4.4 Water contact angle measurements 96
3.4.5 AFM morphology measurements and scratch test 96
3.4.6 UV/Vis measurements 97
3.4.7 FT-IRRAS measurements 97
3.4.8 XPS measurements 98
3.4.9 CV measurements 98
3.4.10 Ellipsometry measurements 98
3.4.11 Thermal properties measurements 99
3.4.12 Nanomechanical properties measurements 99
3.5 References 99

Chapter 4 Influence of Thickness and Scan Rate of Ferrocene-Containing Polymer Brushes in Electrochemistry 106
4.1 Introduction 107
4.2 Results and discussion 109
4.2.1 Break-in period of the electrochemical behaviour for polymer brushes 109
4.2.2 Stability of the polymer brush film 111
4.2.3 Brush dependent as the function of scan rates 112
4.2.4 Influence of scan rates 113
4.2.5 Electrochemical process at a very low scan rate 117
4.2.6 Thickness dependence for the electrochemical process 118
4.2.7 Kinetic parameters of the polymer brush 120

electrochemical process with different thickness

4.3 Conclusions 128

4.4 Experimental section 129

4.4.1 Chemical and materials 129

4.4.2 Electrochemistry measurements 129

4.4.3 Determination of the thickness of polymer brush 129

4.5 References 129

Chapter 5 Tuning the Charge Transport across ITO-Ferrocene-Containing Polymer Brushes // GaOx / EGaIn Junction by Controlling the Brush Thickness 132

5.1 Introduction 133

5.2 Background 137

5.2.1 Tunnelling 137

5.2.2 Electron hopping by space charge limited conduction 137

5.3 Results and discussion 140

5.3.1 Surface characterizations for polymer brush on ITO 140

5.3.2 Statistics of ITO –brush // GaOx / EGaIn junctions 141

5.3.3 Polymer brush thickness (L_{PB}) vs. rectification ration (R) and polymer brush thickness (L_{PB}) vs. current density (J) 143

5.3.4 Durability of the polymer brush samples: tested by EGaIn cone-shape tip junctions 146

5.3.5 Transport mechanism 147

5.3.6 Key parameters for temperature dependent charge transport measurements: E_t, T_c, H_t, and E_a 149

5.3.7 Thickness dependent and side chain dependent for polymer brushes in temperature dependent measurements 153

5.3.8 $J(V)$ in semi-log plot as the function of temperature to 6 nm polymer brush at the voltage $|V| = 3.0$ V 153

5.3.9 Energy diagram for charge transport through Ferrocene-containing polymer brush 154

5.4 Conclusions 158

5.5 Experimental section 158

5.5.1 Chemical and materials 158

5.5.2 Determination of the thickness for polymer brush 159
5.5.3 Determination of density for Fc units by cyclic voltammetry 159
5.5.4 Ultra-photonic spectroscopy measurements 160
5.5.5 Fabrication of junction by EGaIn cone-shape tip 160
5.5.6 Fabrication of junction by EGaIn device 160
5.5.7 Temperature dependent measurements 161
5.6 References 162

Chapter 6 General Conclusions & Outlook 166

Appendix 169
1. Monomers and polymers 169
2. Ellipsometry data related to thickness correlation plots 177
3. Cyclic voltammograms related to thickness correlation plots 182
4. Influence of scan rates in cyclic voltammograms for PFBMA and PFNMA representative polymers brushes 185
5. Statistical Junction for PFMMA, PFBMA, and PFNMA brushes with systematic thickness 187
6. $J(V)$ curves for junctions of PFMMA brush samples measured with microfluidic device on bias $|V| = 3.0$ V at room temperature 191
7. $J(V)$ plots as the function of temperature ranges from 340 K to 250 K for PFMMA polymer brush with 42 ± 1 nm thickness 192
8. $J(V)$ plots as the function of temperature ranges from 340 K to 250 K for PFMMA polymer brush with 36 ± 1 nm thickness 193
9. $J(V)$ plots as the function of temperature ranges from 340 K to 250 K for PFBMA polymer brush with 43 ± 1 nm thickness 194
10. $J(V)$ plots as the function of temperature ranges from 340 K to 250 K for PFNMA polymer brush with 42 ± 1 nm thickness 195

Publication list 196

Summary

The aim of the work described in this Thesis is to investigate the charge transport mechanisms across Fc-containing (Fc ≡Ferrocene) polymer brushes. Such Fc-containing polymer brushes are redox active and were generated by surface initiated atom transfer radical polymerization (SI-ATRP). These polymer brushes (ferrocenylmethyl methacrylate ≡ PMMA, ferrocenylbutyl methacrylate ≡ PBMA, ferrocenylnonyl methacrylate ≡ PNMA) have different side chain lengths which contribute to the different packing structures and mechanical properties. Wet electrochemistry — cyclic voltammetry (CV) is an important method to monitor the growth of polymer brushes and also a good technique to learn the charge transport behaviour based on electrolyte environment. The charge transport behaviour of these polymer brushes was studied by the "EGaIn technique" (which will be defined later) and we have found that the electronic characteristics are not related to the alkyl numbers (length) in side chain but strongly affected by the thickness of brushes.

In **Chapter 1**, a general introduction is given together with the concept of this thesis. In **Chapter 2**, a broad literature overview on growing functional polymer brushes, their applications, and the recent related work based on molecular junction researches is given.

In **Chapter 3**, a series of Fc-containing polymer brushes with different side chains were generated by SI-ATRP with good controllability. A simple packing model was built to simulate the packing configurations of these polymer brushes. According to the Fc redox active signals detected by CV scannings, we were able to estimate the values of the brush thickness. We found that the brush with short side chains is rigid while brushes with longer side chains are soft. Both thermal properties and mechanical properties have proved this statement.

In **Chapter 4,** we carefully studied the CV behaviour of a series polymer brushes, these polymer brushes were found to be electrochemically stable. The electrochemical process strongly depends on the scan rates and the thickness of polymer brushes, in most of the cases, the electrochemical process is quasi-reversible or irreversible. The kinetic parameters of the electrochemical process for polymer brushes show good correlations with the brush thickness.

In **Chapter 5**, we described the work on investigation of electronic characteristics for Fc-containing polymer brushes. By applying the polymer brushes with different side chain lengths in a series of thickness to EGaIn junction measurements, we statistically studied the relationship between the brush thickness and the rectification ratios. Temperature dependent measurements were conducted to understand charge transport mechanism.

Finally, in **Chapter 6**, conclusion and outlook are given. Based on the preliminary studies about the packing configuration of the polymer brushes generated by SI-ATRP, as well as with the electrochemical studies and electronic characteristics studies of such polymer brushes, we improved our understanding of the charge transport behaviour of these Fc-containing polymer brushes. We believe that our work will be useful in the rational design devices in which charge transport via redox active polymer material is important.

List of Tables

Table 2.1	Surface characteristics of ODTS, HMDS, and b-PS brush-modified SiO_2 dielectrics, and the electrical properties of the OFET devices.	35
Table 3.1	Possible combinations for homogenous polymerization system. [a] Homogenous here was defined as the catalyst complexes can completely dissolve in the reaction solvent, so the complexes are able to be prepared in stock solution. [b] Toluene was the reaction solvent, while the catalyst complexes were prepared in stock solution by acetonitrile (ACN). [c] The solvent is mixed by degassed Anisole and DMF in 1:1 (V/V). [d] The M_n data and polydispersity index (PDI) value were collected from gel permeation chromatography (GPC). [e] N.A. indicates no generation of polymers.	63
Table 3.2	Reaction recipe of ATRP reactions. All components were prepared in stock solutions before fully mixed. [a] N.A. indicates no free initiators and no clues about the amount for the surface anchored initiator. [b] After all components mixed together, the total concentration of the monomer may slightly decrease (~0.65M).	64
Table 3.3	Summary of the contact angle values of ITO substrates by series treatment procedures. [*] Bare ITO here referred to ITO substrate taken out of package directly without any pre-treatments. [#] Mean values were calculated from at least 10 samples, σ stands for the standard deviations. [^] Basic cleaning solution is $NH_4OH : H_2O_2 : H_2O$ = 1:1:5 in V:V.	69
Table 3.4	Summary of the contact angle values of Si/SiO_2 substrates by treatment procedures. [*] Bare Si/SiO_2 here referred to Si/SiO_2 substrate taken out of package directly without any pre-treatments. [#] Mean values were calculated from at least 10 samples, σ stands for the standard deviations. [^] Basic cleaning solution is $NH_4OH : H_2O_2 : H_2O$ = 1:1:5 in V:V.	70
Table 3.5	Summary of the voltammetric parameters.	79
Table 3.6	Packing parameters for polymer brushes with different side chain length. r is the coiled column radius of polymer brush. A_{disk} is the area occupied by brush column (which is projected as a disk), $A_{vacancy}$ is the area of vacancy between disks. N_{disk} is the number of disk in unit area.	84
Table 3.7	Apparent Young's modulus ($E_{apparent}$) values for three	91

polymer brushes in air and in DI water and the thermal properties for bulk polymers.

Table 4.1 Summary of the voltammetric parameters. 112

Table 4.2 Summary of the kinetic parameters of electrochemical process and the relationships between the peak currents, peak potentials and potential scan rates for PFMMA brush with a series of thickness. [a,b] σ is the standard deviations for parallel measurements. [c,d,e] σ is the standard deviations for fittings. 125

Table 4.3 Summary of the kinetic parameters of electrochemical process and the relationships between the peak currents, peak potentials and potential scan rates for PFBMA brush with a series of thickness. [a,b] σ is the standard deviations for parallel measurements. [c,d,e] σ is the standard deviations for fittings. 126

Table 4.4 Summary of the kinetic parameters of electrochemical process and the relationships between the peak currents, peak potentials and potential scan rates for PFNMA brush with a series of thickness. [a,b] σ is the standard deviations for parallel measurements. [c,d,e] σ is the standard deviations for fittings. [f] short dashed lines indicate that the thickness was too thin to be measurable via AFM scratch test so that the concentrations afterwards were estimation values. 127

Table 5.1 Statistics for ITO – PFM(B/N)MA brushes // GaO_x / EGaIn junctions. 144

Table 5.2 The parameters for polymer brush samples in the temperature range 250 – 340 K. [a] All thickness were obtained by AFM scratch tests with the images shown in Figure 5.1. [b] All Fc densities were estimated by wet electrochemistry (CV). 152

Table 5.3 Summary of work function values and HOMO levels for corresponding samples. 157

List of Schemes

Scheme 2.1	Mechanism of metal complex-mediated ATRP.	11
Scheme 2.2	"Grafting from" method to immobilize polymer chains on substrate.	13
Scheme 3.1	Synthetic scheme for (A) modification of ITO substrates with silanebromo-initiator, followed by (B) SI-ATRP of FMMA, FBMA, and FNMA. n represents the carbon number of the spacer/linker between the Fc moiety and methacrylate functional group. (C) Ideally standing-up single polymer chain, with N representing the repeating units of monomers, *r* representing the ideal radius of cylindrical column formed by side chains coiling along the polymer backbone (2D profile view), and L_{PB} representing the thickness (theoretically) for polymer brush.	68
Scheme 3.2	Packing model for Fc-containing polymer brushes. (A) Top view for single coiled column, $r_{n=1}$, $r_{n=4}$, and $r_{n=9}$ represent the different side chain (linker) lengths for PFMMA, PFBMA, and PFNMA brush, respectively. (B) Side view (2D effect) for polymer brushes coiled in column shape and stretched away from substrate in idea situation. (C) Top view of ideally hexagonally packed brushes; A_{disk} indicates the projected area of a single polymer.	85
Scheme 3.3	Transition between fully stand-up polymer brush regime and partly collapsed regime.	89
Scheme 4.1	Schematic Illustration of electrochemical measurements on Fc-containing polymer brushes modified ITO substrate with 1.0 M $HClO_4$ aqueous solution as electrolyte, Ag/AgCl as reference electrode, and Pt wire as counter electrode.	109
Scheme 5.1	Schematic structure of ITO-Ferrocene-containing Polymer Brushes // GaO_x / EGaIn Junction. PFMMA ≡ polyferrocenylmethyl methacrylate, PFBMA ≡ polyferrocenylbutly methacrylate, PFNMA ≡ polyferrocenylnonyl methacrylate. L_{PB} stands for the brush thickness.	137
Scheme 5.2	Proposed schematic representation of the energy level diagrams (with respect to vacuum) of ITO – brush // GaO_x / EGaIn junctions: (A) at open circuit (OC), (B) at $V = 0$	157

	V, at V = -1.5 V, at V = +1.5 V for thin polymer brushes (L_{PB} < 15 nm), (C) at V = 0 V, at V = -1.5 V, at V = +1.5 V for thick polymer brushes (L_{PB} > 20 nm). Black dashed lines indicate the width and height of the barrier. Blue (solid and dashed) arrows indicate the route and direction of charge transports, the one with the red dashed crosses indicates the forbidden route.	
Scheme 5.3	The home-built EGaIn set up with cone-shape tip. Camera was used to magnify the observation scope for the contact. Microsyringe is filled with EGaIn, the probe can be manipulated by mircopositioner.	161
Scheme A1	Synthesis route for monomer FBMA.	169
Scheme A2	Synthesis route for monomer FNMA.	172

List of Figures

Figure 2.1	Examples of controlled macromolecular architecture in polymers prepared by ATRP. (A) Controlled composition/microstructure (white dots and red dots indicate the different repeated monomer units). (B) Controlled topology (red lines indicate the polymer main chain and blue lines indicate the graft polymer chains). (C) Controlled functionality (red lines indicate the polymer main chain and blue lines indicate the graft polymer chains, pink dots indicate the functional groups, green triangles indicate the link group for multifunctional polymer chains).	10
Figure 2.2	Synthetic strategies for the preparation of polymer brushes: (A) Physisorption of diblock copolymers via preferential adsorption of the red blocks to the surface (grafting to approach). (B) Chemisorption via reaction of appropriately end-functionalized polymers with complementary functional groups at the substrate surface (grafting to approach). (C) Polymer brushes grown via surface-initiated polymerization techniques (grafting from approach).	13
Figure 2.3	Different architectures of polymer brushes that can be prepared via surface initiated controlled radical polymerization. (A) Block copolymer brushes. (B) Random copolymer brushes. (C) Cross-linked polymer brushes. (D) Free-standing polymer brushes. (E) Hyperbranched polymer brushes. (F) Highly branched polymer brushes. (G) Y-shaped binary mixed polymer brushes. (H) Standard binary mixed brushes. (I) Molecular weight gradient polymer brushes. (J) Grafting density gradient polymer brushes. (K, L) Chemical composition gradient polymer brushes.	14
Figure 2.4	Examples of polymer brushes synthesized by ATRP using “grafting from” approach from various functional substrates.	14
Figure 2.5	Examples for responses of responsive polymer brushes to physical or chemical stimuli. (A) Planar homopolymer brush: a homogeneous smooth layer of stretched chains in good solvent (1), pinned micelles (2) and a layer of collapsed chains (3) in poor solvent. (B) Cylindrical brushes and their responsive conformational changes: bending, contraction, compacting, and coiling.	16

Figure 2.6 Examples of single-molecule (red) and ensemble (green) molecular junctions. (A) Single molecule interrogated using a scanning tunneling microscopy (STM) or conducting probe atomic force microscopy (CP-AFM) tip. (B) Mechanical break junction formed by withdrawal of a sharp metal tip (e.g., STM tip) from a metallic surface. A molecule from solution fills the gap. (C) Example of a liquid metal junction formed by suspending an Hg drop over a metal surface (e.g. Ag) in a solution of thiol molecules, which absorb to form monolayers at both surfaces. Alternatively, a dithiol can be used to form a junction containing a single molecular layer. (D) Cross-wire junction formed at the intersection of two metallic wires, one of which is coated with a monolayer. (E) Planar cross-bar junction made by evaporating a metal onto a molecular layer covalently bonded to a carbon substrate. (F) A junction made using a conducting polymer as the top contact. 17

Figure 2.7 (A) Schematics of the alternative current (AC) modulated STM break junction measurement. (B) Direct current (DC) and AC components of current traces recorded during the pulling away stage in (a) pure mesitylene and in (b-d) mesitylene containing 0.2 mM 1,8′-octanedithiol. 18

Figure 2.8 (A) Illustration of the anatomy of a perfect junction, showing the van der Waals interface between the SAMs and the EGaIn/oxide top electrode. (B) Plot of $\ln|\langle J\rangle|$ (V) at -0.5 V against the chain length of the alkanethiols, given in number of carbons, for all SAMs as measured by a single user across either the odd- or even-numbered n-alkanethiols. The observed values of β from single users are not significantly different from those obtained from measurements of a group of five users. 21

Figure 2.9 Schematic illustration of junctions of the type Ag^{TS}–$SC_nFc//Ga_2O_3/EGaIn$ and the mechanism of charge transport across them. (a) Optical micrograph image of the tunnelling junction, showing a cone-shaped tip of Ga_2O_3/EGaIn suspended from a microneedle in contact with a SAM on a Ag^{TS} surface (left), schematic illustrations of "ideal" tunnelling junctions with SAMs of SC_nFc with n = 10 (middle) or 11(right). (b) Energy level diagrams of the junctions at a bias of +1.0 V (left) and -1.0 V (right). 22

Figure 2.10 The junctions of the form Ag^{TS}-SC_nFcC_{13}-n//Ga_2O_3/EGaIn. (a) Idealized schematic illustrations of the junctions with the Fc units in non-covalent contact with the bottom electrode defined as the left electrode (n = 24

3), (b) in the middle of the junction (n = 6), and (c) in non-covalent contact with the top electrode, defined as the right electrode (n = 13). The corresponding energy level diagrams for coupling with large (d) and minimal (e) molecular frontier orbital broadening. The dotted lines in (e) indicate schematically the flat (i) and ramp-like (ii, iii) electrostatic potential profiles.

Figure 2.11 (A) Molecular structure and synthetic route to OPI-p and OPI monolayers on Au electrodes. (B) Semilog plot of *R* vs. *L* for the Au/molecular wire/Au junctions. The inset shows a linear plot of *R* vs. *L*, demonstrating linear scaling of resistance with length for the long OPI wires. (C) Arrhenius plot for OPI 4, OPI 6, and OPI 10. 25

Figure 2.12 (A1) Molecular structure and (A2) schematic representations of the CP-AFM and (A3) the X-wire junction test structures. Illustration of charge-transport mechanism at 5 K: (B1) direct tunneling in junctions of Ru1 and Ru2 and (B2) sequential tunneling with Coulomb blockade in the Ru3 junctions. The electron flows are shown by arrows. 27

Figure 2.13 (A) *I*-*V* characteristics of Ru1, Ru2 and Ru3 SAMs obtained in CP-AFM, and (B) X-wire junctions at room temperature. (C) The semilog plot of *R* vs. *L* for junctions of Au/SAM/Au CP-AFM junctions. Data from five different tips with five trials are shown and are represented by different symbols. The error bars represent one standard deviation from the mean. 28

Figure 2.14 (A) Junction schematic cross section of carbon molecular junction, consisting of oligomers of bis-thienyl-benzene (BTB) between a carbon substrate and a carbon top contact. (B) Image of complete junction from above, showing three of the four contact probes. 29

Figure 2.15 Schematic representation of the stepwise assembly of the MCMWs in situ on metal surfaces: (A1) Assembly on the gold surface of the MPTP/MB 1:1 “platform” SAM. (A2) Coordination of the MC to the MPTP ligand. (A3) Coordination of the TPT ligand. (A4) The processes (A2) and (A3) are repeated iteratively to increase the length of the MCMWs by one metal-ligand unit up to the desired dimension (up to more than 40 nm). Electrical characterization of MCMWs: (B1) Photograph and schematic representation of the interface of the Au-MCMW/Hg junction. (B2) and (B3) *J*-*V* curves for Fe(II)- and Co(II)–based MWs. (B4) In *J* vs. *L* of the Fe(II)- and Co(II)–based MWs. (C) Energy diagram for junctions incorporating the Fe(II)- and Co(II)–based MWs. 31

Figure 2.16	Schematic representation plots of J versus respectively $1/d$ (A) and $1/d^2$ (B) for the Fe(II)-based MWs.	32
Figure 2.17	(A) Chemical structures of the materials used in the experiment. (B) Schematic diagram showing the b-PS brush modification on SiO_2 dielectrics. (C) XRR curves of b-PS1.6k and b-PS19.5k at room temperature (25 °C).	34
Figure 2.18	(A) Structure of bottom-gate top-contact OFET employed in this study. (B) Outline of process used to grow PMMA brushes from gold surface.	36
Figure 2.19	(A) Schematic illustration of surface-grafted PMMA brush dielectrics for copper phthalocyanine (CuPc) single-crystalline nanoribbon transistors: a) Silicon wafer (Si^{++}) with native oxide layers. b) Immobilization of the initiator. c) PMMA brush grafting via SI-ATRP technique. d) CuPc single-crystalline nanoribbon transistor with PMMA brush dielectric. (B) Schematic illustration of synthesis of surface-grafting PMMA brush on SiO2 as hybrid nanodielectric for organic field-effect transistors.	36
Figure 2.20	Schematic diagram of the top-contact-electrode OFETs fabricated with a PS brush film.	37
Figure 2.21	Schematic diagram illustrating the preparation of the polymer device.	38
Figure 2.22	Current density-voltage curves of the (a) ITO/g-PCEM/Al device (stands for the polymer brushes fabricated devices) and (b) ITO/PECM/Al device (stands for the spin-coating PCEM bulk polymer from solution) as the comparison.	39
Figure 2.23	(a) Schematic of the device fabrication using an integrated shadow mask. (b) Zoomed schematic of the junction structure, corresponding to the area within the white circle in (a). The red line is the poly(glycidyl methacrylate) (PGMA) anchoring layers. Polymer brushes of various compositions and thickness are grown from different concentrations of acrylamide (right) and acrylic acid (left) monomers in polymerizate solution. (c) The memory effect in polymer brush devices.	40
Figure 2.24	Overview of PTPAA brushes (A1) Scheme for the surface-initiated synthesis of PTPAA brush. (A2) Cartoon presentation of a polymer brush and spin-coated film. Right: Properties of the PTPAA brushes in device performance. (B1) Schematic diagram of the diode structure used for current density testing; (B2) Current density *vs.* applied bias for a sandwich structure device of	42

ITO/PTPAA (80 nm)/PEDOT : PSS/Au, with PTPAA brushes (solid line) and PTPAA spin-coated amorphous film (dashes line). Positive bias corresponds to hole injection from the PEDOT : PSS and negative bias corresponds to hole injection from the ITO. (C) Current density *vs.* applied bias for a unipolar diode made with 35 nm PTPAA films: brush (solid line), spin coated (dashed line).

Figure 2.25 The sequential photographs showing the formation of the conical EGaIn/GaO_X top electrode. 44

Figure 3.1 Chemical structures of selected monomers: FMMA, FBMA, and FNMA. 59

Figure 3.2 Chemical structures and abbreviations for all selected ligands and initiators in this work. dnNbpy indicates 4,4'-dinonyl-2,2'bipyridine, PMDETA indicates *N*,*N*,*N*,'*N*,'*N*''-pentamethyldiethyldiethylenetriamine, Me_6TREN indicates tris((*N*,*N*-dimethylamino)ethyl)amine, Me_4Cyclam indicates 1,4,8,11-tetramethyl-1,4,8,11-tetraazacyclotetradecane, EBiB initiator indicates ethyl 2-bromoisobutyrate, and silanebromo initiator indicates 3-trimethoxysilylpropyl 2-bromo-2-methyl-propionate 62

Figure 3.3 (A), (C), and (E) show the semi-logarithmic plots of ATRP with corresponding monomers. (B), (D) and (F) show the degree of polymerization plots of ATRP with corresponding monomer. PDI (in average value) for PFMMA, PFBMA, and PFNMA polymers are 1.4, 1.5 and 1.5, respectively. Dash lines serve as guiding lines. 67

Figure 3.4 Microscopic images of contact angles for corresponding samples in Table 3.3. 69

Figure 3.5 Collections of morphology of AFM images for 30 nm PFMMA brush (A), 32 nm PFBMA brush (B), and 24 nm PFNMA brush (C) with surface roughness (rms): 1.1 nm, 1.0 nm and 0.5 nm, respectively. All thickness shown here were measured by AFM scratches test with brush samples on Si/SiO_2 wafer. 71

Figure 3.6 (A) Morphology of the step height for AFM scratch of representative PFMMA brush sample on Si/SiO_2 wafer. (B) Cross section for corresponding scratch in (A). 72

Figure 3.7 A) UV/Vis spectrum of PFMMA, PFBMA, and PFNMA brush on ITO substrates. (B) The reference spectrum of Fc and free PFMMA polymer in solution. 73

Figure 3.8	FTIR-IRRAS spectrum for PFMMA, PFBMA, and PFNMA brush on ITO substrates with about 30 nm. Peaks assignments are shown upon red arrows.	74
Figure 3.9	(A) XPS survey scans for representative bare ITO, silanebromo-initiator modified ITO and PFMMA brushes with 3 different thicknesses. (B) Element scan for Si 2p. (C) Element scan for Br 3d.	76
Figure 3.10	(A) Overlay of In 3d peaks for intensity comparison. (B) Overlay of Fe 2p peaks for intensity comparison. (C) Intensity of In on the dependence of polymer brush thickness.	76
Figure 3.11	(A) CV scannings for representative PFMMA brushes generated within a serious of polymerization period. (B) Surface coverage of Fc groups estimated at scan rate was 1.00 V/s. The dash line is guiding line for eyes. The error bars represent for CV scannings of 3 individual samples.	78
Figure 3.12	Voltammetric parameters plot as the function of polymerization time.	79
Figure 3.13	The representative cyclic voltammogram for PFMMA brush. E_{pa} stands to the peak potential of the anodic peak, E_{pc} stands for the peak potential of the cathodic peak, and $E_{1/2}$ stands for the formal half-wave potential. Black solid lines and blue dash lines are guide lines for eyes.	81
Figure 3.14	Monomer structure with indicated side chain length using CPK model estimated by Avogadro software (version 1.1.1). Iron (brown), carbon (grey), hydrogen (white), and oxygen (red). Stick-ball structures below show the optimized monomers related to FMMA, FBMA, and FNMA. Cp rings (yellow), carbone (black), hydrogen (grey), and oxygen (red).	82
Figure 3.15	(A) Top view of the macromolecules polymerized by 10 repeating monomer units related to PFMMA, PFBMA, and PFNMA. Cp rings (yellow), carbone (black), hydrogen (grey), and oxygen (red). (B) Top view (left) and side view (right) of the PFNMA macromolecules polymerized by 50 repeating monomers.	83
Figure 3.16	Thickness correlations among CV calculation (□ with black line), AFM scratch test (○), and ellipsometry (○). Black dash lines sever as guiding line. Error bars stand for the standard deviations of 3 individual measurements.	88

Figure 3.17	Statistical histograms of the E values of (A) PFMMA, (B) PFBMA, and (C) PFNMA brushes measured in air (left column, blank histograms) and in DI water (right column, patterned histograms).	91
Figure 3.18	The correlation between glass transition temperature (T_g) for bulk polymers and Young's modulus ($E_{apparent}$, in air) for polymer brushes as the function of the number of CH_2 unit the linker (n).	91
Figure 3.19	TGA curves of PFMMA polymer (M_n = 37.3 kg/mol, black), PFBMA polymer (M_n = 34.9 kg/mol, red) and PFNMA (M_n = 39.5 kg/mol, blue), respectively. At a heating rate of 10°C/min from 40 to 1000°C under N_2 flow.	92
Figure 3.20	DSC traces (the second and third traces) of (A) PFMMA polymer (M_n = 37.3 kg/mol), (B) PFBMA polymer (M_n = 34.9 kg/mol), and (C) PFNMA (M_n = 39.5 kg/mol), respectively. The heating ranges are from 50 to 200°C, -10 to 155°C, and -40 to 100°C, for PFMMA, PFBMA, and PFNMA, respectively. The heating rate is 10°C/min for all.	93
Figure 4.1	(A) Representative CV plots of PFMMA brush (L_{PB} = 40 nm) as the function of scan numbers. (B) Anodic and cathodic current density (I_{pa} in black squares and I_{pa} in black circles) on the dependence of scan numbers. (C) peak-to-peak separation (ΔE) on the dependence of scan numbers. (D) Scan numbers on the dependence of thickness. Dashed lines are guide lines for eyes. Error bars were obtained from repeated measurements on parallel samples. All data referred to PFMMA brushes.	111
Figure 4.2	Representative cyclic voltammograms of PFMMA brush film on ITO substrate in aqueous solution with 1.0M $HClO_4$ as electrolyte by continuously scanning CV curves. Scan rate = 1.00 V/s.	112
Figure 4.3	Dependence of scan rate based on representative samples of PFMMA (A), PFBMA (B), PFNMA (C) brush, respectively, with the scan rates $\boldsymbol{v}$ range from 0.01, 0.02, and 0.05 V/s (insets) and 0.10, 0.20, 0.50, 1.00, 2.00, and 5.00 V/s (main panels).	113
Figure 4.4	Stacked cyclic voltammograms of a representative PFMMA brush sample with large thickness (~55 nm) as the function of scan rates. Note that the panel D has different units for current.	115

Figure 4.5	Plots of voltammetric parameters as the function of scan rates. (A) log(scan rates) *vs.* peak-to-peak separation (ΔE). (B) Peak potential (E_{pa}-$E^{0'}$) *vs.* ln(scan rates). (C) log(scan rates) *vs.* log(I_{pa}) and log(I_{pc}). (D) log(scan rate) *vs.* full width at half maximum (FWHM). Solid lines are fitting lines.	116
Figure 4.6	Cyclic voltammograms of the representative PFMMA brush samples with thickness in (A) 23 nm, (B) 42 nm, and (C) 55 nm. The representative PFBMA brush samples with thickness in (D) 28 nm, (E) 40 nm, and (F) 50 nm. The representative PFNMA brush samples with thickness in (G) 25 nm, (H) 38 nm, and (I) 48 nm at the lowest scan rate (0.001V/s).	118
Figure 4.7	(A) I_{pa} increase depends on scan rates (5.00 V/s – 0.01 V/s) as the function of thickness. (B) I_{pa} increase depends on the square root of scan rates (5.00 V/s – 0.01 V/s) as the function of thickness. (C) I_{pa} increase depends on scan rates as the function of thickness (0.20 V/s – 0.01 V/s). Dashed lines are fitting lines. (D) Peak separations depend on scan rates in *ln* scale (5.00 V/s – 0.01 V/s) as the function of thickness. (E) Voltammetric plots recorded at 1.00 V/s as the function of thickness. (F) I_{pa} (■) and I_{pc} (♦) increases depend on thickness and the inset shows the ratio of I_{pa} vs. I_{pc} depends on thickness.	120
Figure 4.8	(A) The surface charge transfer coefficient, αn_a, as the function of surface coverage of Fc units. (B) The standard rate constant, k^0, as the function of surface coverage of Fc units. (C) The apparent diffusion coefficient, D_{app}, as the function of surface coverage of Fc units. Error bars are from the data fitting. Dash lines are fitting lines.	124
Figure 5.1	AFM scratch test for five representative samples that applied to temperature dependent measurements.	141
Figure 5.2	CV plots for five representative samples that applied to temperature dependent measurements.	141
Figure 5.3	(A) Average $\lvert J\rvert(V)$ curves of the ITO–PFMMA brush// GaO_X / EGaIn in semi-log scale for L_{PB} in 8 nm, 43 nm, respectively. (B) Histograms of the rectification ratio log(R), $R = \lvert J(-1.5V)\rvert/\lvert J(+1.5V)\rvert$ shown with Gaussian fits for corresponding samples in (A).	142
Figure 5.4	The relationships between the thickness of polymer brushes (L_{PB}) and rectification ratios R in log value are shown in (A), (B), and (C), for PFMMA, PFBMA, and	145

PFNMA brushes, respectively. The relationships between the thickness of polymer brushes (L_{PB}) and current density J in log value at +1.5 V and -1.5 V are shown in (D), (E), and (F) for PFMMA, PFBMA, and PFNMA brushes, respectively. Error bars are standard deviations, grey dash lines are served at guide to the eyes.

Figure 5.5 Stability test of current density recorded at constant bias of $|V| = 1.5$ V for 100 scans for 8 nm PFMMA brush sample. (A) J(V) curves of cone-shape tip junction measured the same sample on same spot over 100 scans. (B) Current density values on +1.5 and -1.5 bias as the function of scan numbers. 146

Figure 5.6 Transition points corresponding to PFMMA brush, PFBMA brush and PFNMA brush. 146

Figure 5.7 (A) The stacked average $\log_{10}|J|$ curves of ITO – PFMMA brush // GaO_x / EGaIn junctions for original (black square), 1.5 months after (red dot), and 4.0 months after (blue triangle) junctions. (B) The stacked histograms of the values of R (= $|J(-1.5V)|/|J(+1.5V)|$) with a Gaussian fit to these histograms for corresponding J(V) curves in panel (A), original (black column), 1.5 months after (pink column), and 4.0 months after (blue column). 147

Figure 5.8 (A) Current density J on the dependence of PFMMA brush thickness L_{PB} in log-log plots on negative bias at higher voltages range. (B) Current density J on the dependence of the voltage V on negative bias ($1.2 \text{ V} < |V| < 3.0 \text{ V}$) in log-log scales for PFMMA brush with a group of thickness. Colored dash lines are fitting lines for corresponding plots. Values of slopes (k) are shown. 149

Figure 5.9 J(V) in log-log plots on negative bias in full voltage range ($0 \text{ V} < |V| < 3.0 \text{ V}$) at 300 K for 47 nm PFMMA brush. The solid line indicates the linear fitting at higher voltage ($1.2 \text{ V} < |V| < 3.0 \text{ V}$). 150

Figure 5.10 Thermally activated charge transport across ITO – PFMMA brush // GaO_X / EGaIn junctions. (A) J(V) linear scale plot as the function of T for 47 nm polymer brush sample at the voltage $|V| = 3.0$ V. inset image shows the values of $|J|$ measured at -3.0 and +3.0 V as a function of temperature. (B) J(V) plots in log-log scale at the negative bias ($1.9 \text{ V} < |V| < 3.0 \text{ V}$) as the function of T for 47 nm polymer brush sample. Colored dash lines indicate the linear fitting. (C) Exponent l *vs.* $1/T$ plots.Black dash line indicates the linear fitting. Error bars for all data points indicate the fitting errors from (B). (D) $\ln|J|$ on negative 151

	bias at $\|V\|$ = 3.0 V as the function of $1/T$, black dash line indicates the linear fitting.	
Figure 5.11	(A) J(V) in semi-log plot as the function of temperature for 6 nm polymer brush on the bias $\|V\|$ = 3.0 V. (B) ln$\|J\|$ values on bias $\|V\|$ = 3.0 V as the function of temperature.	154
Figure 5.12	The representative ultra-photon spectra of bare ITO and PFMMA polymer brush (L_{PB} = 12 nm) modified ITO. The cut offs on the left side refer to the work function. The inset figure shows the zoom-in spectra for high energy range (~ 20 eV), and the cut-off for the hump refers to the HOMO level relatives to E_f. Blue dash lines are guide lines for eyes.	155
Figure 5.13	$J(V)$ curves averaged from 10 measurement traces for PMMA brushes with two thicknesses: 6 nm and 15 nm.	157
Figure 5.14	a) Top, b) back and c) side views of PDMS device.	161
Figure A1	^{1}H NMR spectrum by $CDCl_3$ for PFMMA bulk polymer.	175
Figure A2	^{1}H NMR spectrum by $CDCl_3$ for PFBMA bulk polymer.	175
Figure A3	^{1}H NMR spectrum by $CDCl_3$ for PFNMA bulk polymer.	176
Figure A4	Ellipsometry data for samples shown in Figure 3.15(A).	178
Figure A5	Ellipsometry data for samples shown in Figure 3.15(B).	180
Figure A6	Ellipsometry data for samples shown in Figure 3.15(C).	182
Figure A7	CV data for building theoretical thickness plot shown in Figure 3.15(A).	183
Figure A8	CV data for building theoretical thickness plot shown in Figure 3.15(B).	184
Figure A9	CV data for building theoretical thickness plot shown in Figure 3.15(C).	184
Figure A10	Stacked cyclic voltammograms of a representative PFBMA brush sample with large thickness (~48 nm) as the function of scan rates.	185
Figure A11	Plots of voltammetric parameters as the function of scan	186

rates. (A) log(scan rates) *vs.* peak-to-peak separation (ΔE). (B) Peak potential (E_{pa}-$E^{0'}$) *vs.* ln(scan rates). (C) log(scan rates) *vs.* log(I_{pa}) and log(I_{pc}). (D) log(scan rate) *vs.* full width at half maximum (FWHM). Solid lines are fitting lines.

Figure A12 Stacked cyclic voltammograms of a representative PFNMA brush sample with large thickness (~40 nm) as the function of scan rates. 186

Figure A13 Plots of voltammetric parameters as the function of scan rates. (A) log(scan rates) *vs.* peak-to-peak separation (ΔE). (B) Peak potential (E_{pa}-$E^{0'}$) *vs.* ln(scan rates). (C) log(scan rates) *vs.* log(I_{pa}) and log(I_{pc}). (D) log(scan rate) *vs.* full width at half maximum (FWHM). Solid lines are fitting lines. 187

Figure A14 The average $\log_{10}|J|$ curves of ITO – PFMMA brush // GaO_x / EGaIn junctions and histograms of the values of R (= $|J(-1.5V)|/|J(+1.5V)|$) with a Gaussian fit to these histograms. L_{PB} stands for the thickness of PFMMA brush, and σ in parentheses stands for the standard deviation. 188

Figure A15 The average $\log_{10}|J|$ curves of ITO – PFBMA brush // GaO_x / EGaIn junctions and histograms of the values of R (= $|J(-1.5V)|/|J(+1.5V)|$) with a Gaussian fit to these histograms. L_{PB} stands for the thickness of PFBMA brush, and σ in parentheses stands for the standard deviation. 189

Figure A16 The average $\log_{10}|J|$ curves of ITO – PFNMA brush // GaO_x / EGaIn junctions and histograms of the values of R (= $|J(-1.5V)|/|J(+1.5V)|$) with a Gaussian fit to these histograms. L_{PB} stands for the thickness of PFNMA brush, and σ in parentheses stands for the standard deviation. 190

Figure A17 J(V) curves measured at room temperature on bias $|V|$ = 3.0 V with EGaIn device. 191

Figure A18 Thermally activated charge transport across ITO – PFMMA brush // GaO_X / EGaIn junctions. (A) J(V) linear scale plot as the function of T for 42 nm polymer brush sample at the voltage $|V|$ = 3.0 V. inset image shows the values of $|J|$ measured at -3.0 and +3.0 V as a function of temperature. (B) J(V) plots in log-log scale at the negative bias (1.9 V < $|V|$ < 3.0 V) as the function of T for 42 nm polymer brush sample. Colored dash lines indicate the linear fitting. (C) Exponent l *vs.* $1/T$ plots. Black dash line indicates the linear fitting. Error bars for all data points indicate the fitting errors from (B). (D) $\ln|J|$ on negative bias at $|V|$ = 3.0 V as the function of $1/T$, black dash line 192

indicates the linear fitting.

Figure A19 Thermally activated charge transport across ITO – PFMMA brush // GaO_X / EGaIn junctions. (A) J(V) linear scale plot as the function of T for 36 nm polymer brush sample at the voltage $|V| = 3.0$ V. inset image shows the values of $|J|$ measured at -3.0 and +3.0 V as a function of temperature. (B) J(V) plots in log-log scale at the negative bias ($1.9\ V < |V| < 3.0\ V$) as the function of T for 36 nm polymer brush sample. Colored dash lines indicate the linear fitting. (C) Exponent l *vs.* $1/T$ plots. Black dash line indicates the linear fitting. Error bars for all data points indicate the fitting errors from (B). (D) $\ln|J|$ on negative bias at $|V| = 3.0$ V as the function of $1/T$, black dash line indicates the linear fitting. 193

Figure A20 Thermally activated charge transport across ITO – PFBMA brush // GaO_X / EGaIn junctions. (A) J(V) linear scale plot as the function of T for 43 nm polymer brush sample at the voltage $|V| = 3.0$ V. inset image shows the values of $|J|$ measured at -3.0 and +3.0 V as a function of temperature. (B) J(V) plots in log-log scale at the negative bias ($1.9\ V < |V| < 3.0\ V$) as the function of T for 43 nm polymer brush sample. Colored dash lines indicate the linear fitting. (C) Exponent l *vs.* $1/T$ plots. Black dash line indicates the linear fitting. Error bars for all data points indicate the fitting errors from (B). (D) $\ln|J|$ on negative bias at $|V| = 3.0$ V as the function of $1/T$, black dash line indicates the linear fitting. 194

Figure A21 Thermally activated charge transport across ITO – PFNMA brush // GaO_X / EGaIn junctions. (A) J(V) linear scale plot as the function of T for 42 nm polymer brush sample at the voltage $|V| = 3.0$ V. inset image shows the values of $|J|$ measured at -3.0 and +3.0 V as a function of temperature. (B) J(V) plots in log-log scale at the negative bias ($1.9\ V < |V| < 3.0\ V$) as the function of T for 42 nm polymer brush sample. Colored dash lines indicate the linear fitting. (C) Exponent l *vs.* $1/T$ plots. Black dash line indicates the linear fitting. Error bars for all data points indicate fitting errors from (B). (D) $\ln|J|$ on negative bias at $|V| = 3.0$ V as the function of $1/T$, black dash line indicates linear fitting. 195

List of Abbreviations

Fc	Ferrocene
Fc^+	Ferrocenium ion
CuBr	Copper(I) bromide
$CuBr_2$	Copper(II) bromide
Me_4Cyclam	1,4,8,11-tetramethyl-1,4,8,11-tetraazacyclotetradecane
dnNbpy	4,4'-dinonyl-2,2'-bipyridine
EBiB	Ethyl 2-bromoisobutyrate
Silanebromo-initiator	3-trimethoxysilylpropyl 2-bromo-2-methyl-propionate
DMF	*N,N*-dimethylformamide
THF	Tetrahydrofuran
AR EtOH	absolute ethanol
ACN	Acetonitrile
Me_6TREN	Tris((*N,N*-dimethylamino)ethyl)amine
PMDETA	*N,N,N,'N,''N''*-Pentamethyldiethylenetriamine
AFM	Atomic Force Microscopy
CV	Cyclic Voltammetry
WCA	Water Contact Angle
FWHM	Full Width at Half Maximum
SCE	Saturated Calomel Electrode
NHE	Normal Hydrogen Electrode
SHE	Standard Hydrogen Electrode
DI	Deionized
OPI	Oligophenyleneimines
Ru1, Ru2, Ru3	Ruthenium (II) bis(σ-arylacetylide)
BTB	Bis-thienyl-benzene

MCWMs	Metal centres molecular wires
HMDS	Hexamethyldisilazane
ODTS	Octadecyltrichlorosilane
PS	Polystyrene
XRR	X-ray reflectivity
PVF	Poly(vinylferrocene)
PAAc	Poly(acrylic acid)
PTPAA	Poly(triphenylamine acrylate)
PAM	Polyacrylamide
TPA	Triphenylamine
EGDMA	Ethylene glycol dimethacrylate
PEDOT : PSS	Poly(3,4-ethylene dioxythiophene) doped with poly(styrene sulfonate)
NBA	n-butyl acetate
NMP	Nitroxide-mediate polymerization
ROMP	Ring-opening metathesis polymerizations
SI-ROMP	Surface-initiated ring-opening metathesis polymerizations
CuPc	Copper phthalocyanine
PCEM	Poly(2-(N-carbazolyl)ethyl methacrylate)
WORM	Write-once read many times
PGMA	Poly(glycidyl methacrylate)
FTIR-IRRAS	Fourier Transform Infrared Spectroscopy- Infrared Reflection Absorption Spectroscopy
UV/Vis	Ultraviolet–visible spectroscopy
CRP	Controllable Radical Polymerization
RAFT	Reversible Addition-Fragmentation Chain Transfer Polymerization
ATRP	Atom Transfer Radical Polymerization
SI-ATRP	Surface-initiated Atom Transfer Radical Polymerization

TGA	Thermogravimetric Analysis
DSC	Differential Scanning Calorimetry
PDI	Polydispersity Index
Endo	Endothermic
NMR	Nuclear Magnetic Resonance
SFA	Surface Forces Apparatus
UPS	Ultraviolet Photoelectron Spectroscopy
HOMO	Highest Occupied Molecular Orbital
LUMO	Lowest Unoccupied Molecular Orbital
IP	Ionization Potential
WF	Work Function
VBM	Valence Band Maximum
E_f	Fermi level
rms	Root Mean Square
SAMs	Self-assembled Monolayers
UHV	Ultra-High Vacuum
XPS	X-ray Photoelectron Spectroscopy
a. u.	Atomic units
EGaIn	Eutectic alloy Gallium and Indium
GaO_X	Gallium Oxide
ITO	Indium Tin Oxide
PDMS	Polydimethylsiloxane
RT	Room Temperature
FMMA	Ferrocenylmethyl methacrylate
FBMA	Ferrocenylbutyl methacrylate
FNMA	Ferrocenylnonyl methacrylate
PFMMA	Polyferrocenylmethyl methacrylate
PFBMA	Polyferrocenylbutyl methacrylate

PFNMA	Polyferrocenylnonyl methacrylate
L_{PB}	Thickness/Length of Polymer Brush
ILC	Injection Limited Conduction
SCLC	Space Charge Limited Conduction
TFSCLC	Trap Free Space Charge Limited Conduction
TFLSCLC	Trap Filling Space Charge Limited Conduction

List of Symbols

I_{on}	Current in the conducting direction
I_{off}	Current in the insulating direction
T_g	Glass transition temperature
M_n	The number average molecular weight
M_w	The weight average molecular weight
F	The applied load
	Faraday constant = 96500 C/mol
r_{tip}	The radius of the colloidal probe
r	Radius of column in polymer brush packing
	Linear relation coefficient
n	Refractive index
	The carbon number of the linker
	Number of electrons per mole of reaction
N	Number of repeating units of monomers
v	The Poisson's ration of the polymer films
v *or* c	Speed of light = 3.0×10^8 m/s
E	The apparent Young's modulus
A	Electrical contact area
N_A	Avogadro constant
N_{disk}	Number of disk in per cm^2
A_{total}	Total area that expose to electrolyte, equals 1 as we assumed
$A_{each\ disk}$	Occupied area for each disk
$A_{vacancy}$	Occupied area for vacancy among the disks
υ	Scan rate
Γ_{Fc}	Surface coverage/density of Fc
Cp	Cyclopentadiene

d	Thickness of the SAMs
	Thickness of the polymer/polymer brush film
$E_{1/2}$	Half-wave potential
E_{fwhm}	Full width at half maximum
E_{pa}	Peak oxidation potential
E_{pc}	Peak reduction potential
$E^{0'}$	Apparent formal potential
$E_{1/2}$	Formal half-wave potential
ΔE_p	Peak separation
ΔE_{ME}	Molecule-electrode offset energy
I_{pa}	Anodic peak current
I_{pc}	Cathodic peak current
i_p	Anodic/cathodic peak current
R	Gas constant = 8.31447 J/(Kmol)
T	Temperature = 298.15 K
Q_{tot}	Total charge
D_{app}	Apparent diffusion coefficient
C_0^*	Concentration of the electroactive species in the film
k^0	Standard rate constant
α	Transfer coefficient
σ_{log}	Log-standard deviation
σ	Standard deviation
V	Applied bias
J	Current density
X	Redox-active group
ε_s	Relative permittivity or Material permittivity
ε_0	Vacuum permittivity = 8.854×10^{-12} C/(Vm)
Φ	Work function

h	Planck's constant = 6.626×10^{-34} J▪s
e *or* q	Elementary charge = 1 eV = 1.602×10^{-19} C
λ	Wavelength
E_a	Activation barrier
μ	Mobility
N_v	Carrier density
H_t	Trap density
E_t	Trap energy
k_B	Boltzman constant = 1.38×10^{-23} J/K
T_c	Characteristic temperature
l	A defined parameter = T_c / T
k	Slope of the linear fitting

Chapter 1

General Introduction

1.1 Introduction

Molecular electronics studies the applications of molecular building blocks as electronic components, and now they influence the mechanism of charge transport in devices[1] such as memories[2], diodes[3,4] and switches[5]. Developing molecular electronic devices with desirable electronic components is one of the major goals in molecular electronics. The challenges for the design of the molecular electronic devices mainly centre on three aspects: (1) the lack of knowledge of the mechanism of charge transports through organic matters,[6] (2) how the supramolecular structures of these organic matters would affect the device performance[7], and (3) what the role of the contacts between molecules and electrodes could play[8].

Polymers are interesting candidates to use as building blocks in electronic devices because their properties can be fine-tuned to optimize electronic performance of the desired electronic function via chemical synthesis.[9,10] The polymer-electrode interfaces have different properties than the bulk materials and are difficult to control.[11] Especially challenging are to control the energy level alignment of the system which, for instance, plays a crucial role in charge injection rates.[12-19] The supramolecular structure of the polymer itself – the way the polymer chains interact with each other and the electrode – is equally important and plays, for instance, an important role in the mobility.[12,16,20-27]

Polymer brushes are a kind of molecular brush/polymer that consists of end-tethered polymer chains stretching away from the substrate with the distance between grafting points (*d*) is smaller than the chain end-to-end distance.[28] These brushed form well-

defined structures with the polymer chains in vertical position with respect to the surface normal and are therefore popular choice in surface science.[29-33] For instance, polymer brushes have been used in plications related to energy storage,[34-36] photovoltaics,[37-40] biofouling,[41-43] self-cleaning surfaces,[44-46] and as active component in smart materials.[9,30]

Polymer brushes are typically a few to a hundred nanometers thick and thus fall in between the nanometer length scale of SAMs and hundreds of nm thick layers of organic thin films. Therefore we it seems to be interesting to replace SAMs as the active component with polymer brushes in electronic devices because polymer brushes allow to induce electronic function and are potentially more stable than SAMs.[9] From a fundamental point of view, these brushes in principle allow for studying the mechanism of charge transport at the nm length scales where tunnelling dominates (as is the case in SAM based junctions) and the 10-100 nm length scale where hopping dominates (as is the case in polymer thin films). A transition from tunnelling to hopping has only been observed in a handful of systems. [47-51]

In this thesis, we replaced the simple, small molecules of a SAM polymer brushes in junction and investigated their charge transport behaviour in two-terminal junctions. Here used polymer brushes decorated with ferrocene (Fc) moieties[52,53] as the functional groups because Fc has excellent electrochemical characteristics (stable and reversible) and provides a low lying HOMO (highest occupied molecular orbital) which is needed to tune the charge transport phenomena. We used the well-known EGaIn technique to fabricate the junctions and with this platform[54] we studied the mechanism of charge transport as function of bias, temperature and both length of the polymer brush and tether that connects the Fc to the back bone of the polymer brush.

Chapter 1

This thesis is organized as follows. Chapter 2 gives a detailed literature of polymer brushes. We introduce the background for growing functional polymer brushes and review their applications as well as recent progress in molecular electronics. Chapter 3 describes in detail the synthesis and characterization of the polymer brushes with controllable thickness and different tether lengths that connect the Fc units to the polymer. Along with structural characterization we also investigated the thermal s as well as the mechanical properties of the brushes. Interestingly, brushes with small tethers are fully standing up and form near-ideal structures in air (i.e., without the support of a liquid). Chapter 4 describes long-range electrochemical behaviour of the Fc-containing polymer brushes, by cyclic voltammetry as a function of the length of the side chain and the thickness of the brush. It was found that the electrochemical process strongly depended on the scan rates and the thickness of polymer brush, rather than the side chain length: electrochemical process can achieve reversible behaviour at either very low san rate (such as 0.005V/s) or with very thin brush (such as 5 nm). Chapter 5 describes our main findings on charge transport studies based on EGaIn junctions: 3 sets of Fc-containing polymer brushes were measured by EGaIn techniques, and the rectification ratios were listed to help estimating the charge transport mechanism. Furthermore, the temperature dependent measurements were conducted to reveal the space charge limited conduction as electron hopping mechanism for thick polymer brush in more detail. Finally, Chapter 6 summarizes the main conclusions of this thesis and discusses briefly what directions of research could be pursued next.

1. 2 References

1. Coskun, A.; Spruell, J. M.; Barin, G.; Dichtel, W. R.; Flood, A. H.; Botros, Y. Y. and Stoddart, J. F., *Chem. Soc. Rev.* **2012,** *41* (14), 4827-4859.

2. Zhu, H.; Hacker, C. A.; Pookpanratana, S. J.; Richter, C. A.; Yuan, H.; Li, H.; Kirillov, O.; Ioannou, D. E. and Li, Q., *Appl. Phys. Lett.* **2013,** *103* (5), 053102.

3. Nijhuis C. A.; Reus, W. F. and Whitesides, G. M., *J. Am. Chem. Soc.* **2010,** *132* (51), 18386-18402.

4. Nijhuis, C. A.; Reus, W. F.; Barber, J. R.; Dickey, M. D. and Whitesides, G. M., *Nano lett.* **2010,** *10* (9), 3611-3619.

5. Dionne, E. R.; Sultana, T.; Norman, L. L.; Toader, V. and Badia, A., *J. Am. Chem. Soc.* **2013,** *135* (46), 17457-17468.

6. Lindsay, S. M.and Ratner, M. A., *Adv. Mater.* **2007,** *19* (1), 23-31.

7. Kornilovitch, P. E.; Bratkovsky, A. M. and Stanley Williams, R., *Phys. Rev. B.* **2002,** *66* (16), 165436-165447.

8. Haick, H. and Cahen, D., *Prog. Surf. Sci.* **2008,** *83* (4), 217-261.

9. Azzaroni, O., *J. Polym. Sci. Pol. Chem.* **2012,** *50* (16), 3225-3258.

10. Jaiswal, M. and Menon, R., *Polym. Int.* **2006,** *55* (12), 1371-1384.

11. Joanny, J. F., *Interface Sci.* **2003,** (11), 157-158.

12. Snaith, H. J.; Whiting, G. L.; Sun, B.; Greenham, N. C.; Huck, W. T. S.; Friend, R. H., *Nano lett.* **2005,** *5* (9), 1653-1657.

13. Yoon, M.-H.; Kim, C.; Facchetti, A. and Marks, T. J., *J. Am. Chem. Soc.* **2006,** *128* (39), 12851-12869.

14. Park, S. H.; Lee, H. S.; Kim, J.-D.; Breiby, D. W.; Kim, E.; Park, Y. D.; Ryu, D. Y.; Lee, D. R. and Cho, J. H., *J. Mater. Chem.* **2011,** *21* (39), 15580-15587.

15. Park, K.; Park, S. H.; Kim, E.; Kim, J.-D.; An, S.-Y.; Lim, H. S.; Lee, H. H.; Kim, D. H.; Ryu, D. Y.; Lee, D. R. and Cho, J. H., *Chem. Mater.* **2010,** *22* (18), 5377-5382.

16. Whiting, G. L.; Snaith, H. J.; Khodabakhsh, S.; Andreasen, J. W.; Breiby, D. W.; Nielsen, M. M.; Greenham, N. C.; Friend, R. H. and Huck, W. T. S., *Nano lett.* **2006,** *6* (3), 573-578.

17. Alonzi, M.; Lanari, D.; Marrocchi, A.; Petrucci, C. and Vaccaro, L., *RSC Advances* **2013,** *3* (46), 23909-23923.

18. Rutenberg, I. M.; Scherman, O. A.; Grubbs, R. H.; Jiang, W.; Garfunkel, E. and Bao, Z., *J. Am. Chem. Soc.* **2004,** *126* (13), 4062-4063.

19. Pinto, J. C.; Whiting, G. L.; Khodabakhsh, S.; Torre, L.; Rodríguez, A.; Dalgliesh, R. M.; Higgins, A. M.; Andreasen, J. W.; Nielsen, M. M.; Geoghegan, M.; Huck, W. T. S. and Sirringhaus, H., *Adv. Funct. Mater.* **2008,** *18* (1), 36-43.

20. Marsh, R. A.; Hodgkiss, J. M.; Albert-Seifried, S. and Friend, R. H., *Nano Lett.* **2010,** *10* (3), 923-930.

21. Kim, J.-S.; Ho, P. K. H.; Murphy, C. E. and Friend, R. H., *Macromolecules* **2004,** *37* (8), 2861-2871.

22. Howard, I. A.; Laquai, F.; Keivanidis, P. E.; Friend, R. H. and Greenham, N. C., *J. Phys. Chem. C* **2009,** *113* (50), 21225-21232.

23. Huettner, S.; Sommer, M.; Hodgkiss, J.; Kohn, P.; Thurn-Albrecht, T.; Friend, R. H.; Steiner, U. and Thelakkat, M., *ACS Nano* **2011,** *5* (5), 3506-3515.

24. Guo, X.; Facchetti, A. and Marks, T. J., *Chem. Rev.* **2014,** *114* (18), 8943-9021.

25. Chang, J.-F.; Sun, B.; Breiby, D. W.; Nielsen, M. M.; Sölling, T. I.; Giles, M.; McCulloch, I. and Sirringhaus, H., *Chem. Mater.* **2004,** *16* (23), 4772-4776.

26. Coropceanu, V.; Li, H.; Winget, P.; Zhu, L. and Brédas, J.-L., Annu. Rev. Mater. Res. **2013,** *43* (1), 63-87.

27. Zhang, X.; Shim, J. W.; Tiwari, S. P.; Zhang, Q.; Norton, J. E.; Wu, P.-T.; Barlow, S.; Jenekhe, S. A.; Kippelen, B.; Bredas, J.-L. and Marder, S. R., *J. Mater. Chem.* **2011,** *21* (13), 4971-4982.

28. Milner, S. T., *Science* **1991,** *251*, 905-915.

29. Chen, T.; Ferris, R.; Zhang, J.; Ducker, R. and Zauscher, S., Prog. Polym. Sci. **2010,** *35* (1–2), 94-112.

30. Minko, S., *J. Macromol. Sci., Polym. Rev.* **2006,** *46* (4), 397-420.

31. Yameen, B. and Farrukh, A., *Chem.-Asian J.* **2013,** *8* (8), 1736-1753.

32. Langer, R., *Acc.Chem. Res.* **2000,** *33* (2), 94-101.

33. Ishaug-Riley, S. L.; Okun, L. E.; Prado, G.; Applegate, M. A. and Ratcliffe, A., *Biomaterials* **1999,** *20* (23–24), 2245-2256.

34. Wang, Q.; Evans, N.; Zakeeruddin, S. M.; Exnar, I. and Grätzel, M., *J. Am. Chem. Soc.* **2007,** *129* (11), 3163-3167.

35. Sum, E. and Skyllas-Kazacos, M., *J. Power. Source.* **1985,** *15* (2–3), 179-190.

36. Vlad, A.; Singh, N.; Rolland, J.; Melinte, S.; Ajayan, P. M. and Gohy, J. F., *Sci. Rep.* **2014,** *4* (4315), 1-7.

37. Kim, J. S.; Park, J. H.; Lee, J. H.; Jo, J.; Kim, D.-Y. and Cho, K., *Appl. Phys. Lett.* **2007,** *91* (11), 112111-112114.

38. Choi, J. K.; Jin, M. L.; An, C. J.; Kim, D. W. and Jung, H. T., *ACS Appl. Mater. Interfaces.* **2014,** *6* (14), 11047-11053.

39. Knesting, K. M.; Hotchkiss, P. J.; MacLeod, B. A.; Marder, S. R. and Ginger, D. S., *Adv. Mater.* **2012,** *24* (5), 642-646.

40. MacLeod, B. A.; Horwitz, N. E.; Ratcliff, E. L.; Jenkins, J. L.; Armstrong, N. R.; Giordano, A. J.; Hotchkiss, P. J.; Marder, S. R.; Campbell, C. T. and Ginger, D. S., *J. Phys. Chem. Lett.* **2012,** *3* (9), 1202-1207.

41. Banerjee, I.; Pangule, R. C. and Kane, R. S., *Adv. Mater.* **2011,** *23* (6), 690-718.

42. Li, Y.; Giesbers, M.; Gerth, M. and Zuilhof, H., *Langmuir* **2012,** *28* (34), 12509-12517.

43. Yang, J.; Chen, H.; Xiao, S.; Shen, M.; Chen, F.; Fan, P.; Zhong, M. and Zheng, J., *Langmuir* **2015,** *31* (33), 9125-9133.

44. Howarter, J. A. and Youngblood, J. P., *Adv. Mater.* **2007,** *19* (22), 3838-3843.

45. Zhang, L.; Zhang, Z. and Wang, P., *NPG Asia Mater.* **2012,** *4*, e8.

46. Anastasiadis, S. H., *Langmuir* **2013**, 29 (30), 9277-9290.

47. Ho Choi, S.; Kim, B. and Frisbie, C. D., *Science*, **2008**, *320*, 1482-1486.

48. Kim; Beebe, J. M.; Jun, Y.; Zhu, X. Y.; Frisbie, C. D., *J. A. C. S.* **2006,** *128* (15), 4970-4971.

49. Luo, L.; Balhorn, L.; Vlaisavljevich, B.; Ma, D.; Gagliardi, L. and Frisbie, C. D., *J. Phys. Chem. C* **2014,** *118* (46), 26485-26497.

50. Luo, L.; Choi, S. H. and Frisbie, C. D., *Chem. Mater.* **2011,** *23* (3), 631-645.

51. Beebe, J.; Kim, B.; Gadzuk, J.; Daniel Frisbie, C. and Kushmerick, J., *Phys. Rev. Lett.* **2006,** *97* (2).

52. Luo, L.; Benameur, A.; Brignou, P.; Choi, S. H.; Rigaut, S. and Frisbie, C. D., *J. Phy. Chem. C* **2011,** *115* (40), 19955-19961.

53. Kealy, T. J. and Pauson, P. L., *Nature* **1951,** *168* (4285), 1039-1040.

54. Amer, W.; Wang, L.; Amin, A.; Ma, L. and Yu, H., *J. Inorg. Organomet. P.* **2010,** *20* (4), 605-615.

55. Chiechi, R. C.; Weiss, E. A.; Dickey, M. D. and Whitesides, G. M., *Angew Chem* **2008,** *47* (1), 142-144.

Chapter 2

Applications of Functional Polymer Brushes in Molecular Electronic Field

In this chapter we reviewe some earlier works based on two aspects: (1) Synthesis and characterizations of polymer brushes and their applications in molecular organic field. (2) Charge transport studies based on (macro)molecular junctions, where the both two electrodes (top and bottom electrodes) and the materials in between are the key components. In the end of the review, we summarize the limitations and gaps in previous reported work, followed by introducing the objective, significance and scope of our current work.

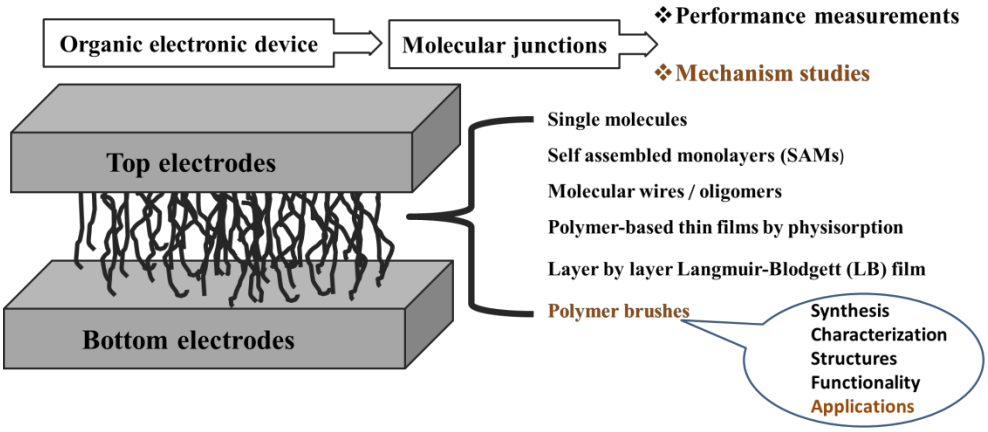

Chapter 2

2.1 Introduction

Polymers, unlike small molecules or oligomers, consist of nearly unlimited numbers of monomers. This makes it possible for polymers to have more complex structure to tune their properties. Polymer brushes[1], which align perpendicularly to the surface, in principle, are stable against delamination and are an important branch in polymer field. Both the synthesis techniques and characterization techniques for polymers are mature after almost 60 years' development.[2] Section 2.2 gives more background on the functional polymer/polymer brush synthesis.

To date, charge transport through polymer or polymer based devices is a hot field, and it is essential to improve the stability of the devices and performance by understanding the basic physics. To investigate the charge transport mechanisms, some fundamental studies, such as electric characteristics, are required.

The term "molecular junction" came into use in the few last decade, and a molecular junction incorporates one or more molecules in electrical contact with two conductors, such that electrons are transmitted through the molecules.[3] Molecular junctions can be consisted of self-assembled monolayers (SAMs), or molecular wires (e.g., conjugated oligomers). Previous applications of polymers in electronics are in the form of polymer thin films, and there are few studies on polymer brushes in this area. Section 2.3 gives an overview of the development of organic electronic devices and their related charge transport studies in past decades, including some examples of polymer brushes applications in this field. Section 2.4 describes the limitations and gaps in previous work. Section 2.5 and 2.6, a summary will be given in the final part of this review as well as the objective and scope of my current work.

Chapter 2

2.2 Synthesis of functional polymer brush by controlled methods

A polymer is a macromolecule composed of repeating subunits linked by covalent chemical bonds.[2] The excellent and some particular mechanical and technical properties of polymers resulted from their high molecular mass. In terms of polymer brush, it is a kind of surface immobilized polymer, whose chains at one side are end-tethered on the substrate and the other side stretch away from the substrate.[1,4,5] They are grafted from the substrates with chemical bonds. Polymer thin films, as an analogy of polymer brushes, however, are normally made by spin-coating or simply casting a polymer solution on a surface, forming a physisorbed thin film.[6] These thin films that provide little control over film structure compared with polymer brushes, the latter one also, in principle, provides better control over the size, sequence, conformation and spatial distribution of functional building blocks.[7] In the following subsections, we will generally introduce the synthesis methods for functional polymer brushes.

2.2.1 Living radical/controlled polymerization (CRP)

Functional polymers with special physical or chemical properties have replaced other materials in many areas including electrical or optical microelectronics. There are several methods to generate functional polymers, among which, a technique called "controlled/living radical polymerization" (CRP) developed in 1990s[8] has gained significant attention in the past decade.

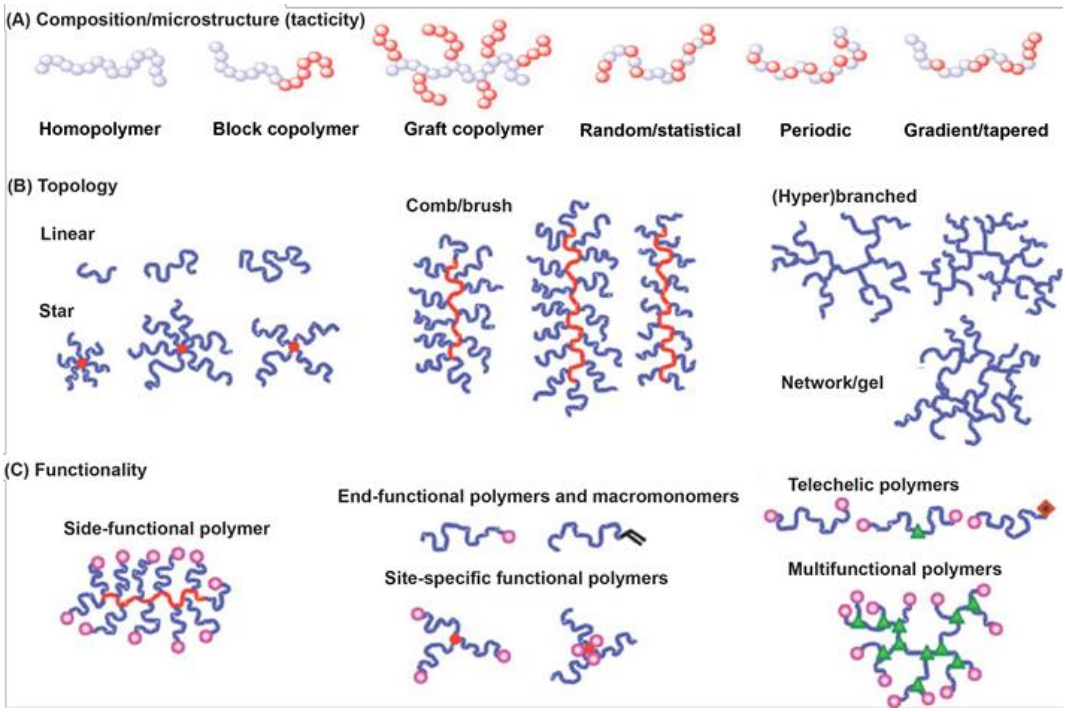

Figure 2.1 Examples of controlled macromolecular architecture in polymers prepared by ATRP. (A) Controlled composition/microstructure (white dots and red dots indicate the different repeated monomer units). (B) Controlled topology (red lines indicate the polymer main chain and blue lines indicate the graft polymer chains). (C) Controlled functionality (red lines indicate the polymer main chain and blue lines indicate the graft polymer chains, pink dots indicate the functional groups, green triangles indicate the link group for multifunctional polymer chains).[9] Reprinted with permission: 2009, Nature Publishing Group.

The CRP, where chain termination reactions are absent and all chains are instantaneously initiated and grow simultaneously[9], is a quite popular technique to access to new functional and well-defined polymers.[10] As one of the most outstanding CPR techniques, atom transfer radical polymerization (ATRP)[11,12] gives access to polymers with precisely controlled molecular weight, relatively low polydispersity index (PDI = M_w/M_n < 1.1), and controlled molecular architecture in terms of chain topology (stars, cycles, combs, brushes, regular networks), composition (block, graft, alternating, gradient copolymers), and diverse functionalities (See Figure 2.1).[9] Current status and future perspectives in ATRP are presented by Krzysztof Matyjaszewski in his recent review.[13]

2.2.2 Surface-initiated atom transfer radical polymerization (SI-ATRP)

ATRP is based on the reversible reaction of an alkyl halide (RX, as initiator, R represents for the alkyl part), with a low oxidation-state metal complex (Mt^m/L, as catalyst). Mt^m represents the metal ion in oxidation state m, and L is a ligand (normally the charges of ionic species are omitted for simplicity). This reaction yields radicals and the corresponding high-oxidation-state metal complex with a coordinated halide ligand (X-Mt^{m+1}/L, as deactivator).[14] Many polymerizations have been carried out under homogeneous catalyst conditions which usually offer better control due to the sufficient high concentration of deactivator comparing to heterogeneous catalyst condidions.[15] The equilibrium is shown in Scheme 2.1.

Scheme 2.1 Mechanism of metal complex-mediated ATRP.[13] Reprinted with permission: 2012, American Chemical Society.

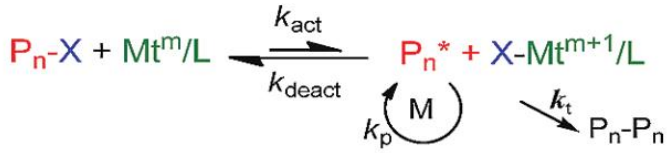

In this equilibrium, P_n-X is macromolecular dormant species: the polymer chain with halogen active head. Mt^m/L is the transition metal species in lower oxidation state m with L as ligand, playing as activator. M represents the monomers in solution with k_p as the rate constants of propagation. P_n^* is the growing radical. X-Mt^{m+1}/L is the transition metal species in higher oxidation state, coordinated with the halide ligands. k_t is the sum of k_{tc} (the combination rate constant) and k_{td} (the disproportionation rate constant). P_n-P_n represents the termination by chain-chain coupling. The total reaction rate K_{ATRP} is determined by the rate constant of activation, k_{act} and the rate constant of deactivation,

k_{deact}. Normally, the polymerization proceeds in a controlled manner (high conversion and low dispersity) when $k_{deact} > k_{act}$.

There are mainly two approaches to fabricate polymer brushes with covalent attachment: "grafting to" approaches and "grafting from" approaches.[16] The former one involves the attachment of a living polymer to a separately prepared backbone polymer containing reactive functional moieties along the chain. While the shortcoming of this is that the grafting density is limited since the attachment will become progressively more difficult with the increasing steric congestion between the already grafted chains and the incoming macromolecular units from solution. Hence, in turn it precludes the access of new polymer chains to grafting sites on the surface.[7] On the other side, the "grafting from" approach involves the preparation of the backbone polymer with a predetermined number of initiation sites which are subsequently used to initiate polymerization.[17] This approach is more attractive since it can achieve higher grafting density. However, one of the disadvantages of this approach is that the grafting reactions are not easy to quantify.[18] Figure 2.2 shows three synthetic strategies for the preparation of polymer brushes including "grafting to" approach and "grafting from" approach.

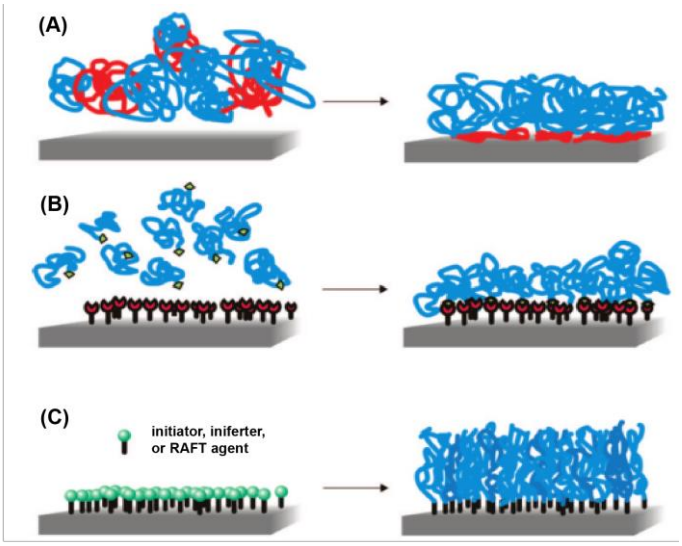

Figure 2.2 Synthetic strategies for the preparation of polymer films: (A) Physisorption of diblock copolymers via preferential adsorption of the red blocks to the surface (grafting to approach). (B) Chemisorption via reaction of appropriately end-functionalized polymers with complementary functional groups at the substrate surface (grafting to approach). (C) Polymer brushes grown via surface-initiated polymerization techniques (grafting from approach).[16] Reprinted with permission: 2009, American Chemical Society.

For the "grafting from" approach, the initiator employed is not a simple alkyl halide (a free, small molecule, such as 2-bromoisobutyryl bromide, which is commonly applied to solution polymerization) but consists of an anchoring group (could be thiol[19,20], carboxylic acid,[21] phosphoric acid[22] and alkoxysilane[20,23] or chlorosilane[24,25], which dependents on the selection of substrates), an aliphatic alkyl spacer,[26] and an ATRP initiator group (alkyl halide).

Scheme 2.2 "Grafting from" method to immobilize polymer chains on substrate.

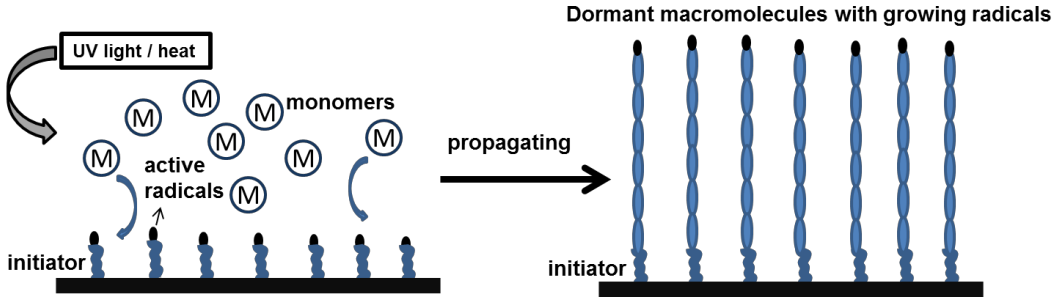

This initiator is not free but anchored on the surface, such ATRP is defined as surface-initiated atom transfer radical polymerization (SI-ATRP). It is chemically extremely versatile, can tolerate a relatively high degree of impurities and is compatible with a large assortment of monomers and functional groups. A variety of polymer brush architectures could be prepared through SI-ATRP, as is shown in Figure 2.3.[16]

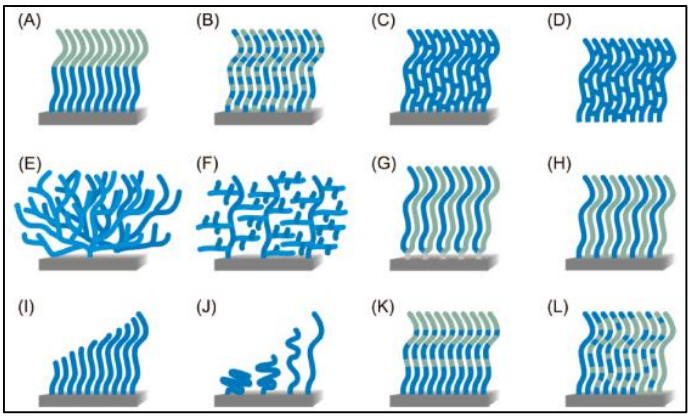

Figure 2.3 Different architectures of polymer brushes that can be prepared via surface initiated controlled radical polymerization. (A) Block copolymer brushes. (B) Random copolymer brushes. (C) Cross-linked polymer brushes. (D) Free-standing polymer brushes. (E) Hyperbranched polymer brushes. (F) Highly branched polymer brushes. (G) Y-shaped binary mixed polymer brushes. (H) Standard binary mixed brushes. (I) Molecular weight gradient polymer brushes. (J) Grafting density gradient polymer brushes. (K, L) Chemical composition gradient polymer brushes.[16] Reprinted with permission: 2012, American Chemical Society.

Figure 2.4 shows examples of "grafting from" approaches used to tether functional polymer brushes on a wide variety of substrates.[27] To date, a variety of substrates have been applied to SI-ATRP, such as indium tin oxide (ITO),[28] silicon wafer,[29] silica,[30] gold particles,[31] flat gold[32,33] and copper,[34] celluloses,[35] carbon nanotubes[36] and graphene/graphene oxide[37-41].

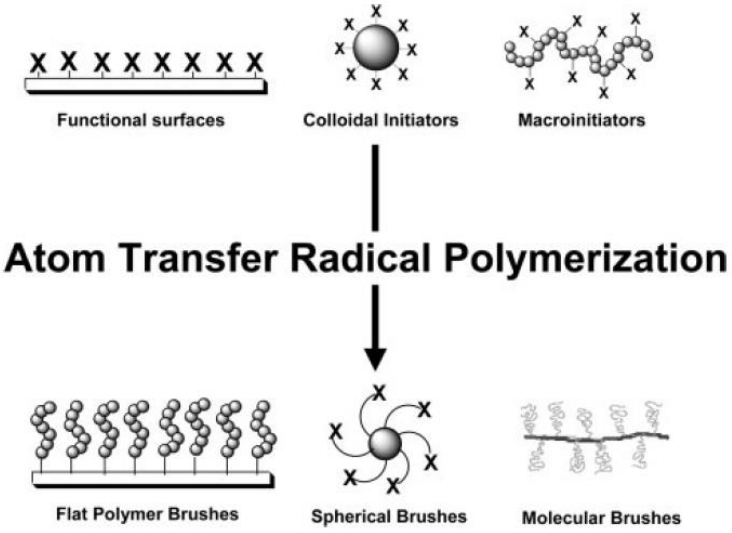

Figure 2.4 Examples of polymer brushes synthesized by ATRP using "grafting from" approach from various functional substrates.[27] Reprinted with permission: 2003, John Wiley and Sons.

2.2.3 Properties of functional polymer brushes

Multicomponent polymers/polymer brushes, possessing more complex structures than homopolymers, naturally offer more possibilities for surface modification. Applying functional polymer brushes as thin films for surface functionalization have attracted great attentions to create varieties of intelligent surfaces. The physical properties of functional polymers include the solution properties, bulk properties, and thin film properties.[42] Normally, for functional polymer brushes, control the molecular conformation using external stimuli (light, solvent, magnetic field and so on) may activate the related physical properties. Such changes in physical properties may in turn affect the chemical response of the polymers/polymer brushes, then the surface properties of the material will vary in response to environment variations. We define them as the responsive polymers/polymer brushes for their direct stimulus controls of physicochemical properties. Nowadays, polymer brushes for the light-switchable, thermal responsive, redox responsive, pH-responsive and so on[7,43-46], have an enormous potential to functionalize the surface, fabricating the multifunctional devices. Different functional groups contribute different effects to polymer brush in certain situation, which makes them have their practical applications. Omar Azzaroni[7], Basit Yameen[44] and Sergiy Minko[43] have reviewed some practical application of such so-call “responsive” polymer brush. However, this “responsive” polymer brush field is not in the scope for the main target in our research so here in this literature review we will not discuss them in details. In the following sections, we will put our focuses on another aspect: applications of polymer brushes in organic electronic devices.

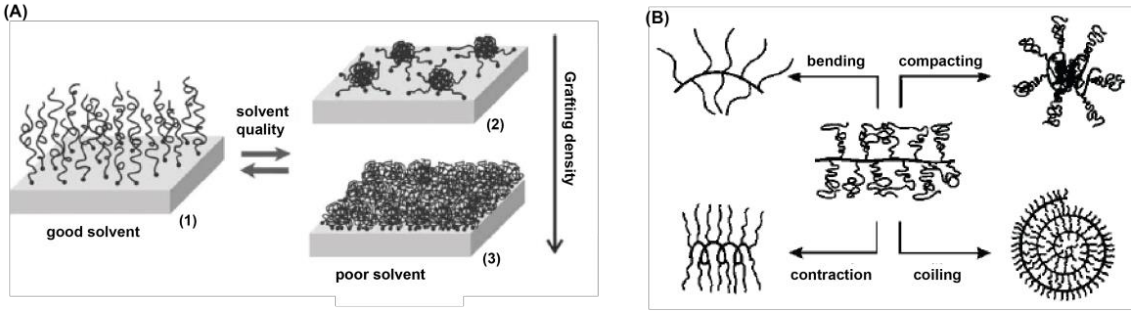

Figure 2.5 Examples for responses of responsive polymer brushes to physical or chemical stimuli. (A) Planar homopolymer brush: a homogeneous smooth layer of stretched chains in good solvent (1), pinned micelles (2) and a layer of collapsed chains (3) in poor solvent. (B) Cylindrical brushes and their responsive conformational changes: bending, contraction, compacting, and coiling.[43] Reprinted with permission: 2006, Taylor and Francis Group.

2.3 Development of organic electronic devices: studies on charge transport process

Material science that concerns the synthesis, characterizations, design and applications of organic small molecules or macromolecules (polymers) are generally defined as the organic electronic field. The materials applied in such organic electronic devices show desirable electronic properties, for instance, conductivity, resistance, and capacitance and so on. Organic electronic materials are built from organic small and large molecules utilizing synthetic approaches, which are different with the conventional inorganic conductors and semiconductors. Categories for these organic materials are roughly classified as: single molecules, self-assembled monolayers (SAMs), molecular wires/oligomers, polymer thin film through physisorption, and polymer brushes. In the following sections, we will present some literature to enumerate the applications.

2.3.1 Molecular junctions

The basic elements of molecular junctions, generally speaking, include three aspects: two electrodes (top electrode and bottom electrode), and one organic material (the

molecules) in between. To date, a large number of studies have shown the great interests in the relationship between molecular structures and intrinsic charge transport properties.

Molecular junctions are readily divided into two types: single molecule and self-assembled monolayers (SAMs).[47] Six examples of these two types of junctions are shown in Figure 2.6. As we can see from the examples, there are different length scales applied to the molecular junction studies, for instances, SAMs with short molecular distance (~ 1 nm to 2 nm) or some long, π-conjugated oligomers with relatively longer molecular distance (> 10 nm).

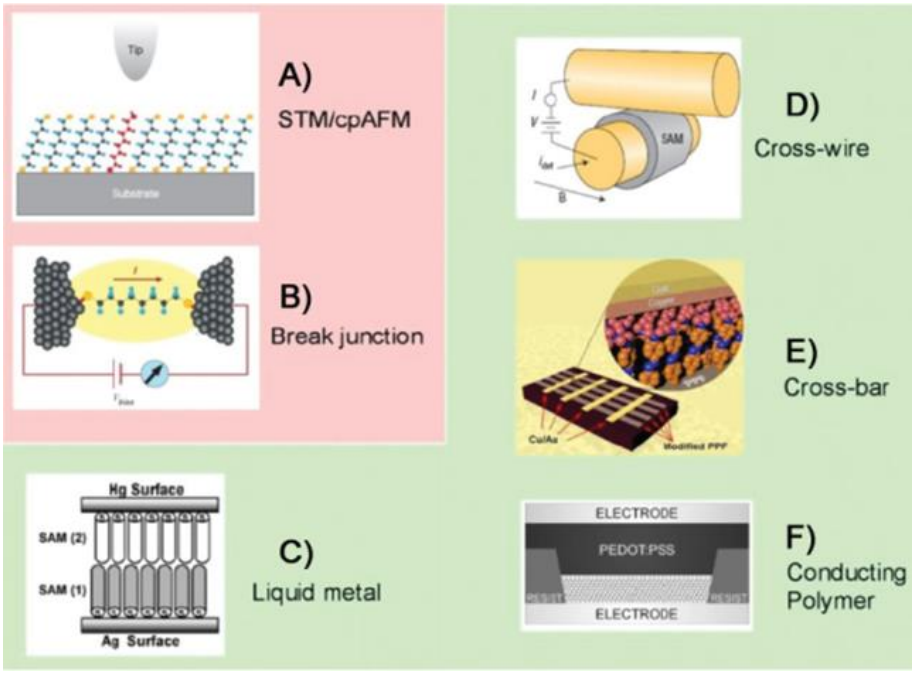

Figure 2.6 Examples of single-molecule (red) and ensemble (green) molecular junctions. (A) Single molecule interrogated using a scanning tunneling microscopy (STM) or conducting probe atomic force microscopy (CP-AFM) tip. (B) Mechanical break junction formed by withdrawal of a sharp metal tip (e.g., STM tip) from a metallic surface. A molecule from solution fills the gap. (C) Example of a liquid metal junction formed by suspending an Hg drop over a metal surface (e.g. Ag) in a solution of thiol molecules, which absorb to form monolayers at both surfaces. Alternatively, a dithiol can be used to form a junction containing a single molecular layer. (D) Cross-wire junction formed at the intersection of two metallic wires, one of which is coated with a monolayer. (E) Planar cross-bar junction made by evaporating a metal onto a molecular layer covalently bonded to a carbon substrate. (F) A junction made using a conducting polymer as the top contact.[47] Reprinted with permission: 2009, Taylor and Francis Group.

2.3.1.1 Single-molecule based junctions

The single molecule junction was first proposed about half century ago.[48] Experimental studies of such junctions include Langmuir–Blodgett (LB) films[49] or SAMs, both of which involve many molecules, and single molecule junction[50] involves limited molecules (ideally only one). Single molecule junctions are often realized using scanning tunneling microscopy (STM) or conducting probe atomic force microscopy (CP-AFM) based break junction technique.[51]

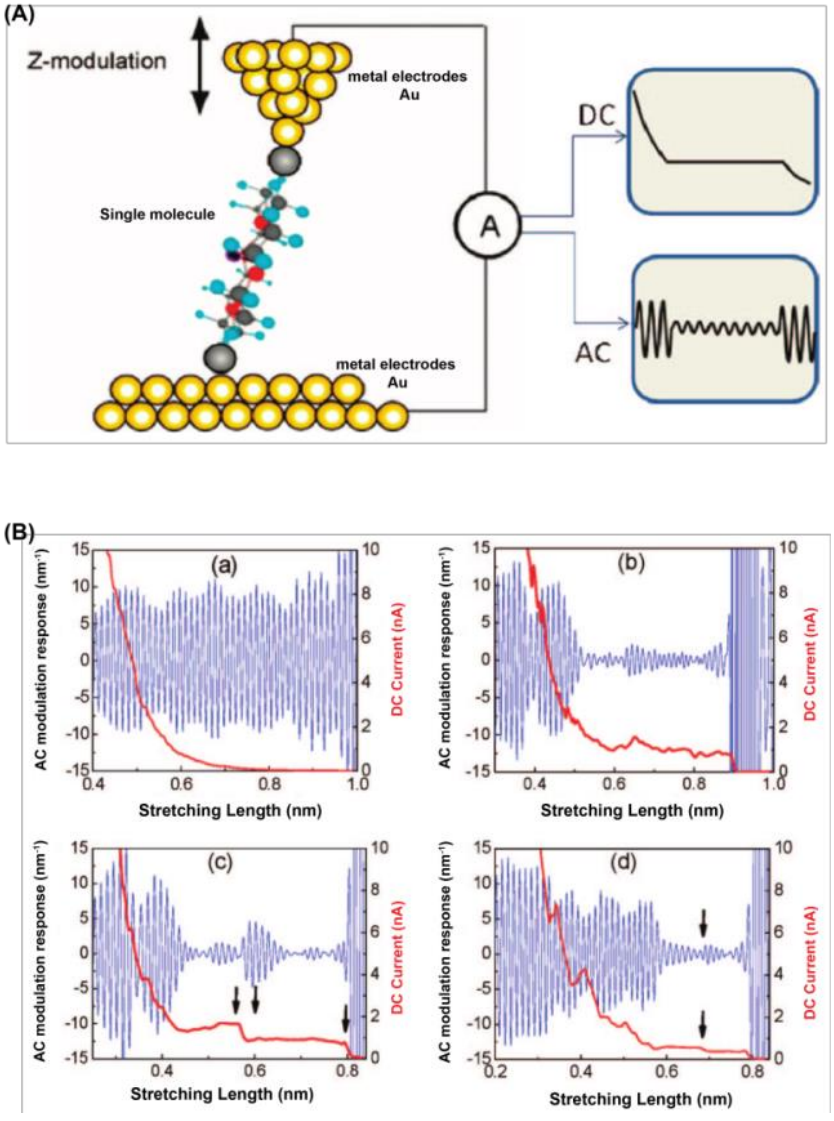

Figure 2.7 (A) Schematics of the alternative current (AC) modulated STM break junction measurement. (B) Direct current (DC) and AC components of current traces recorded during the pulling away stage in (a) pure mesitylene and in (b-d) mesitylene containing 0.2 mM 1,8′-octanedithiol.[51] Reprinted with permission: 2008, American Chemical Society.

The basic principle of the method is sketched in Figure 2.7(A). By moving an STM tip towards an electrode gradually, tunneling current could reach a preset value, then pulling the tip back until the current decrease to zero. A large number of transient current traces could be generated during the individual pulling stage, which is a controllable and automatically repeated process. The usual current transient traces are given by the direct current (DC) component, but the alternative current (AC) component measures the current response induced by the tip-substrate distance modulation.[51] Figure 2.7(B) shows several examples of the DC and AC components of the current transient curves measured in pure mesitylene and in mesitylene containing 0.2 mM octanedithiol. It is worth noting in pure mesitylene, the DC component is a smooth exponential decay curve. The AC component plotted in the figure is normalized by the DC component and by the z modulation amplitude (A_0).

2.3.1.2 SAMs based molecular junctions

One important component that applied commonly in the molecular junctions is SAMs. We studied the charge transport on SAM-based tunnelling junction with EGaIn technique (which will be discussed in the following subsections).[52-54] In the past, the defects of the molecular junctions,[55] the effects of molecular length[54], structure[56], and contact-dependent[52] transport characteristics were carefully studied.

Rectification ratio (R, as is shown in eq 2.1) is the ratio between electrical currents through the junction in the conducting and insulating directions, which is used to obtain a quantitative value for the $R = I_{on}/I_{off}$. This ratio could be used to judge if the material may be a good rectifier.

$$R = |J(-V)| / |J(V)| \qquad (2.1)$$

Another important parameter, β, in both single molecule and SAM-based junctions describes the attenuation of the current through the junction as a function of the distance between the contacts (as is shown in eq 2.2)

$$J = Be^{-\beta d} \qquad (2.2)$$

where J is the current density, B is a constant, and d is the distance between top and bottom contacts. In general, d is approximately presented by the length of the molecule of interest, although changes in molecular length with added methylene groups are predictable, the absolute value of d may be affected by contact geometry and composition.[47]

Figure 2.8 shows the work that compared charge transport across SAMs of n-alkanethiols containing odd and even numbers of methylenes.[54] They formed metal-SAMs//GaO_X/EGaIn junctions ("-" stands for a chemisorbed contact, "/" indicates the interface between the GaO_X and bulk EGaIn, "//" indicates the presence of a non-covalent interface) by ultraflat template-stripped silver (Ag^{TS}) surfaces supporting the SAMs and top electrodes of eutectic gallium-indium (EGaIn with a thin layer of GaO_X[57,58]) contacting the SAMs. Conical electrodes of EGaIn partially conform to SAMs, generating high yields of working junctions. The charge transport between n-alkanethiols with odd and even numbers of methylenes was observed to be different, as is shown in the plots from Figure 2.8(B).

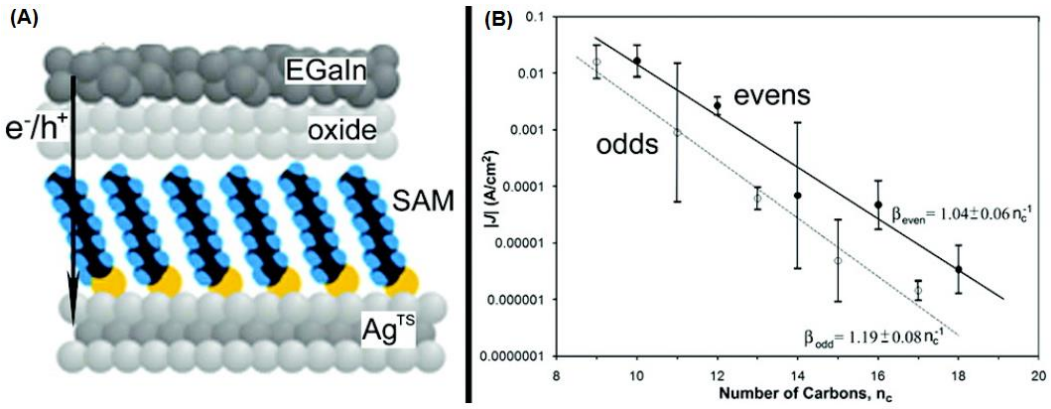

Figure 2.8 (A) Illustration of the anatomy of a perfect junction, showing the van der Waals interface between the SAMs and the EGaIn/oxide top electrode. (B) Plot of ln|<*J*>| (V) at -0.5 V against the chain length of the alkanethiols, given in number of carbons, for all SAMs as measured by a single user across either the odd- or even-numbered n-alkanethiols. The observed values of β from single users are not significantly different from those obtained from measurements of a group of five users.[54] Reprinted with permission: 2011, American Chemical Society.

A molecular electronic device is technically complicated to design and fabrication because it consists of at least two electrodes, an organic component and two (different) organic/inorganic interfaces. It is challenging to singling out the contribution of each of these components. Nijhuis et al. further studied the complex physical-organic systems in certain molecular electronic devices, relating the performance and electronic function of devices to the chemical structure and intermolecular interactions of the organic component inside them.[53] They have found that, experimentally subtle changes in the intermolecular van der Waals interactions in the active component of a molecular diode may dramatically impact the performance of the device. Particularly, an odd-even effect as the number of alkyl units varied in a Fc-alkanethiolate SAMs was observed: for odd number Fc-alkanethiolate SAMs, the rectify currents were 10 times more efficiently, giving a 10% higher yield in working devices, and having two to three times more reproducibly than junctions made from an even number SAMs.

The key conception of this work is shown by schematic illustration in Figure 2.9. The difference in the tilt angle of the Fc units with respect to the surface normal suggests the different interactions in the molecule-electrode interface. The energy diagram depicts that at negative/forward bias, when the molecular diode allows current to pass through, the highest occupied molecular orbitals (HOMO) level centred at the Fc units falls between the energy windows of both Fermi levels of two electrodes, participating in the mechanism of charge transport (Figure 2.9 b, right). It is a two-step mechanism of charge transport involves both tunnelling and hopping: an electron firstly tunnels from the

HOMO of the Fc across the alkyl chain to the bottom electrode, followed by hopping of an electron to the Fc unit in a second step. The length of the alkyl chain determined the width of the tunnelling barrier. While at positive/reverse bias, when the diode blocks the current, this HOMO level cannot participate in the mechanism of charge transport since it falls below both Fermi levels of two electrodes (Figure 2.9 b, left). As a result, the whole tunnelling barrier is formed as the whole length of the molecules (alkyl length and Fc unit distance).

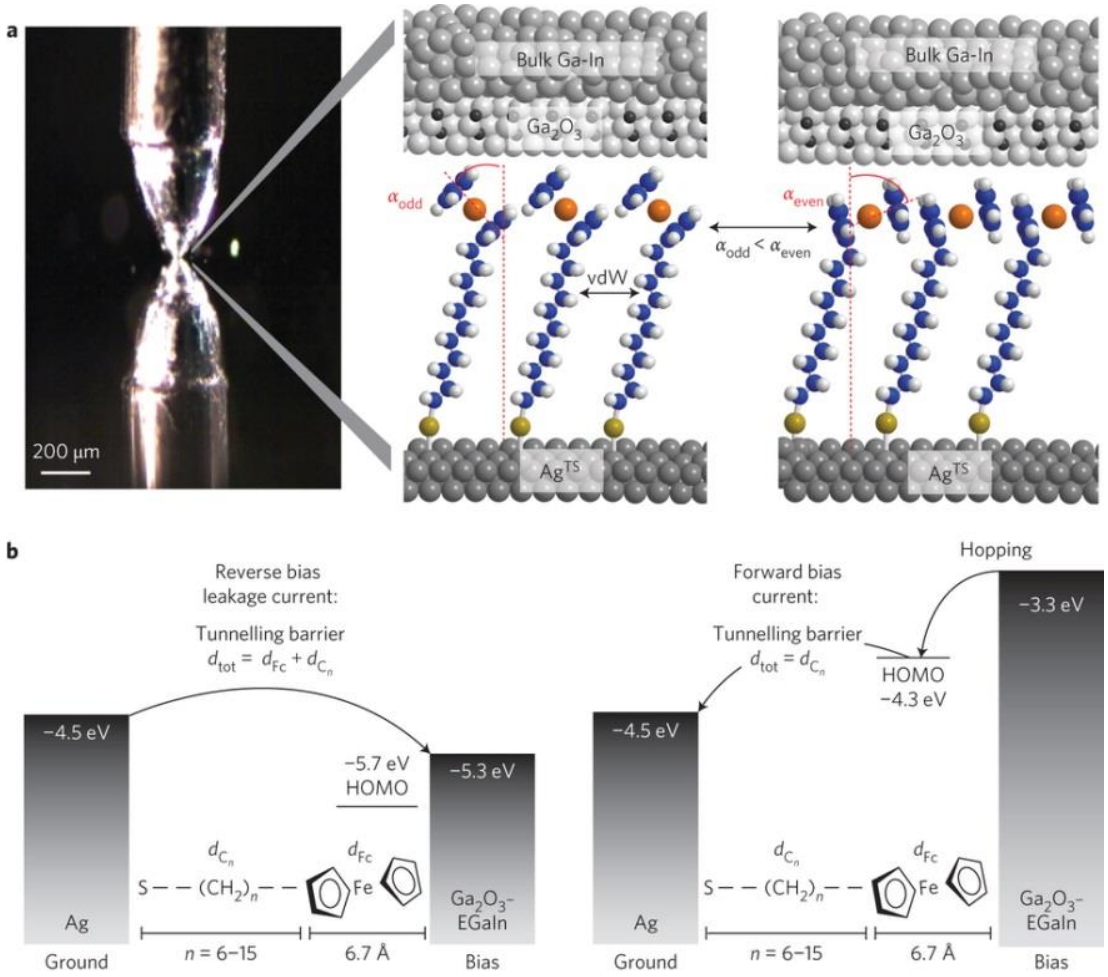

Figure 2.9 Schematic illustration of junctions of the type Ag^{TS}–SC_nFc//Ga_2O_3/EGaIn and the mechanism of charge transport across them. (a) Optical micrograph image of the tunnelling junction, showing a cone-shaped tip of Ga_2O_3/EGaIn suspended from a microneedle in contact with a SAM on a Ag^{TS} surface (left), schematic illustrations of "ideal" tunnelling junctions with SAMs of SC_nFc with n = 10 (middle) or 11(right). (b) Energy level diagrams of the junctions at a bias of +1.0 V (left) and -1.0 V (right).[53] Reprinted with permission: 2013, Nature Publishing Group.

Controlling the strength of the molecule-electrode coupling to optimize device performance is another challenge in molecular electronics. Yuan et al. showed that non-covalent contacts between the active molecular component, such as a ferrocenyl-alkanethiol SAM and the electrodes allow for robust coupling with minimal energy broadening of the molecular level.[56] They have found that the large energy broadening, leakage currents and poor device performance were resulted from the strong chemisorbed contacts through the ferrocenyl. It is possible to control the direction of rectification by subtly altering the ferrocenyl-electrode coupling parameters via gradually shifting the ferrocenyl from the top to the bottom of the SAMs. Such demonstrated control of the molecule-electrode coupling is important in rational designing of materials which rely on charge transport through organic-inorganic interfaces.

Figure 2.10 indicates the concept of the work described above. The schematics illustrate that the spatial disposition of the HOMO level (centred on Fc units) with respect to the electrodes can be controlled as a function of *n* (*n* stands for the alkyl linkers which are flexible and the average Fc–electrode distances estimated by molecular dynamic simulations). In Figure 2.10, the dashed arrows indicate how the Fc unit couples to the electrodes and the curved arrows in the energy diagrams (d and e) indicate the bias-dependent change.

Fabrication of the molecular electronic device by such SAMs based junction and study their charge transport behaviour is another tough task in this field. Channels in small arrays implanted polydimethylsiloxane (PDMS), and generated the SAMs based junctions by pumping EGaIn into the channels as top electrode, and ultraflat metal substrate as bottom electrode. The device fabrication procedures will be further discussed in later subsections.[59,60]

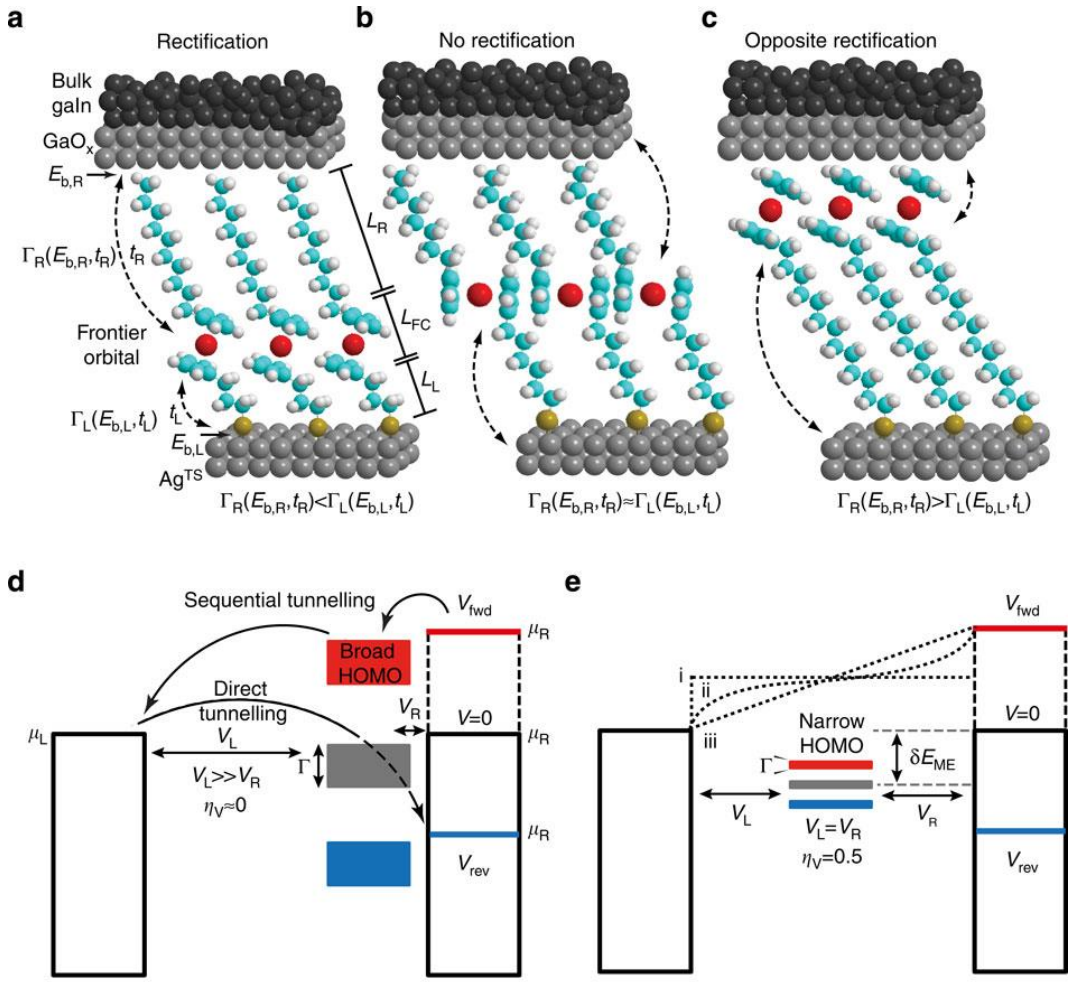

Figure 2.10 The junctions of the form Ag^{TS}-SC_nFcC_{13-n}//Ga_2O_3/EGaIn. (a) Idealized schematic illustrations of the junctions with the Fc units in non-covalent contact with the bottom electrode defined as the left electrode (n = 3), (b) in the middle of the junction (n = 6), and (c) in non-covalent contact with the top electrode, defined as the right electrode (n = 13). The corresponding energy level diagrams for coupling with large (d) and minimal (e) molecular frontier orbital broadening. The dotted lines in (e) indicate schematically the flat (i) and ramp-like (ii, iii) electrostatic potential profiles.[56] Reprinted with permission: 2015, Nature Publishing Group.

2.3.1.3 Molecular wires/oligomers based molecular junctions

Instead of normal alkanethiolate SAM based molecular junctions, the molecular wires/oligomers based junction is also a hot topic in electronics. The dominant mechanism of charge transport across molecular junctions is determined by molecular length.[61,62] Hence, they applied molecular wires/oligomers to the molecular junctions

studies since molecular wires/oligomers normally possess longer molecular length and the molecular length is possible to control by synthesis.

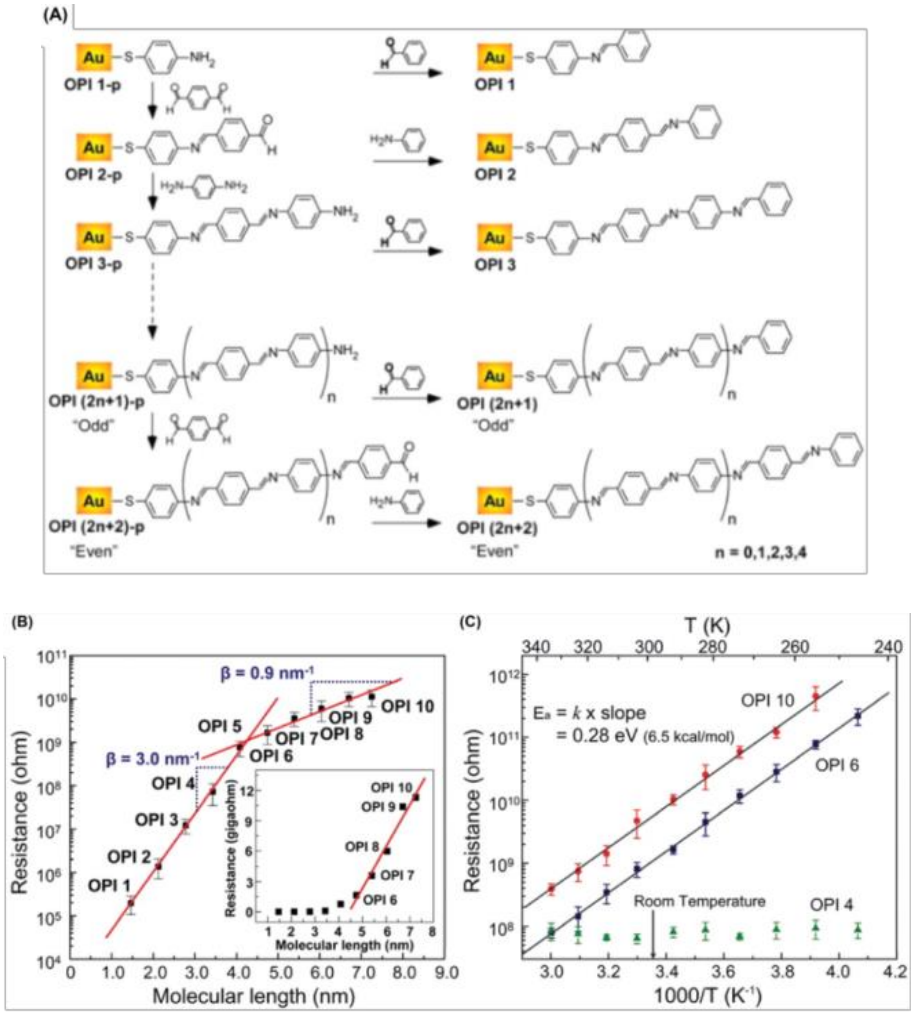

Figure 2.11 (A) Molecular structure and synthetic route to OPI-p and OPI monolayers on Au electrodes. (B) Semilog plot of *R* vs. *L* for the Au/molecular wire/Au junctions. The inset shows a linear plot of *R* vs. *L*, demonstrating linear scaling of resistance with length for the long OPI wires. (C) Arrhenius plot for OPI 4, OPI 6, and OPI 10.[63] Reprinted with permission: 2008, The American Association for the Advancement of Science.

Frisbie et al[63,64] used a conducting tip of an atomic force microscope (AFM) as the top contact to measure the conductivities of a series oligophenyleneimines (OPI), with the lengths ranging from 1.5 to 7.3 nm immobilized on Au bottom electrodes. The charge transport was observed to be efficient through so-called "molecular wires" with such

long distance. They have found that the dominant mechanism of charge transport across these junctions was tunnelling for molecular wires shorter than ~ 4 nm, while the mechanism changes to hopping for molecular wires exceeding ~ 4 nm in length. Figure 2.11 shows the structure of the molecular wires and the main results from their charge transport investigations.

Figure 2.11(A) shows the molecular structure of OPI-p (the OPI wire precursors) and the OPI wires, together with their synthetic routes. Figure 2.11(B) shows the results of the transport characteristics. They have found that for long OPI wires, the relation between the resistance and molecular length is flatter with the β value is about 0.9 nm^{-1}. Such small β suggests that hopping is the principal transport mechanism.[65-67] The inset in Figure 2.11(B) shows a linear plot of R vs. L for long wires that is consistent with hopping. Furthermore, the temperature dependence measurements verified that the change in transport mechanism happens with the length-dependent measurements, as is shown in Figure 2.11(C). We can observe that both OPI 6 and OPI 10 show strongly thermally activated transport, indicating hopping dominates. While for OPI 4, the resistance is independent of temperature from 246 to 333 K, which is expected for tunnelling. Such conduction mechanism transition from tunnelling to hopping was considered to happen near 4 nm.

The electrical transport behaviour of a series of redox active conjugated molecular wires were also studied as the function of temperature and molecular length by Frisbie et al.[62,68-69] Figure 2.12(A1) shows the molecular structures of the target molecular wires. The wires consist of covalently coupled ruthenium(II) bis(σ-arylacetylide) complexes (Ru1-Ru3) whose length ranges from 2.4 to 4.9 nm. These molecules are unique as they possess multiple metal-redox centres that are well-coupled by conjugated ligands. The

electrical properties were probed by conductive probe-atomic force microscopy (CP-AFM) and cross-wire junctions, as are illustrated in Figure 2.12(A2) and (A3). In both test structures, the *I-V* traces were obtained over ± 1.0 V, and the top Au electrode was brought into contact with a SAM of ruthenium complexes formed on the bottom Au electrode.

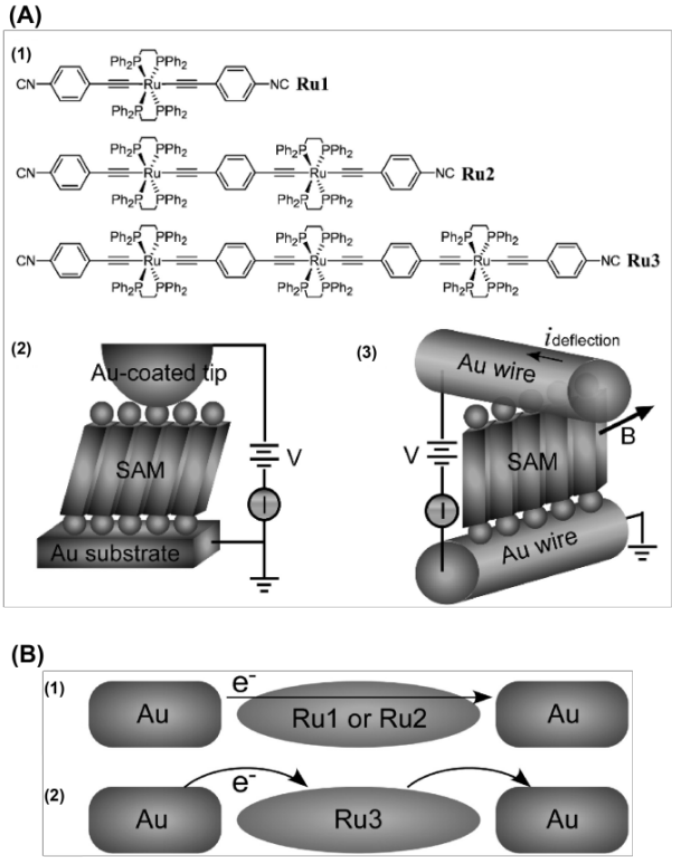

Figure 2.12 (A1) Molecular structure and (A2) schematic representations of the CP-AFM and (A3) the X-wire junction test structures. Illustration of charge-transport mechanism at 5 K: (B1) direct tunneling in junctions of Ru1 and Ru2 and (B2) sequential tunneling with Coulomb blockade in the Ru3 junctions. The electron flows are shown by arrows.[68] Reprinted with permission: 2007, American Chemical Society.

Figure 2.13(A) and (B) displayed the average *I-V* curves from 10 traces obtained from CP-AFM and X-Wire junctions. The current has been normalized to the maximum current at 1.0 V for direct comparison of *I-V* curve shapes. Very similar *I-V* curves have been exhibited in these two test platforms.

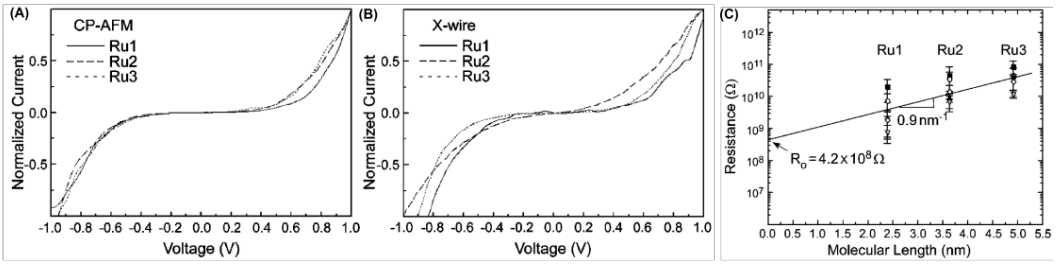

Figure 2.13 (A) *I-V* characteristics of Ru1, Ru2 and Ru3 SAMs obtained in CP-AFM, and (B) X-wire junctions at room temperature. (C) The semilog plot of *R* vs. *L* for junctions of Au/SAM/Au CP-AFM junctions.[68] Data from five different tips with five trials are shown and are represented by different symbols. The error bars represent one standard deviation from the mean. Reprinted with permission: 2007, American Chemical Society.

CP-AFM was also used to investigate the molecular length dependence, as is shown in Figure 2.13 (C). The key results from these measurements show that the resistance (*R*) is nearly independent of molecular length (*L*). X-wire geometry was used to conduct the low temperature *I-V* characteristics. As observed, the average *I-V* traces of Ru1 and Ru2 were nearly indistinguishable from those measured at room temperature (data are not shown here). While for Ru3, the coulomb block-like behaviour was observed in the junctions.

The principal charge transport mechanism at low temperature is illustrated in Figure 2.12(B). Direct tunnelling is expected to be the principle charge-transport mechanism for Ru1 and Ru2 whose length is 2.4 and 3.6 nm, respectively. However, the direct tunnelling is believed to diminish substantially for Ru3 whose molecular length is about 4.9 nm, and hopping mechanism has taken over the charge transport.

McCreey et al. have applied oligomers to junction systems as well by using even larger range of molecular length (4.5 nm ~ 22 nm), which have greatly extended the distance range of charge transport in molecular electronic devices. In their work, they have investigated the frontier between molecular and organic electronics by describing

the electrical characteristics of conjugated molecular junctions of the structure carbon/molecule/carbon/Au over a wide range of thickness.[70,71]

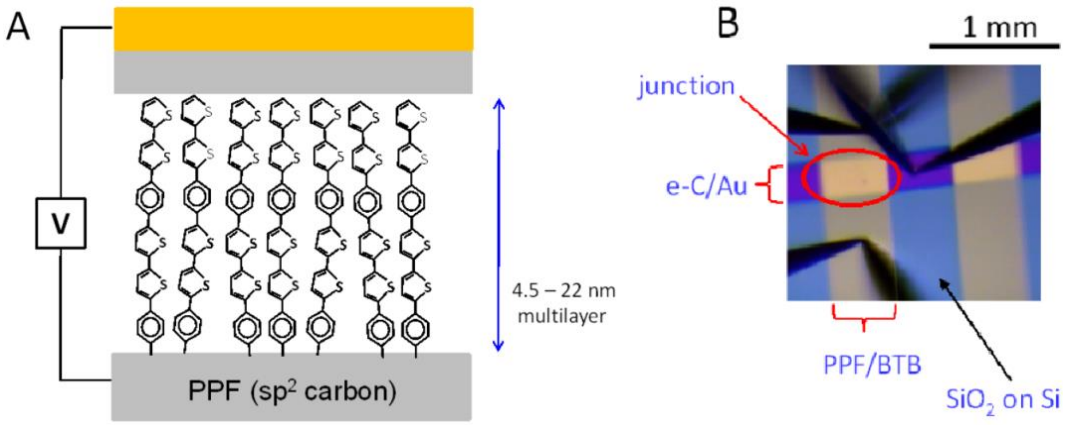

Figure 2.14 (A) Junction schematic cross section of carbon molecular junction, consisting of oligomers of bis-thienyl-benzene (BTB) between a carbon substrate and a carbon top contact. (B) Image of complete junction viewed from above, showing three of the four contact probes.[70]

Unlike many other groups employ SAMs with thiolate bonds anchored on metallic substrates, here they have taken an alternative approach to form the bottom electrode: using carbon electrodes. Figure 2.14 shows the junction structure. There are three distinct transport mechanisms been observed for 4.5 ~ 22 nm thick oligo(thiophene) layers between carbon contacts: when d < 8 nm, it was observed as direct tunneling, while when d > 16 nm, it was observed as activated hopping for high temperature and low bias. The third mechanism is consistent with field-induced ionization of HOMO or interface states to generate charge carriers when $d = 8 \sim 22$ nm.[70]

The quantum mechanical tunneling was observed in great majority of molecular electric devices with the transport distance around 5 nm between the contacts that have been investigated to date.[72-74] There is a general agreement that the conductance scales exponentially with length, with an attenuation coefficient (β) in this distance range. Not

too many molecular electronic systems have been investigated over 5 nm, while the work done by McCreey have bridged the gap between short-range tunneling in molecular junctions and activated hopping in bulk organic films.

Rampi et al showed a study that by incorporating a large number of metal centres into rigid molecular backbones, very long (up to 40 nm) and highly "conductive" metal centres molecular wires (MCMWs) have been obtained.[75] They applied a large-area test-bed junction, Au-MCMW/Hg, to investigate the electrical properties of MCMWs. It has indicated that the "conductance" of these metal centred molecular wires did not decrease significantly even for very long molecular wires but depended on the nature of the incorporated redox centre. The energy gap between the Fermi levels of the electrodes and the energy levels of the molecules results in the current flow through junctions.

Figure 2.15 shows the stepwise assembly of the molecular wires and their electrical characterizations, as well as the proposed energy diagrams of their charge transport process. They have selected Fe(II) and Co(II) ions as metal centres (MCs) because they can provide for both low-lying energy states and easy coordination reaction to terpy-based ligands.[75]

A mixed SAM consisting of a 1:1 ratio of terpyridine-based ligand and mercaptobenzene as lateral spacer were used as "anchoring platform" to obtain highly organized structures of MCMWs, as is shown in Figure 2.15(A). By bringing a naked Hg-drop electrode into contact with the MCMWs SAMs on the Au electrode, a junction was formed, as is shown in Figure 2.15(B1).[76] In Figure 2.15(B2) and (B3), the *J-V* curves showed clearly that the current values measured for junctions incorporating SAMs, for 14-nm-long Co(II)-based MWs, it decreased by half an order of magnitude, and for 20-nm-long Fe(II)-based MWs, it decreased by one and a half order of magnitude.

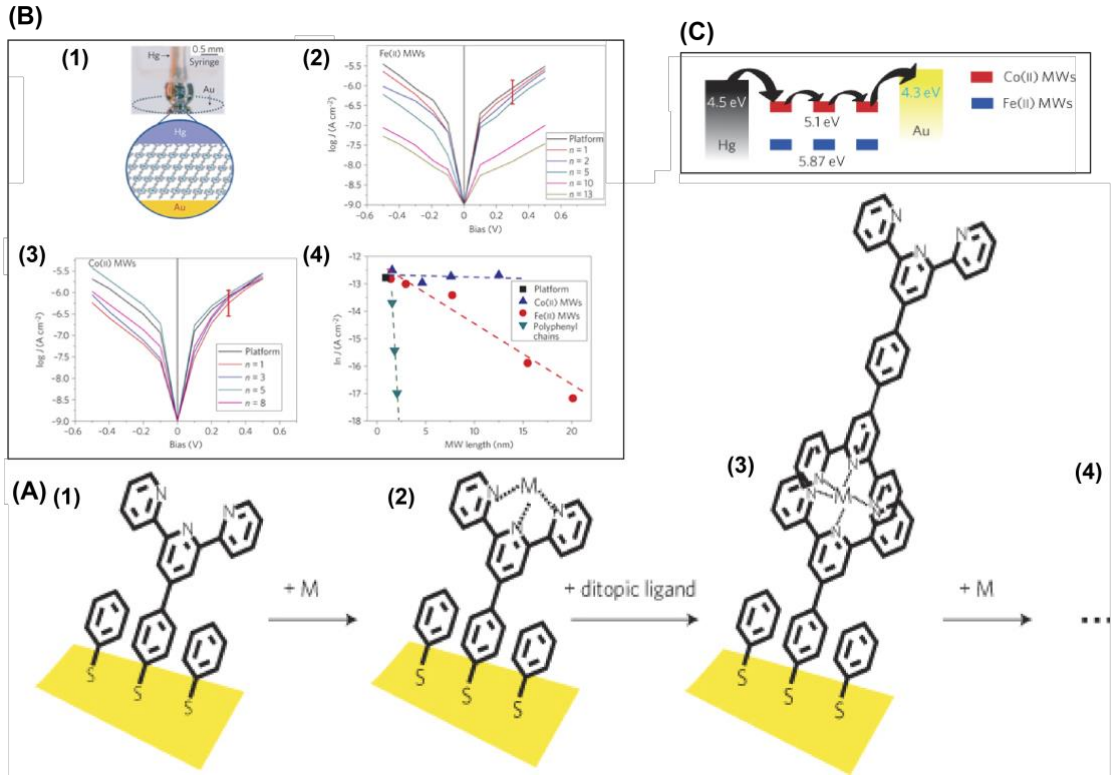

Figure 2.15 Schematic representation of the stepwise assembly of the MCMWs in situ on metal surfaces: (A1) Assembly on the gold surface of the 4'-(4-mercaptophenyl)-2-2':6'2-terpyridine (MPTP)/MC 1:1 "platform" SAM. (A2) Coordination of the MC to the MPTP ligand. (A3) Coordination of the TPT ligand. (A4) The processes (A2) and (A3) are repeated iteratively to increase the length of the MCMWs by one metal-ligand unit up to the desired dimension (up to more than 40 nm). Electrical characterization of MCMWs: (B1) Photograph and schematic representation of the interface of the Au-MCMW/Hg junction. (B2) and (B3) *J-V* curves for Fe(II) - and Co(II) – based MWs. (B4) In *J* vs. *L* of the Fe(II) - and Co(II) – based MWs. (C) Energy diagram for junctions incorporating the Fe(II) - and Co(II) – based MWs.[75] Reprinted with permission: 2009, Nature Publishing Group.

While a single tunneling mechanism could not fully model the charge transfer process occurring across these MWs and it was believed that a multistep electron/hole hopping mechanism between redox sites is likely to be more possible to complete the model. The energy level diagram is shown in Figure 2.15(C). According to theory[77], a linear dependence of the current values on $1/N$, where N is the number of redox centres would be in favour of an intramolecular directional hopping, whereas in contrast a linear dependence on $1/N^2$ would suggest that a non-directional diffusion mechanism is operative. The quasi-linear plot of J vs $1/d$ reported in Figure 2.16(A) and the evident curvature of J vs $1/d^2$ reported in Figure 2.16(B) indicated that the charge-transfer

process in these MCMWs occurs predominantly via an intramolecular hopping mechanism. The condition necessary for a hopping regime to become operative is that the energy of the molecular states reaches the electrode Fermi level. This condition is usually provided by decreasing the HOMO-LUMO gap as a result of extending the length of conjugated MWs.

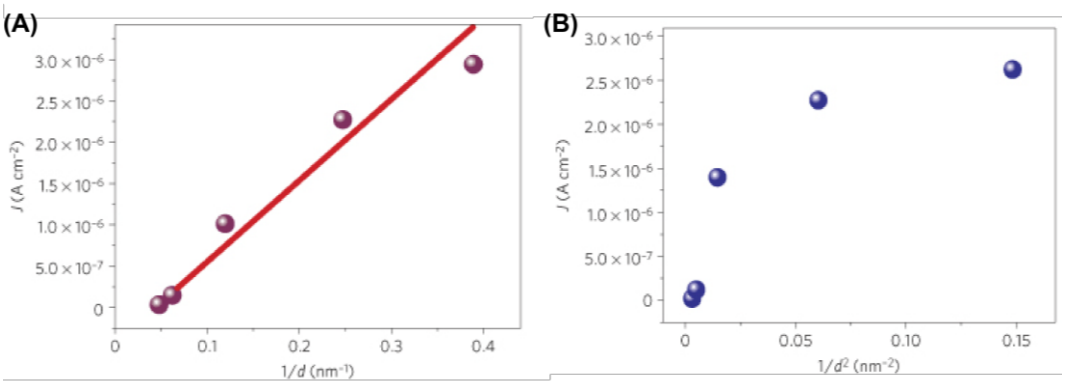

Figure 2.16 Schematic representation plots of J versus respectively (A) $1/d$ and (B) $1/d^2$ for the Fe(II)-basedMWs.[75] Reprinted with permission: 2015, Nature Publishing Group.

Such molecular electronic devices mentioned above involved, single or a few (< 10) molecules, or SAMs as active the component.[78] However, neither of them can outperform polymer based electronic devices in the aspect of stability, aging and costs. That is the single molecular based, SAMs based, molecular wires based devices have had limited potential for applications because of their low conductance or extreme sensitivity to the junction structure and high operation voltages.[79] In the following subsection, we will further review some studies on polymer brush involved organic electronic devices.

2.3.2 Polymer brush applications in organic electronic devices

Polymers at interfaces are a field which has fascinated physicists and chemists now for nearly half a century, with respect to both basic and applied research. Polymer is another interesting candidate for the charge transport studies. Unlike oligomer which is a

molecular complex consisted of a few monomer units, polymer at least, in principle, consists of a nearly unlimited numbers of monomers. Strictly speaking, polymer is macromolecule which makes such junction may not simply be considered as "molecular" junctions but "macromolecular" junctions. But here in this review, we generalize those polymer based junctions still as molecular junctions. Up to now, many cases applied only polymer thin film to fabricate the electronic device, while Huck et al applied polymer brushes to the junction devices.[80,81]

Polymer brush can be considered as nanoscale "soft" building blocks which are able to bring in varieties of functionalities — from redox activity and photophysical properties to biocompatibility and capacity for energy storage.[7] Different functional groups contribute different effects to polymer brush in a certain situation, which makes them have their practical applications.

2.3.2.1 Applications in field-effect transistor (FET) devices

The integration of polymer thin film on electrode supports plays a major part to modify the nanoscale interfacial phenomena.[82] For example, in Tobin J. Mark's work, they described a general approach for probing semiconductor-dielectric interfacial chemistry effects on FET performance parameters using bilayer gate dielectrics.[82] In this case, the bilayer structure made by various spin-coated polymers/hexamethyldisilazane (HMDS) on 300 nm SiO_2/p^+-Si. However, such spin-coated polymer thin film has little control over film structures and may suffer from the delamination from the surface or dissolution when spin-coating the hole-transport layer on top.

Alternatively, polymer brushes come into the picture as valuable tools to tune the electronic properties of surfaces with macromolecular assemblies. Cho et al. applied

polymer brush to fabricate the bilayer instead of spin-coated polymer thin film.[83,84] They also investigated crystalline nanostructures and film morphologies of pentacene films deposited on a polymer brush organic interlayer in high performance organic field-effect transistors (OFETs). Here polymer brushes were grafted onto the oxide substrates by spin-coating and thermal annealing (this technique could be considered as "grafting to" approaches[85]). Such OFETs fabricated on top of the polymer brushes exhibited not only a higher degree of control over the morphology and the arrangement of the polymer interface but also the excellent device performance.

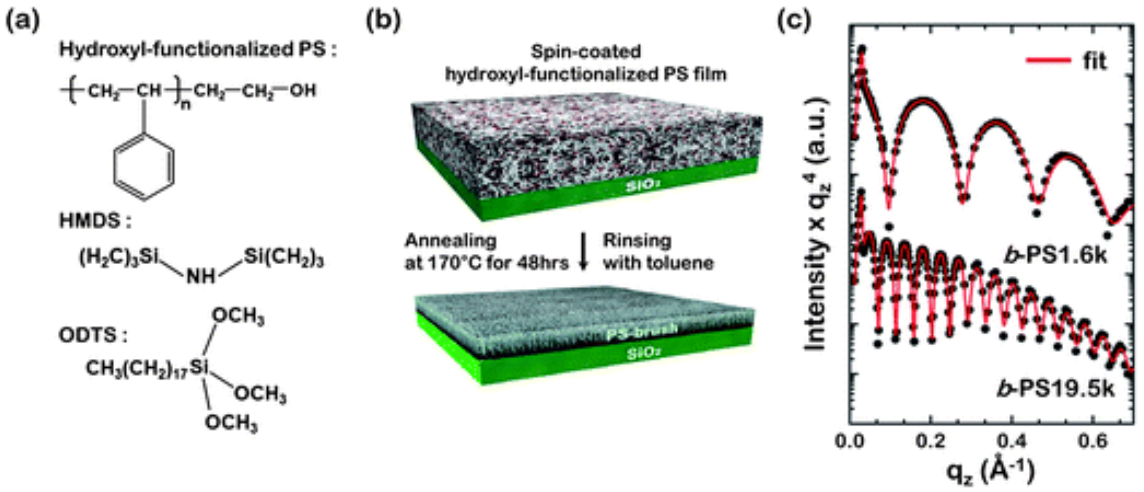

Figure 2.17 (A) Chemical structures of the materials used in the experiment. (B) Schematic diagram showing the b-PS brush modification on SiO_2 dielectrics. (C) X-ray reflectivity (XRR) curves of b-PS1.6k and b-PS19.5k at room temperature (25 °C).[83] Reprinted with permission: 2011, Royal Society of Chemistry.

The chemical structures of compounds used to modify the SiO_2 surface in this system were shown in Figure 2.17(A). The end-hydroxyl groups of PS-OH that spin-coated from a toluene solution diffused to and reacted with the SiO_2 surface, producing PS brushes (b-PS) on the substrate, where Figure 2.17(B) depicts a schematic representation of b-PS formation via the "grafting to" method. They believed that polymer brushes can produce covalent linkages and strongly adherent polymeric layers, and they form densely packed

pinhole-free films. Compared with conventional dielectric surface treatments, such as octadecyltrichlorosilane (ODTS) and hexamethyldisilazane (HMDS), this pentacene OFETs fabricated on top of the polystyrene (PS) brushes showed dramatically improved device performance. XRR measurements were performed to determine the thickness and surface roughness of the grafted PS layer, which is shown in Figure 2.17(C). The basic surface characterizations and the device electrical properties are shown in Table 2.1.

Table 2.1 Surface characteristics of ODTS, HMDS, and b-PS brush-modified SiO_2 dielectrics and the electrical properties of the OFET devices.[83] Reprinted with permission: 2011, Royal Society of Chemistry.

Dielectric surface modification	Dielectric surface properties				OFET properties	
	Thickness/Å	Surface roughness/Å	Surface energy/mJ m^{-2}	Field-effect mobility/$cm^2V^{-1}s^{-1}$	On/Off current ratio	V_m/V
ODTS	17.2 (±0.5)	2.7 (±0.5)	25.6 (±2.3)	0.21(±0.08)	3.6×10^5	8.2(±0.8)
HMDS	5.2(±0.3)	2.1(±0.3)	43.6(±1.2)	0.32(±0.11)	4.2×10^5	4.1(±1.6)
b-PS 1.6k	32.2(±1.5)	2.1(±0.4)	40.1(±3.5)	0.68 (±0.06)	1.1×10^7	-1.6(±1.2)
b-PS 19.5k	115.6 (±2.1)	2.8 (±0.3)	39.4 (±1.8)	0.82 (±0.05)	5.3×10^7	-2.9(±1.5)

Huck et al. developed organic transistor with polymer brush gate dielectrics generated by SI-ATRP.[86] These OFETs were fabricated from PMMA derived brushes as shown in Figure 2.18(A) and the brush generation is shown in Figure 2.18(B). Polymer brush films produced here were considered to be smooth and pinhole-free even at very low thickness. Addition of ethylene glycol dimethacrylate (EGDMA) cross-linker to the reaction produced films that contained chemical cross-links throughout their interior. The electrical properties of the PMMA brush films were probed by measurement of capacitors fabricated from the brush films. Sandwich capacitor structures of the PMMA brush films were created with the ink-jet printed conductive polymer poly(3,4-ethylene dioxythiophene) doped with poly(styrene sulfonate) (PEDOT : PSS) as the top electrode. The reference device was made with much thicker PMMA spin-coated thin film from n-butyl acetate (NBA) solvent. The capacitance-frequency characteristics of PMMA brush containing device and PFMMA spin-coated thin film containing device show difference

that the leakage current through the brush structures at 30 V/μm average to 6×10^{-8} A/cm^2, slighter higher than the 3×10^{-8} measured for the spin coated thin film structures.

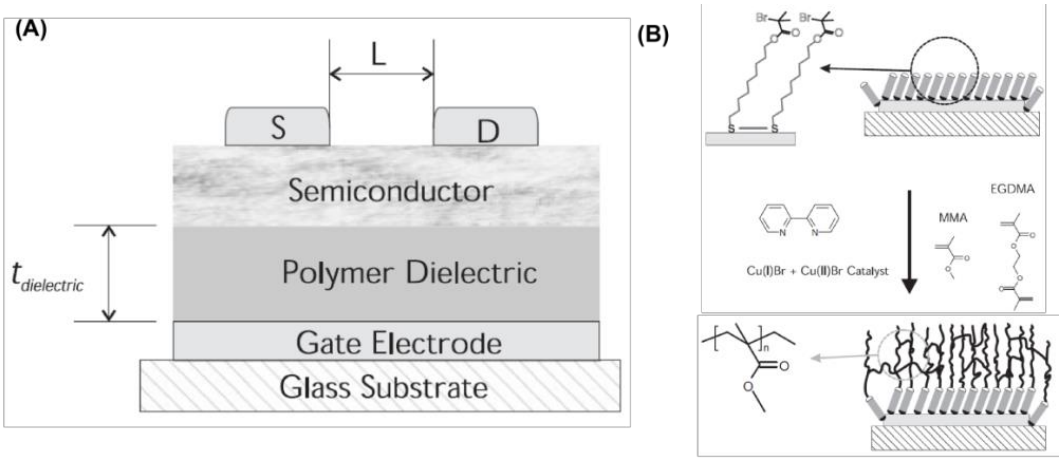

Figure 2.18 (A) Structure of bottom-gate top-contact OFET employed in this study. (B) Outline of process used to grow PMMA brushes from gold surface.[86] Reprinted with permission: 2008, John Wiley and Sons.

Rutenberg et al.[87] applied polymer brushes generated by surface-initiated ring-opening metathesis polymerizations (SI-ROMP) as gate insulators. While in their work, the pinhole free polymer brush films could be produced when the brushes were grown over 400 nm thickness. The source-gate shorts in their FETs were caused by lower thickness films contained large pinholes.

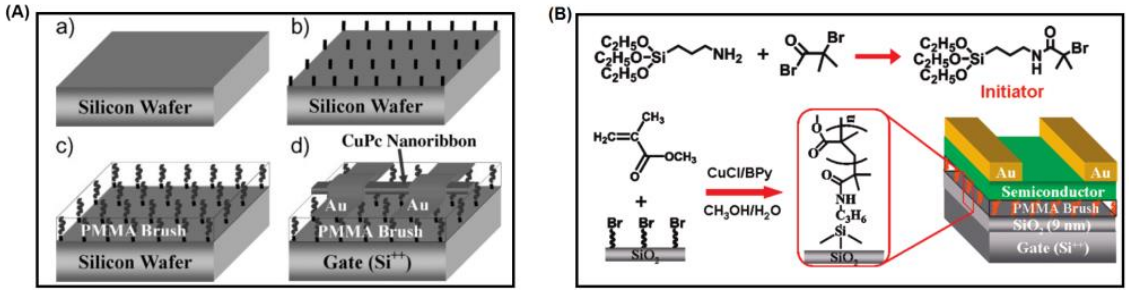

Figure 2.19 (A) Schematic illustration of surface-grafted PMMA brush dielectrics for copper phthalocyanine (CuPc) single-crystalline nanoribbon transistors: a) Silicon wafer (Si^{++}) with native oxide layers. b) Immobilization of the initiator. c) PMMA brush grafting via SI-ATRP technique. d) CuPc single-crystalline nanoribbon transistor with PMMA brush dielectric. (B) Schematic illustration of synthesis of surface-grafting PMMA brush on SiO_2 as hybrid nanodielectric for organic field-effect transistors.[88] Reprinted with permission: 2009, John Wiley and Sons.

Chi et al.[88,89] used polymer brushes combined with inorganic oxide hybrid nanodielectrics that show smooth surface topography (device structure shows in Figure 2.19), high capacitance values and low leakage current densities. These results may open a way to build ultrathin dielectrics for high performance transistor and circuit, as well as for microelectronics, nanoelectronics, and organic electronics.

Kim and his coworkers[90] introduced an ultrathin polystyrene (PS) brush film on SiO_2 dielectrics, and then various vacuum- and solution-processable organic semiconductors upon such PS-coupled dielectrics can develop highly ordered crystalline structures that provide higher field-effect mobilities than other surface-modified systems, and negligible hysteresis in OFETs, as is shown in Figure 2.20.

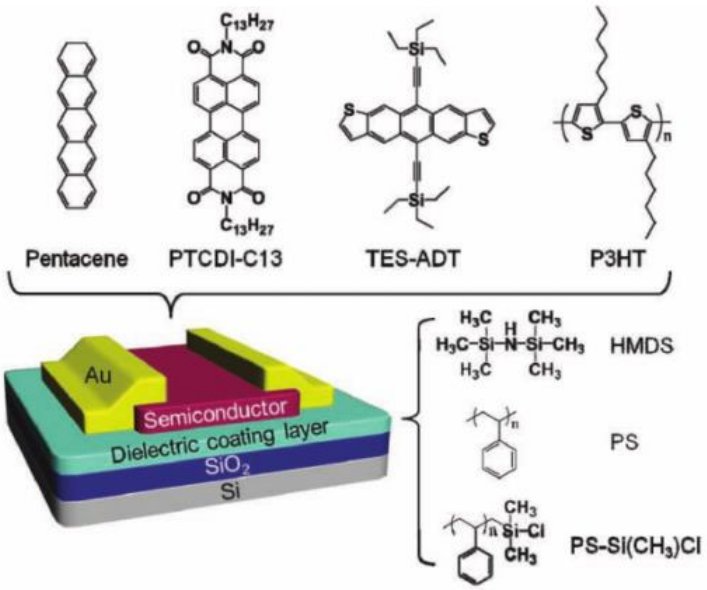

Figure 2.20 Schematic diagram of the top-contact-electrode OFETs fabricated with a PS brush film.[90] Reprinted with permission: 2011, John Wiley and Sons.

2.3.2.2 Applications in memory effect devices

Polymers are usually deposited by spin-coating on a variety of inorganic substrates in the fabrication of memory device.[91] However, incompatibility between inorganic

electrodes, with organic thin film may result in the delamination of the spin-coated or vacuum-sublimated organic layer and a high resistance in such device. Alternatively, with the polymer film covalently attached to the inorganic surface, by using polymer brush film, the problems associated with the inorganic substrate/organic polymer interface may be minimized.

Poly(2-(N-carbazolyl)ethyl methacrylate) (PCEM) brushes have been successfully prepared on silicon surface via SI-ATRP to fabricate memory device by Shang et al (see Figure 2.21).[92] In their work, polymer brushes containing pendant carbazole, and memory behaviours were first observed in such polymer brushes. Conductance switching with an ON/OFF current ratio up to 10^5 was observed in this polymer brush based memory device.

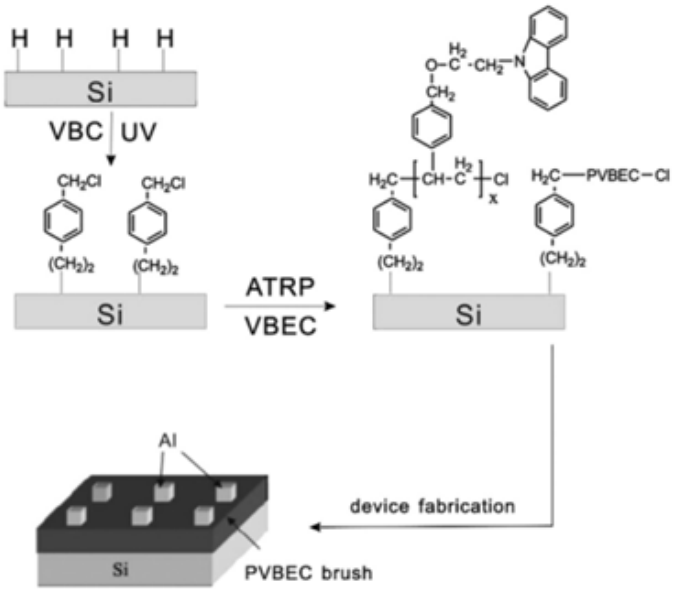

Figure 2.21 Schematic diagram illustrating the preparation of the polymer device.[92] Reprinted with permission: 2011, Elsevier.

They claimed that both the ON and OFF states are stable under a constant read voltage stress of 1.0 V and even can endure 10^6 read cycles under a pulse read voltage.

The switching performance of the Si-g-PVBEC/Al device ("g" stands for "graft" here) is superior to that of the conventional spin-coated Si/PVBEC/Al device.

Another similar work was also conducted by Shang et al.[93] They put the polymer brush films between the bottom ITO electrode and Al top electrode to fabricate the ITO-g-PCEM/Al device. The device exhibits two conductivity states and can be switched from the initial low conductivity (OFF) state to the high-conductivity (ON) state. They also claimed that the device behaves as a write-once read many times (WORM) memory. Compared with that of the conventional ITO/PCEM/Al device fabricated by spin-coating, the switching voltage is lower in the ITO-g-PCEM/Al memory device. Comparison results are shown in Figure 2.22.

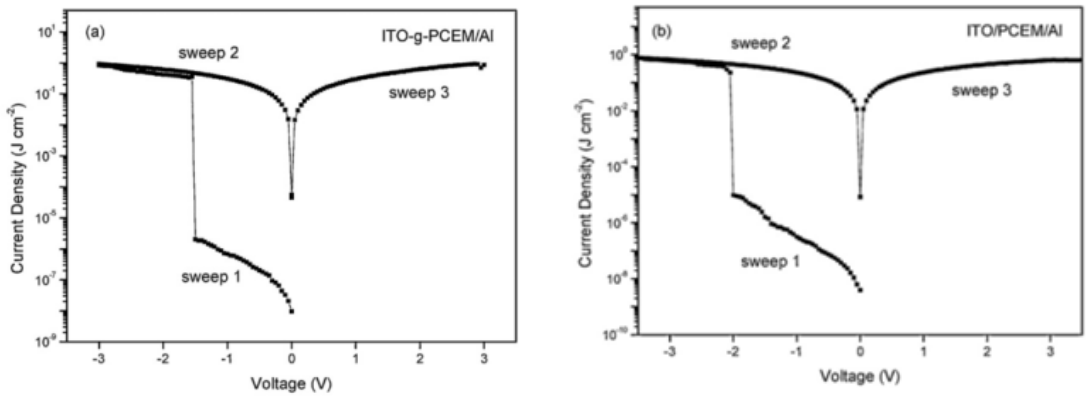

Figure 2.22 Current density-voltage curves of the (a) ITO/g-PCEM/Al device (stands for the polymer brushes fabricated devices) and (b) ITO/PECM/Al device (stands for the spin-coating PCEM bulk polymer from solution) as the comparison.[93] Reprinted with permission: 2012, Elsevier.

Zhitenev et al[94] fabricated devices by using integrated shadow masks. Reversible switching was observed between conducting (ON) and nonconducting (OFF) states in the devices. In Figure 2.23(a), firstly the bottom metal contacts (Ti, 150 Å/Au, 50 Å, orange colored) were evaporated (evaporation direction shown by arrow 1). The electrodes were

separated by a bridge of width between 150 and 500 nm. Next, a polymer layer was grown (arrow 2, dark blue). Finally, deposition of the top contact (Au, 150 Å, yellow) was carried out from a different angle (arrow 3). The overall transport properties were determined by the small junction (shown by the white circle). The size of the junction was controlled by the dimensions of the bridge and by the angle of the evaporation steps.

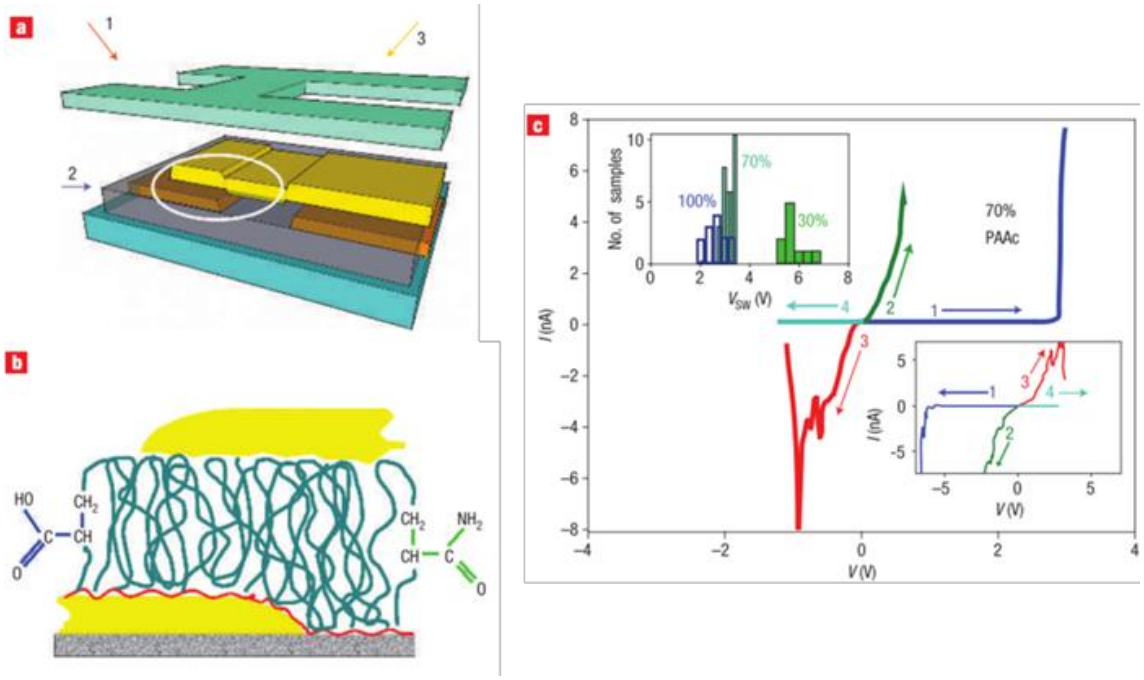

Figure 2.23 (a) Schematic of the device fabrication using an integrated shadow mask. (b) Zoomed schematic of the junction structure, corresponding to the area within the white circle in (a). The red line is the poly(glycidyl methacrylate) (PGMA) anchoring layers. Polymer brushes of various compositions and thickness are grown from different concentrations of acrylamide (right) and acrylic acid (left) monomers in polymerization solution. (c) The memory effect in polymer brush devices.[94] Reprinted with permission: 2007, Nature Publishing Group.

Memory effect in polymer brush device is shown in Figure 2.23(C). The device shown here was made with 70% poly(acrylic acid) PAAc. *I-V* curves 1 to 4 were each measured by increasing the voltage starting from 0 V. Curve 1 shows initially that the junction was non-conducting at all applied voltages. Above a switching voltage V_{sw} (~ 2.9 V in this device), the current rapid increased and the device switched to a high-

conductance "ON" state. Curve 2 shows the "ON" state was stable at small applied voltages. Curve 3 shows a large voltage of the opposite polarity switched the device back into the low-conductance "OFF" state. Curve 4 shows the reinstated "OFF" stable was stable as small applied voltages. The top inset shows the histograms of the initial switching voltage V_{sw} measured on devices having different PAAc / polyacrylamide (PAM) ratios. The switching voltages were measured on devices with an average brush thickness of 8 to 13 nm. As the switching voltage scales linearly with the thickness of the device, they have scaled all of the measured voltages to that of a 10-nm-thick film. The bottom inset shows the switching behaviour does not depend on the polarity of V_{sw}, as shown in this device (30% concentration of PAAc), where V_{sw} in negative.

2.3.2.3 Polymer brush enhance the charge transport characteristics

Considerable progress has been made in the development of electronic devices based on charge-transporting organic molecules over the past decade. The ultimate utility of these devices, however, has been limited by the low long-range mobility of charges within these materials. Huck and his co-workers reported the use of polymer brushes as a method for alignment of hole-transporting polymer chains.[80,81]

In this work[80], they showed that charge-transporting polymer chains in the brush conformation can be synthesized from a variety of substrates of interest, displaying a high degree of stretching and showing up to a 3 orders of magnitude increase in current density normal to the substrates as compared with a spin-coated film. Brushes composed of poly(triphenylamine acrylate) (PTPAA) exhibited a respectable hole transport mobility in amorphous films. PTPAA is comprised of an inert backbone with active TPA side chains. Charge transport is likely to occur predominantly through hopping between adjacent TPA units. See Figure 2.24.

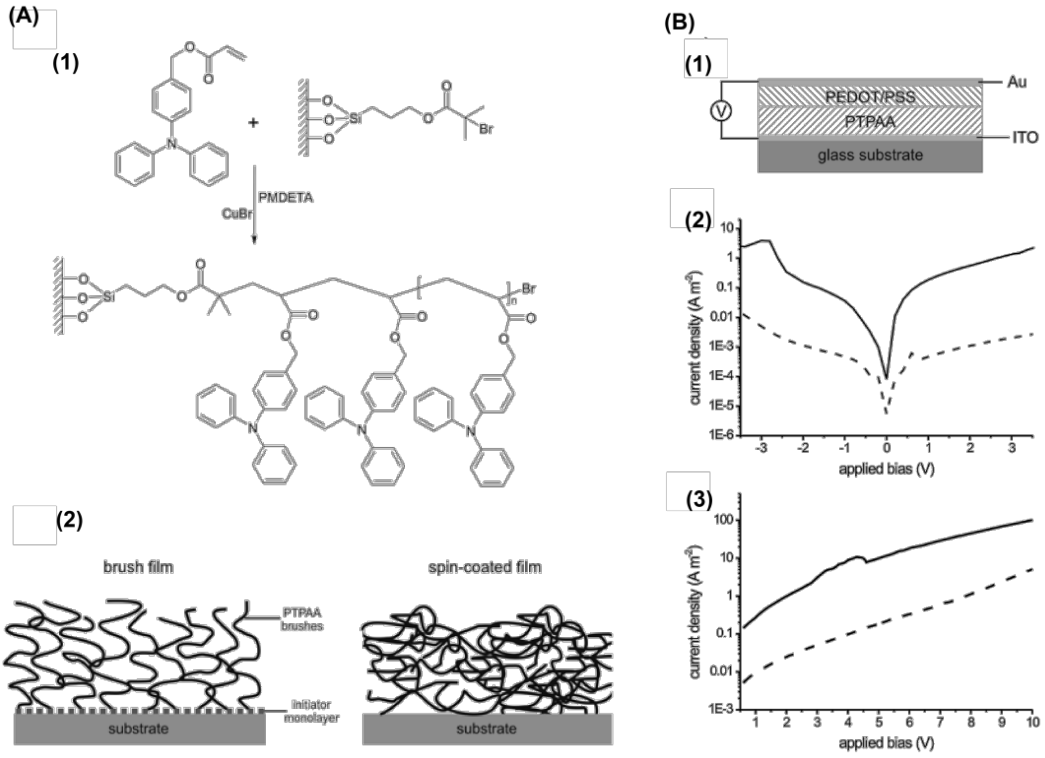

Figure 2.24 Overview of PTPAA brushes (A1) Scheme for the surface-initiated synthesis of PTPAA brush. (A2) Cartoon presentation of a polymer brush and spin-coated film. Right: Properties of the PTPAA brushes in device performance. (B1) Schematic diagram of the diode structure used for current density testing; (B2) Current density *vs.* applied bias for a sandwich structure device of ITO/PTPAA (80 nm)/PEDOT : PSS/Au, with PTPAA brushes (solid line) and PTPAA spin-coated amorphous film (dashes line). Positive bias corresponds to hole injection from the PEDOT : PSS and negative bias corresponds to hole injection from the ITO. (C) Current density *vs.* applied bias for a unipolar diode made with 35 nm PTPAA films: brush (solid line), spin coated (dashed line).[80] Reprinted with permission: 2006, American Chemical Society.

2.3.3 Electrodes applied to molecular junctions

As mentioned before, several kinds of electrodes are commonly used in the molecular junction measurements. Both top and bottom electrodes fabrication procedures are the critical steps in the junction fabrications. There are several good reviews summarized various cases where electronic junctions/devices fabricated by different kinds of electrodes with either single molecules or SAMs.[78,95] In this subsection, we only highlight some cases related to our own work.

2.3.3.1 Top electrodes: hard contact

Evaporated solid metal and conducting probe of scanning probe microscopy are commonly used as hard contact top electrode. Generally, such as Au[96], Pb[97], and so on, have been evaporated directly at top electrodes, while the vapour-phased atoms of the metals have the trend to easily penetrate the nanometer scaled materials and cause filaments or shorts.[98] The electrode/material interfaces are hard to be well controlled or understood, which may result in the instability, low reproducibility and large distribution of data. Frisbie et al. applied conducting probe-atomic force microscopy (CP-AFM) to characterize the conjugated molecular wires of different length.[63,64] The CP-AFM is using the AFM tip as top electrode, has proven to be an efficient way to measure monolayer molecular junction on the order of a few hundred molecules.[99,100] However, variations in the tip radius and the tip vibration may induce some uncertainties in the numbers of molecules in the junction, which result in some variations in the *J-V* characteristics. Hard contact is not an ideal contact technique since it is very easy to obtain shorts circuit. Therefore, to reduce the probability of short circuit, the common idea is to make "soft" contacts of these solid metals.

2.3.3.2 Top electrodes: soft contact

The first liquid metal used as soft contact top electrode is Mercury (Hg).[101-103] While the high surface tension and easily formation of amalgam make it difficult to for stable junctions. Gradually, top electrode with autologous or introduced protection layers are applied to improve the quality of junctions, such as conductive polymer based (usually PEDOT : PSS[104]) top electrodes, liquid metal protected by SAMs, graphene protected top electrode, and eutectic gallium indium (EGaIn/GaO_X). This so-called EGaIn

technique we used in our studies to form polymer brush-based junctions. Figure 2.25 shows the formation of conical EGaIn/GaO_X top electrode.

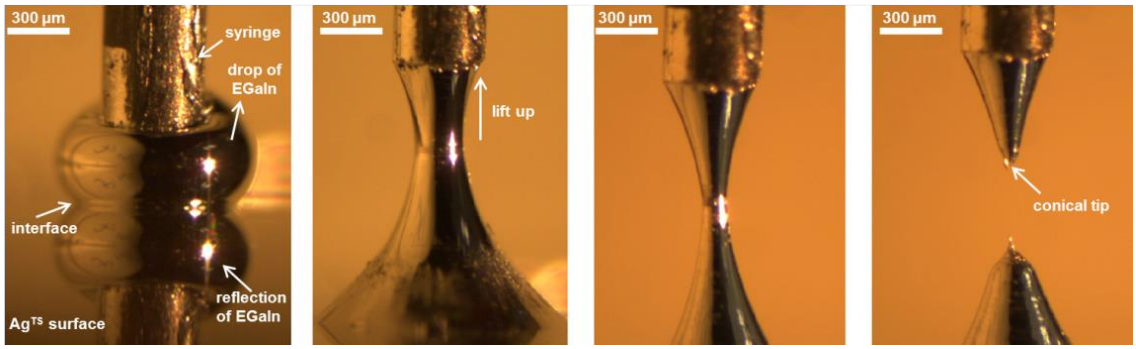

Figure 2.25 The sequential photographs showing the formation of the conical EGaIn/GaO_X top electrode.

EGaIn is a non-Newtonian fluid consisting of 75% Ga, 25% In by weight (m. p. = 15.5 °C), covering by ~ 0.7 nm GaO_X layer.[105] Therefore, it is able to form non-destructive conical shape tips with small diameters (usually in micrometer scale). The conductivity of this GaO_X layer is about 10^{-4} Ω▪cm^2. Similar to the Hg drop top electrode, the EGaIn was filled within a micro-syringe incorporated with a needle of 300-500 μm^2 in diameter. A drop of EGaIn was squeezed out and contacted with clean sacrificial metal surface (Au or Ag) and then slowly lifted up to form a conical tip till the tip broke with the bulk EGaIn. Then the sacrificial surface was replaced with the SAMs modified substrates, the tip was pushed down slowly to contact with the substrates by a micromanipulator to form a junction. This technique allows forming junctions with high yields, good stability and large amount of statistically data. The electrical properties of junctions are comparable with other techniques.[106] The controversies of EGaIn techniques are always focus on the GaO_X layer, which focus on the intrinsic physical and chemical properties of GaO_X and the interface between SAMs and GaO_X. The spontaneously formed GaO_X layer is conductive and forms an ohmic contact with SAMs.[57] To date, EGaIn system still has some uncertainties requires to be clarified. The

most obvious one is that the top electrodes show user-to-user different sometimes. This is mainly determined by the shape of the EGaIn tips, size of junctions and the applied press during contacting. To address these questions, a standard procedure of the formation of the conical shape tip of EGaIn is required. In EGaIn technique, the statistical tools for analysing measurements of charge transport is necessary since a number of experimental factors contribute to the difficulty of this field. Reus et al.[107] reported their efforts on using statistical tools to analyse the data generated by EGaIn junction.

2.3.3.3 Bottom electrodes: metal surface

Metal surfaces, such as Au, Ag, Al, and Pt, Cu, are the most commonly used bottom electrodes.[108,109] The quality of bottom electrodes will affect not only the yield of junctions but also the electrical characteristics of the junctions. There are mainly two types of metal surface, one is as deposited surfaces and the other one is template-stripped surfaces.[110] The latter one utilizes curable glue to peel off the metallic thin film from the substrates where the metals were initially deposited. This method produces high quality surfaces and large grains.[52,54]

2.3.3.4 Bottom electrodes: non-metal surface

Some semiconductors, such as highly doped Si[111], indium tin oxide (ITO)[112], GaAs[113] and carbon based bottom electrodes (graphene or graphite)[114] also have been used as bottom electrodes besides the metal surface. These semiconductors have different physical properties but the main issues that have been considered are the surface roughness, cleanness and the compatibility with the SAMs formation procedures.

2.3.4 Molecular electronic devices: EGaIn based device

The top and bottom electrodes with the materials in between compose the whole molecular electronic devices. Those devices based on single molecules or SAMs are good testbeds for studying the molecule-electrode interfaces at the nanoscales and the charge transport across molecules.[78,95] Developing methods to fabricate devices that generate data with high reproducibility in terms of precision are important.

Nijhuis et al. applied EGaIn/GaO_X top electrodes within microfluidic channels and integrated with micro-arrays as bottom electrodes to fabricate on-chip molecular diodes.[59,60] Comparing with other approaches that reply on cross-bar or nano/micropore configurations,[47] this technique does not require patterning of the bottom-electrodes. This method also minimizes the potential error associated with cone-shaped tips of GaO_X/EGaIn suspended from a syringe such as vibrations, pressure at which the tip is brought in contact with the SAM, or drift of the tip with respect to the SAM. Furthermore, it is difficult to carry out temperature dependent measurement due to the limitation by the drift of the tip. This reversible soft top contact produced comparable data with the cone-shape tip systems and is able to conduct temperature dependent measurement over the range of 110-293 K.

2.4 Limitations and gaps in previous work

From the above review, we can see that polymer brushes have applications in multiple research fields, including responsive sensor (polyelectrolyte brush or redox active brush, but this part is not discussed in details in previous sections) and organic devices (field-effect transistor or memory effect). Most relevant here are research areas using polymer brushes in molecular electronics studies. Those reported studies on molecular junctions normally applied single molecules, SAMs, and short-distance molecular wires/oligomers

to fabricate the device. These studies paved the way for studying the charge transport along long molecules. Further research on the mechanism studies of the charge transport along longer distance molecules is imperative. In terms of polymer brush, studies on charge transport characteristics of such macromocecules in electronic devices are rare.

Will the charge transport mechanism change as the distance of the (macro)molecules change? Is this change similar with the reported observations in SAMs or oligomers based junctions? Will the EGaIn technique also be applicable for polymer/polymer brush based junctions/devices? To answer these questions, we need to define the aims of our study.

2.5 Purpose, significance and scope of our work

We use Ferrocene[115,116] (Fc) moieties as the functional groups for polymer brush because Fc has some excellent electrochemical characteristics, such as low oxidation potential, fast electron-transfer rate, high levels of stability in its two redox states, low cost and well-defined synthetic procedures for many derivatives. The main aim of this study was to build a junction device fabricated by Fc-containing polymer brush with EGaIn techniques to investigate the charge transport behaviour along (macro)molecules in systematic length range (from 2 nm to 60 nm). In addition, we also studied the brushes by wet electrochemistry to learn more about the packing structure of polymer brush.This study may have significant impact on both fundamental studies, such as charge transport mechanism discussion, and practical applications, such as polymer brush-based device fabrication. It is also understood that using polymer brush as molecular junction element is a new discovery and as such, there may be a few problematic issues involved. For example, the packing structure of the polymer brush would affect the charge transport behaviour.

2.6 Summary

In this chapter, firstly, we reviewed the techniques commonly used in functional polymer synthesis field. Secondly, we reviewed the recent developments of organic electronic devices which involves in the molecular junctions, including single-molecular based junction, SAMs based junction, molecular wire/oligomer based junction. The typical applications of functional polymer brush have been listed and literatures have been showed as examples in the organic electronic field. In the third place, we introduced the properties of the components of the electrodes for those junctions and their device fabrications. Finally, we summarized the limitations and gaps in those prior studies and highlight our research objectives.

2.7 References

1. Milner, S. T., *Science* **1991,** *251*, 905-915.
2. Braun, D.; Cherdron H.; Rehahn, M.; Ritter, H. and Voit, B. (**2013**). *Polymer Synthesis: Theory and Practice Fundamentals, Methods, Experiments. 5th Edition*. Springer Heidelberg, New York, Dordrecht, London.
3. McCreery, R. L., *Chem. Mater.* **2004,** *16* (23), 4477-4496.
4. Boyes, S. G.; Granville, A. M.; Baum, M.; Akgun, B.; Mirous, B. K. and Brittain, W. J., *Surf. Sci.* **2004,** *570* (1-2), 1-12.
5. Edmondson, S.; Osborne, V. L. and Huck, W. T., *Chem. Soc. Rev.* **2004,** *33* (1), 14-22.
6. Dyer, D. J., *Adv. Funct. Mater.* **2003,** *13* (13), 667-671.
7. Azzaroni, O., *J. Polym. Sci. Pol. Chem.* **2012,** *50* (16), 3225-3258.
8. Braunecker, W. A. and Matyjaszewski, K., Prog. Polym. Sci. **2007,** *32* (1), 93-146.
9. Matyjaszewski, K. and Tsarevsky, N. V., *Nat. Chem.* **2009,** *1* (4), 276-288.
10. Tang, B. Z.; Tsarevsky, N. V. and Sumerlin, B. S., (**2013**) *Fundamentals of controlled/living Radical Polymerization*, London, RSC Polymer Chemistry Series.
11. Ayres, N., *Polym. Rev.* **2011,** *51* (2), 138-162.
12. Matyjaszewski, K. and Xia, J. H., *Chem. Rev.* **2001,** *101*, 2921-2990.

13. Matyjaszewski, K., *Macromolecules* **2012,** *45* (10), 4015-4039.

14. Tsarevsky, N. V. and Matyjaszewski, K., *Chem. Rev.* **2007,** *107* (6), 2270-2299.

15. Percec, V.; Barboiu, B.; Neumann, A.; Ronda, J. C. and Zhao, M., *Macromolecules* **1996,** *29* (10), 3665-3668.

16. Barbey, R.; Lavanant, L.; Paripovic, D.; Schüwer, N.; Sugnaux, C.; Tugulu, S. and Klok, H. A., *Chem. Rev.* **2009,** *109* (11), 5437-5527.

17. Sumerlin, B. S.; Neugebauer, D. and Matyjaszewski, K., *Macromolecules* **2005,** *38* (3), 702-708.

18. Zhao, B. and Brittain, W. J., *Prog. Polym. Sci.* **2000,** *25* (5), 677-710.

19. Huang, W.; Skanth; Baker, G. L. and Bruening, M. L., *Langmuir* **2001,** *17* (5), 1731-1736.

20. Saha, S.; Bruening, M. L. and Baker, G. L., *ACS Appl. Mater. Interfaces* **2011,** *3* (8), 3042-3048.

21. Yan, C.; Zharnikov, M.; Gölzhäuser, A. and Grunze, M., *Langmuir* **2000,** *16* (15), 6208-6215.

22. Kim, B. Y.; Ratcliff, E. L.; Armstrong, N. R.; Kowalewski, T. and Pyun, J., *Langmuir* **2009,** *26* (3), 2083-2092.

23. Markovich, I.; Mandler, D., *J. Electroanal. Chem.* **2001,** *500* (1–2), 453-460.

24. Barbey, R. and Klok, H. A., *Langmuir* **2010,** *26* (23), 18219-18230.

25. Li, J.; Wang, L.; Liu, J.; Evmenenko, G.; Dutta, P. and Marks, T. J., *Langmuir* **2008,** *24* (11), 5755-5765.

26. Huang, C.; Tassone, T.; Woodberry, K.; Sunday, D. and Green, D. L., *Langmuir* **2009,** *25* (23), 13351-13360.

27. Pyun, J.; Kowalewski, T. and Matyjaszewski, K., *Macromol. Rapid. Commun.* **2003,** *24* (18), 1043-1059.

28. Li, Y.; Giesbers, M.; Gerth, M. and Zuilhof, H., *Langmuir* **2012,** *28* (34), 12509-12517.

29. Ejaz, M.; Yamamoto, S.; Ohno, K.; Tsujii, Y. and Fukuda, T., *Macromolecules* **1998,** *31* (17), 5934-5936.

30. Morinaga, T.; Ohno, K.; Tsujii, Y. and Fukuda, T., *European Polymer Journal* **2007,** *43* (1), 243-248.

31. Huang, W.; Kim, J. B.; Bruening, M. L. and Baker, G. L., *Macromolecules* **2002,** *35* (4), 1175-1179.

32. Kim, J. B.; Bruening, M. L. and Baker, G. L., *J. Am. Chem. Soc.* **2000,** *122* (31), 7616-7617.

33. Bao, Z.; Bruening, M. L. and Baker, G. L., *J. Am. Chem. Soc.* **2006,** *128* (28), 9056-9060.

34. Chen, R.; Zhu, S. and Maclaughlin, S., *Langmuir* **2008,** *24* (13), 6889-6896.

35. Lindqvist, J.; Nyström, D.; Östmark, E.; Antoni, P.; Carlmark, A.; Johansson, M.; Hult, A. and Malmström, E., *Biomacromolecules* **2008,** *9* (8), 2139-2145.

36. Zhang, Y.; He, H. and Gao, C., *Macromolecules* **2008,** *41* (24), 9581-9594.

37. Badri, A.; Whittaker, M. R. and Zetterlund, P. B., *J. Polym. Sci., Part A: Polym. Chem.* **2012,** *50* (15), 2981-2992.

38. Gonçalves, G.; Marques, P. A. A. P.; Barros-Timmons, A.; Bdkin, I.; Singh, M. K.; Emami, N. and Grácio, J., *J. Mater. Chem.* **2010,** *20* (44), 9927-9935.

39. Yang, Y.; Wang, J.; Zhang, J.; Liu, J.; Yang, X. and Zhao, H., *Langmuir* **2009,** *25* (19), 11808-11814.

40. Steenackers, M.; Gigler, A. M.; Zhang, N.; Deubel, F.; Seifert, M.; Hess, L. H.; Lim, C. H.; Loh, K. P.; Garrido, J. A.; Jordan, R.; Stutzmann, M. and Sharp, I. D., *J. Am. Chem. Soc.* **2011,** *133* (27), 10490-10498.

41. Ou, B.; Zhou, Z.; Liu, Q.; Liao, B.; Yi, S.; Ou, Y.; Zhang, X. and Li, D., *Polym. Chem.* **2012,** *3* (10), 2768.

42. Sheiko, S. S.; Sumerlin, B. S. and Matyjaszewski, K., *Prog. Polym. Sci.* **2008,** *33* (7), 759-785.

43. Minko, S., *J. Macromol. Sci., Polym. Rev.* **2006,** *46* (4), 397-420.

44. Yameen, B. and Farrukh, A., *Chem.-Asian J.* **2013,** *8* (8), 1736-1753.

45. Langer, R., *Acc.Chem. Res.* **2000,** *33* (2), 94-101.

46. Ishaug-Riley, S. L.; Okun, L. E.; Prado, G.; Applegate, M. A. and Ratcliffe, A., *Biomaterials* **1999,** *20* (23–24), 2245-2256.

47. McCreery, R. L. and Bergren, A. J., *Adv. Mater.* **2009,** *21* (43), 4303-4322.

48. Aviram, A. and Ratner, M. A., *Chem. Phys. Lett.* **1974,** *29* (2), 277-283.

49.Martin, A. S.; Sambles, J. R. and Ashwell, G. J., *Phys. Rev. Lett.* **1993,** *70* (2), 218-221.

50. Elbing, M.; Ochs, R.; Koentopp, M.; Fischer, M.; von Hänisch, C.; Weigend, F.; Evers, F.; Weber, H. B. and Mayor, M., *Proc. Natl. Acad. Sci. U. S. A.* **2005,** *102* (25), 8815-8820.

51. Xia, J. L.; Diez-Perez, I. and Tao, N. J., *Nano Lett.* **2008,** *8* (7), 1960-1964.

52. Nijhuis, C. A.; Reus, W. F. and Whitesides, G. M., *J. Am. Chem. Soc.* **2010,** *132* (51).

53. Nerngchamnong, N.; Yuan, L.; Qi, D. C.; Jiang, L; Thompson, D. and Nijhuis, C. A., *Nat. Nanotechnol.* **2013,** *8* (2), 113-118.

54. Thuo, M. M.; Reus, W. F.; Nijhuis, C. A.; Barber, J. R.; Kim, C.; Schulz, M. D. and Whitesides, G. M., *J. Am. Chem. Soc.* **2011,** *133* (9), 2962-2975.

55. Jiang, L.; Sangeeth, C. S. S.; Wan, A.; Vilan, A. and Nijhuis, C. A., *J. Phys. Chem. C* **2015,** *119* (2), 960-969.

56. Yuan, L.; Nerngchamnong, N.; Cao, L.; Hamoudi, H.; del Barco, E.; Roemer, M.; Sriramula, R. K.; Thompson, D. and Nijhuis, C. A., *Nat. Commun.* **2015,** *6* (6324), 1-11.

57. Wimbush, K. S.; Fratila, R. M.; Wang, D.; Qi, D.; Liang, C.; Yuan, L.; Yakovlev, N.; Loh, K. P.; Reinhoudt, D. N.; Velders, A. H. and Nijhuis, C. A., *Nanoscale* **2014,** *6* (19), 11246-11258.

58. Lorenz, M. R.; Woods, J. F. and Gambino, R. J., *J. Phys. Chem. Solids.* **1967,** *28* (3), 403-404.

59. Nijhuis, C. A.; Reus, W. F.; Barber, J. R.; Dickey, M. D. and Whitesides, G. M., *Nano letters* **2010,** *10* (9), 3611-3619.

60. Wan, A.; Jiang, L.; Sangeeth, C. S. S. and Nijhuis, C. A., *Adv. Funct. Mater.* **2014,** *24* (28), 4442-4456.

61. Nitzan, A. and Ratner, M. A., *Science* **2003,** *300* (5624), 1384-1389.

62. Luo, L.; Choi, S. H. and Frisbie, C. D., *Chem. Mater.* **2011,** *23* (3), 631-645.

63. Ho Choi, S.; Kim, B. and Frisbie, C. D., *Science* **2008,** *320* (5882), 1482-1486.

64. Choi, S. H.; Risko, C.; Delgado, M. C. R.; Kim, B.; Brédas, J. L. and Frisbie, C. D., *J. Am. Chem. Soc.* **2010,** *132* (12), 4358-4368.

65. Davis, W. B.; Svec, W. A.; Ratner, M. A. and Wasielewski, M. R., *Nature* **1998,** *396* (6706), 60-63.

66. Giese, B., *Acc. Chem. Res.* **2000,** *33* (9), 631-636.

67. Grozema, F. C.; Berlin, Y. A. and Siebbeles, L. D. A., *J. Am. Chem. Soc.* **2000,** *122* (44), 10903-10909.

68. Kim; Beebe, J. M.; Olivier, C.; Rigaut, S.; Touchard, D.; Kushmerick, J. G.; Zhu, X. Y. and Frisbie, C. D., *J. Phys. Chem. C* **2007,** *111* (20), 7521-7526.

69. Luo, L.; Benameur, A.; Brignou, P.; Choi, S. H.; Rigaut, S. and Frisbie, C. D., *J. Phys. Chem. C* **2011,** *115* (40), 19955-19961.

70. Yan, H.; Bergren, A. J.; McCreery, R.; Della Rocca, M. L.; Martin, P.; Lafarge, P. and Lacroix, J. C., *Proc. Natl. Acad. Sci.* **2013,** *110* (14), 5326-5330.

71. Sayed, S. Y.; Fereiro, J. A.; Yan, H.; McCreery, R. L. and Bergren, A. J., *Proc. Natl. Acad. Sci. U. S. A.* **2012,** *109* (29), 11498-11503.

72. Bergren, A. J.; McCreery, R. L.; Stoyanov, S. R.; Gusarov, S. and Kovalenko, A., *J. Phys. Chem. C* **2010,** *114* (37), 15806-15815.

73. Yan, H.; Bergren, A. J. and McCreery, R. L., *J. Am. Chem. Soc.* **2011,** *133* (47), 19168-19177.

74. Martin, P.; Della Rocca, M. L.; Anthore, A.; Lafarge, P. and Lacroix, J. C., *J. Am. Chem. Soc.* **2012,** *134* (1), 154-157.

75. Tuccitto, N.; Ferri, V.; Cavazzini, M.; Quici, S.; Zhavnerko, G.; Licciardello, A. and Rampi, M. A., *Nat. Mater.* **2009,** *8* (1), 41-46.

76. Haag, R.; Rampi, M. A.; Holmlin, R. E. and Whitesides, G. M., *J. Am. Chem. Soc.* **1999,** *121* (34), 7895-7906.

77. Nitzan, A., *Annu. Rev. Phys. Chem.* **2001,** *52* (1), 681-750.

78. Akkerman, H. B. and de Boer, B., *J. Phys.: Condens. Matter* **2008,** *20* (1), 013001.

79. Capozzi, B.; Xia, J.; Adak, O.; Dell, E. J.; Liu, Z.-F.; Taylor, J. C.; Neaton, J. B.; Campos, L. M. and Venkataraman, L., *Nat. Nanotechnol.* **2015,** *10* (6), 522-527.

80. Whiting, G. L.; Snaith, H. J.; Khodabakhsh, S.; Andreasen, J. W.; Breiby, D. W.; Nielsen, M. M.; Greenham, N. C.; Friend, R. H. and Huck, W. T. S., *Nano lett.* **2006,** *6* (3), 573-578.

81. Snaith, H. J.; Whiting, G. L.; Sun, B.; Greenham, N. C.; Huck, W. T. S.; Friend, R. H., *Nano lett.* **2005,** *5* (9), 1653-1657.

82. Yoon, M.-H.; Kim, C.; Facchetti, A. and Marks, T. J., *J. Am. Chem. Soc.* **2006,** *128* (39), 12851-12869.

83. Park, S. H.; Lee, H. S.; Kim, J.-D.; Breiby, D. W.; Kim, E.; Park, Y. D.; Ryu, D. Y.; Lee, D. R. and Cho, J. H., *J. Mater. Chem.* **2011,** *21* (39), 15580-15587.

84. Park, K.; Park, S. H.; Kim, E.; Kim, J.-D.; An, S.-Y.; Lim, H. S.; Lee, H. H.; Kim, D. H.; Ryu, D. Y.; Lee, D. R. and Cho, J. H., *Chem. Mater.* **2010,** *22* (18), 5377-5382.

85. Alonzi, M.; Lanari, D.; Marrocchi, A.; Petrucci, C. and Vaccaro, L., *RSC Advances* **2013,** *3* (46), 23909-23923.

86. Pinto, J. C.; Whiting, G. L.; Khodabakhsh, S.; Torre, L.; Rodríguez, A.; Dalgliesh, R. M.; Higgins, A. M.; Andreasen, J. W.; Nielsen, M. M.; Geoghegan, M.; Huck, W. T. S. and Sirringhaus, H., *Adv. Funct. Mater.* **2008,** *18* (1), 36-43.

87. Rutenberg, I. M.; Scherman, O. A.; Grubbs, R. H.; Jiang, W.; Garfunkel, E. and Bao, Z., *J. Am. Chem. Soc.* **2004,** *126* (13), 4062-4063.

88. Li, L.; Zhang, Y.; Li, H.; Tang, Q.; Jiang, L.; Chi, L.; Fuchs, H. and Hu, W., *Adv. Funct. Mater.* **2009,** *19* (18), 2987-2991.

89. Li, L.; Hu, W.; Chi, L. and Fuchs, H., *J. Phys. Chem. B.* **2010,** *114* (16), 5315-5319.

90. Kim, S. H.; Jang, M.; Yang, H.; Anthony, J. E. and Park, C. E., *Adv. Funct. Mater.* **2011,** *21* (12), 2198-2207.

91. Ling, Q. D.; Liaw, D. J.; Zhu, C.; Chan, D. S. H.; Kang, E. T. and Neoh, K. G., *Prog. Polym. Sci.* **2008,** *33* (10), 917-978.

92. Wei, Y.; Gao, D.; Li, L. and Shang, S., *Polymer* **2011,** *52* (6), 1385-1390.

93. Liu, Y.; Lv, S.; Li, L. and Shang, S., *Synth. Met.* **2012,** *162* (13-14), 1059-1064.

94. Zhitenev, N. B.; SidorenkoA; Tennant, D. M. and Cirelli, R. A., *Nat. Nanotechnol.* **2007,** *2* (4), 237-242.

95. Song, H.; Reed, M. A. and Lee, T., *Adv. Mater.* **2011,** *23* (14), 1583-1608.

96. Kim, T. W.; Wang, G.; Lee, H. and Lee, T., *Nanotechnology* **2007,** *18* (31), 315204.

97. Honciuc, A.; Metzger, R. M.; Gong, A. and Spangler, C. W., *J. Am. Chem. Soc.* **2007,** *129* (26), 8310-8319.

98. Haick, H. and Cahen, D., *Acc. Chem. Res.* **2008,** *41* (3), 359-366.

99. Luo, L.; Balhorn, L.; Vlaisavljevich, B.; Ma, D.; Gagliardi, L. and Frisbie, C. D., *J. Phy. Chem. C* **2014,** *118* (46), 26485-26497.

100. Wei, Z.; Li, T.; Jennum, K.; Santella, M.; Bovet, N.; Hu, W.; Nielsen, M. B.; Bjornholm, T.; Solomon, G. C.; Laursen, B. W. and Norgaard, K., *Langmuir* **2012,** *28* (8), 4016-4023.

101. York, R. L.; Nguyen, P. T. and Slowinski, K., *J. Am. Chem. Soc.* **2003,** *125* (19), 5948-5953.

102. Tran, E.; Rampi, M. A. and Whitesides, G. M., *Angew. Chem.* **2004,** *116* (29), 3923-3927.

103. Levine, I.; Weber, S. M.; Feldman, Y.; Bendikov, T.; Cohen, H.; Cahen, D. and Vilan, A., *Langmuir* **2011,** *28* (1), 404-415.

104. Akkerman, H. B.; Blom, P. W. M.; de Leeuw, D. M. and de Boer, B., *Nature* **2006,** *441* (7089), 69-72.

105. Cademartiri, L.; Thuo, M. M.; Nijhuis, C. A.; Reus, W. F.; Tricard, S.; Barber, J. R.; Sodhi, R. N. S.; Brodersen, P.; Kim, C.; Chiechi, R. C. and Whitesides, G. M., *J. Phys. Chem. C* **2012,** *116* (20), 10848-10860.

106. Wang, G.; Kim, T. W. and Lee, T., *J. Mater. Chem.* **2011,** *21* (45), 18117-18136.

107. Reus, W. F.; Nijhuis, C. A.; Barber, J. R.; Thuo, M. M.; Tricard, S. and Whitesides, G. M., *J. Phys. Chem. C* **2012,** *116* (11), 6714-6733.

108. Laibinis, P. E.; Whitesides, G. M.; Allara, D. L.; Tao, Y. T.; Parikh, A. N. and Nuzzo, R. G., *J. Am. Chem. Soc.* **1991,** *113* (19), 7152-7167.

109. Rhodes, C. L.; Lappi, S.; Fischer, D.; Sambasivan, S.; Genzer, J. and Franzen, S., *Langmuir* **2008,** *24* (2), 433-440.

110. Weiss, E. A.; Chiechi, R. C.; Kaufman, G. K.; Kriebel, J. K.; Li, Z.; Duati, M.; Rampi, M. A. and Whitesides, G. M., *J. Am. Chem. Soc.* **2007,** *129* (14), 4336-4349.

111. Yaffe, O.; Scheres, L.; Puniredd, S. R.; Stein, N.; Biller, A.; Lavan, R. H.; Shpaisman, H.; Zuilhof, H.; Haick, H.; Cahen, D. and Vilan, A., *Nano lett.* **2009,** *9* (6), 2390-2394.

112. Chockalingam, M.; Darwish, N.; Le Saux, G. and Gooding, J. J., *Langmuir* **2011,** *27* (6), 2545-2552.

113. Nesher, G.; Vilan, A.; Cohen, H.; Cahen, D.; Amy, F.; Chan, C.; Hwang, J. and Kahn, A., *J. Phys. Chem. C* **2006,** *110* (29), 14363-14371.

114. Wang, G.; Kim, Y.; Choe, M.; Kim, T. W. and Lee, T., *Adv. Mater.* **2011,** *23* (6), 683-683.

115. Kealy, T. J. and Pauson, P. L., *Nature* **1951,** *168* (4285), 1039-1040.

116. Amer, W.; Wang, L.; Amin, A.; Ma, L. and Yu, H., *J. Inorg. Organomet. Polym. Mater.* **2010,** *20* (4), 605-615.

Chapter 3

Side Chain Effects in the Packing Structure and Stiffness of Redox-Responsive Ferrocene-Containing Polymer Brushes

In this chapter we describe the work on preparation of ferrocene-containing polymer brushes with different side chain lengths by surface-initiated atom transfer radical polymerization (SI-ATRP). The polymer brushes are characterized by cyclic voltammetry to determine the surface coverage of the ferrocene (Fc) units, their thickness in air by atomic force microscopy (AFM) and ellipsometry, and their mechanical properties by AFM-based nanoindentation. The results are compared against an ideal packing model and we conclude that brushes with short linkers between the Fc units and the polymer back bone are stiff and stand up in air up to 40 nm tall. In contrast, polymers with long linkers collapse and do not stand up in air. Our results indicate that the stiffness and packing structure of Fc-containing polymer brushes are affected by the length of the linkers between the Fc and polymer back bone.

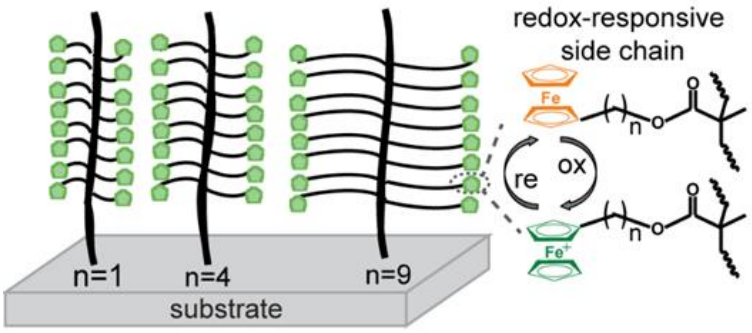

Chapter 3

3.1 Introduction

Generally speaking, polymer brushes are kind of surface immobilized polymers, whose chains in one side are end-tethered on substrate and the other side stretch away from the substrate.[1-3] Polymer thin film is an analogy of polymer brush, but it is normally spin-coated or simply casted on the certain surface, forming a physisorbed thin film.[4] In principles, polymer brushes allow for better control over the size, sequence, conformation and spatial distribution of functional building blocks.[5] Functional polymer brushes have the stimulus-responsive and "smart" properties.

The direct stimulus control over the physicochemical properties of so-called "responsive" polymers/polymer brushes, e.g., light-switchable, thermal responsive, redox responsive, pH-responsive, salt responsive and so-forth, have attracted significant attention in material research because of their potential applications in areas such as surface wettability control, antifouling, sensing and drug delivery.[5-9] Different functional moieties contribute different effects to polymer brushes in certain situation, which makes polymer brushes have their practical applications.

The redox-active moiety ferrocene (Fc) is often incorporated in polymers either as an integral part of the polymer backbone or as lateral substituents because of its high stability and high degree of reversibility in switching between redox states.[10,11] Either as an integral part of the backbone or as lateral substituents, Fc-containing polymers have attracted great attentions since the early 1950s[12-14] and their interesting properties, such as redox, mechanical, photophysical, and optoelectronic properties have been well-characterized.[10,15-21]

Polymers with Fc moieties fixed in the main chain, such as poly(ferrocenylsilane) (PFS) have been studied by Manners et al.[16,22-24]. These PFS polymers form "smart

surface" which has high sensitivity in the response to external redox stimuli, and they have the potential to be excellent chemical sensors. Polymeric structures, with Fc moieties located on the side chains are also popular. For instance, poly(vinylferrocene) (PVF),[12,25] poly(ferrocenylethylene),[26] and ferrocene-containing (meth)acrylates,[27-30] their synthesis and electrochemical properties were well studied.

In recently years, Hardy et al.[31] reported the synthesis of side chain Fc-containing (meth)acrylate polymers by atom transfer radical polymerization (ATRP) and measured the thermal and redox properties of these polymers. The glass transition temperature (T_g) of the bulk polymers were found to decrease over 100º with the increasing linker length (the number of the carbon-carbon bonds in alkyl side chain changed from 1 to 8) while the thermal stability did not seem to be affected. The electrochemical properties of these polymers depend on the length of the linker and presence of other groups. For example, the half wave potential ($E_{1/2}$) was influenced by the linkers between the Fc unit and acrylates or methacrylates unit in the monomers or the backbone of polymers: $E_{1/2}$ increased by 0.2 eV with the number of carbon-carbon bonds in alkyl chain (i.e., linker) increasing from 4 to 13. Instead of ATRP, Fc-containing methacrylate polymers with pendant Fc groups were also generated via radical addition fragmentation chain transfer (RAFT).[32] Those examples however discussed bulk polymers synthesised in solution with little or no information about possible applications. Gallei et al.[33-36] reported Fc containing polymers tethered to surfaces (silica wafers or nanoparticles). These smart materials made it possible to change the surface wettability from ~40° to ~100° by switching the redox state of the Fc units. Kim et al.[37] synthesized and electrochemically characterized the Fc-functional polymethacrylate brushes supported by indium tin oxide (ITO) electrodes. They found that, on the one hand, the anodic peak potential (E_{pa}) shifted to more positive while cathodic peak potentials (E_{pc}) shifted to more negative

potential resulting in an increase of $\Delta E_p = E_{pa} - E_{pc}$ from 0.2 eV to 1.2 eV for the same polymer brush measured in the different organic electrolyte solvent (acetonitrile and tetrahydrofuran, respectively); one the other hand, when using the same organic electrolyte solvent (acetonitrile), the broadening of the cathodic peaks is from 0.1 V to 0.4 V (as comparing the full width at half maximum) for the different block copolymers (difference in variation of the Fc-containing blocking sequence). Daasbjerg et al.[38] studied the electrochemical properties of Fc containing polymer brushes generated on a diazonium-based initiator layer and found that the electron transfer rate exponentially decreased by 1.8 order of magnitude with the dry thickness of this initiator monolayer increasing from 0.5 ± 0.1 to 4.4 ± 0.4 nm.

However, although all listed works were dealing with the Fc-containing polymer/polymer brushes, only few studies in details about how the side chain length (distance between the acrylate group and Fc moiety) could affect the polymer behaviour, in particular electrochemical, thermal and nanomechanical properties.

The nanomechanical, or elastic properties, of polymer brushes are relevant in applications involving cell adhesion[39] or bending rigidity[40]. These properties are determined by the chain length, the grafting density, and the primary structure of the grafted chains.[41,42] Vancso et al. demonstrated that the grafting density can be estimated by measuring brush-brush interaction force under compression.[41] One of their studies showed that the apparent Young's modulus of poly(N-isopropylacrylamide) brushes increases from 0.5 MPa to 1.6MPa with a factor of 20 decrease of grafting density.[41] These properties are crucial for the understanding of the physical performance of polymer brushes and also play an important role in applications.

Chapter 3

In our work, we formed polymer brushes from ferrocenylmethyl methacrylate (FMMA), ferrocenylbutyl methacrylate (FBMA) and ferrocenylnonyl methacrylate (FNMA), on ITO and Si/SiO_2 wafers. Instead of being fixed in polymer backbone,[24,43] these Fc moieties are attached as pendants in the side chains (See Figure 3.1), "grafting from" approach in surface initiated atom transfer radical polymerization (SI-ATRP)[5,44,45] was applied to fabricate the polymer brushes with different thickness (2 ~ 60 nm) by controlling the polymerization time. In these polymers, the Fc units are linked to the methacrylate backbone of the polymer via an alkyl chain of a length of 1, 4, and 9 CH_2 units, respectively. We found that stiffness (Young's modulus in air from 3.2 ± 1.2 MPa to 1.4 ± 0.6 MPa, and in water from 2.1 ± 0.4 MPa to 1.0 ± 0.6 MPa), and glass transition temperature (T_g from 148.5 °C to -3.5 °C) both decreased with the increasing linker length. Polymers with a linker length of 1 CH_2 unit are very stiff and form well-defined brushes while polymers with longer linkers, i.e., 4 and 9 CH_2 units, are soft and do not pack well. We believed that our findings will help to improve design strategies of redox-active polymer brushes.

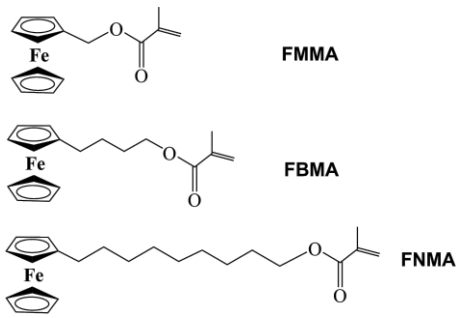

Figure 3.1 Chemical structures of selected monomers: FMMA, FBMA, and FNMA.

We can examine the redox active properties of Fc pendent groups of these polymer brushes, and estimate the Fc surface coverage, which in return, can monitor the growth

of the polymer brushes, and roughly quantize their theoretical thickness. Herein, theoretical thickness was roughly estimated by a simple packing model based on the amount of Fc groups obtained from cyclic voltammetry (CV), and their actual thickness was evaluated by AFM scratch test and ellipsometry. In this contribution we report that the different side chain length of each monomer may result in different thermal properties for bulk polymers, which is consistent with works by others.[31] The packing configurations and nanomechanical properties for corresponding polymer brushes are affected by different side chain length as well, and the values of Yong's modulus we obtained are quite resonable.[46]

Different kinds of surface could be used for polymer brush to grow on,[47-55] among which, Au surface, ITO surface and Si/SiO_2 wafer surface are commonly used. In some related studies, thiol/disulfide containing an initiator moiety, $BrCH(CH_3)COO(CH_2)_{11}SH$ or $(BrC(CH_3)_2COO(CH_2)_{11}S)_2$) molecules for ATRP are commonly used for Au substrate.[56-58] However, it has to be noted that SI-ATRP from Au has some limitations, since the Au-S bond energy is ~30-40 kcal/mol, which is fairly weak and is thermally unstable at elevated temperatures ($\geq$ 60°C).[48,59-62] Comparably, the Si-O-Si bond dissociation energy is 96-133 kcal/mol, which makes the anchored monolayer more stable to circumvent the detachment.[63] This Si-O-Si bond is applicable for the rest two substrates.

ITO is a mixture of In_2O_3 (90 wt%) and SnO_2 (10 wt%) and has good electrical conductivity, which could act as good platform for studies on electrical characteristics. Si/SiO_2 substrate possess very smooth surface that can act as a good reference substrate in terms of the surface characterizations.

Chapter 3

The reaction conditions for ATRP were optimized and results are shown in subsection 3.2.1-3.2.3, followed by SI-ATRP procedures shown in subsection 3.2.4. Basic surface characterizations, including water contact angle (WCA), atomic force microscopy (AFM), ultraviolet-visible spectroscopy (UV/Vis), Fourier Transform infrared reflection-absorption spectroscopy (FT-IRRAS), X-ray photoelectron spectroscopy (XPS) are shown in subsection 3.2.5. Cyclic voltammetry (CV) was applied in this work to monitor the growth of polymer brush by detecting the redox active response from Fc groups. The results are shown in subsection 3.2.6. In subsection 3.2.7-3.2.8, an ideal packing model for polymer brushes with different side chain length were built, based on which we estimated the theoretical thickness of polymer brushes, and compare against the actual thickness measured by AFM scratch and ellipsometry. In the last two subsections, we showed the results about mechanical properties for polymer brushes and the thermal properties for corresponding bulk polymers. Conclusions will be given in section 3.3, followed by, experimental section (section 3.4).

3.2 Results and discussion

3.2.1 Selections of catalyst and solvent for ATRP reactions

ATRP has been successfully mediated by a variety of metals, including Ti, Mo, Re, Fe, Ru, Os, Rh, Co, Ni, Pd, and Cu. Among them, complexes of Cu have been found as the most efficient catalysts.[64] The structure of the initiator (alkyl halide), the catalysts (ligands and transition metals) and the reaction medium control the equilibrium constants in ATRP. Generally, ATRP equilibrium constants increase strongly with solvent polarity, by stabilization of more polar Cu(II) species, and also with temperature.[65] For alkyl halide, the reactivity depends on the structure of the alkyl group and transferable (pseudo)-halogen. On one hand, reactivity of alkyl halides follows the order of 3° >

2° >1°, in agreement with bond dissociation energy needed for homolytic bond cleavage. On the other hand, alkyl halide reactivity follows the order I > Br > Cl.[66] Low values of the ATRP equilibrium constants may be enhanced by using more powerful catalysts.[67]

Ligands are served to increase the solubility of transition metals in monomer/solvent. The range of activity of ATRP catalyst complexes covers over 6 orders of magnitudes. The general order of Cu complex activity in ATRP for ligands is tetradentate (cyclic-bridged) > tetradentate (branched) > tetradentate (cyclic) > tridentate > tetradentate (linear) > bidentate ligands. The nature of nitrogen atoms in ligands also plays a role in the activity of the Cu complexes and follows the order: bipyridine < multidentate amine (e.g. PMDETA) < tripodal amine (e.g. Me_6TREN) < some cyclic amine (Me_4Cyclam).[67] The equilibrium constants for ATRP were well studied by Krzysztof Matyjaszewski.[68]

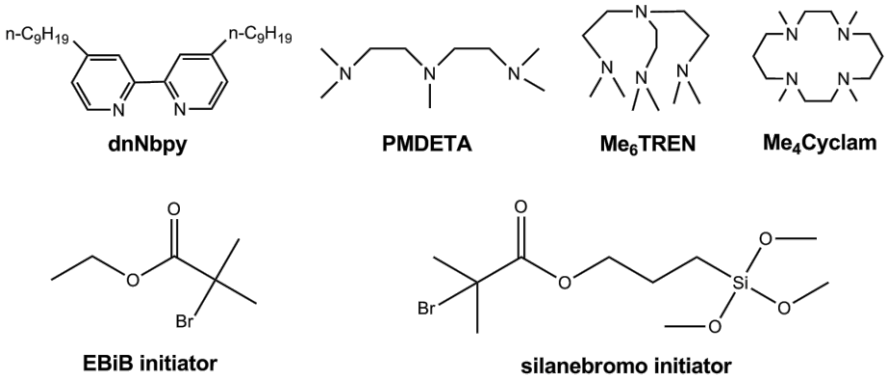

Figure 3.2 Chemical structures and abbreviations for all selected ligands and initiators in this work. dnNbpy indicates 4,4'-dinonyl-2,2'bipyridine, PMDETA indicates *N*,*N*,*N*,'*N*,'*N*''-pentamethyldiethyldiethylenetriamine, Me_6TREN indicates tris((*N*,*N*-dimethylamino)ethyl)amine, Me_4Cyclam indicates 1,4,8,11-tetramethyl-1,4,8,11-tetraazacyclotetradecane, EBiB initiator indicates ethyl 2-bromoisobutyrate, and silanebromo initiator indicates 3-trimethoxysilylpropyl 2-bromo-2-methyl-propionate.

To perform a well controllable SI-ATRP, it is essential to select proper initiator, catalyst and reaction solvent. Figure 3.2 shows the selected ligands and initiators we

applied in preliminary work. Table 3.1 shows the summary of combinations for all the catalyst and reaction solvent we have tried. Among these combinations, only Anisole/DMF mixed solvent can provide homogenous complexes (indicates that all components can dissolve in the solvent, forming a clear and homogenous solution) with high efficient catalysis. The most efficient ligand is Me_4Cyclam which can quickly promote the polymerization in the shortest time with the highest molecular weight. The reaction temperature was determined by corresponding solvents. To achieve a real "living"/controllable ATRP, the ratio between monomers and catalyst is also need to be considered, here we applied the ratio as monomer : catalyst : initiator = 100 : 1 : 1 to conduct these polymerizations.

Table 3.1 Possible combinations for homogenous polymerization system. [a] Homogenous here was defined as the catalyst complexes can completely dissolve in the reaction solvent, so the complexes are able to be prepared in stock solution. [b] Toluene was the reaction solvent, while the catalyst complexes were prepared in stock solution by acetonitrile (ACN). [c] The solvent is mixed by degassed Anisole and DMF in 1:1 (V/V). [d] The M_n data and polydispersity index (PDI) value were collected from gel permeation chromatography (GPC).[e] N.A. indicates no generation of polymers.

homogenous complexes system[a]							
monomer	FMMA						
Ligand	Me_6TREN			PMDETA		dnNbpy	Me_4Cyclam
initiator	EBiB						
Solvent	ACN	Toluene[b]	Anisole/DMF[c]	Toluene	THF	Toluene	Anisole/DMF
Temp.	60℃	60℃	60℃	60℃	40℃	60℃	60℃
Time	90 h	90 h	90 h	90 h	90 h	90 h	17 h
M_n[d] (g/mol)	N.A.[e]	N.A.	4000	N.A.	N.A.	N.A.	20500
PDI	N.A.	N.A.	1.1	N.A.	N.A.	N.A.	1.4

3.2.2 Reaction recipe for ATRP reactions

It is worth noting that the only difference between the solution ATRP and the surface ARTP is about the initiator location characteristics. In solution case, initiator was free in solution, whereas in surface case, the initiator was anchored on the surface. The concentration of free initiator can be controlled in solution case while it is not possible in surface case.

Furthermore, the persistent radical effect in CRP suggested that a sufficient concentration of deactivator is required to provide reversible deactivation of chains during propagation.[69] There are commonly two methods to ensure sufficient concentration of deactivator in the reaction: (1) In some previous CRP experiments, the "sacrificial" initiator was present in solution.[49,70,71] The free/untethered "sacrificial" initiator terminated in solution, thereby spontaneously forming a sufficient amount of the deactivator. (2) Instead of adding the "sacrificial" initiator, some groups chose to add a sufficient amount of the deactivators at the beginning of the reaction.[69] We applied the second method in this work to avoid the free polymers generated by "sacrificial" initiator would have physical adsorption on the polymer brushes, which may not easy to be rinsed off. The reaction recipe shown in Table 3.2 was the ones we used for all the polymerizations.

Table 3.2 Reaction recipe of ATRP reactions. All components were prepared in stock solutions before fully mixed. [a] N.A. indicates no free initiators and no clues about the amount for the surface anchored initiator. [b] After all components mixed together, the total concentration of the monomer may slightly decrease (~0.65M).

		Solution case		Surface case		
	Monomer	Initiator	Catalyst	Initiator	Catalyst1	Catalyst2
Sol.	FMMA FBMA FNMA	EBiB	CuBr/ Me_4Cyclam	N.A.[a]	CuBr/ Me_4Cyclam	$CuBr_2$/ 2dnNbpy
Ratio	100	1	1/1	---	1/1	1/1
Conc. (mM)[b]	0.680	0.007	0.007	---	0.007	0.007
Temp.	60 ~ 65 ℃					

3.2.3 Polymerization kinetics studies: a "living" growth

Based on the optimal reaction condition, we generated bulk polymers with 3 different monomers by controllable ATRP. Monomer conversions could be determined from the concentration of the residual monomer ([*M*]) by gas chromatography (GC)[72,73] or Nuclear Magnetic Resonance (NMR)[74,75]. Gel permeation chromatography (GPC) as a kind of size-exclusion chromatography (SEC), was applied to measure the M_n, M_w and PDI values. In some polymer brush cases, to estimate the molecular weight for corresponding anchored polymer chains, the isolated sacrificial polymers (generated by "sacrificial/free" initiator[76] in solution) could be directly analysed by GPC at different time intervals.[72,74,77] Cleavage of the polymer brush from the surface to get free polymers and measuring them by GPC is another method to obtain the molecular weight to corresponding polymer brushes.[78]

In our work, we never added "sacrificial/free" initiator or cleaved polymer brushes from surface to obtain the free polymer. ATRP in solution case was applied to examine the degree of polymerization and kinetic behaviour of polymerization under chosen recipe (see Table 3.2).

The semi-logarithmic plots, as one of the features in controlled/"living" radical polymerization, first-order kinetic behaviour should be observed in ATRP. In this behaviour, if the concentration of the active propagating species [P^*] is constant, the polymerization rate with respect to the log of the monomer concentration is a linear function of time. A downward curvature suggests that there is a decrease in [P^*] that may result from termination reaction due to some side reactions. As can be seen in Figure 3.3(A), (C), and (E), a linear regime is observed for polymerization times shorter than 50

min which indicates the controlled living character of the process. As such the molecular weight as a function of polymerization time can be well-controlled.

In terms of the degree of polymerization, it is the number average molecular weight (M_n) is a linear function of monomer conversion in ideal ATRP. Here, all three monomers yielded ~ 80% conversion to give polymers with high molecular weight (M_n: 25 ~ 35 kg mol^{-1}) with polydispersity index (PDI) < 1.6. The slopes of the linear regime for semi-logarithmic plots indicate that the FMMA reacted faster than FBMA and FNMA during the propagation stage. As we can see from Figure 3.3(B), the M_n as the function of the conversion shows a well linear line, indicating that there is a slow initiation in this ATRP. For Figure 3.3(D) and 3.3(F), the plots for PFBMA and PFNMA polymers, they show downward curvatures, indicating a slow initiation with a relatively fast chain-chain termination. From the molecular structure, the inherent reason for different trends in the degree of polymerization for PFMMA and PFBMA, PFNMA is believed due to the different side chain length: longer side chains result in more flexible arms which may obstruct the radical to continuously conducting polymerization, so FMMA with shorter side chain length showed more controllable behaviour.

Experimental details for determination of monomer conversions and molecular weight are shown in subsection 3.4.2. Below we show the semilogrithmic plots and degree of polymerization plots for polymerizations of three monomers.

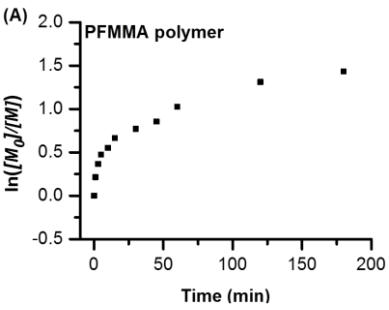

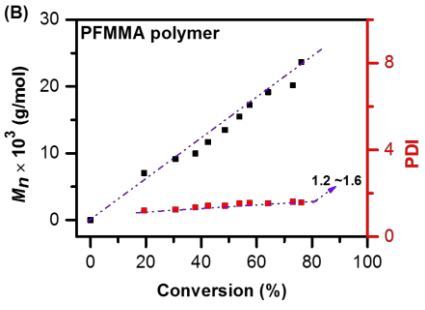

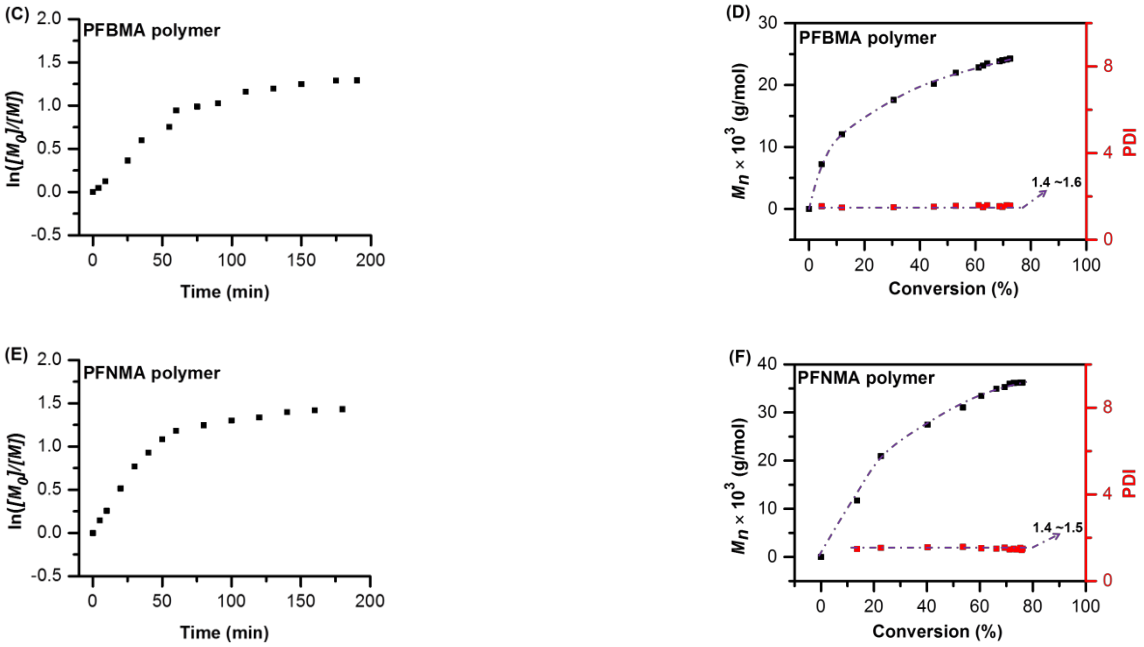

Figure 3.3 (A), (C), and (E) show the semi-logarithmic plots of ATRP with corresponding monomers. (B), (D) and (F) show the degree of polymerization plots of ATRP with corresponding monomer. PDI (in average value) for PFMMA, PFBMA, and PFNMA polymers are 1.4, 1.5 and 1.5, respectively. Dash lines serve as guiding lines.

3.2.4 SI-ATRP for Fc-containing polymer brushes

Surface requires proper treatment (cleaning and activation) before surface modification since bare ITO or Si/SiO_2 wafer carry contaminations on the surface so is hydrophobic. In the subsection 3.4.3 shows the experimental details on surface cleaning, activation and modification.

Scheme 3.1 outlines the synthesis of PFMMA (n = 1), PFBMA (n = 4), and PFNMA (n = 9) polymer brushes by forming a monolayer of the silanebromo-initiator on a cleaned ITO surface, followed by SI-ATRP. The silanebromo-initiator monolayer was formed by vapour deposition (see subsection 3.4.3). This silanebromo-initiator modified substrate was applied to SI-ATRP without other treatments.

Starting the SI-ATRP, preheated (to 60ºC) mixed solutions (including monomers and catalysts) were added into sample vials containing silanebromo-initiator modified ITO or

Si/SiO_2 substrates. Sample vials were kept in glovebox the whole reaction period, polymer brushes with different thickness were obtained by removing the substrates from polymerization solution after a set of reaction time (ranges from several minutes to several hours). Substrates were rinsed by toluene and AR EtOH and dried under a flow of N_2. There was no free polymer generated in the reaction solution.

3.2.5 Polymer brush surface characterizations

In terms of polymer brush, the common characterization techniques mainly involve in the surface characterizations, such as water contact angle (WCA)[35,79-81], X-ray photoelectron spectroscopy (XPS)[55,80-83], reflectance Fourier transform infrared (reflectance FTIR) spectroscopy[47,62,79,83,84] and Ultraviolet-visible spectroscopy (UV/Vis)[36].

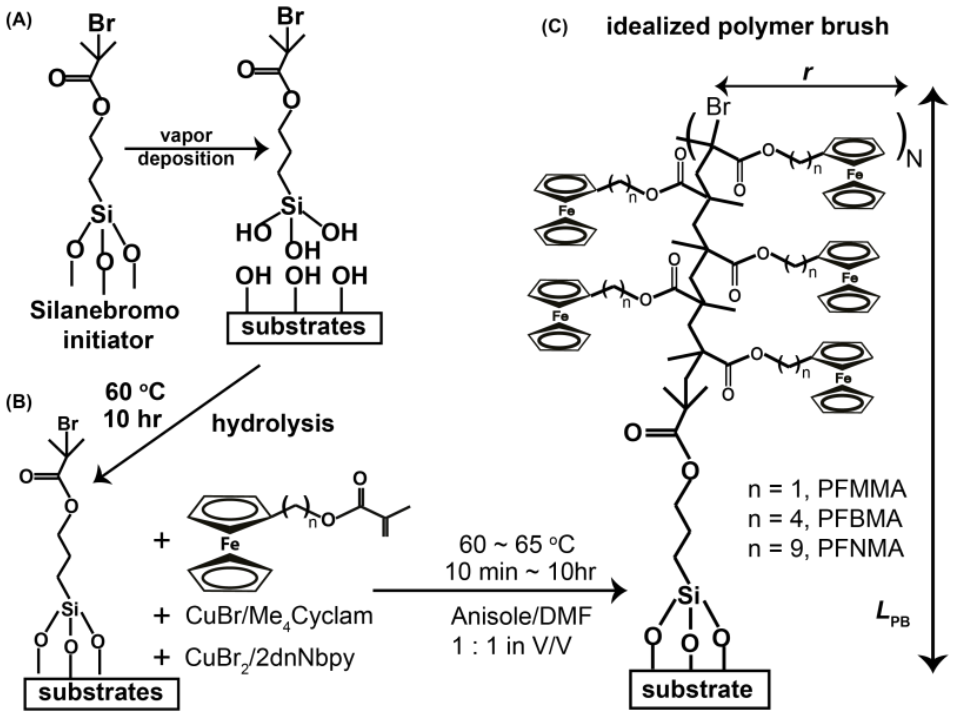

Scheme 3.1 Synthetic scheme for (A) modification of ITO substrates with silanebromo-initiator, followed by (B) SI-ATRP of FMMA, FBMA, and FNMA. n represents the carbon number of the spacer/linker between the Fc moiety and methacrylate functional group. (C) Ideally standing-up single polymer chain, with N representing the repeating units of monomers, *r* representing the ideal radius of cylindrical column formed by side chains coiling along the polymer backbone (2D profile view), and L_{PB} representing the thickness (theoretically) for polymer brush.

3.2.5.1 Water contact angle measurements

Experimental details for WCA measurement is given in subsection 3.4.4. The wettability of the surface before and after silanebromo-initiator and polymer brush modification is shown. Table 3.3 and Table 3.4 show the summary of the contact angle values for ITO substrates and Si/SiO_2 wafer, respectively. Figure 3.4 shows the microscope images for corresponding contact angles.

Table 3.3 Summary of the contact angle values of ITO substrates by treatment procedures. * Bare ITO here referred to ITO substrates taken out of package directly without any pre-treatments. # Mean values were calculated from at least 10 samples, σ stands for the standard deviations. ^ Basic cleaning solution is $NH_4OH : H_2O_2 : H_2O$ = 1:1:5 in V:V

Treatment procedures	Mean values# (σ)
Bare ITO*	92.8^{o} ($\pm 2.1^{o}$)
ITO cleaned with 3 min UV/O_3 plasma (120 W power)	35.4^{o} ($\pm 1.1^{o}$)
ITO cleaned with basic cleaning solution^ at 80 °C for 30 min (**1**)	53.6^{o} ($\pm 2.4^{o}$)
1 modified with 90 min UV/O_3 light exposure (50 W)	15.4^{o} ($\pm 1.4^{o}$)
1 modified with 3 min UV/O_3 plasma treatment (120 W) (**2**)	10.4^{o} ($\pm 0.9^{o}$)
2 after vapour deposition of silanebromo-initiator (**3**)	96.3^{o} ($\pm 2.7^{o}$)
3 after formation of PFMMA polymer brush with 25 nm (**4**)	91.1^{o} ($\pm 3.3^{o}$)
3 after formation PFBMA polymer brush for 20 nm	89.7^{o} ($\pm 5.2^{o}$)
3 after formation PFNMA polymer brush for 15 nm	93.6^{o} ($\pm 2.2^{o}$)
3 after formation PFMMA polymer brush for 40 nm (**5**)	94.5^{o} ($\pm 4.8^{o}$)

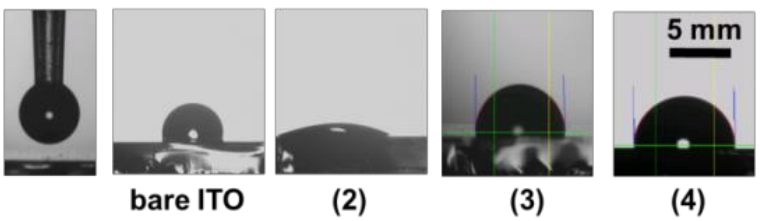

Figure 3.4 Microscopic images of contact angles for corresponding samples in Table 3.3.

Table 3.4 Summary of the contact angle values of Si/SiO_2 substrates by treatment procedures. * Bare Si/SiO_2 here referred to Si/SiO_2 substrates taken out of package directly without any pre-treatments. # Mean values were calculated from at least 10 samples, σ stands for the standard deviations. ^ Basic cleaning solution is $NH_4OH : H_2O_2 : H_2O$ = 1:1:5 in V:V.

Treatment procedures	Mean values# (σ)
Bare Si/SiO_2 *	96.4^{o} ($\pm 1.9^{o}$)
Si/SiO_2 cleaned with 3 min UV/O_3 plasma (120 W power)	27.9^{o} ($\pm 1.4^{o}$)
Si/SiO_2 cleaned with basic cleaning solution^ at 80 °C for 30 min (**1**)	48.5^{o} ($\pm 2.1^{o}$)
1 modified with 90 min UV/O_3 light exposure (50 W)	12.4^{o} ($\pm 1.1^{o}$)
1 modified with 3 min UV/O_3 plasma treatment (120 W) (**2**)	11.7^{o} ($\pm 0.7^{o}$)
2 after vapour deposition of silanebromo-initiator (**3**)	96.0^{o} ($\pm 2.9^{o}$)
3 after formation of PFMMA polymer brush with 25 nm (**4**)	92.2^{o} ($\pm 3.4^{o}$)

Bare ITO is hydrophobic due to the contaminations on the surface, basic solution cleaning, UV/O_3 exposure or UV/O_3 plasma may modify the surface with some OH group to make the surface more hydrophilic. After the silanebromo-initiator vapor deposition, the surface changed back to hydrophobic again due to the alkane-silane layer. The Fc-containing polymer brush is mainly consisted of alkane chains, so the surface keeps the hydrophobic properties after growing the polymer brush, and the thickness of the polymer brush will not change too much about the property. Si/SiO_2 wafer shows the similar surface properties before and after modifications.

3.2.5.2 AFM measurements

Experimental details for AFM measurement is given in subsection 3.4.5. Figure 3.5 shows the AFM morphology images for polymer brushes on ITO substrates. The root-mean-square (rms) surface roughness values for these three polymer brushes with similar thickness are 1.1 nm, 1.0 nm, and 0.5 nm, respectively (all measured over an area of 2 × 2 μm^2). They are much lower than the bare ITO surface (rms ~3.5 nm). This observation indicates that the polymer brushes produce uniform thin films on the substrates. We did

not observe mushroom-like polymer brushes. This observation indicates that the polymer brushes produce uniform thin films on substrate.

The AFM images show that the grain size of PFNMA brush is larger than PFMMA and PFBMA brush, which we believe is due to the different packing configuration (will be carefully discussed below): the PFMMA are stiff and form rigid brushes because of the short side chain length (n = 1), resulting in smaller grain sizes. In contrast, brushes with n = 4 or 9 are more flexible and soft, and these brushes tend to collapse/not fully extended. Below we show that indeed the Young's modulus of the brushes decreases with increasing side chain length.

Since the polymerization conditions were the same for brush growth on Si/SiO_2 substrates and ITO substrates, the brush thickness is considered to be same in both cases. Figure 3.6 shows the thickness of representative PFMMA brush sample measured by AFM scratch test (over an area of 10 × 10 μm^2). Polymer brushes on Si/SiO_2 substrates instead of ITO substrates were applied for AFM scratch tests since Si/SiO_2 substrates have much flatter surface so that clear scratches with readable step height could be obtainable.

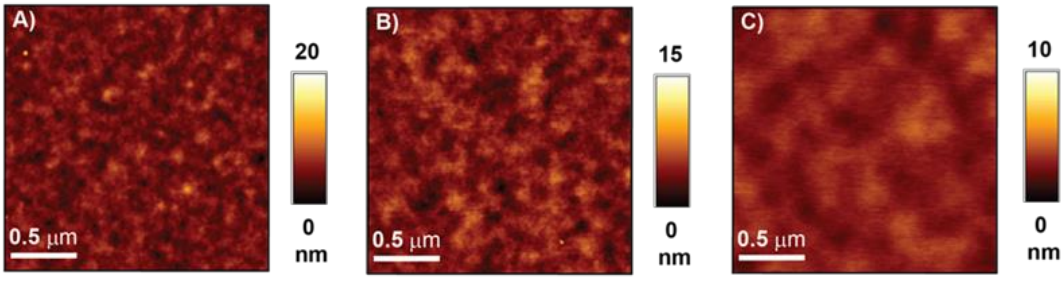

Figure 3.5 Collections of morphology of AFM images for 30 nm PFMMA brush (A), 32 nm PFBMA brush (B), and 24 nm PFNMA brush (C) with surface roughness (rms): 1.1 nm, 1.0 nm and 0.5 nm, respectively. All thicknesses shown here were measured by AFM scratch test with brush samples on Si/SiO_2 wafer.

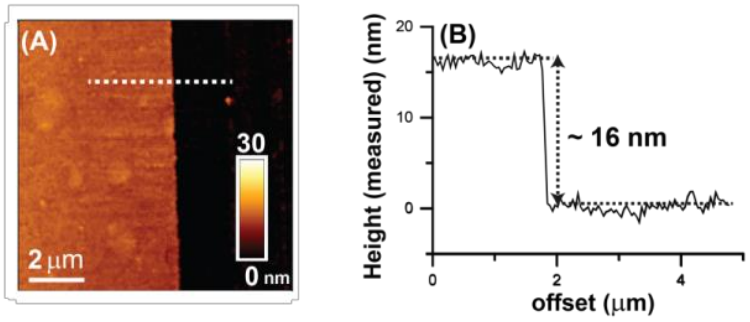

Figure 3.6 (A) Morphology of the step height for AFM scratch of representative PFMMA brush sample on Si/SiO_2 wafer. (B) Cross section for corresponding scratch in (A).

3.2.5.3 UV/Vis spectroscopy measurements

Experimental details for UV/Vis measurement is given in subsection 3.4.6. Results are shown in Figure 3.7 for three samples with similar thickness. UV/Vis spectra of three samples (PFMMA, PFBMA, and PFNMA brush) with similar thickness are shown in Figure 3.7(A). Comparing with these three samples, we have found that there are two peaks in lower wavelength sharp and narrow, they are character peaks for Fc groups. Thickness of the polymer brush may slightly affect the intensity of the absorbance, but will not affect the peak shift. Figure 3.7(B) shows the reference spectra from free polymer (PFMMA generated in solution case) in THF solvent and ferrocene in THF solvent. As we can see, the peaks at 440nm and 335nm are contributed from ferrocene. As for the broad and shallow peaks at ~700nm, we believed they are caused by the large measurement noise/spectrum baseline compared to low signal from the polymer brushes samples. According to the UV/Vis peaks of polymer brushes, we can roughly calculate the energy band gaps for the samples, which are 2.82eV and 3.70eV for peaks at 440nm and 335nm, respectively. The formula we used for the calculation is shown in eq 3.1:

$$E_{\text{band gap}} = h \times c/\lambda \qquad (3.1)$$

Where the h is the Planck's constant, 6.626×10^{-34} J▪s, c is the speed of light, 3.0×10^{8} m/s, λ is the wavelength of the peak, and the conversion factor is 1eV = 1.6×10^{-19} J.

Based on the calculation, the HOMO-LUMO gap is 2.82 eV, which belonged to the Fc's HOMO-LUMO band gap.

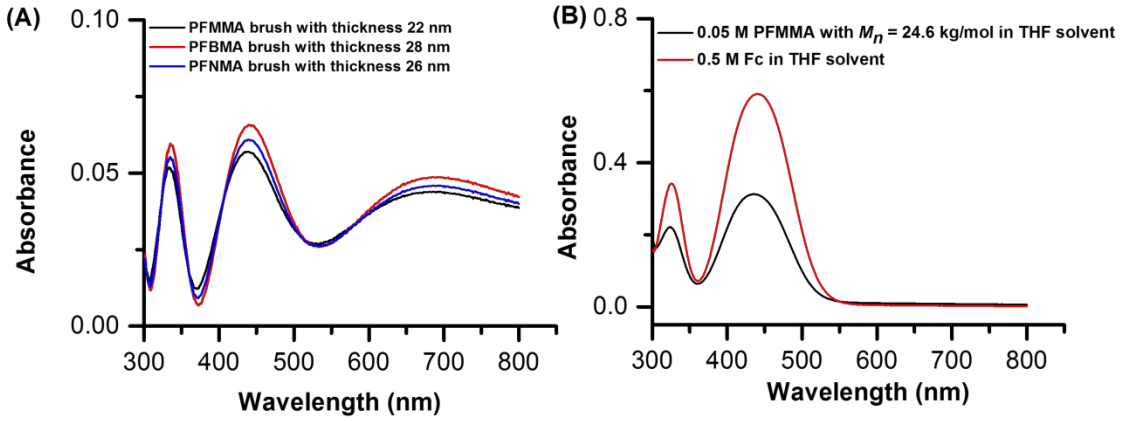

Figure 3.7 (A) UV/Vis spectrum of PFMMA, PFBMA, and PFNMA brush on ITO substrates. (B) The reference spectrum of Fc and free PFMMA polymer in solution.

3.2.5.4 FT-IRRAS spectroscopy measurements

Experimental details for FT-IRRAS measurement is given in subsection 3.4.7. Figure 3.8 shows the spectra of three polymer brushes. Peaks at 2953 ~ 2955 cm^{-1} and 3093 ~ 3097 cm^{-1} associate with ν_a CH_2 and ν_a CH of the C_p ring, respectively, and a peak at 1728 ~ 1730 cm^{-1} is from the C=O stretching vibration. All the peaks located in range 600 cm^{-1} ~ 1500 cm^{-1} belong to the C_p rings, which are fingerprint spectrum and the assignments are shown in the spectra.

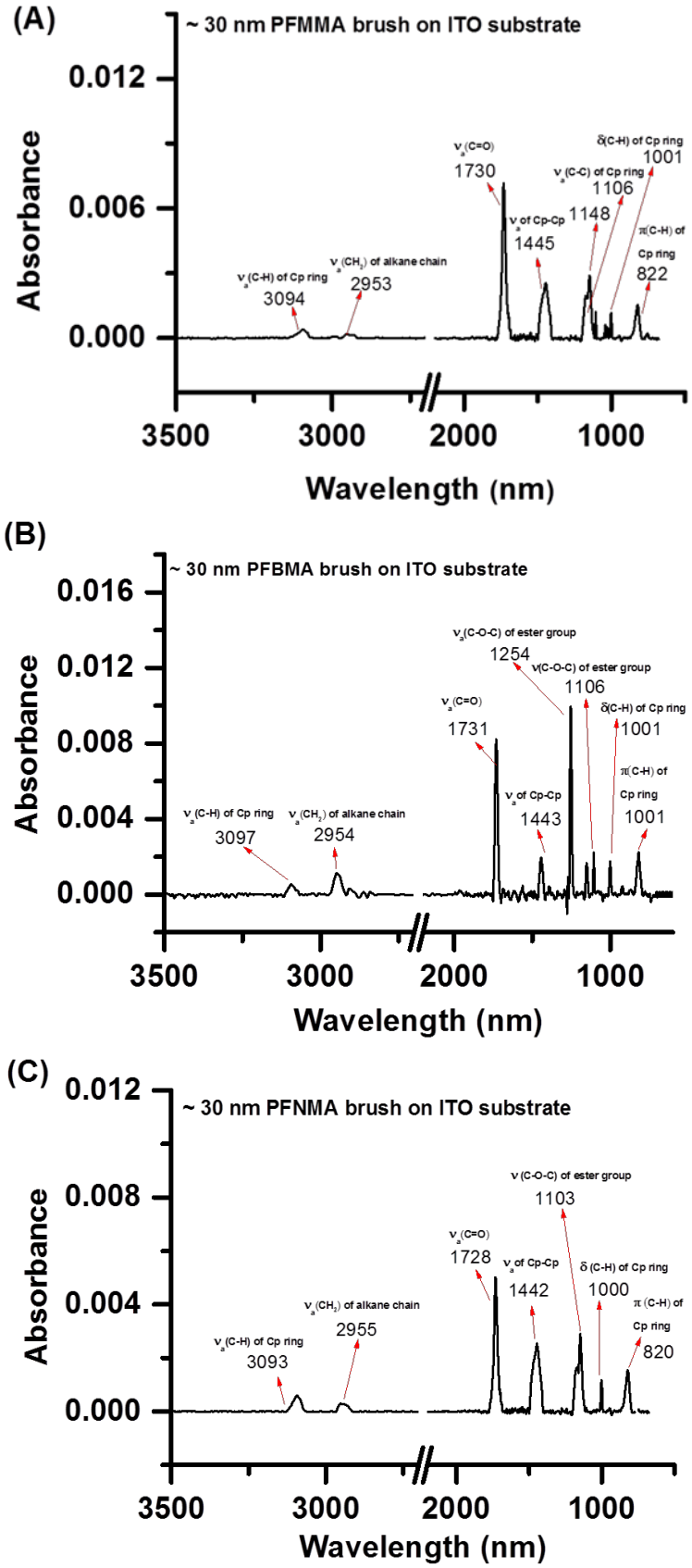

Figure 3.8 FTIR-IRRAS spectrum for PFMMA, PFBMA, and PFNMA brush on ITO substrates with about 30 nm. Peaks assignments are shown upon red arrows.

3.2.5.5 XPS spectroscopy measurements

Experimental details for XPS measurement is given in subsection 3.4.8. Four representative samples modified by silanebromo-initiator and polymer brush in variable thickness were measured, comparing with the background spectrum of bare ITO. Survey scans are shown in Figure 3.9(A), in which we can observe all characteristic peaks (all are indicated in figure), and Figure 3.9(B) and (C) display the element scans for Si and Br, which are only possible to observe in silanebromo-initiator modified ITO and polymer brush with very thin thickness modified ITO.

Figure 3.10 shows the comparisons of the signal of indium (In) and iron (Fe). We have found good correlation between the intensity of each element. The intensity of In and Sn were attenuated with the increased thickness of polymer brushes, as expected. The intensity of Fe increase with the increased thickness of polymer brushes, while it is approximately constant when the thickness beyond 10nm, which is due to detection limitation (penetrate range ~10 nm) of the XPS.

It is worth noting that for the 40 nm or beyond polymer brush, they are too thick to be conductive, when the electrons were excited out, no more electrons could be compensated from ground, which to be considered the samples were charged, and the rest of the electrons from the element will be more bound by the nucleus, it made the binding energy shift to slightly higher values. As can be seen in Figure 3.10(B) 40 nm polymer brush, the peak at 708 eV moves to slightly higher binding energy than the other two. Figure 3.10(C) shows the thickness plots against intensity of In, the attenuation of intensity suggests that the thickness of polymer brush is increasing.

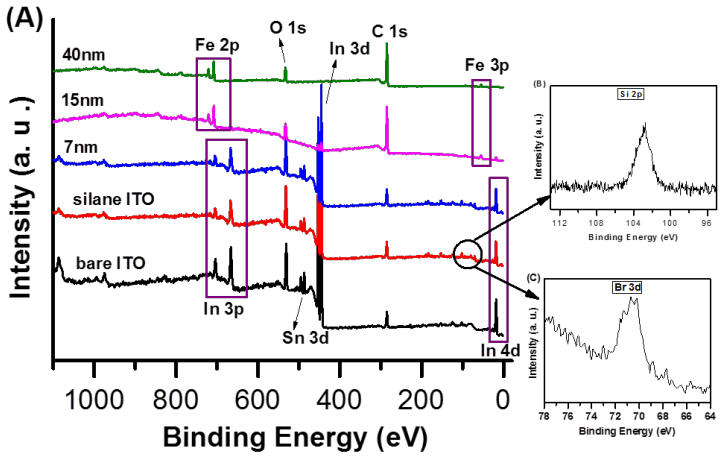

Figure 3.9 (A) XPS survey scans for representative bare ITO, silanebromo-initiator modified ITO and PFMMA brushes with 3 different thicknesses. (B) Element scan for Si 2p. (C) Element scan for Br 3d.

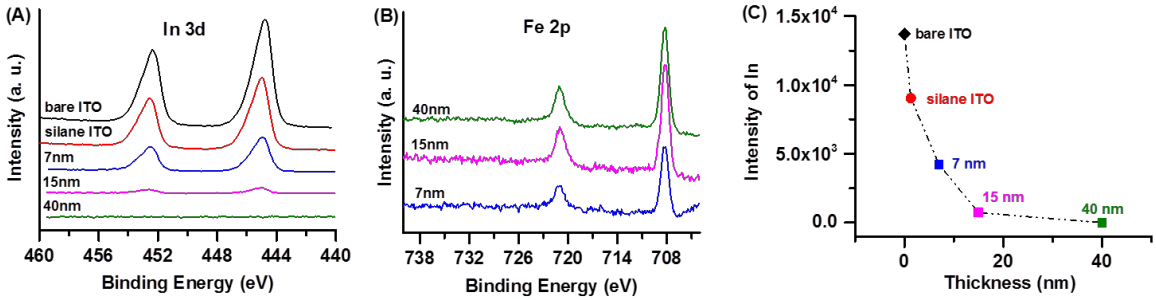

Figure 3.10 (A) Overlay of In 3d peaks for intensity comparison. (B) Overlay of Fe 2p peaks for intensity comparison. (C) Intensity of In on the dependence of polymer brush thickness.

Results shown in subsection 3.2.5 indicate that SI-ATRP is successful: all surface characterizations show us that we have gained Fc-containing polymer brushes with desirable thickness by controlled methods. We can apply these designed polymer brushes to further investigations such as wet electrochemistry and charge transport studies.

3.2.6 Wet electrochemistry: Cyclic Voltammetry (CV)

According to the SI-ATRP procedures mentioned above (see Scheme 3.1 for synthetic scheme), ITO or Si/SiO_2 substrates were taken away from polymerization solution in a set of reaction time to obtain polymer brushes with different thickness.

The redox active properties of these polymer brushes could be examined by CV with assumptions that (1) the number of Fc groups incorporated into the polymer brushes increases proportional with the thickness growth and (2) all the Fc groups are involved in the electrochemical reactions. Detailed investigations on electrochemistry will be carefully discussed in Chapter 4.

Figure 3.11(A)-(C) shows the cyclic voltammograms (CV) recorded at a scan rate 1.00 V/s in 1.0 M aquous $HClO_4$ electrolyte as a function of the polymerization time of PFMMA, PFBMA, and PFNMA polymer brushes on ITO. It is clearly visible that the current densities (I_{pa} and I_{pc}), peak separation (ΔE_p), and voltammetric waves (full width of half maximum, FWHM) are increasing with the increasing polymerization time (see Table 3.5 and Figure 3.12) indicating the increasing number of Fc groups contribute to the electrochemical communications.

The surface coverage of Fc groups (Γ_{Fc} in mol cm^{-2}) estimated by eq 3.2 could be an indicator for the growth of polymer brushes. The growth trend is shown in Figure 3.11(D)-(F).

$$\Gamma_{Fc} = Q_{tot} / n A F \qquad (3.2)$$

Here Γ_{Fc} is the surface coverage of Fc groups (mol cm^{-2}), Q_{tot} is the total charge (C), n is the number of electrons per mole of reaction, here n = 1. F is the Faraday constant (96500 C mol^{-1}), A is the surface area of the electrode exposed to the electrolyte solution (A = 0.2376 cm^2).

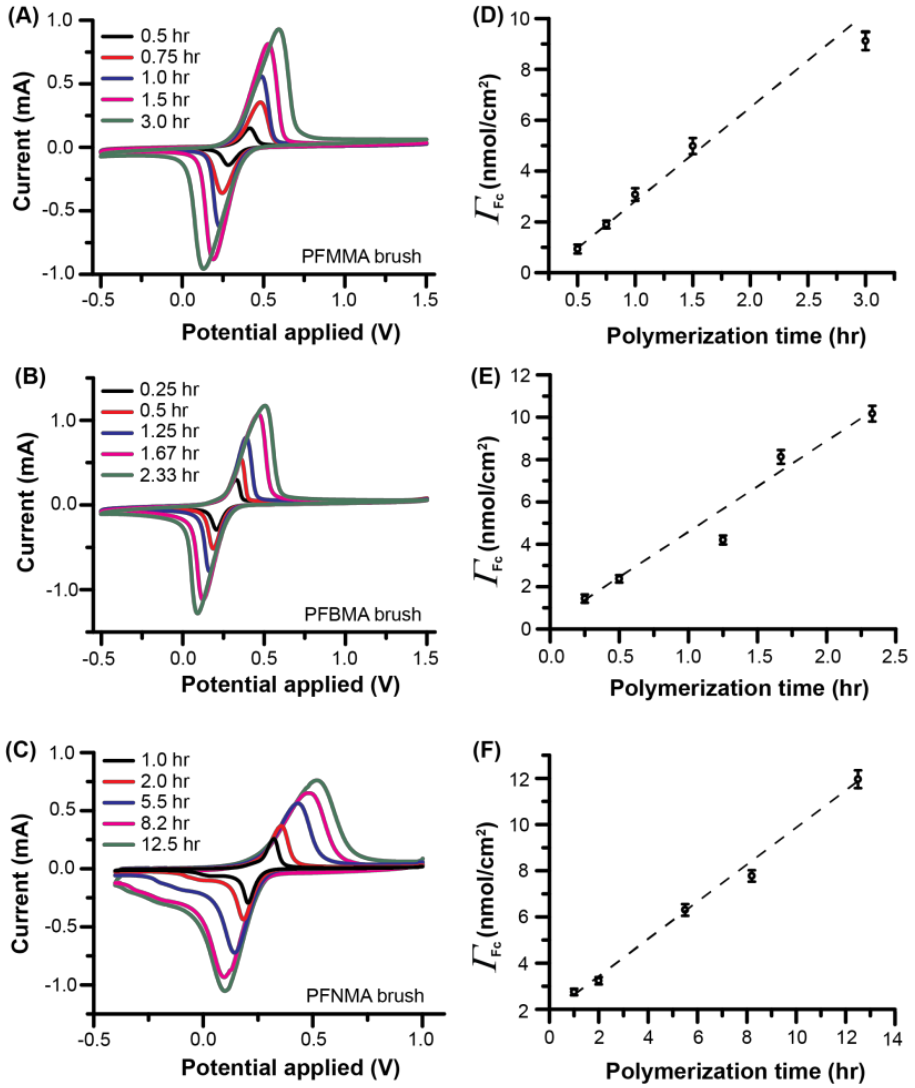

Figure 3.11 (A) CV scannings for representative PFMMA brushes generated within a serious of polymerization period. (B) Surface coverage of Fc groups estimated at scan rate was 1.00 V/s. The dash line is guiding line for eyes. The error bars represent for CV scannings of 3 individual samples.

CV was applied to roughly monitor the growth of polymer brushes. Table 3.5 summarizes the voltammetric parameters obtained from three groups of polymer brushes generated within certain polymerization periods, including current density, peak potentials, peak separations, and full width at half maximum (FWHM) of redox peaks. Figure 3.12 shows these parameters plot against polymerization times.

Table 3.5 Summary of the voltammetric parameters.

Brush	Time (hr)	I_{pa} (mA)	I_{pc} (mA)	E_{pa} (V)	E_{pc} (V)	ΔE (V)	$FWHM_{pa}$ (V)	$FWHM_{pc}$ (V)
PFMMA	**0.5**	0.14	0.13	0.42	0.28	0.13	0.09	0.09
	0.75	0.34	0.35	0.48	0.25	0.23	0.13	0.12
	1.0	0.54	0.61	0.49	0.23	0.26	0.14	0.12
	1.5	0.80	0.87	0.53	0.19	0.34	0.17	0.15
	3.0	0.91	0.93	0.60	0.14	0.46	0.21	0.20
PFBMA	**0.25**	0.24	0.22	0.34	0.20	0.14	0.09	0.09
	0.5	0.46	0.44	0.37	0.18	0.19	0.09	0.09
	1.25	0.74	0.74	0.40	0.16	0.24	0.11	0.10
	1.67	1.01	1.08	0.47	0.12	0.35	0.17	0.13
	2.33	1.09	1.21	0.53	0.09	0.44	0.21	0.15
PFNMA	**1.0**	0.30	0.34	0.32	0.21	0.11	0.06	0.06
	2.0	0.42	0.50	0.35	0.18	0.17	0.09	0.09
	5.5	0.63	0.82	0.43	0.14	0.29	0.16	0.14
	8.2	0.76	1.01	0.48	0.10	0.38	0.22	0.17
	12.5	0.85	1.17	0.52	0.10	0.42	0.25	0.19

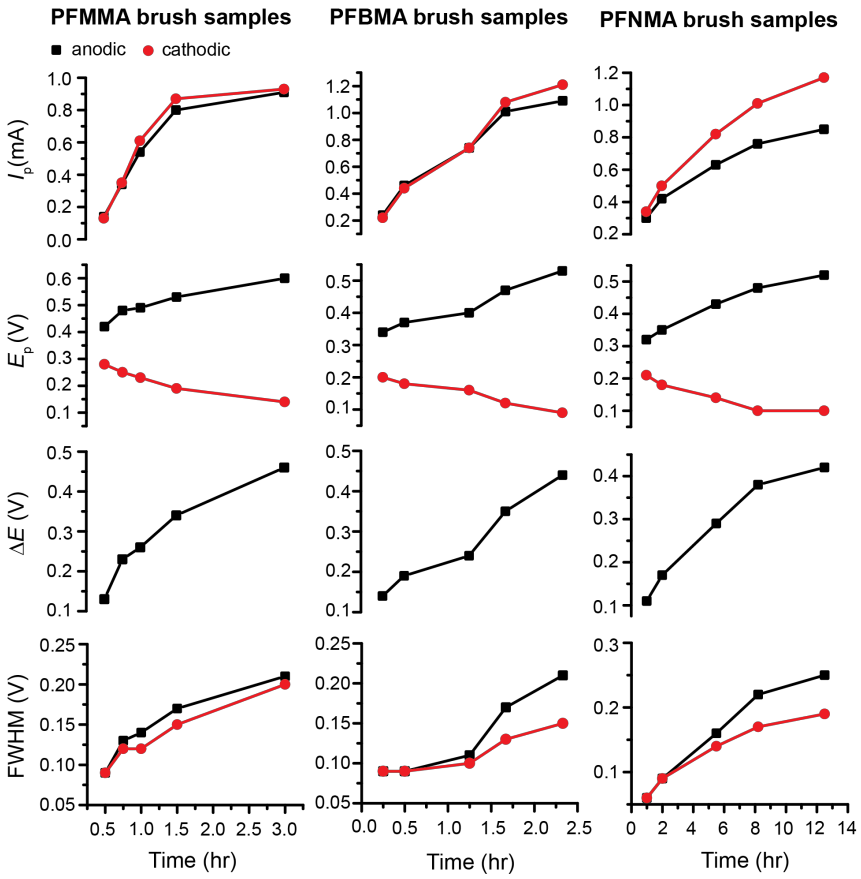

Figure 3.12 Voltammetric parameters plot as the function of polymerization time.

The results displayed in Table 3.5 and Figure 3.12 all indicate that with the polymer brush growing, there are increasing number of Fc groups involving in the electrochemical communications, which result in higher current density (I_p). The thicker brushes are, the larger peak potential separations (ΔE) are, suggesting that the electrochemical processes are getting more complex. Hence, there are more detailed studies shown in Chapter 4 focusing on pure electrochemistry of Fc-containing polymer brushes.

Besides to be used as a dynamic electrochemical method to investigate the electrochemical behaviour, CV is also used to estimate the HOMO-LUMO energy levels, relative to vacuum, of the polymer material. The oxidation process corresponds to removal of the electrons from the HOMO energy level, while the reduction corresponds to electron addition to the LUMO energy of the material. Here we use eq 3.3 to estimate the energy level of the HOMO:

$$E_{HOMO} = E_{abs,\ NHE} - eE_{1/2,NHE} \qquad (3.3)$$

Where e is the elementary charge (eV), $E_{abs,\ NHE}$ is -4.5 eV, means the absolute potential energy of the normal hydrogen electrode (NHE), which is also called as standard hydrogen electrode (SHE). The $E_{1/2,NHE}$ is the $E_{1/2}$ vs NHE, and here $E_{1/2}$ is the formal half-wave potential. The reference electrode we used in this work is Ag/AgCl in 3.0mol/kg KCl aqueous solution, this reference electrode has the potential vs NHS is 0.21 V at 25°C, so the $E_{1/2,NHE}$ value actually equals the sum of 0.21 and $E_{1/2}$. Scan rate was 1.0V/s. In Figure 3.13 we show the one example of cyclic voltammograms to indicate the $E_{1/2}$ position. The HOMO level estimated by this method shows the value of 5.1 eV.

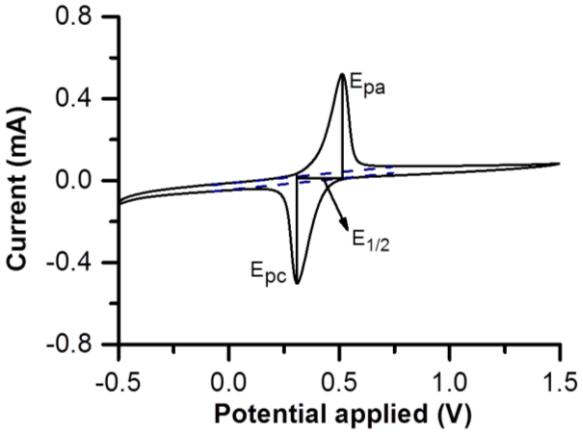

Figure 3.13 The representative cyclic voltammogram for PFMMA brush. E_{pa} stands to the peak potential of the anodic peak, E_{pc} stands for the peak potential of the cathodic peak, and $E_{1/2}$ stands for the formal half-wave potential. Black solid lines and blue dash lines are guide lines for eyes.

3.2.7 Ideal packing model

Few years ago, Hosono et al. reported a polymer brush consisted of a polymethacrylate backbone densely grafted to a paraffinic side chains containing three azobenzene units.[85] They claimed that the polymer brush was able to form into a freestanding film in which the polymer backbone aligned hometropically to the surface with backbone itself was likely extended, and consequently, the polymer brush adopted a cylindrical shape. Here we applied the similar ideal to build our model.

3.2.7.1 Estimations of side chain length by software

Here all the polymer brushes are also considered as cylindrical columns packed hexagonally as shown in Scheme 3.2(B) and (C).[85-87] We estimated the diameters of each polymer column from spacing-filling model (which is also called as CPK models). To determine the radius of each cylindrical column, we estimated the theoretical length of these side chains by Avogadro software using van de Waals radius was used but scaling of 50%.[88] PFMMA side chain is considered as the Fc-CH_2-O-CO-C-, the total side length is 0.8 nm. PFBMA brush has longer side chains, which is considered as the Fc-CH_2-CH_2-

CH_2-CH_2-O-CO-C-, and the length is 1.2 nm. They coiled relatively loosely around backbone and larger cluster of Fc bulky groups could be viewed. PFNMA brush has the longest side chains, which is considered as the Fc-CH_2-CH_2-CH_2-CH_2-CH_2-CH_2-CH_2-CH_2-O-CO-C-, and the length is 1.8 nm. See Figure 3.14 for models drawn by Avogadro software (version 1.1.1).

The three monomers which were optimized using Gaussian Calculation[89] — B3LYP/6-31G* are shown in Figure 3.14 as stick-ball structure. The Cp rings for FBMA and FNMA monomers have some twist but for FMMA monomer such twist is not obvious.

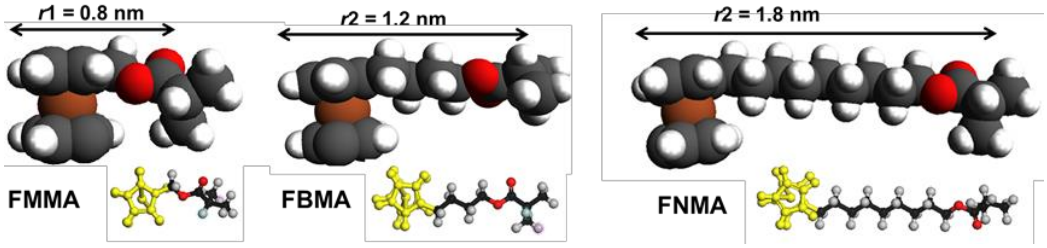

Figure 3.14 Monomer structure with indicated side chain length using CPK model estimated by Avogadro software (version 1.1.1). Iron (brown), carbon (grey), hydrogen (white), and oxygen (red). Stick-ball structures below show the optimized monomers related to FMMA, FBMA, and FNMA. Cp rings (yellow), carbone (black), hydrogen (grey), and oxygen (red).

3.2.7.2 Tacticity in polymer brush — the most stable conformation

In the polymer brush, the backbone is made up of chiral carbon centres. This leads to three possible tacticities — isotactic, syndiotactic and atactic arrangements. The polymers shown in Figure 3.15 were built using the polymer building tools in Materials Studio 6.1. The polymers displayed here are in the isotactic arrangement, which is the most stable conformation in theory. Figure 3.15(A) shows the top view of the macromolecules polymerized by 10 repeating monomer units. The more complex coiled conformation for longer polymer chain was extrapolated by stacking more monomer

units, in this case we applied 50 units of FNMA as example, see Figure 3.15(B) which shows a nice helix upon the coiling, and PFMMA brush and PFBMA brush have the similar helix structure. However, there is one more aspect that we cannot ignore: with the longer side chain, like PFNMA brush, practically, the side chain itself may also have the coiling or twist to some extent. Here we just simplified the circumstance and applied an ideal situation.

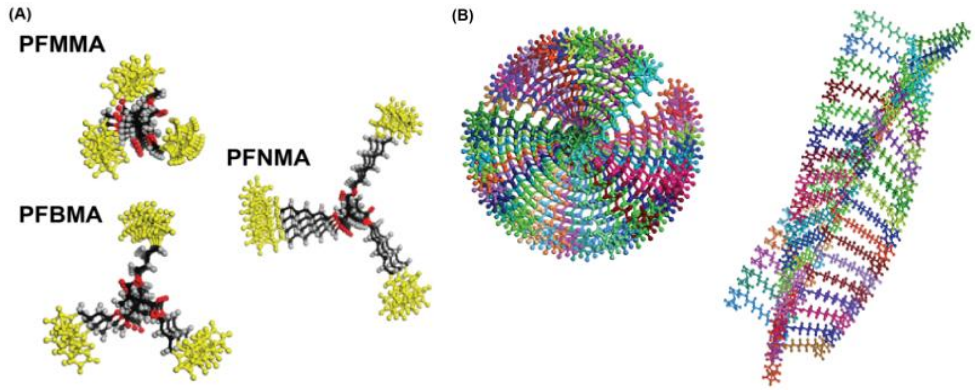

Figure 3.15 (A) Top view of the macromolecules polymerized by 10 repeating monomer units related to PFMMA, PFBMA, and PFNMA. Cp rings (yellow), carbone (black), hydrogen (grey), and oxygen (red). (B) Top view (left) and side view (right) of the PFNMA macromolecules polymerized by 50 repeating monomers.

3.2.7.3 Calculations for model parameters

We assumed the polymer brushes are fully standing-up on ITO substrates with side chain coiling in column shape. To simplify the complex packing configuration, we projected those brush columns to disks. As assumed, these disks are packing hexagonally with vacancies around each disk (N_{disk}). In hexagonal close packing, each disk has 6 other disks around it, so there are 6 vacancies; every 3 disks share 1 vacancy, so only 1/3 of each vacancy belongs to each disk which means 1 disk possesses of 6 × (1/3) vacancy ($N_{vacancy}$). We have equations as follows:

$$A_{\text{total}} = N_{\text{disk}} \times A_{\text{disk}} + N_{\text{vacancy}} \times A_{\text{vacancy}} \quad (3.4)$$

$$N_{\text{disk}} = 2\, N_{\text{vacancy}} \quad (3.5)$$

$$A_{\text{total}} = N_{\text{disk}} \times (A_{\text{disk}} + \frac{1}{2} A_{\text{vacancy}}) \quad (3.6)$$

$$A_{\text{disk}} = \pi r^2 \quad (3.7)$$

$$A_{\text{vacancy}} = \sqrt{3} r^2 - 3 \times (\frac{\pi}{6}) r^2 \quad (3.8)$$

r here is the coiled column radius of each polymer brush. Based on this packing model, theoretical thickness of these polymer brushes could be estimated according to the surface coverage of Fc groups detected by CV scaning. We considered each column (polymer chain) contains monomers (Fc groups) along the chain in average, as $N_{\text{average-Fc}}$. We assumed the total area that exposed to electrolyte is $A_{\text{total}} = 1$, then the number of disk in per cm^2 is N_{disk}. Then we deduced the equations below.

$$N_{\text{disk}} = 1 \Big/ (A_{\text{disk}} + \frac{1}{2} A_{\text{vacancy}}) \quad (3.9)$$

$$N_{\text{Fc}} = \Gamma_{\text{Fc}} \times N_{\text{A}} \quad (3.10)$$

$$N_{\text{average-Fc}} = N_{\text{Fc}} / N_{\text{disk}} \quad (3.11)$$

A_{disk} (cm^2) and A_{vacancy} (cm^2) are shown in eq 3.7 and eq 3.8, respectively. $N_{\text{average-Fc}}$ represents the average number of Fc groups in each polymer chain. N_{Fc} represents the Fc number in unit area (cm^{-2}). N_{disk} represents the number of disk in unit area (cm^{-2}). N_{A} is 6.022×10^{23} mol^{-1}. Knowing the value of r, we are able to estimate the number of disk in unit area. From CPK models and these calculations, we estimated the diameter of the polymer chains and their packing parameters, which are listed in Table 3.6.

Table 3.6 Packing parameters for polymer brushes with different side chain length. r is the coiled column radius of polymer brush. A_{disk} is the area occupied by brush column (which is projected as a disk), A_{vacancy} is the area of vacancy between disks. N_{disk} is the number of disk in unit area.

brush	n	r (nm)	$A_{disk} \times 10^{-14}$ (cm^2)	$A_{vacancy} \times 10^{-14}$ (cm^2)	$N_{disk} \times 10^{14}$ (cm^{-2})
PFMMA	1	0.8	2.0	0.1	0.5
PFBMA	4	1.2	4.5	0.2	0.2
PFNMA	9	1.8	10.2	0.5	0.1

3.2.7.4 Packing model for polymer brushes

Because the surface coverage of the polymer chains is not known, we cannot directly determine the number of Fc groups in each polymer chain of the brush as the electrochemical measurements only determine the surface coverage of the Fc groups. For the sake of comparison, we estimated the polymer brush thicknesses and packing densities using a simple model (see Scheme 3.2) by assuming all the brush chains ideally stretch away from substrates/fully extended and packed hexagonally.

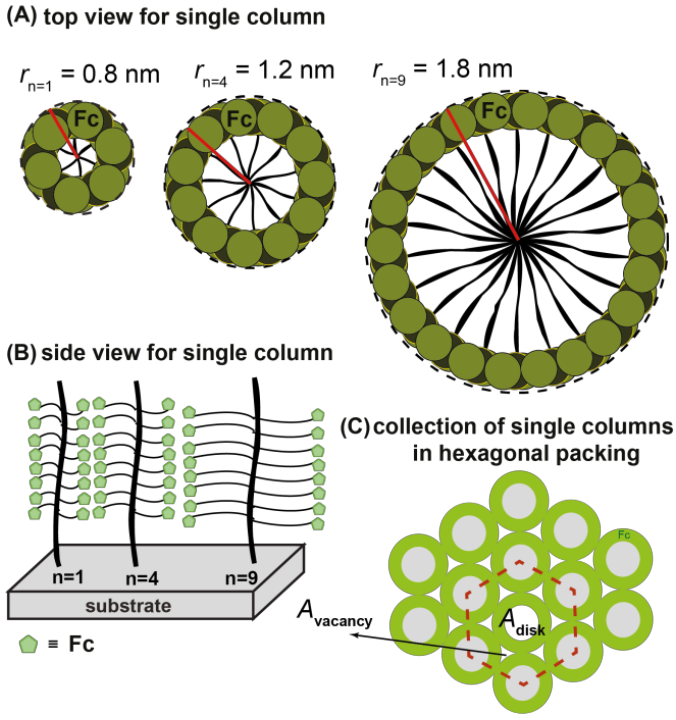

Scheme 3.2 Packing model for Fc-containing polymer brushes. (A) Top view for single coiled column, $r_{n=1}$, $r_{n=4}$, and $r_{n=9}$ represent the different side chain (linker) lengths for PFMMA, PFBMA, and PFNMA brush, respectively. (B) Side view (2D effect) for polymer brushes coiled in column shape and stretched away from substrate in idea situation. (C) Top view of ideally hexagonally packed brushes; A_{disk} indicates the projected area of a single polymer.

To simplify our model, here we ignored the possibility of interlocked side chains and assume the ideal structure from which we then derive surface coverages of the polymers and the number of Fc groups per polymer chain. The brush thicknesses that are obtained by this simple model are then compared against the experimental data obtained by ellipsometry and AFM scratch as described later.

3.2.8 Thickness correlations

Thickness determination is an essential parameter for polymer brush. People have usually applied following techniques to determine the brush thickness: (1) Patterned polymer brush,[45] it could be fabricated using photolithography[71], microcontact printing (μCP)[4,71,90,91], or even an inkjet printer[92]. These patterns could be scanned using AFM by the contrast between the brush modified area and nonbrush modified area. Thickness determination by this method could be quiet accurate while the pattern fabrication itself is the limitation for universal samples. (2) AFM scratch test[37,84], is also a commonly used method and similar with fabricating patterns, it can simply remove partial material to make the contrast manually. This technique is benefit and easy to handle for samples with silicon wafer substrate due to its non-defect and ultra-flat surface. (3) Ellipsometry is another powerful technique to measure the thickness by measure the change of polarization upon reflection or transmission and compares it to a model.[47,58,62,71,83,90] The advantage is that as an optical technique, spectroscopic ellipsometry is non-destructive and contactless, while one weakness of it is the need to model the data. Most models assume the sample is composed of a small number of discrete, well-defined layers that are optically homogeneous and isotropic, while practically, samples may have defects and non-uniform that result in the deviations in model fitting.

Here in this work, we determined the thickness of PFMMA, PFBMA, and PFNMA polymer brushes using CV, AFM scratch test, and ellipsometry. The last two measurements were conducted in air. Figure 3.15 shows the experimental thickness plotted against the estimated thickness obtained from the simple model as the function of the average number of Fc groups per brush chain (presented as $N_{\text{average-Fc}}$). Linear growing features up to certain polymer thickness were observed for all three brushes, indicating a controllable SI-ATRP process within certain polymerization period. At longer polymerization time, the polymer brushes continue to grow but the experimental thickness increases slowly and the polymer brushes are thinner than the theoretical estimations.

There are two reasons for such slowing down increase: (1) living polymerization gradually lost its control so the chain termination happens to stop the growing.[58,93,94] (2) Practically, longer polymer brushes are prone to collapse instead of standing up as we expected in ideal packing model.[95] Such collapse results in the nonlinear thickness increase in actual case.

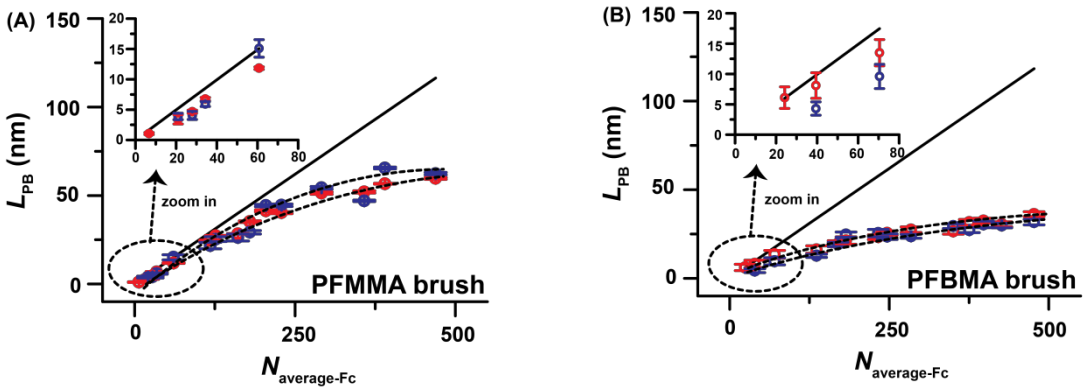

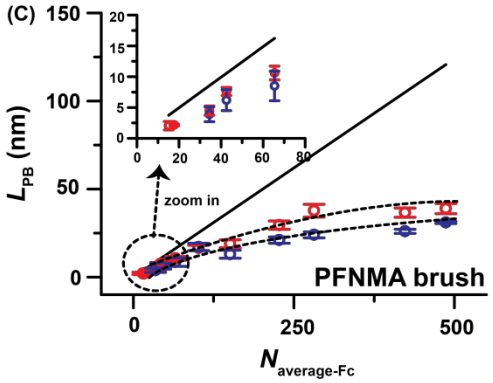

Figure 3.16 Thickness correlations among CV calculation (□ with black line), AFM scratch test (○), and ellipsometry (○). Black dash lines sever as guiding line. Error bars stand for the standard deviations of 3 individual measurements.

As we can see from Figure 3.16, all polymer brushes have the trend to collapse when they grow too thick. For PFBMA and PFNMA brush, the thickness values increase linearly with $N_{average\text{-}Fc}$ when they reach 10 nm, while for PFMMA brush, the linear growing continued beyond 15 nm, till 40 nm. Comparing with the correlations between the theoretical thickness and actual thickness, we can observe that the best correlation is from PFMMA brush till it reaches 40 nm, and the worst correlation is from PFNMA brush: the deviation gradually becomes larger even if polymer brush is still very thin. This indicates that PFMMA brush is more close to the ideal brush than the other two, and the simple model remarkably work well for PFMMA brush.

We believed that such different increasing trend may attribute to the side chain effect: in dry state, with shorter side chain length, PFMMA brush is more rigid and stiff, it is able to stand up as we expected, and behaves well up to 40 nm. In terms of the PFBMA and PFNMA brush, they have longer side chain lengths, making them more soft and flexible, their packing may not be as good as we assumed, leading to much worse correlations. This observation is in good agreement with the morphologies of polymer brush on ITO substrates measured by AFM.

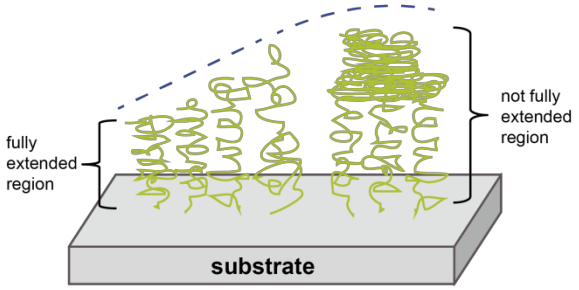

Scheme 3.3 Transition between fully stand-up polymer brush regime and partly collapsed regime.

Comparing with these three thickness estimation techniques, we concluded that actual thickness could be estimated more precisely by ellipsometry or AFM scratch test, while CV give quick access to a first impression of the brush structure. Furthermore, CV could help building the packing model: the polymer configuration and structure could be indirectly estimated by CV.

3.2.9 Nanomechanical response of polymer brushes measured by colloidal probe AFM

These measurements were conducted using the colloidal AFM based force spectroscopy method as describes.[96-98] It is a widely used technique to probe interactions between surfaces. Typical AFM probe tip can easily penetrate into the brush due to high local pressure. Hence spherical colloid particles can be used as probes with radii on the order of micrometers attached to AFM cantilevers.[99] Such colloidal probe AFMs benefit from the knowledge of the geometry of the probe, and distribute the pressure on the sample surface over a larger contact area, while the force sensitivity of the AFM is maintained.

The apparent elastic moduli of the polymer brushes were estimated from the nanoindentation curves using the Hertz model as described elsewhere:[97,98]

$$F = \frac{4\sqrt{r_{tip}}}{3(1-v^2)} E\delta^{\frac{3}{2}} \quad (3.12)$$

$$F = k\left(\left|D - D_0\right|\right) \quad (3.13)$$

$$\delta = \left|Z - Z_0\right| - \left|D - D_0\right| \quad (3.14)$$

Where F is the applied load, r_{tip} is the radius of the colloidal probe (2.50 ± 0.05 μm), v is the Poisson's ration of the polymer films (assumed to be 0.5), E is the apparent Young's modulus of polymer films, δ is the deformation of the polymer films, and k is the calibrated spring constant of the cantilever, Z denotes the piezo-extension, Z_0 represents the piezo-extension at which tip-surface contact occurs, D is the values of deflection of the cantilever, and D_0 is the deflection of the cantilever when tip-surface contact occurs. A constant applied force was employed during the indentation measurement. To avoid a substrate effect on the measured values, the initial 10% of the approach curve was used to measure the Young's modulus of the polymer brush film. By fitting the force curves (based on 200 individual measurements) acquired during normal-force measurements into equations above, we can obtain the apparent Young's modulus, E, for the polymer brush films. The measurements were conducted in air and DI water condition. E values were estimated in a range of 1.4 MPa ~ 3.2 MPa in air, and 0.9 MPa ~2.1 MPa in DI water, respectively. As observed, E values for all polymer brushes are smaller in DI water environment than in air, which may because the high capillary force affects the force distance curve when we measured in air condition.[100-103] Figure 3.17 shows the histograms and distributions of E in both air and DI conditions and the results are summarized in Table 3.7. The results indicates that PFMMA brush is the most rigid brush while the PFNMA brush is the softest brush, PFBMA brush stays in middle. The mechanical properties may be affected by the packing structure of each brush which is attributed to the side chains length.[31]

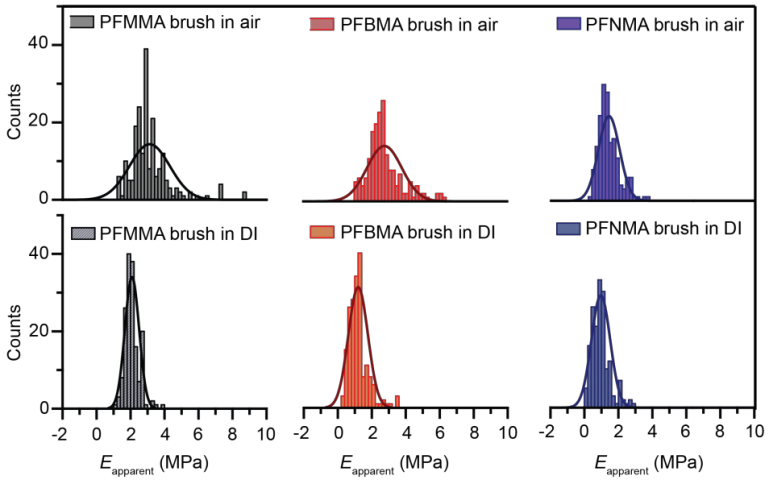

Figure 3.17 Statistical histograms of the *E* values of (A) PFMMA, (B) PFBMA, and (C) PFNMA brushes measured in air (left column, blank histograms) and in DI water (right column, patterned histograms).

Table 3.7 Apparent Young's modulus ($E_{apparent}$) values for three polymer brushes in air and in DI water and the thermal properties for bulk polymers.

	Polymer brushes		
	PFMMA	PFBMA	PFNMA
Thickness (nm)	30 ± 2	30 ± 3	30 ± 3
$E_{apparent}$ (MPa) in air	3.2 ± 1.2	2.8 ± 1.0	1.4 ± 0.6
$E_{apparent}$ (MPa) in DI water	2.1 ± 0.4	1.2 ± 0.6	1.0 ± 0.6
	Bulk polymers		
	PFMMA	PFBMA	PFNMA
M_n (kg/mol)	37.3	34.9	39.5
PDI	1.6	1.6	1.6
T_D (°C)	210	209	209
T_g (°C)	148.5	61.5	-3.5

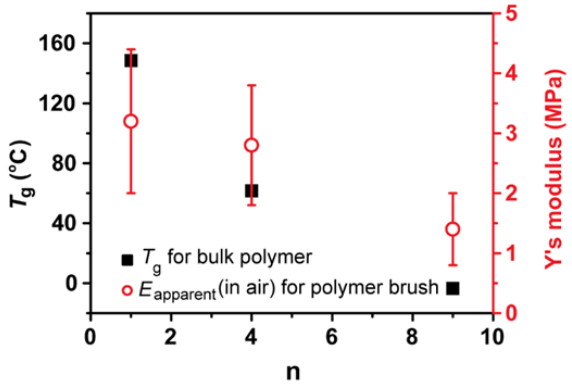

Figure 3.18 The correlation between glass transition temperature (T_g) for bulk polymers and Young's modulus ($E_{apparent}$, in air) for polymer brushes as the function of the number of CH_2 unit the linker (n).

3.2.10 Thermal properties of Fc-containing bulk polymers

For thermal stability, TGA curves show three weight-loss stages these bulk polymers (see Figure 3.19). These bulk polymers are all stable below 210°C, which is the decomposed temperature, T_D, showed in Table 3.7. Most of polymer backbone and organic side groups decomposed when heated up 500 °C ~ 600 °C. The final weight percent of PFBMA polymer and PFNMA polymer decreases obviously compared to PFMMA polymer. The reason was expected to be the side chain effect that was in agreement with other's reports.[31] For DSC, the midpoint of the change in slope of the baseline in DCS curves obtained from the second and third scans were collected as the glass transition temperature (T_g) values for these polymers (see Figure 3.20). T_g values are shown in Table 3.7. The value of T_g increases with decreasing n from T_g = -3.5 °C for n = 9 to T_g = 148.5 °C for n = 1. The thermal behaviours of these polymers displayed an obvious correlation with the length of side chain.[31] In general, low T_g values suggest the polymer is soft while high T_g values indicates rigid polymer structure.[104,105] We find an excellent agreement between stiffness and T_g as T_g increases with increasing Young's modulus as shown in Figure 3.18.

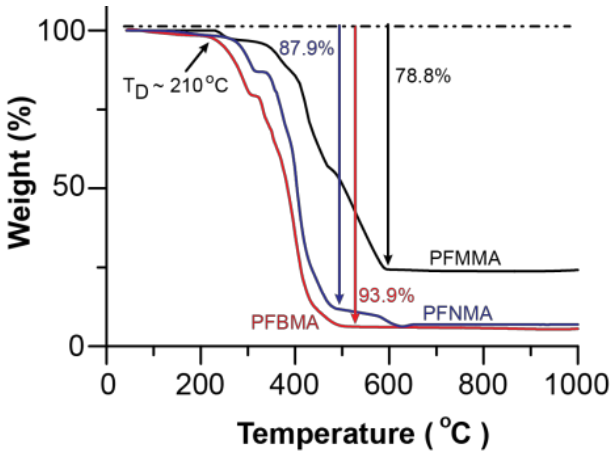

Figure 3.19 TGA curves of PFMMA polymer (M_n = 37.3 kg/mol, black), PFBMA polymer (M_n = 34.9 kg/mol, red) and PFNMA (M_n = 39.5 kg/mol, blue), respectively. At a heating rate of 10°C/min from 40 to 1000°C under N_2 flow.

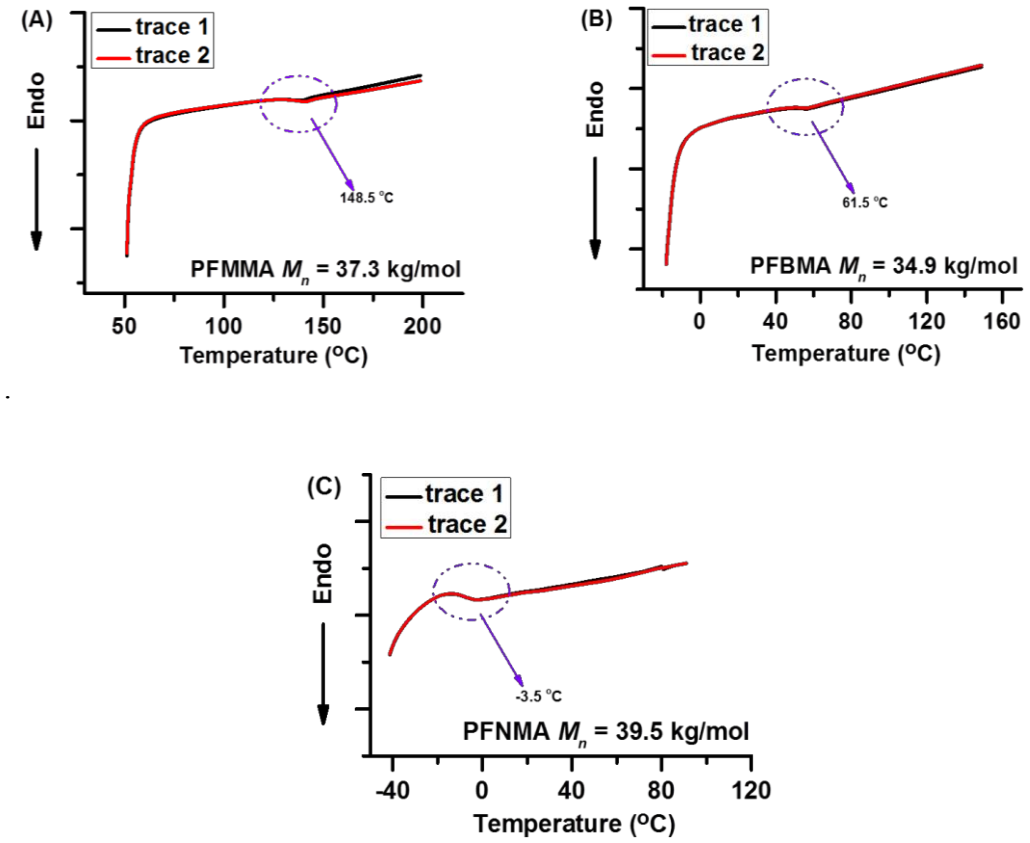

Figure 3.20 DSC traces (the second and third traces) of (A) PFMMA polymer (M_n = 37.3 kg/mol), (B) PFBMA polymer (M_n = 34.9 kg/mol), and (C) PFNMA (M_n = 39.5 kg/mol), respectively. The heating ranges are from 50 to 200°C, -10 to 155°C, and -40 to 100°C, for PFMMA, PFBMA, and PFNMA, respectively. The heating rate is 10°C/min for all.

3.3 Conclusions

We prepared a series of Fc-containing polymer brushes by SI-ATRP with different linker lengths between the Fc unit and the polymer backbone. With electrochemistry (i.e., CV) we could quantify the number of Fc groups per unit of surface area. Using an ideal packing model allowed us to estimate the polymer thickness which we could compare against experimentally obtained brush thicknesses. The brushes were characterized using several methods to obtain the experimental thickness from which we concluded that PFMMA brush (i.e., the linker length is a single CH_2 unit) is stiff and stands up in air, following the ideal model up to 40 nm (or roughly 200 monomers) very well. In contrast,

both the PFBMA and PFNMA brushes with long linkers are soft and form collapsed structures, resulting in not well-packed layers.

To prove the stiffness of these polymer brushes, we examined their nanomechanical properties. The mechanical properties of these brushes are nicely reflected in the increase of the Young's modulus with decreasing linker length following the order PFMMA > PFBMA > PFNMA. This order is in a good agreement with the change in T_g of the corresponding solution grown polymers. These observations support the conclusion that PFMMA brush with the shortest side chain is the stiffest while the PFBMA and PFNMA brushes with longer side chain length are softer.

Within such Fc containing polymer brush, the different mechanical properties and redox active properties combine together, making the potentials to integration of polymer brushes into micromechanical devices, such as mechanical transduction of chemical stimuli.

3.4 Experimental section

3.4.1 Chemicals and materials

ferrocenylmethyl methacrylate, ferrocenylbutly methacrylate, ferrocenylnonyl methacrylate (FMMA, FBMA, FNMA, respectively, 95%, PICHEMICALS),were repurified by flashing a silica gel plug with hexane (85%, ACS, MTEDIA), copper (I) bromide (CuBr) (99.999%, Aldrich), copper (II) bromide ($CuBr_2$) (99.999%, Aldrich), 1,4,8,11-tetramethyl-1,4,8,11-tetraazacyclotetradecane (Me_4Cyclam, 98%, Aldrich), 4,4'-dinonyl-2,2'-bipyridine (dnNby, 97%, Aldrich), ethyl 2-bromoisobutyrate (EBiB, 95%, Aldrich), 3-trimethoxysilylpropyl 2-bromo-2-methyl-propionate (silanebromo-initiator, 95%, GELEST), anisole (99%, Aldrich), *N,N*-dimethylformamide (DMF,

99.8%, Aldrich), tetrahydrofuran (THF, 99%, MTEDIA), toluene (95%, EMSURE), aluminum oxide (Al_2O_3, activated neutral, Aldrich), were used without further purification. Basic cleaning solution (NH_4OH : H_2O_2 : H_2O = 1:1:5 in V:V), absolute ethanol (AR EtOH, EMSURE), deionized water (DI water, obtained from a Millipore-Q water system) were used for substrates cleaning. Indium tin oxide (ITO) (Singapore optics shop, 101×101×1.1 mm, ITO layer thickness ~ 180nm, sheet resistance ~ 10Ω sq^{-1}) and Silicon (Si/SiO_2, 100, p-type, University Wafers, USA)

3.4.2 Determination of monomer conversion and molecular weight

Bulk polymers were characterized by ^1H NMR on a Bruker 400 MHz spectrometer. Gel Permeation Chromatography (GPC system equips with Waters 2690 Separations Module, Waters 2420 ELS Detector, and a Phenogel column. The measurements were performed at 40℃ using HPLC THF as eluent with a flow rate of 1.0 mL/min. The system was calibrated with PMMA standards) were used to measure the relative molecular weights (M_n) and molecular weight distribution (PDI). Following completion the reaction, reaction mixture was taken and diluted with THF and passed through a neutral aluminum oxide plug to remove residual copper complexes from the media, polymers were isolated by precipitating in n-hexane, the precipitations were performed twice and were dried in vacuum oven at 40 °C overnight, yielding yellow solids. The yellow solids were dissolved in HPLC THF, followed by filtering with 0.22μM microfilter and characterized by GPC.

3.4.3 Activation and modification for substrates

ITO and Si/SiO_2 substrates were cleaned by base cleaning solution, followed by rinsing with DI water and AR EtOH and bellowing to dry with N_2. Washing by base

cleaning solution may activate the surface with some OH group, making the surface hydrophilic. The surfaces were further activated by UV/O_3 exposure for 90 min or UV/O_3 plasma for 3 min, becoming even more hydrophilic. Vapour deposition for silianebromo-initiator were conducted in a desiccator with vacuum valve. With 10 µl silanebromo-initiator in desiccator, vacuum was sucked for 15 min before sealing. The desiccator was placed in 60℃ ~ 65℃ oven for overnight. Silanebromo-initiator modified substrates were applied to SI-ATRP without other treatments. After the vapor deposition of silanebromo-initiator, the surface changed back to hydrophobic again due to the alkane-silane layer. This silanebromo-initiator layer was fixed on the surface firmly with the strong chemical bond, quick ultrasonication can help to remove the multiply physisorbed alkane-silane layer and leave only monolayer of silanebromo-initiator on the surface.

3.4.4 Water contact angle measurement

Contact Angle Goniometry (CA) (ramé-hart. Inc, DROPimage Advanced software) was used for characterizing the hydrophobicity/hydrophobicity of the surface before and after silanebromo-initiator and polymer brush modification. 3µl water droplet was hung on the mircropipette, slowly move down the droplet to tough the substrate gently. Angles between water and substrate were measured by imaging via camera. 5 droplets were applied to one substrate to take average values.

3.4.5 AFM morphology measurement and scratch test

The Nanowizard III instrument (JPK Instruments AG, Berlin, Germany) equipped with NanoWizard head and controller was used for the AFM experiments. The morphology and thickness of the polymer brushes were measured by tapping mode AFM

imaging under ambient conditions using standard silicon probes (k ~ 40 N/m, Tap 300AL-G, Budget sensors). All the images were processing using the JPK data processing software (Version 4.2). Normally 5 μm × 5 μm image or 2 μm × 2 μm image with 256 × 256 lines were scanned for morphology measurement. Polymer brushes on Si/SiO_2 wafer instead of ITO substrates were applied for AFM scratch test since normally wafer has much more flat surface (rms ~ 0.5 nm), which can provide us clear scratches with readable step height. Normally 20 μm × 20 μm image or 10 μm × 10 μm image with 128 × 128 lines were scanned for morphology measurement.

3.4.6 UV/Vis measurements

Ultraviolet and visible spectroscopy (UV/ViS) (PerkinElmer UV/Vis/NIR Spectrometer Lambola 750) was used to record the UV/Vis spectra of polymer brushes on ITO substrate. Simply treated by base cleaning solution, an unmodified bare ITO substrate was used as a background to confirm surface attachment of polymer brushes. Scanning ranges from 800 to 250 nm, and data interval 1.00, scan speed 266.75 nm/min, cycle number is 1.

3.4.7 FT-IRRAS measurements

Infra-red reflection absorption spectroscopy (IRRAS) (PerkinElmer FT-IR spectrometer equipped with a liquid N_2-cooled MCT detector) was also used for the surface characterization. Similarly, simply treated by base cleaning solution, an unmodified bare ITO substrate was used as a background to confirm surface attachment of polymer brushes. Before background measurement, 500 ml liquid N_2 was filled in the cooler and 10 min was required to stable the equipment. Target sample with ~ 30 nm polymer brushes on ITO substrate in 1.2×1.2 cm^2 size. The IR beam was p-polarized

with a ZnSe polarizer to increase the sensitivity, and the spectrometer was operated at a resolution 4 cm^{-1} and average 500 scans.

3.4.8 XPS measurements

XPS (Thermo Scientific Theta Probe XPS with monochromatic Al Kα X-ray, *hv* = 1486.6eV) is another qualitative technique utilized to confirm the growth of polymer brushes. Sample size was as small as 0.8 × 0.8 cm^2 and was loaded into the vacuum chamber as quick as possible after rinsing by EtOH and drying by N_2 flow. Ultrahigh vacuum was applied for at least 1 ~ 2 hrs before the measurements.

3.4.9 CV measurements

AUTOLAB PGSTAT302N with NOVA 1.10 software was used for measuring the surface coverage of Fc groups. It consists of a custom built electrochemical cell, equipped with a platinum counter electrode, which was placed in a Faraday cage, a Ag/AgCl reference electrode and the ITO substrates with polymer brushes served as a working electrode. Cyclic voltammograms were recorded in an aqueous (aq.) solution 1.0 M $HClO_4$, between -0.5 V to 1.5 V at a scan rate of 1.00 V/s.

3.4.10 Ellipsometry measurements

Elliposmetry (Variable Angle Spectroscopic Ellipsometor, V.A.S.E., M190-1700, Digipol) was used to determine the polymer brush thickness on Si/SiO_2 substrates. We varied the wavelength from 600 nm to 1100 nm at three angles (65°, 70°, and 75°). The fitting model was based on a 3-layer model to extract the polymer brush thickness: 0.5 mm Si wafer (fixed), 4.5 nm SiO_2 layer (fixed), and unknown Cauchy layer. Refractive indices *n* of 1.45 was used for initiator layers, 1.60, 1.60, and 1.55 were used for FMMA,

FBMA and FNMA polymer brush films, respectively. Data were recorded from three different spots of substrate.

3.4.11 Thermal properties measurements

The thermal properties of bulk polymers (PFMMA, M_n = 37.3 kg/mol; PFBMA, M_n = 34.9 kg/mol; PFNMA, M_n = 39.5 kg/mol) were studied using thermogravimetric analysis (TGA, 2960 Simultaneous DTA-TGA, TA instruments) at a heating rate of 10°C/min from 40 to 1000°C under N_2 flow and differential scanning calorimetry (DSC, 2920 Differential Scanning Calorimeter, TA instruments) at a heating rate of 10°C/min from -40 to 200°C under air flow. For DSC scanning, there were totally three complete scan cycles from -40 to 200°C. Curves have to be completely repeatable for the last two scans.

3.4.12 Nanomechanical properties measurements

The force measurements by colloidal AFM probes were conducted in both air and liquid environment. A typical measurement was performed in the force volume imaging mode with a *z*-ramp size of 1 μm, a scan rate of 1 Hz, a deflection trigger of 200 nm, and a scanning area of 15 μm × 15 μm. To ensure the Young's modulus measurements in air and DI water were conducted in the same area, the DI water was gently injected into the AFM liquid cell by using syringe after the dry condition experiment, and an equilibrium time of 5 mins were applied.

3.5 References

1. Milner, S. T., *Science* **1991,** *251*, 905-915.

2. Boyes, S. G.; Granville, A. M.; Baum, M.; Akgun, B.; Mirous, B. K. and Brittain, W. J., *Surf. Sci.* **2004,** *570* (1-2), 1-12.

3. Edmondson, S.; Osborne, V. L. and Huck, W. T., *Chem. Soc. Rew.* **2004,** *33* (1), 14-22.

4. Dyer, D. J., *Adv. Funct. Mater.* **2003,** *13* (13), 4.

5. Azzaroni, O., *J. Polym. Sci., Part A: Polym. Chem.* **2012,** *50* (16), 3225-3258.

6. Minko, S., *J. Macromol. Sci., Polym. Rev.* **2006,** *46* (4), 397-420.

7. Yameen, B. and Farrukh, A., *Chem. -Asian J.* **2013,** *8* (8), 1736-1753.

8. Langer, R., *Acc. Chem. Res.* **2000,** *33* (2), 94-101.

9. Ishaug-Riley, S. L.; Okun, L. E.; Prado, G.; Applegate, M. A. and Ratcliffe, A., *Biomaterials* **1999,** *20* (23–24), 2245-2256.

10. Gracia, R. and Mecerreyes, D., *Polym. Chem.* **2013,** *4* (7), 2206-2214.

11. Kealy, T. J. and Pauson, P. L., *Nature* **1951,** *168* (4285), 1039-1040.

12. Neuse, E. W. and Rosenberg, H., *J. Macromol. Sci., Polym. Rev.* **2007,** *4* (1), 1-145.

13. Ciardelli, F.; Tsuchida, E. and Wöhrle, D., (1996) *Macromolecule-metal Complexes*. Berlin, Springer.

14. Wöhrle, D. and Pomogailo, A. D., (2007) *Metal Complexes and Metals in Macromolecules: Synthesis, Structures, and Properties,* Europe, Wiley-VCH Verlag GmbH & Co.

15. Whittell, G. R.; Hager, M. D.; Schubert, U. S. and Manners, I., *Nat. Mater.* **2011,** *10* (3), 176-188.

16. Rider, D. A. and Manners, I., *Polym. Rev.* **2007,** *47* (2), 165-195.

17. Zhao, D.; Ren, B.; Liu, S.; Liu, X. and Tong, Z., *Chem. Commun.* **2006,** (7), 779-781.

18. Smith, T. M. and Nelson, G. L., *Polym. Adv. Technol.* **2006,** *17* (9-10), 746-753.

19. Whittell, G. R. and Manners, I., *Adv. Mater.* **2007,** *19* (21), 3439-3468.

20. Pittman, C. U. and Carraher, C. E., (2006) *Frontiers in Transition Metal-Containing Polymers: Organometallic Polymers: The Early Days*, Europe, John Wiley & Sons, pp 1-44.

21. Pomogailo, A., (2007) *Metal Complexes and Metals in Macromolecules: Synthesis, Structure, and Properties*, *Chapter 4*, *Polymerization of Metal-containing Monomers (MCMs) as a Method for Incorporating Metals in Macromolecules.* Wiley-VCH Verlag GmbH & Co., pp 97-171.

22. Rider, D. A.; Winnik, M. A. and Manners, I., *Chem. Commun.* **2007,** (43), 4483-4485.

23. Ahmed, R.; Patra, S. K.; Chabanne, L.; Faul, C. F. J. and Manners, I., *Macromolecules* **2011,** *44* (23), 9324-9334.

24. Bellas, V. and Rehahn, M., *Angew. Chem. Int. Ed.* **2007,** *46* (27), 5082-5104.

25. Daum, P. and Murray, R. W., *J. Phys. Chem.* **1981,** *85* (4), 389-396.

26. Nelson, J. M.; Nguyen, P.; Petersen, R.; Rengel, H.; Macdonald, P. M.; Lough, A. J.; Manners, I.; Raju, N. P.; Greedan, J. E.; Barlow, S. and O'Hare, D., *Chem. Eur. J.* **1997,** *3* (4), 573-584.

27. Yang, Y.; Xie, Z. and Wu, C., *Macromolecules* **2002,** *35* (9), 3426-3432.

28.Pittman, C. U.; Lai, J. C. and Vanderpool, D. P., *Macromolecules* **1970,** *3* (1), 105-107.

29. Pittman, C. U. and Hirao, A., *J. Polym. Sci., Polym. Chem. Ed.* **1977,** *15* (7), 1677-1686.

30. Pittman, C. U. and Hirao, A., *J. Polym. Sci. Polym. Chem. Ed.* **1978,** *16* (6), 1197-1209.

31. Hardy, C. G.; Ren, L.; Tamboue, T. C. and Tang, C., *J. Polym. Sci., Part A: Polym. Chem.* **2011,** *49* (6), 1409-1420.

32. Herfurth, C.; Voll, D.; Buller, J.; Weiss, J.; Barner-Kowollik, C. and Laschewsky, A., *J. Polym. Sci., Part A: Polym. Chem.* **2012,** *50* (1), 108-118.

33. Gallei, M.; Tockner, S.; Klein, R. and Rehahn, M., *Macromol. Rapid. Commun.* **2010,** *31* (9-10), 889-896.

34. Gallei, M.; Schmidt, B. V.; Klein, R. and Rehahn, M., *Macromol. Rapid. Commun.* **2009,** *30* (17), 1463-1469.

35. Elbert, J.; Gallei, M.; Rüttiger, C.; Brunsen, A.; Didzoleit, H.; Stühn, B. and Rehahn, M., *Organometallics* **2013,** *32* (20), 5873-5878.

36. Mazurowski, M.; Gallei, M.; Li, J.; Didzoleit, H.; Stühn, B. and Rehahn, M., *Macromolecules* **2012,** *45* (22), 8970-8981.

37. Kim, B. Y.; Ratcliff, E. L.; Armstrong, N. R.; Kowalewski, T. and Pyun, J., *Langmuir* **2009,** *26* (3), 2083-2092.

38. Lillethorup, M.; Torbensen, K.; Ceccato, M.; Pedersen, S. U. and Daasbjerg, K., *Langmuir* **2013,** *29* (44), 13595-13604.

39. Mizutani, A.; Kikuchi, A.; Yamato, M.; Kanazawa, H. and Okano, T., *Biomaterials* **2008,** *29* (13), 2073-2081.

40. Evans, E. and Rawicz, W., Phys. Rev. Lett. **1997**, *79* (12), 2379-2382.

41. Kutnyanszky, E. and Vancso, G. J., Eur. Polym. J. **2012,** *48* (1), 8-15.

42. Sui, X.; Chen, Q.; Hempenius, M. A. and Vancso, G. J., *Small* **2011,** *7* (10), 1440-1447.

43. Shi, W.; Cui, S.; Wang, C.; Wang, L.; Zhang, X.; Wang, X. and Wang, L., *Macromolecules* **2004,** *37* (5), 1839-1842.

44. Granville, A. M. and Brittain, W. J., (2005), *Polymer Brushes*, *Chapter 1 Recent Advances in Polymer Brush Synthesis.* Wiley-VCH Verlag GmbH & Co., pp 33-50.

45. Zhou, X.; Liu, X.; Xie, Z. and Zheng, Z., *Nanoscale* **2011,** *3* (12), 4929-4940.

46. Daniels, C. A., (1989), *Polymers: Structure and Properties*. Technomic Publishing Company, Inc., Lancaster, Pennsylvania, U.S.A

47. Bao, Z.; Bruening, M. L. and Baker, G. L., *J. Am. Chem. Soc.* **2006,** *128* (28), 9056-9060.

48. Huang, W.; Skanth; Baker, G. L. and Bruening, M. L., *Langmuir* **2001,** *17* (5), 1731-1736.

49. Ejaz, M.; Yamamoto, S.; Ohno, K.; Tsujii, Y. and Fukuda, T., *Macromolecules* **1998,** *31* (17), 5934-5936.

50. Zhang, Y.; He, H. and Gao, C., *Macromolecules* **2008,** *41* (24), 9581-9594.

51. Lindqvist, J.; Nyström, D.; Östmark, E.; Antoni, P.; Carlmark, A.; Johansson, M.; Hult, A. and Malmström, E., *Biomacromolecules* **2008,** *9* (8), 2139-2145.

52. Chen, R.; Zhu, S. and Maclaughlin, S., *Langmuir* **2008,** *24* (13), 6889-6896.

53. Morinaga, T.; Ohno, K.; Tsujii, Y. and Fukuda, T., *Eur. Polym. J.* **2007,** *43* (1), 243-248.

54. Badri, A.; Whittaker, M. R. and Zetterlund, P. B., *J. Polym. Sci., Part A: Polym. Chem.* **2012,** *50* (15), 2981-2992.

55. Li, Y.; Giesbers, M.; Gerth, M. and Zuilhof, H., *Langmuir* **2012,** *28* (34), 12509-17.

56. Huang, W.; Kim, J. B.; Bruening, M. L. and Baker, G. L., *Macromolecules* **2002,** *35* (4), 1175-1179.

57. Kim, J. B.; Bruening, M. L. and Baker, G. L., *J. Am. Chem. Soc.* **2000,** *122* (31), 7616-7617.

58. Jones, D. M.; Brown, A. A. and Huck, W. T. S., *Langmuir* **2002,** *18* (4), 1265-1269.

59. Ulman, A., *Chem. Rev.* **1996,** *96* (4), 1533-1554.

60. Schlenoff, J. B.; Li, M. and Ly, H., *J. Am. Chem. Soc.* **1995,** *117* (50), 12528-12536.

61. Bain, C. D.; Troughton, E. B.; Tao, Y. T.; Evall, J.; Whitesides, G. M. and Nuzzo, R. G., *J. Am. Chem. Soc.* **1989,** *111* (1), 321-335.

62. Saha, S.; Bruening, M. L. and Baker, G. L., *ACS Appl. Mater. Interfaces* **2011,** *3* (8), 3042-3048.

63. Jones, R. G.; Ando, W. and Chojnowski, J., (2013) *Silicon-containing polymers: the science and technology of their synthesis and applications*. Springer Science & Business Media.

64. Braunecker, W. A. and Matyjaszewski, K., *Prog. Polym. Sci.* **2007,** *32* (1), 93-146.

65. Matyjaszewski, K., *Macromolecules* **2012,** *45* (10), 4015-4039.

66. Tsarevsky, N. V. and Matyjaszewski, K., *Chem. Rev.* **2007,** *107* (6), 2270-2299.

67. Teodorescu, M. and Matyjaszewski, K., *Macromol. Rapid. Commun.* **2000,** *21* (4), 190-194.

68. Tang, W.; Tsarevsky, N. V. and Matyjaszewski, K., *J. Am. Chem. Soc.* **2006,** *128* (5), 1598-1604.

69. Matyjaszewski, K.; Miller, P. J.; Shukla, N.; Immaraporn, B.; Gelman, A.; Luokala, B. B.; Siclovan, T. M.; Kickelbick, G.; Vallant, T.; Hoffmann, H. and Pakula, T., *Macromolecules* **1999,** *32* (26), 8716-8724.

70. Husseman, M.; Malmström, E. E.; McNamara, M.; Mate, M.; Mecerreyes, D.; Benoit, D. G.; Hedrick, J. L.; Mansky, P.; Huang, E.; Russell, T. P. and Hawker, C. J., *Macromolecules* **1999,** *32* (5), 1424-1431.

71. Schmelmer, U.; Jordan, R.; Geyer, W.; Eck, W.; Gölzhäuser, A.; Grunze, M. and Ulman, A., *Angew. Chem. Int. Ed.* **2003,** *42* (5), 559-563.

72. Queffelec, J.; Gaynor, S. G. and Matyjaszewski, K., *Macromolecules* **2000,** *33* (23), 8629-8639.

73. Matyjaszewski, K.; Patten, T. E. and Xia, J., *J. Am. Chem. Soc.* **1997,** *119* (4), 674-680.

74. Zhai, S.; Shang, J.; Yang, D.; Wang, S.; Hu, J.; Lu, G. and Huang, X., *J. Polym. Sci., Part A: Polym. Chem.* **2012,** *50* (4), 811-820.

75. Wang, J. S. and Matyjaszewski, K., *Macromolecules* **1995,** *28* (23), 7901-7910.

76. Turgman-Cohen, S. and Genzer, J., *Macromolecules* **2012,** *45* (4), 2128-2137.

77. Grande, C. D.; Tria, M. C.; Felipe, M. J.; Zuluaga, F. and Advincula, R., *Eur. Phys. J. E: Soft Matter Biol. Phys.* **2011,** *34* (2), 1-10.

78. Patil, R. R.; Turgman-Cohen, S.; Šrogl, J.; Kiserow, D. and Genzer, J., *ACS Macro Lett.* **2015,** *4* (2), 251-254.

79. Liu, X.; Sun, K.; Wu, Z.; Lu, J.; Song, B.; Tong, W.; Shi, X. and Chen, H., *Langmuir* **2012,** *28* (25), 9451-9459.

80. Fulghum, T. M.; Taranekar, P. and Advincula, R. C., *Macromolecules* **2008,** *41* (15), 5681-5687.

81. Xu, L. Q.; Wan, D.; Gong, H. F.; Neoh, K. G.; Kang, E. T. and Fu, G. D., *Langmuir* **2010,** *26* (19), 15376-15382.

82. Paoprasert, P.; Spalenka, J. W.; Peterson, D. L.; Ruther, R. E.; Hamers, R. J.; Evans, P. G. and Gopalan, P., *J. Mater. Chem.* **2010,** *20* (13), 2651-2658.

83. Iruthayaraj, J.; Chernyy, S.; Lillethorup, M.; Ceccato, M.; Røn, T.; Hinge, M.; Kingshott, P.; Besenbacher, F.; Pedersen, S. U. and Daasbjerg, K., *Langmuir* **2010,** *27* (3), 1070-1078.

84. Zhang, N.; Pompe, T.; Amin, I.; Luxenhofer, R.; Werner, C. and Jordan, R., *Macromol. Biosci.* **2012,** *12* (7), 926-936.

85. Hosono, N.; Kajitani, T.; Fukushima, T.; Ito, K.; Sasaki, S.; Takata, M. and Aida, T., *Science* **2010,** *330* (6005), 808-811.

86. Zhang, M. and Müller, A. H. E., *J. Polym. Sci., Part A: Polym. Chem.* **2005,** *43* (16), 3461-3481.

87. Sheiko, S. S.; Sumerlin, B. S. and Matyjaszewski, K., *Prog. Polym. Sci.* **2008,** *33* (7), 759-785.

88. Hanwell, M.; Curtis, D.; Lonie, D.; Vandermeersch, T.; Zurek, E. and Hutchison, G., *J. Cheminf.* **2012,** *4* (1), 1758-2946.

89. Frisch, M. J.; Trucks, G. W.; Schlegel, H. B.; Scuseria, G. E.; Robb, M. A.; Cheeseman, J. R.; Scalmani, G.; Barone, V.; Mennucci, B.; Petersson, G. A.; Nakatsuji, H.; Caricato, M.; Li, X.; Hratchian, H. P.; Izmaylov, A. F.; Bloino, J.; Zheng, G.; Sonnenberg, J. L.; Hada, M.; Ehara, M.; Toyota, K.; Fukuda, R.; Hasegawa, J.; Ishida, M.; Nakajima, T.; Honda, Y.; Kitao, O.; Nakai, H.; Vreven, T.; Montgomery Jr., J. A.; Peralta, J. E.; Ogliaro, F.; Bearpark, M. J.; Heyd, J.; Brothers, E. N.; Kudin, K. N.; Staroverov, V. N.; Kobayashi, R.; Normand, J.; Raghavachari, K.; Rendell, A. P.; Burant, J. C.; Iyengar, S. S.; Tomasi, J.; Cossi, M.; Rega, N.; Millam, N. J.; Klene, M.; Knox, J. E.; Cross, J. B.; Bakken, V.; Adamo, C.; Jaramillo, J.; Gomperts, R.; Stratmann, R. E.; Yazyev, O.; Austin, A. J.; Cammi, R.; Pomelli, C.; Ochterski, J. W.; Martin, R. L.;

Morokuma, K.; Zakrzewski, V. G.; Voth, G. A.; Salvador, P.; Dannenberg, J. J.; Dapprich, S.; Daniels, A. D.; Farkas, Ö.; Foresman, J. B.; Ortiz, J. V.; Cioslowski, J.; Fox, D. J. *Gaussian 09*, Gaussian, Inc.: Wallingford, CT, USA, 2009.

90. Shah, R. R.; Merreceyes, D.; Husemann, M.; Rees, I.; Abbott, N. L.; Hawker, C. J. and Hedrick, J. L., *Macromolecules* **2000,** *33* (2), 597-605.

91. Jones, D. M.; Smith, J. R.; Huck, W. T. S. and Alexander, C., *Adv. Mater.* **2002,** *14* (16), 1130-1134.

92. Emmerling, S. G. J.; Langer, L. B. N.; Pihan, S. A.; Lellig, P. and Gutmann, J. S., *Macromolecules* **2010,** *43* (11), 5033-5042.

93. Mastan, E.; Xi, L. and Zhu, S., *Macromol. Theory Simul.* **2015**, *24* (2), 89-99.

94. Pinto, J. C.; Whiting, G. L.; Khodabakhsh, S.; Torre, L.; Rodríguez, A.; Dalgliesh, R. M.; Higgins, A. M.; Andreasen, J. W.; Nielsen, M. M.; Geoghegan, M.; Huck, W. T. S. and Sirringhaus, H., *Adv. Funct. Mater.* **2008,** *18* (1), 36-43.

95. Leermakers, F. A. M. and Egorov, S. A., *Soft matter* **2013,** *9* (12), 3341-3348.

96. Butt, H. J.; Kappl, M.; Mueller, H.; Raiteri, R.; Meyer, W. and Rühe, J., *Langmuir* **1999,** *15* (7), 2559-2565.

97. Kutnyanszky, E. and Vancso, G. J., *Eur. Polym. J.* **2012,** *48* (1), 8-15.

98.Sui, X.; Chen, Q.; Hempenius, M. A. and Vancso, G. J., *Small* **2011,** *7* (10), 1440-1447.

99. Halperin, A. and Zhulina, E. B., *Langmuir* **2010,** *26* (11), 8933-8940.

100.Zitzler, L.; Herminghaus, S. and Mugele, F., *Phys. Rev. B* **2002,** *66* (15), 155436.

101. Jang, J.; Schatz, G. C. and Ratner, M. A., *J. Chem. Phys.* **2004,** *120* (3), 1157-1160.

102. Malotky, D. L.; Chaudhury, M. K., *Langmuir* **2001,** *17* (25), 7823-7829.

103. Uzhegova, N. I.; Svistkov, A. L.; Lauke, B. and Heinrich, G., *Int. J. Eng. Sci.* **2014,** *75* (0), 67-78.

104. Kute, V. and Banerjee, S., *Macromol. Chem. Phys.* **2003,** *204* (17), 2105-2112.

105. Ghaemy, M.; Berenjestanaki, F. R. and Bazzar, M., *Des. Monomers Polym.* **2013,** *17* (2), 101-110.

Influences of Thickness and Scan Rate of Ferrocene-containing Polymer Brushes in Electrochemistry

In this chapter we describe the electrochemistry of Fc-containing polymer brushes with different thickness. By carefully studied the cyclic voltammetry (CV) behaviour of a series polymer brushes, we learned that such polymer brushes are electrochemically stable and the electrochemical process strongly depends on the scan rates and the thickness of polymer brushes: the effect of scan rates and polymer brush thickness restricted each other, only at very low scan rate and with small thickness, the electrochemical process can achieve to reversible behaviour, otherwise, in most of the cases, the electrochemical process will be quasi-reversible or irreversible. The kinetic parameters of the electrochemical process for polymer brush show good correlations with brush thickness.

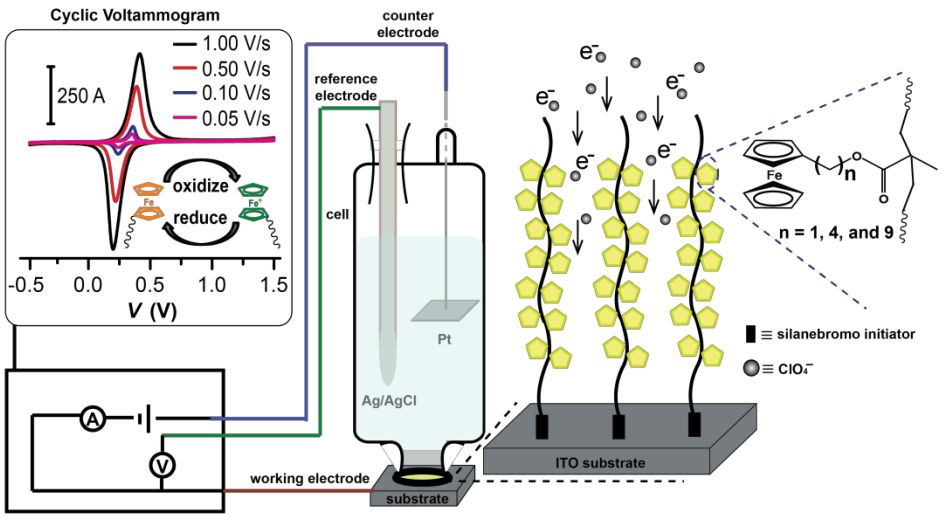

Chapter 4

4.1 Introduction

Macromolecular architectures at interfaces, for instance, polymer modified electrodes, are able to tune the material properties at the nanoscale. Polymer modified electrodes could be categorized as polymer thin film coated electrode or polymer brush decorated electrode.

Redox-active polymers/polymer brushes possess the controllable electrical stimulus that provides opportunities for using them in applications such as drug delivery[1], artificial muscles[2,3], molecular sensors[4], and electrochromic devices[5]. These applications require good understanding of the charge transfer process of the polymer modified electrode.[6-8] One of the advantages for polymer brushes is that they make device fabrication more stable and sometime can even represent different properties in fundamental studies.[9]

Comparing with redox active monolayer[10]/molecular wires[11], polymer brush has longer backbone. The perpendicular orientation of the chains with respects to the substrate makes redox active polymer brushes attractive since that is important for efficient transport of charges.

The difference between normal non-conjugated polymer brushes and the redox active polymer brushes is that charges move through a delocalized conjugated chain for the former one, while the charge transport occurs through electron hopping or electron exchange reaction between redox centres for the latter one. The most commonly used redox-active groups in prior studies is the ferrocene-based redox unit.[12-15] Other well-known redox active groups are some metal complexes,[16] such as Os-containing,[17] Ru-containing,[18] Fe-containing,[19] or phenothiazine redox moieties.[20] Electrochemistry is a powerful surface characterization technique for the redox active moieties containing

species,[18,21,22] or even non redox active moieties containing species[23,24] by using redox active couples in solution.

In our work, we focused on the study of Fc-containing polymer brushes. To overview the complex long-rang electrochemical process of Fc-containing polymer brush on ITO electrode, in this work, we applied polyferrocenylmethyl methacrylate ≡ PFMMA brush, polyferrocenylbutyl methacrylate ≡ PFBMA brush, and ferrocenylnonyl methacrylate ≡ PFNMA brush with a series thickness to the electrochemical studies.

Mainly techniques, such as cyclic voltammetry (CV), electrical impedance spectroscopy (EIS) or chronocoulometry (CA), are commonly used to study the redox polymer modified electrodes. There are both intrinsic and external factors that may affect the redox properties of the polymers[25], for example, some intrinsic factors: (i) the nature and localization of the redox center and (ii) conjugation of the backbone or between redox centers and (iii) ionic and conductivity properties of the redox polymer. And some external factors: (i) film thickness, (ii) kinetic processes associated with the slower electronic oxidation-reduction process of polymers, (iii) the nature of electrolyte, and the (iv) the type of electrochemical cell and the working and reference counter-electrodes.

In Chapter 3, we have shown some CV results and here in Chapter 4 we will carefully study the electrochemical behaviour in details. A background introduction is given in section 4.1, and section 4.2 will mainly display the results and discussion. In subsection 4.2.1, the break-in period of the electrochemical behaviour is shown. The stability of polymer brush film under continuously electrochemical scanning was examined and is shown in subsection 4.2.2. From subsection 4.2.3 to 4.2.6, we carefully discussed the brush dependence, scan rate dependence and thickness dependence for the

electrochemical process for these polymer brushes. Furthermore, we list all the electrochemical kinetic parameters of the polymer brushes with different thickness under such electrochemical process. Conclusions will be given in section 4.3, followed by section 4.4, experimental section.

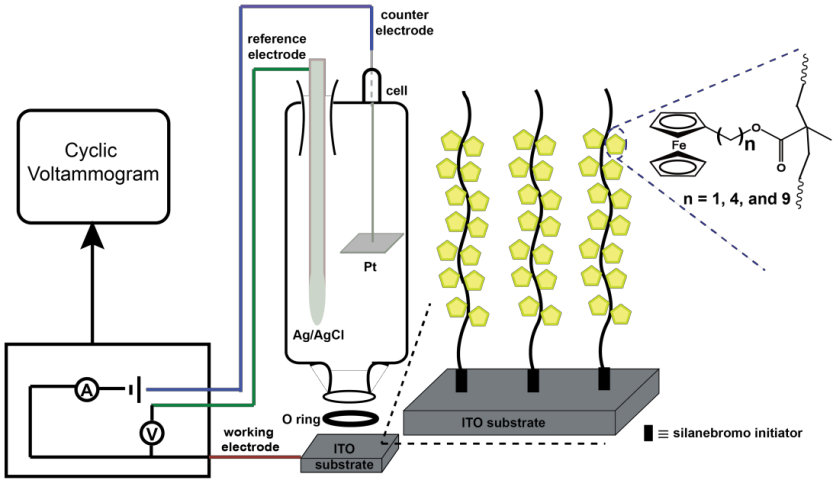

Scheme 4.1 Schematic Illustration of electrochemical measurements on Fc-containing polymer brushes modified ITO substrate with 1.0 M $HClO_4$ aqueous solution as electrolyte, Ag/AgCl as reference electrode, and Pt wire as counter electrode.

4.2 Results and discussion

4.2.1 Break-in period of the electrochemical behaviour for polymer brushes

The electrochemical behaviors of polymer films or polymer brushes usually undergo a break-in period to reach a stable state. A break-in period indicates that usually the neutral site redox polymer films require several CV scans before a steady current-potential pattern is observed.[14] This is an effect can be viewed in a virgin film (a polymer thin film without immersing or scanning with electrolyte solution) which has low ambient internal electrolyte concentration.[26] The time of the break-in period depends on film thickness. This behavior is common in other redox polymer system.[14,26-28] In our system, we have found that in 1.0 M $HClO_4$ electrolyte, the peak current of the polymer brush increased

gradually with each successive sweep, and then reached a steady state. For thin polymer brush (L_{PB} < 15 nm), it was easy to achieve the stable state at scan rate = 1.00 V/s in the voltage window -0.5 V ~ 1.5 V within 3 or 4 cycles. Thick polymer brush (L_{PB} > 20 nm) required more scan numbers to achieve the stable state. This thickness dependence of the break-in effect is plotted in Figure 4.1(D). Error bars were collected from parallel measurements.

This thickness dependence observation is consistent with the conclusion that we have drawn in Chapter 3: thinner polymer brush is prone to be fully extended while thicker polymer brush is prone to be collapsed such that the electrochemical accessibility will decrease accordingly. Typical CV plots presenting the break-in period effect are shown in Figure 4.1(A). Unless otherwise stated, each CV discussed in the following section is a stable one. Here we took PFMMA brush L_{PB} = 40 nm as an example to show this break-in effect. Figure 4.1(A) displays the stacked CV plots from the 1st scan to the 40th scan. As can be seen from Figure 4.1(B) and (C), the current density (both I_{pa} and I_{pc}) gradually increased from the 1st scan to the 40th scan. The peak-to-peak separation (ΔE) also increased during the continuous scan. At the end of the break-in period (reaching to the stable state), the current density became stable, and the peak-to-peak separation ceased increasing.

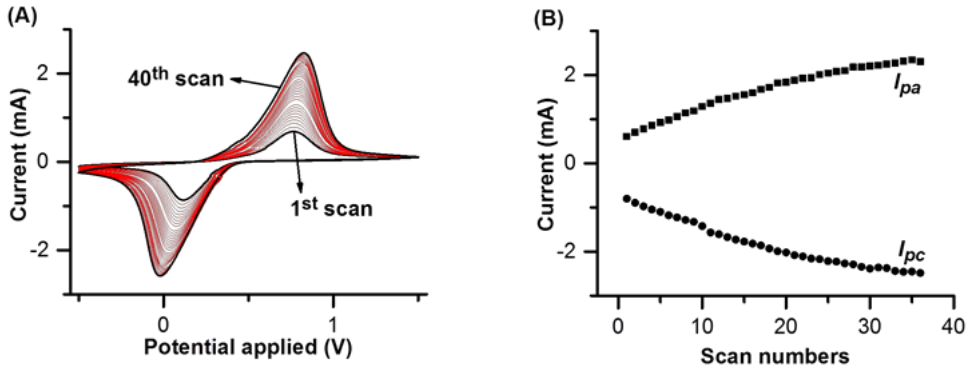

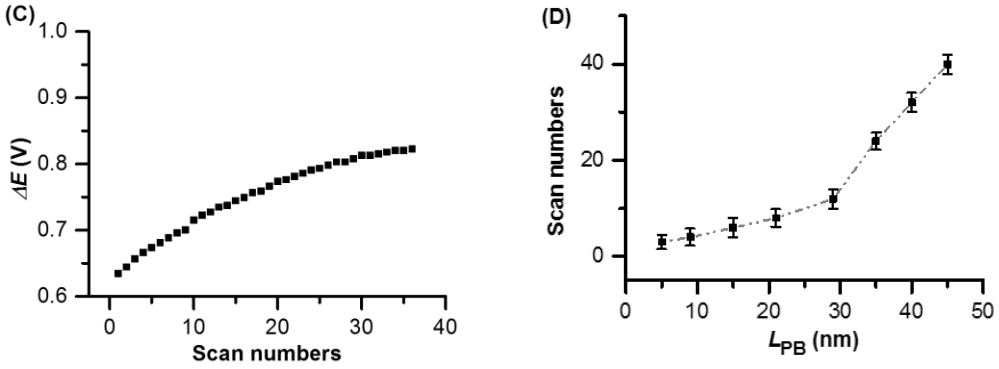

Figure 4.1 (A) Representative CV plots of PFMMA brush (L_{PB} = 40 nm) as the function of scan numbers. (B) Anodic and cathodic current density (I_{pa} in black squares and I_{pa} in black circles) on the dependence of scan numbers. (C) peak-to-peak separation (ΔE) on the dependence of scan numbers. (D) Scan numbers on the dependence of thickness. Dashed lines are guide lines for eyes. Error bars were obtained from repeated measurements on parallel samples. All data referred to PFMMA brushes.

4.2.2 Stability of the polymer brush film

After the break-in period, the polymer brushes are electrochemically stable during further CV scan. Representative cyclic voltammograms of PFMMA brush (L_{PB} ~ 20 nm) on ITO for stability test are shown in Figure 4.2. Voltammetric parameters are listed in Table 4.1, in which we summarized all the voltammetric parameters. Both the anodic and cathodic peak (E_{pa} and E_{pc}) positions did not shift too much and the percentage value shown in the parentheses demonstrate that the decay of the current density is small enough to be neglected.

Based on this test, we observed that during normal scan ranges (maximum 10 scans for one measurement) there is no significant decrease of I_{pa} and I_{pc}, and we have noticed that there is no desorption of polymer brush on the ITO substrates, indicating the Fc and Fc^+ possess a relatively high stability in the polymer brush film, so this small decay could be neglected in the following study. This observation is consistent with some previous reported results.[14,15,29,30] The slight reduction in peak currents might be due to loss of

electroactivity or due to the decomposition of Fc rather than loss material from the film.[29]

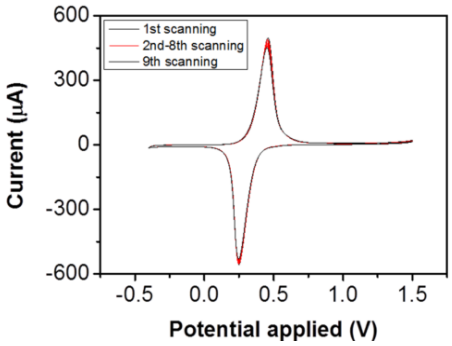

Figure 4.2 Representative cyclic voltammograms of PFMMA brush film on ITO substrate in aqueous solution with 1.0M $HClO_4$ as electrolyte by continuously scanning CV curves. Scan rate = 1.00 V/s.

Table 4.1 Summary of the voltammetric parameters.

scan number	E_{pa} (mV)	E_{pc} (mV)	ΔE_p[a] (mV)	I_{pa} (μA)	I_{pc} (μA)	ΔI_{pa} (μA)	ΔI_{pc} (μA)
1st scan	459	249	210	491	554	45 (8%)[b]	28 (5%)[c]
9th scan	452	247	205	449	526		

[a] $\Delta E_p = | E_{pa} - E_{pc} |$.
[b,c] values in parentheses shows the decays of current intensity in percentage.

4.2.3 Brush dependence as a function of scan rates

In this section, we studied the scan rate dependent of PFMMA, PFBMA, and PFNMA brush, respectively, for the electrochemical process in $HClO_4$ electrolyte at room temperature with different scan rates are: v = 0.01, 0.02, 0.05, 0.10, 0.20, 0.50, 1.00, 2.00, and 5.00 V/s (Figure 4.3). Samples here were selected from polymer brushes with similar surface coverages of Fc units (average values for Γ_{Fc} is 6.47 ± 0.33 nmol/cm^2), whose values were estimated from CV recorded at scan rate v = 0.01V/s to compare the electrochemical behaviour. The main panels show the scan rates 0.10, 0.20, 0.50, 1.00, 2.00, and 5.00 V/s, and the insets show the scan rates 0.01, 0.02, and 0.05V/s, respectively. Note that the potential windows for Figure 4.3(C) are different. Comparing

the CVs for these 3 kinds of polymer brushes, we observed no obvious differences among them: all panels show that the anodic peak E_{pa} shift to the anodic and the cathodic peak E_{pc} shift to the cathodic with increasing the scan rates v. So the peak separation ΔE gradually increases with the scan rates. This is an obvious scan rate dependent performance, which will be carefully discussed in the following section.

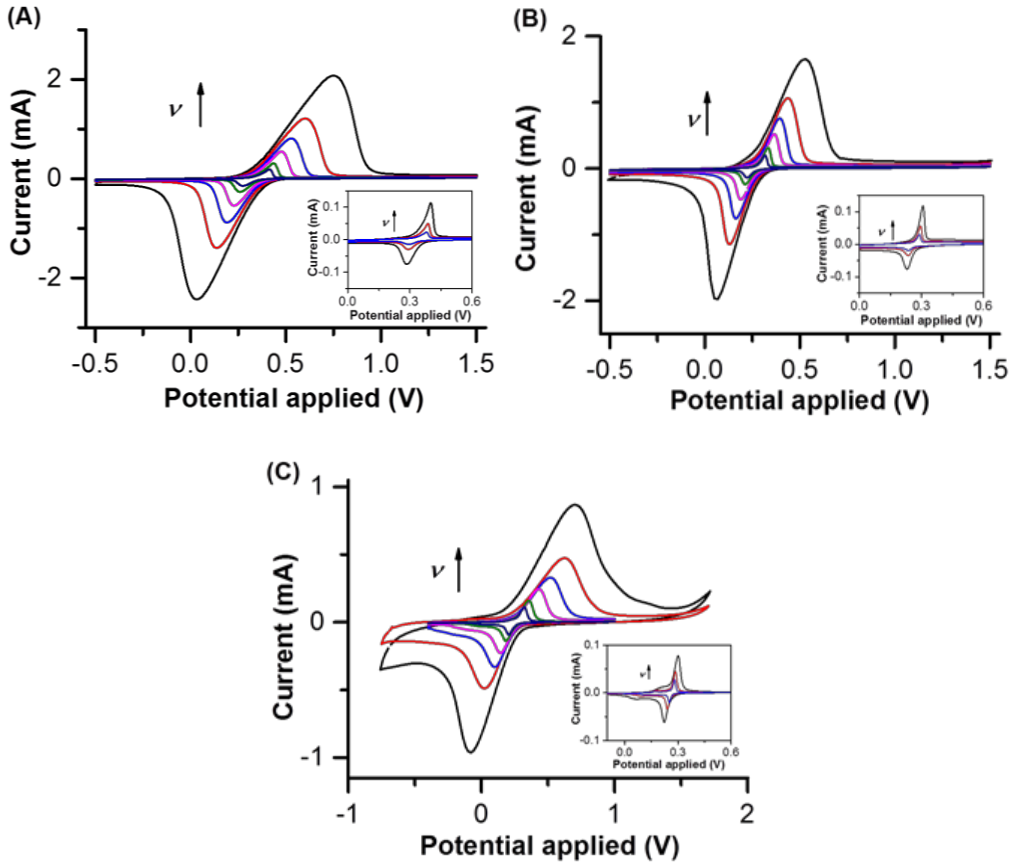

Figure 4.3 Dependence of scan rate based on representative samples of (A) PFMMA, (B) PFBMA, (C) PFNMA brush, respectively, with the scan rates ν range from 0.01, 0.02, and 0.05 V/s (insets) and 0.10, 0.20, 0.50, 1.00, 2.00, and 5.00 V/s (main panels).

4.2.4 Influence of scan rates

In this section, we further studied the scan rates dependency of relatively thicker polymer brush (L_{PB} = 55 nm PFMMA brush as example) in 1.0 M $HClO_4$ electrolyte with a series of scan rates: 0.001, 0.002, 0.005, 0.010, 0.020, 0.050, 0.100, 0.200, 0.500,

1.000, 2.000, 5.000 V/s and 10.000 V/s. The corresponding CV plots vs. scan rates are presented in Figure 4.4. Figure 4.5 summarizes the voltammetric parameters plotted as a function of scan rate.

It is obvious that the peaks shift to more positive values for anodic peaks and more negative for cathodic peaks with increasing scan rate. This observation indicates that at lower scan rates range (v < 0.2 V/s), the peak to peak separations, ΔE, are much smaller than at higher scan rates range (v > 0.2 V/s). Figure 4.5(A) shows the relationship between ΔE and scan rates in log scale. ΔE is one of the important factors to judge if the electrochemical process is a reversible, quasi-reversible or irreversible process. An electrochemical process with ΔE < 200 mV and similar total charge in anodic and cathodic reaction is considered to be a quasi-reversible process, and the one with ΔE ≈ 60 mV is considered to be a reversible process. As can be observed from this plot, the process was quasi-reversible at low scan rates range (0.001 < v < 0.02 V/s), but irreversible at high scan rates (0.02 < v < 5.0 V/s). The rates of the electron transfer through the brush film and the transfer between the brush film and the electrode are slow, hence when the potential was scanned at a lower scan rate, the electrode reaction could reach completion, and the CV exhibited quasi-reversible or nearly reversible features. Vice versa, when potential was scanned at higher rates, the electrode reaction could not reach completion in time, resulting in irreversible features. Figure 4.5(B) shows the peak potential (E_p-$E^{0'}$) as the function of the logarithm of scan rate. We can observe that the peak potentials shift with increasing scan rate, but the relationship was nonlinear (in this case, we only plotted the voltammetric parameters from anodic reaction to show the trend, the ones from cathodic reaction were omitted). At slow scan rates, the difference of peak potential with scan rate changed slightly. Along with the increasing scan rate, the difference of peak potential with scan rate increased. According to the theory of CV, in a

reversible electrode process, the peak potential is independent of scan rate. At the same time, in an irreversible process there is a linear relationship between the peak potential and the logarithm of the scan rate. The curvature plot showed in Figure 4.5(B) indicates that the electrochemical process of PFMMA brush film on ITO electrode was complex: the whole scan rate dependent electrochemical process is neither simply reversible nor irreversible.

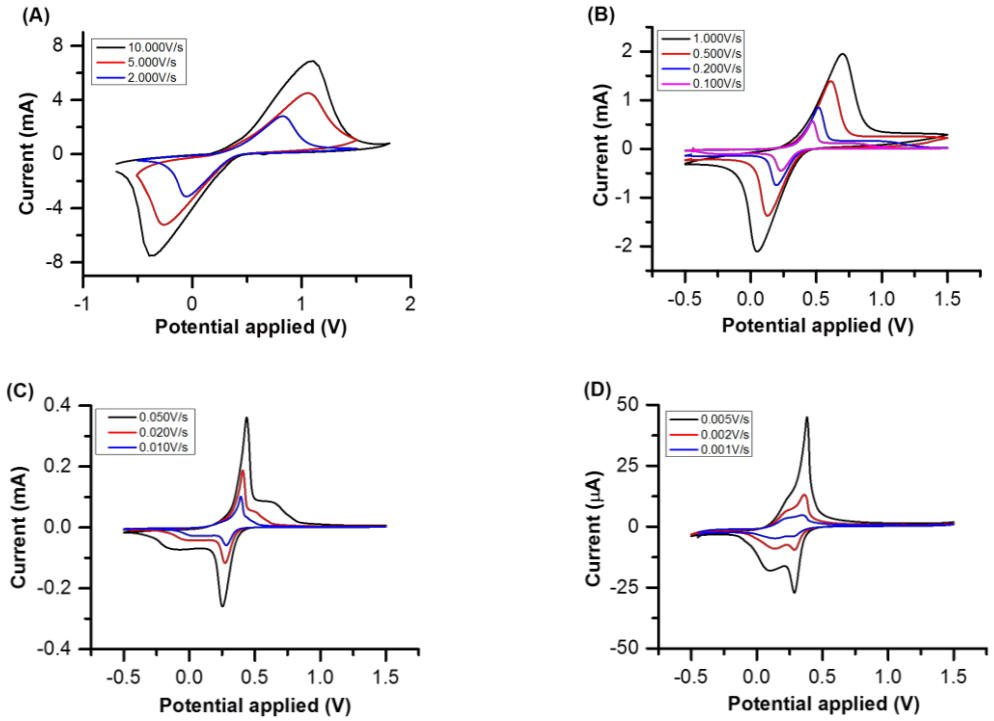

Figure 4.4 Stacked cyclic voltammograms of a representative PFMMA brush sample with large thickness (~55 nm) as the function of scan rates. Note that the panel D has different units for current.

Figure 4.5(C) shows the plots of log (current intensity) *vs.* log (scan rate), which clearly exhibiting curvature. As we can see, the slope is close to be 1 at low scan rates, as normally would be expected for a surface confined reversible redox behavior, while at higher scan rates, the slope is close to 0.5, as normally would be expected for a diffusional redox behavior. Figure 4.5(D) shows the scan rates dependent of full width at half maximum (FWHM) for both anodic and cathodic peak. These FWHM values are

larger than the idea value of 90.6mV, suggesting some degree of lateral interaction between the Fc moieties or heterogeneous distribution of the redox centers. Error bars represent the peak assignment errors are all omitted in Figure 4.5(A) ~ (D). We believed that, at low scan rates, most of the redox centers can exchange electrons with the ITO electrode, while upon elevation of the scan rate, the part of the electrochemically accessible redox centers is decreasing.

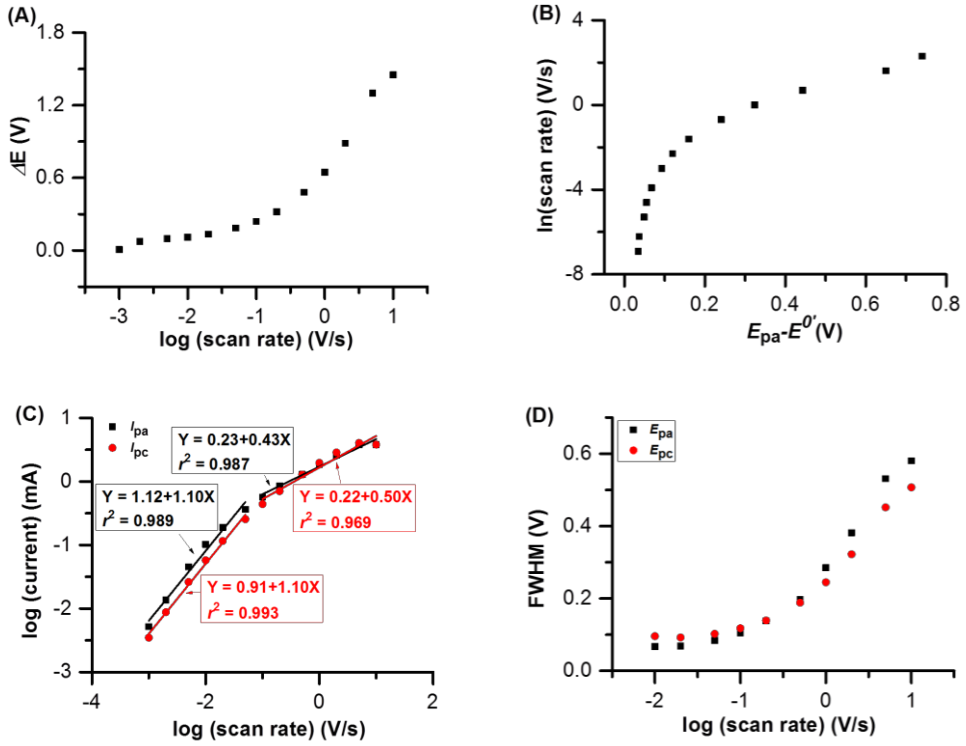

Figure 4.5 Plots of voltammetric parameters as the function of scan rates. (A) log(scan rates) *vs.* peak-to-peak separation (ΔE). (B) Peak potential (E_{pa}-$E^{0'}$) *vs.* ln(scan rates). (C) log(scan rates) *vs.* log(I_{pa}) and log(I_{pc}). (D) log(scan rate) *vs.* full width at half maximum (FWHM). Solid lines are fitting lines.

In terms of PFBMA and PFNMA brush sample with similar thickness, corresponding CV plots and parameters plots are shown in Appendix (Figure A7-A10). Similar trends can be observed from these two samples, indicating that such scan rate dependence performance is independent on polymer brush.

4.2.5 Electrochemical process at a very low scan rate

In order to investigate the electrochemical process in more detail, we showed CVs recorded at a low scan rate (0.001V/s). Generally, voltammertic waves recorded at scan rates ranging from 10.000 V/s to 0.100 V/s (see Figure 4.4 for example), there were obvious peak-to-peak separations (ΔE) but only main peaks were observed. However, when the scan rates were low (< 0.050V/s), ΔE decreased and the peak splitting was observed.

Wave shapes are sensitive to scan rates. Here we show 3 voltammertic waves for PFMMA, PFBMA, and PFNMA brush with thickness around 20 nm, 40 nm and 50 nm recorded at a scan rate of 0.001V/s. As can be seen from Figure 4.6, in all cases we observed multiple peaks. This peak splitting indicates that the microenvironment of all Fc units is not homogenous.

It is worth to note that the scan rate v = 0.050V/s is not the strict transition point to judge if these peak splittings will show. On one hand, for thicker brush, the peak splittings may show at even lower scan rate. This observation is consistent with the explanation mentioned above: more Fc units may be buried in thicker brush, which require even slower scan to allow the charge have enough time to transport. The degree of splitting depends on the brush thickness, one the other hand, at the same scan rate, thinner brush is, and more extra voltrammetric waves and even larger ΔE could be observed.

We did not present even thinner polymer brush here due to (1) the dependence of current intensity on brush thickness (will discuss later) and (2) the dependence of current intensity on scan rate: at such low scan rate (v = 0.001V/s), polymer brush thinner than 10 nm (roughly estimated thickness value) are not able to show readable/clear

voltammetric waves, which were limited by the design of the electrochemical cell and other factor.

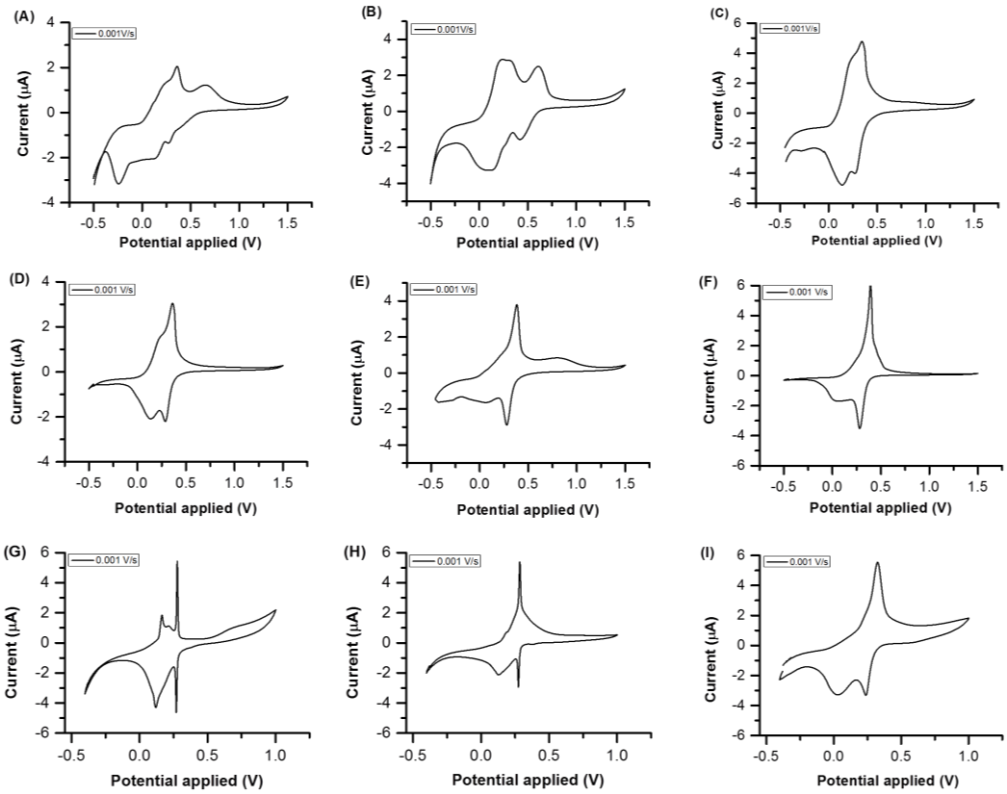

Figure 4.6 Cyclic voltammograms of the representative PFMMA brush samples with thickness in (A) 23 nm, (B) 42 nm, and (C) 55 nm; the representative PFBMA brush samples with thickness in (D) 28 nm, (E) 40 nm, and (F) 50 nm; the representative PFNMA brush samples with thickness in (G) 25 nm, (H) 38 nm, and (I) 48 nm. All were collected at the lowest scan rate (0.001V/s).

4.2.6 Thickness dependence for the electrochemical process

Here we show PFMMA brush as example to investigate the thickness dependent for the electrochemical process. Figure 4.7(A) - (C) show the scan rate dependency as the function of thickness of the PFMMA brush. Full range of scan rates is from 5.0V/s to 0.01V/s, where the scan rates have nonlinear relationship with I_{pa} for the whole series of thickness, as can be seen from Figure 4.7(A). While the I_{pa} scales linearly with square-root of the scan rates in full scan rate range for all thickness, as is shown in Figure 4.7(B). However, in Figure 4.7(C), if we only focus on the low scan rate regime, linear

relationship between scan rates and I_{pa} is observed (indicating that with slower scan rates, the electrochemical process is more close to quasi-reversible. Electrochemical process for polymer brush shows quasi-reversibility only at lower scan rates (0.1V/s to 0.01V/s), while at higher scan rates (5V/s to 0.2V/s), the process always shows irreversible behavior. The thinner brushes, the lower scan rates, the smaller ΔE, as is shown in Figure 4.7(D). ΔE increases with both the thickness and the scan rates. This also shows us the evidence that, the thicker the polymer brush, the more complex the structure is, and less redox active species are electrochemically accessible, resulting in higher chance for the ions/counterions obey the diffusional process.

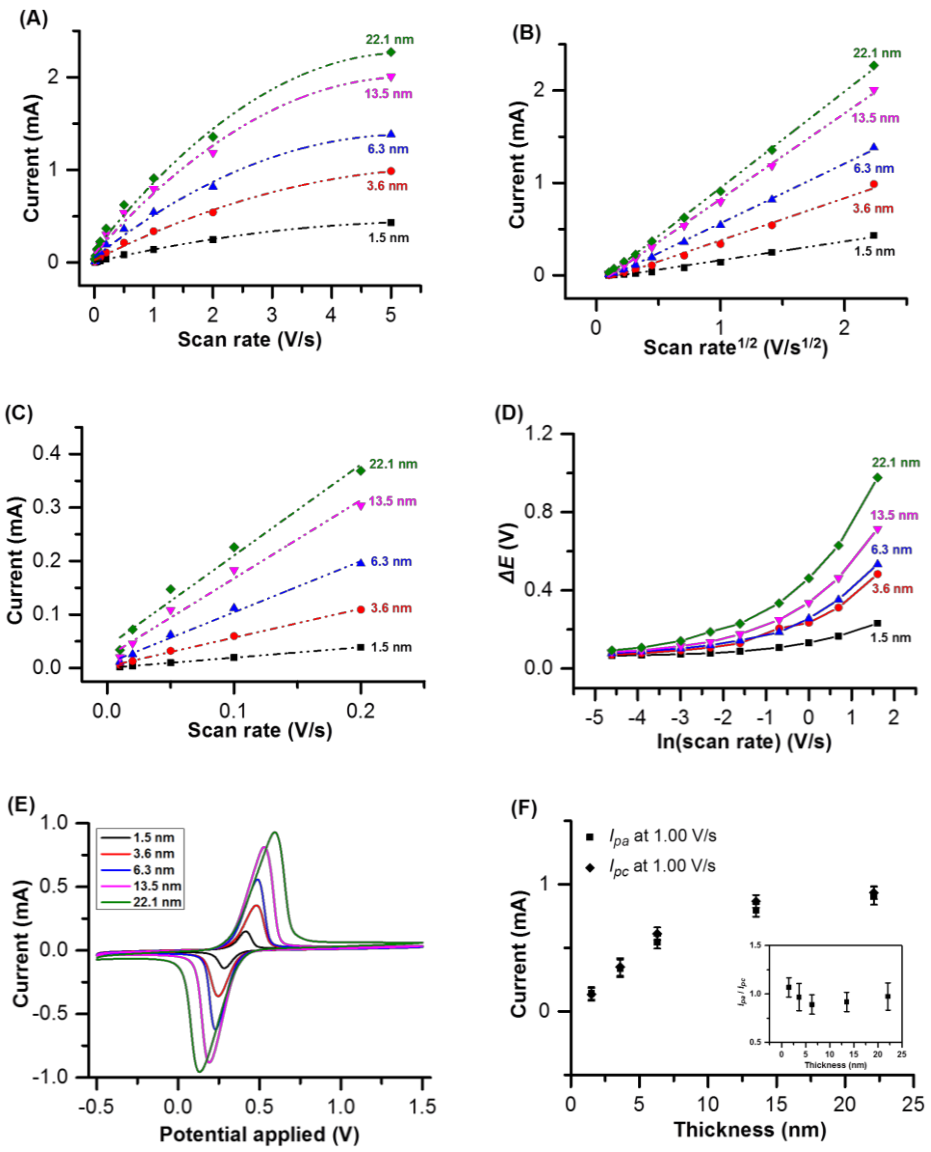

Figure 4.7 Electrochemical process of PFMMA brush: (A) I_{pa} increase depends on scan rates (5.00 V/s – 0.01 V/s) as the function of thickness. (B) I_{pa} increase depends on the square root of scan rates (5.00 V/s – 0.01 V/s) as the function of thickness. (C) I_{pa} increase depends on scan rates as the function of thickness (0.20 V/s – 0.01 V/s). Dashed lines are fitting lines. (D) Peak separations depend on scan rates in ln scale (5.00 V/s – 0.01 V/s) as the function of thickness. (E) Voltammetric plots recorded at 1.00 V/s as the function of thickness. (F) I_{pa} (■) and I_{pc} (♦) increases depend on thickness and the inset shows the ratio of I_{pa} vs. I_{pc} depends on thickness.

Figure 4.7(E) shows the typical voltammetric waves recorded at v = 1.0 V/s for the series of PFMMA brushes, we observed that the current intensities increase with the thickness of brush film. Figure 4.7(F) shows the corresponding current density of anodic and cathodic reactions in Figure 4.7 (E), inset image in Figure 4.7(E) suggests that the ratio of anodic current intensity and cathodic current intensity is constant at 1. Error bars represent the peak assignment errors and are all omitted in Figure 4.7(A)-(D), except in Figure 4.7(F).

4.2.7 Kinetic parameters of the polymer brush electrochemical process with different thickness

For a diffusion-controlled electrode process of the surface-anchored redox species, I_p and ΔE can be expressed as follows:

$$I_p = 0.4958nF(\frac{\alpha F}{RT})^{\frac{1}{2}} AD_O^{\frac{1}{2}} C_0^* v^{\frac{1}{2}} \qquad (4.1)$$

$$I_p = 0.227nFAC_0^* k^0 \exp[(-\frac{\alpha F}{RT})(E_p - E^{0'})] \qquad (4.2)$$

$$\Delta E = (RT\alpha F)(\ln(\frac{RTk^0}{2.184\alpha FD_O}) - \ln v) \qquad (4.3)$$

In which, I_p is the peak current in A, F is the Faraday constant, R and T have their usual meaning, A is the film area covering the electrode surface in cm^2, C_0^* is the concentration of the electroactive species in the film in mol/cm^3, v is the potential scan rate in V/s, $E^{0\prime}$ is the apparent formal potential measured at scan rate v = 1.0V/s. [$E^{0'} = \frac{(E_{pa} + E_{pc})}{2}$]. We

determined the film thickness (L_{PB}) by AFM scratch or ellipsometry, and then C_0^* can be obtained from $C_0^* = \Gamma / L_{PB}$. α is the surface charge-transfer coefficient for the surface-anchored redox species. This coefficient is a measure of the symmetry of the energy barrier. D_o here is the common diffusion coefficient of the electroactive species in cm^2/s.

In the quasi-reversible and totally irreversible electrochemical process, the peak current and potential follow the scan rates dependence. The main equations are presented above. Here we explain the procedure for calculating each kinetic parameter individually. The transfer coefficient, α, is a measure if the symmetry of the energy barrier, and is related to both peak current and peak potential. k^0 is the standard rate constant in cm/s. In one-step, one-electrode process, if we consider the special case in which the interface is at equilibrium with a solution in which $C_0^* = C_R^*$, in this situation, $E = E^{0'}$. k_f and k_b represent for the homogeneous rate constant for "forward" and "backward" reactions, respectively, and there $k_f = k_b = k^0$, then we have the standard rate constant. D_{app} presents the diffusion coefficient of the ions / counterions / electrons / electroactive species which we have well explained later. α can be derived from eq 4.3, which we re-state as eq 4.4:

$$\Delta E = (RT\alpha F)\ln(\frac{RTk^0}{2.184\alpha F D_{app}}) - (RT\alpha F)\ln\nu \qquad (4.4)$$

In which, the module "$RT\alpha F$" is the slope for the ΔE vs. lnν plot and we considered the "$(RT\alpha F)\ln(\frac{RTk^0}{2.184\alpha F D_{app}})$" as a constant module as the intercept for the plot. In the scan rates dependent measurement, we obtained a series values for ΔE as the function of scan rates. Here we only applied the scan rates ranging from 0.50 V/s to 5.00 V/s (irreversible electrochemical process region). The slope value can be obtained by a linear fitting of eq 4.6. The R, T and F have their usual meanings and the values are known. With the value

of α, we can continue to obtain the value of D_{app}, based on eq 4.1 by plotting the linear relation between I_p and $v^{1/2}$, the slope is function of D_{app}. Eq 4.5 and eq 4.6 can be derived by combining eq 4.1 and eq 4.2:

$$\ln(k^0) + [(-\frac{\alpha F}{RT})(E_p - E^{0'})] = \ln 2.184 + 0.5\ln[(\frac{\alpha F}{RT})D_{app}v] \quad (4.5)$$

$$\ln v = 2[\ln(k^0) - \ln 2.184] - \ln[(\frac{\alpha F}{RT})D_{app}] + 2(\frac{\alpha F}{RT})(E_p - E^{0'}) \quad (4.6)$$

In which, the intercept module contains the relationship between k^0 and D_{app}, with the already known value of D_{app}, we can continue to obtain the value of k^0.

Table 4.2 - 4.4 list all the kinetic parameters obtained from 3 kinds of polymer brush (PFMMA, PFBMA, and PFNMA brush, respectively) with a series of thickness. Under our circumstances, considerations of analogous reactions in homogeneous solution showed that such a process is equivalent to diffusion. The apparent diffusion coefficient observed for a species, D_{app}, is composed of contributions from the physical movement of the species and the electron transfer process. In our case, the macroscopic physical movement of the species is neglected since our redox species are immobilized on the surface rather than diffused in the solution. However, since the redox active groups are the pendants in the polymer brush, we believed there are still some motions for the segmental polymer side chains in such polymer brush. Therefore, the D_{app} here actually is more likely to be the diffusion coefficient for combinations of ions / counterions / electrons / redox active species within the film at a modified electrode.

Figure 4.8 shows the plots for kinetic parameters of the electrochemical process for PFMMA brush as the function of thickness. PFBMA and PFNMA brush have the similar trend and more parameters for the series of PFMMA, PFBMA and PFNMA samples are listed in Table 4.3 and Table 4.4. α values is one of the important factors to express the

electron exchange efficiency on the electrode surface, that is, the reversibility of the electrode process. As we can see from Figure 4.8(A), α value decreased exponentially with the surface coverage of Fc units. Here we still have no understanding why this decrease is exponential. The decrease α values indicates less reversible for the electrochemical process for system with more Fc units. k^0 simply is a measure of the kinetic facility of a redox couple. A system with large k^0 will achieve equilibrium on a short time scale, but a system with smaller k^0 will be sluggish. Comparing the k^0 values along this series of PFMMA brush samples, we found the higher surface coverage of Fc units is, the larger k^0 values is, demonstrating that the electron transfer equilibrium would be faster to be achieve in the system with more Fc units. The increase trends follow the function of polynomial with a degree of 2. The corresponding equations are shown in the Figure 4.8(B). As we mentioned before, D_{app} presents the diffusion of ions/counterions/electrons/redox active species in the film. The values of D_{app} increase with the surface coverage of Fc units as the function of polynomial with a degree of 3. The corresponding equations are shown in the Figure 4.8(C). As we know that the motion of ions / counterions in the film is for the requirement of electroneutrality. We believed the rate of ions / counterions diffusion into the polymer brush film is relatively slow. The total diffusional charge transport contains the ions / contertions / electrons transport and segmental polymer side chains motion within the polymer. Since the present system represents much higher structural complexity due to the multiple redox centers randomly bound to the electrode-tethered polymer chains at different distance from the electrode surface, this diffusion-controlled behavior of the surface-modified electrode could be explained by the quasi-diffusional translocation of the redox units bound to the flexible polymer chains tethered to the electrode surface. This D_{app} increasing trend indicates that the larger value for the diffusion coefficient would be

resulted from the thicker brush with more redox species that involved in the charge transport process. In all these cases, we estimated the Γ_{Fc} by the CV recorded at the scan rates followed the quasi-reversible electrochemical process, that is, at lower scan rate (v = 0.1 V/s), rather than routine scan rate (v = 1.0 V/s) to avoid underestimating Γ_{Fc} values.

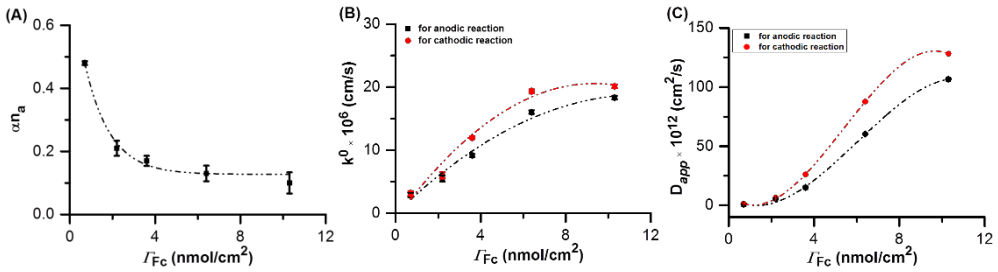

Figure 4.8 (A) The surface charge transfer coefficient, αn_a, as the function of surface coverage of Fc units. (B) The standard rate constant, k^0, as the function of surface coverage of Fc units. (C) The apparent diffusion coefficient, D_{app}, as the function of surface coverage of Fc units. Error bars are from the data fitting. Dash lines are fitting lines.

Table 4.2 Summary of the kinetic parameters of electrochemical process and the relationships between the peak currents, peak potentials and potential scan rates for PFMMA brush with a series of thickness. [a,b] σ is the standard deviations for parallel measurements. [c,d,e] σ is the standard deviations for fittings.

Γ_{Fc} (σ)[a] (nmol/cm^2)	L_{PB}(σ)[b] (nm)	$C_0 \times 10^3$ (mol/cm^3)	αn_α (σ)[c]	$k^0 \times 10^6$ (σ)[d] (cm/s)	$D_{app} \times 10^{12}$ (σ)[e] (cm^2/s)	Scan rate (V/s)	Equation	r^2
0.7 (0.09)	1.5(0.1)	4.7	0.48 (0.05)	2.47 (0.05)	0.82 (0.05)	0.01-5	$I_{pa}(\mu A) = -40.28+204.05\nu^{1/2}$	0.994
				3.15 (0.05)	1.33 (0.05)	0.01-5	$I_{pc}(\mu A) = 70.33-260.12\nu^{1/2}$	-0.977
						0.5-5	$\Delta E = 0.137+0.054\ln\nu$	0.987
2.2 (0.29)	3.6 (0.2)	6.1	0.21 (0.07)	5.50 (0.07)	5.42 (0.07)	0.01-5	$I_{pa}(\mu A) = -78.93+457.39\nu^{1/2}$	0.995
				6.02 (0.07)	6.49 (0.07)	0.01-5	$I_{pc}(\mu A) = 101.55-500.35\nu^{1/2}$	-0.993
						0.5-5	$\Delta E = 0.259+0.122\ln\nu$	0.963
3.6 (0.50)	6.3 (0.1)	5.7	0.17 (0.05)	9.16 (0.05)	15.20 (0.05)	0.01-5	$I_{pa}(\mu A) = -81.71+645.47\nu^{1/2}$	0.999
				12.01 (0.05)	26.13 (0.05)	0.01-5	$I_{pc}(\mu A) = 165.61-846.16\nu^{1/2}$	-0.995
						0.5-5	$\Delta E = 0.271+0.152\ln\nu$	0.989
6.4 (0.84)	13.5 (0.2)	4.7	0.13 (0.07)	16.04 (0.07)	60.31 (0.07)	0.01-5	$I_{pa}(\mu A) = -103.23+928.45\nu^{1/2}$	0.999
				19.35 (0.07)	87.77 (0.07)	0.01-5	$I_{pc}(\mu A) = 190.21-1116.99\nu^{1/2}$	-0.997
						0.5-5	$\Delta E = 0.359+0.203\ln\nu$	0.985
10.3 (1.34)	22.1(0.2)	4.7	0.10 (0.05)	18.36 (0.05)	106.72 (0.05)	0.01-5	$I_{pa}(\mu A) = -95.11+1042.54\nu^{1/2}$	0.999
				20.12 (0.05)	128.23 (0.05)	0.01-5	$I_{pc}(\mu A) = 161.95-1138.70\nu^{1/2}$	-0.999
						0.5-5	$\Delta E = 0.488+0.279\ln\nu$	0.986

Table 4.3 Summary of the kinetic parameters of electrochemical process and the relationships between the peak currents, peak potentials and potential scan rates for PFBMA brush with a series of thickness. [a,b] σ is the standard deviations for parallel measurements. [c,d,e] σ is the standard deviations for fittings.

Γ_{Fc} (σ)[a] (nmol/cm^2)	L_{PB}(σ)[b] (nm)	$C_0 \times 10^3$ (mol/cm^3)	αn_α (σ)[c]	$k^0 \times 10^6$ (σ)[d] (cm/s)	$D_{app} \times 10^{12}$ (σ)[e] (cm^2/s)	Scan rate (V/s)	Equation	r^2
5.8 (0.88)	5.8 (0.3)	10	0.37 (0.05)	1.88 (0.05)	0.38 (0.05)	0.01-5	$I_{pa}(\mu A) = -31.66+267.21\nu^{1/2}$	0.999
				2.25 (0.05)	0.54 (0.05)	0.01-5	$I_{pc}(\mu A) = 65.08-320.31\nu^{1/2}$	-0.991
						0.5-5	$\Delta E = 0.142+0.069\ln\nu$	0.991
6.9 (1.05)	6.2 (0.4)	11.8	0.27 (0.05)	3.21 (0.05)	1.35 (0.05)	0.01-5	$I_{pa}(\mu A) = -51.23+505.75\nu^{1/2}$	1.000
				3.83 (0.05)	1.93 (0.05)	0.01-5	$I_{pc}(\mu A) = 115.10-604.54\nu^{1/2}$	-0.994
						0.5-5	$\Delta E = 0.190+0.095\ln\nu$	0.978
10.6 (1.61)	11.6 (0.4)	9	0.21 (0.07)	6.22 (0.07)	6.60 (0.07)	0.01-5	$I_{pa}(\mu A) = -38.63+725.55\nu^{1/2}$	1.000
				7.37 (0.07)	9.28 (0.07)	0.01-5	$I_{pc}(\mu A) = 132.67-892.38\nu^{1/2}$	-0.998
						0.5-5	$\Delta E = 0.243+0.123\ln\nu$	0.984
15.3 (2.32)	14.5 (0.3)	11.1	0.14 (0.02)	6.38 (0.02)	10.57 (0.02)	0.01-5	$I_{pa}(\mu A) = 16.70+946.04\nu^{1/2}$	0.998
				8.16 (0.02)	17.29 (0.02)	0.01-5	$I_{pc}(\mu A) = 129.80-1209.87\nu^{1/2}$	-1.000
						0.5-5	$\Delta E = 0.368+0.188\ln\nu$	0.984
16.7 (2.53)	19.3 (0.4)	8.1	0.12 (0.05)	8.21 (0.05)	24.51 (0.05)	0.01-5	$I_{pa}(\mu A) = 53.82+989.44\nu^{1/2}$	0.998
				10.95 (0.05)	43.63 (0.05)	0.01-5	$I_{pc}(\mu A) = 120.55-1318.51\nu^{1/2}$	-1.000
						0.5-5	$\Delta E = 0.455+0.213\ln\nu$	0.992

Table 4.4 Summary of the kinetic parameters of electrochemical process and the relationships between the peak currents, peak potentials and potential scan rates for PFNMA brush with a series of thickness. [a,b] σ is the standard deviations for parallel measurements. [c,d,e] σ is the standard deviations for fittings. [f] short dashed lines indicate that the thickness was too thin to be measurable via AFM scratch test so that the concentrations afterwards were estimation values.

$\Gamma_{Fc}(\sigma)^a$ (nmol/cm^2)	$L_{PB}(\sigma)^b$ (nm)	$C_0 \times 10^3$ (mol/cm^3)	$\alpha n_\alpha (\sigma)^c$	$k^0 \times 10^6 (\sigma)^d$ (cm/s)	$D_{app} \times 10^{12} (\sigma)^e$ (cm^2/s)	Scan rate (V/s)	Equation	r^2
0.4 (0.05)	---[f]	13.0	0.45 (0.05)	0.49 (0.05)	0.02 (0.005)	0.01-5	$I_{pa}(\mu A) = -0.265+85.61\nu^{1/2}$	0.997
				0.80 (0.05)	0.05 (0.005)	0.01-5	$I_{pc}(\mu A) = 11.1-114.4\nu^{1/2}$	-0.999
						0.5-5	$\Delta E = 0.06+0.058\ln\nu$	0.995
1.1(0.13)	---	13.0	0.31 (0.05)	0.74 (0.05)	0.03 (0.005)	0.01-5	$I_{pa}(\mu A) = -6.083+95.08\nu^{1/2}$	0.999
				0.95 (0.05)	0.06 (0.005)	0.01-5	$I_{pc}(\mu A) = 13.99-120.94\nu^{1/2}$	-1.000
						0.5-5	$\Delta E = 0.11+0.084\ln\nu$	-0.987
1.9 (0.23)	1.7(0.3)	12.1	0.22 (0.05)	0.82 (0.05)	0.07 (0.005)	0.01-5	$I_{pa}(\mu A) = -0.100+104.969\nu^{1/2}$	0.995
				1.15 (0.05)	0.19 (0.005)	0.01-5	$I_{pc}(\mu A) = 23.33-176.16\nu^{1/2}$	-0.989
						0.5-5	$\Delta E = 0.29+0.122\ln\nu$	0.986
4.8 (0.58)	3.1(0.2)	15.3	0.12 (0.07)	1.65 (0.07)	0.90 (0.07)	0.01-5	$I_{pa}(\mu A) = -11.21+352.76\nu^{1/2}$	0.996
				1.62 (0.07)	0.87 (0.07)	0.01-5	$I_{pc}(\mu A) = 22.67-346.92\nu^{1/2}$	-0.998
						0.5-5	$\Delta E = 0.43+0.223\ln\nu$	0.999
6.1 (0.73)	4.7 (0.3)	13.0	0.10 (0.07)	3.01 (0.07)	1.31 (0.07)	0.01-5	$I_{pa}(\mu A) = -48.43+702.15\nu^{1/2}$	0.984
				3.31 (0.07)	2.00 (0.07)	0.01-5	$_{Ipc}(\mu A) = 121.4-753.1\nu^{1/2}$	0.988
						0.5-5	$\Delta E = 0.28+0.183\ln\nu$	0.991

4.3 Conclusions

By cyclic voltammetry (CV) the electrochemical behaviour of Fc-containing polymer brush anchored on ITO substrate was investigated. The three kinds of polymer brush with different side chain lengths did not have very obvious different performance. However, we have found that the electrochemical process strongly depends on the scan rates and the thickness of polymer brush. The effects of scan rates and polymer brush thickness restricted each other.

Only at very low scan rate and with small thickness, the electrochemical process can achieve to reversible behaviour, otherwise, in most of the cases, the electrochemical process will be quasi-reversible and totally irreversible. In polymer brush, some of the Fc units are buried inside the polymer chains, most of the Fc units are not in the same microenvironment. At very low scan rate (v = 0.001V/s) we are able to observe multiple peaks, and the degree of peak splitting may dependent on the thickness of the brush: thinner brushes show more obvious splitting and even more peaks.

The kinetic parameters of the electrochemical process for polymer brush show good correlations with brush thickness. Surface charge-transfer coefficient, α, expresses the reversibility of the electrochemical process, lower value indicates lower reversibility for thicker brush film. The standard rate constant, k^0, measures the kinetic facility of a redox couple. Thicker brush film has higher surface coverage of Fc units, hence the electron transfer equilibrium would be achieved faster in the electrochemical process. The apparent diffusion coefficient, D_{app}, presents the diffusion of ions/counterions (electrons in some statements) in the film. For thicker brush film, more redox species would involve in the electron transfer process.

Chapter 4

4.4 Experimental section

4.4.1 Chemicals and materials

PFMMA, PFBMA, and PFNMA brushes were generated in advance by the method shown in Chapter 3. Absolute ethanol (AR EtOH, EMSURE), toluene (95%, EMSURE), deionized water (DI water, obtained from a Millipore-Q water system) were used for substrates cleaning. Indium tin oxide (ITO) (Singapore optics shop, 101×101×1.1 mm, ITO layer thickness ~ 180nm, sheet resistance ~ 10Ω sq^{-1}) was used as bottom electrode. Perchloric acid ($HClO_4$, Alfa-aesar, 1.0 M in aqueous solution) was used for electrolyte.

4.4.2 Electrochemistry measurements

PGSTAT302N with NOVA 1.10 software was used for measuring the surface coverage of Fc groups. We used a custom built electrochemical cell placed in a Faraday cage equipped with platinum counter electrode, a Ag/AgCl reference electrode and the ITO substrate served as a working electrode. To perform the cyclic voltammotry measurements, voltammograms were recorded in an aqueous solution 1.0 M $HClO_4$, between -0.5 V to 1.5 V (or -0.8 V to 1.8 V in some cases) at a series of scan rates, unless noted for special case. These scan rates range from 0.001 V/s to 10.000 V/s.

4.4.3 Determination of the thickness for polymer brush

Polymer brush thickness was estimated by AFM scratch test and variable angle spectroscopic ellipsometry. Here we applied both two measurements on Si/SiO_2 wafer substrate instead of ITO substrate. Experimental details were shown in Chapter 3.

4.5 References

Chapter 4

1. Pillay, V.; Tsai, T.-S.; Choonara, Y. E.; du Toit, L. C.; Kumar, P.; Modi, G.; Naidoo, D.; Tomar, L. K.; Tyagi, C. and Ndesendo, V. M. K., *J. Biomed. Mater. Res., Part A.* **2014,** *102* (6), 2039-2054.

2. Smela, E., *Adv. Mater.* **2003,** *15* (6), 481-494.

3. Hempenius, M. A.; Cirmi, C.; Savio, F. L.; Song, J. and Vancso, G. J., *Macromol. Rapid. Commun.* **2010,** *31* (9-10), 772-783.

4. Kang, H.; Liu, R.; Sun, H.; Zhen, J.; Li, Q. and Huang, Y., *J. Phys. Chem. B* **2012,** *116* (1), 55-62.

5. Dobbelin, M.; Marcilla, R.; Pozo-Gonzalo, C. and Mecerreyes, D., *J. Mater. Chem.* **2010,** *20* (36), 7613-7622.

6. Harper, A. and Anderson, M. R., *Sensors* **2010,** *10* (9), 8248-8274.

7. Shipway, A.; Katz, E. and Willner, I., (2001) *Molecular Memory and Processing Devices in Solution and on Surfaces.* Berlin, Heidelberg, Springer, Vol. 99, pp 237-281.

8. Elanchezhian, V. S. and Kandaswamy, M., *Inorg. Chem. Commun.* **2009,** *12* (2), 161-165.

9. Azzaroni, O., *J. Polym. Sci., Part A: Polym Chem.* **2012,** *50* (16), 3225-3258.

10. Eckermann, A. L.; Feld, D. J.; Shaw, J. A. and Meade, T. J., *Coord. Chem. Rev.* **2010,** *254* (15-16), 1769-1802.

11. Grelaud, G.; Gauthier, N.; Luo, Y.; Paul, F.; Fabre, B.; Barrière, F.; Ababou-Girard, S.; Roisnel, T. and Humphrey, M. G., *J. Phys. Chem. C* **2014,** *118* (7), 3680-3695.

12. Akhoury, A.; Bromberg, L. and Hatton, T. A., *J. Phys. Chem. B* **2013,** *117* (1), 333-342.

13. Lillethorup, M.; Torbensen, K.; Ceccato, M.; Pedersen, S. U. and Daasbjerg, K., *Langmuir* **2013,** *29* (44), 13595-13604.

14. Wang, X.; Wang, L.; Wang, J. and Chen, T., *J Phys. Chem. B* **2004,** *108* (18), 5627-5633.

15. Cheng, Z.; Ren, B.; Gao, M.; Liu, X. and Tong, Z., *Macromolecules* **2007,** *40* (21), 7638-7643.

16. Maeda, H.; Sakamoto, R. and Nishihara, H., *Polymer* **2013,** *54* (17), 4383-4403.

17. Tam, T. K.; Ornatska, M.; Pita, M.; Minko, S. and Katz, E., *J. Phys. Chem. C* **2008,** *112* (22), 8438-8445.

18. Luo, L.; Benameur, A.; Brignou, P.; Choi, S. H.; Rigaut, S. and Frisbie, C. D., *J. Phys. Chem. C* **2011,** *115* (40), 19955-19961.

19. Katagiri, S.; Sakamoto, R.; Maeda, H.; Nishimori, Y.; Kurita, T. and Nishihara, H., *Chem. Eur. J.* **2013,** *19* (16), 5088-5096.

20. Golriz, A. A.; Kaule, T.; Untch, M. B.; Kolman, K.; Berger, R. and Gutmann, J. S., *ACS Applied. Mater. Interfaces* **2013,** *5* (7), 2485-2494.

21. Kim, B. Y.; Ratcliff, E. L.; Armstrong, N. R.; Kowalewski, T. and Pyun, J., *Langmuir* **2009,** *26* (3), 2083-2092.

22. Yu, B.; Hu, H.; Wang, D.; Huck, W. T. S.; Zhou, F. and Liu, W., *J. Mater. Chem.* **2009,** *19* (43), 8129-8134.

23. García, T. A.; Gervasi, C. A.; Rodríguez Presa, M. J.; Otamendi, J. I.; Moya, S. E. and Azzaroni, O., *J. Phys. Chem. C* **2012,** *116* (26), 13944-13953.

24. Motornov, M.; Tam, T. K.; Pita, M.; Tokarev, I.; Katz, E. and Minko, S., *Nanotechnology* **2009,** *20* (43), 434006.

25. Gracia, R. and Mecerreyes, D., *Polym. Chem.* **2013,** *4* (7), 2206-2214.

26. Daum, P. and Murray, R. W., *J. Phys. Chem.* **1981,** *85* (4), 389-396.

27. Huo, J.; Wang, L.; Yu, H.; Deng, L.; Ding, J.; Tan, Q.; Liu, Q.; Xiao, A. and Ren, G., *J. Phys. Chem. B* **2008,** *112* (37), 11490-11497.

28. Kaufman, F. B.; Schroeder, A. H.; Engler, E. M.; Kramer, S. R. and Chambers, J. Q., *J. Am. Chem. Soc.* **1980,** *102* (2), 483-488.

29. Nguyen, M. T.; Diaz, A. F.; Dement'ev, V. V. and Pannell, K. H., *Chem. Mater.* **1994,** *6* (7), 952-954.

30. Casado, C. M.; Cuadrado, I.; Morán, M.; Alonso, B.; Barranco, M. and Losada, J., *Appl. Organomet. Chem.* **1999,** *13* (4), 245-259.

Tuning the Charge Transport across ITO-Ferrocene-containing Polymer Brushes // GaO_x / EGaIn Junction by Controlling the Brush Thickness

In this chapter we described the work on electronic characteristics for Fc-containing polymer brushes. By applying the polymer brushes with different side chain lengths in a series of thickness to EGaIn junction measurements, we statistically studied the relationship between the brush thickness and the rectification ratios. We found that polymer brushes with thinner thickness do not rectify the current while the polymer brushes with thicker thickness do rectify the current at the negative bias. In order to understand this change in the charge transport mechanism, we also conducted temperature dependent measurements. This measurement allowed us to identify the mechanism as a function of the thickness of the brushes: for the thinner brush, the charge transport may be dominated by electron tunnelling, while for the thicker brush, the charge transport may be dominated by electron hopping, and is electron space charge limited hopping.

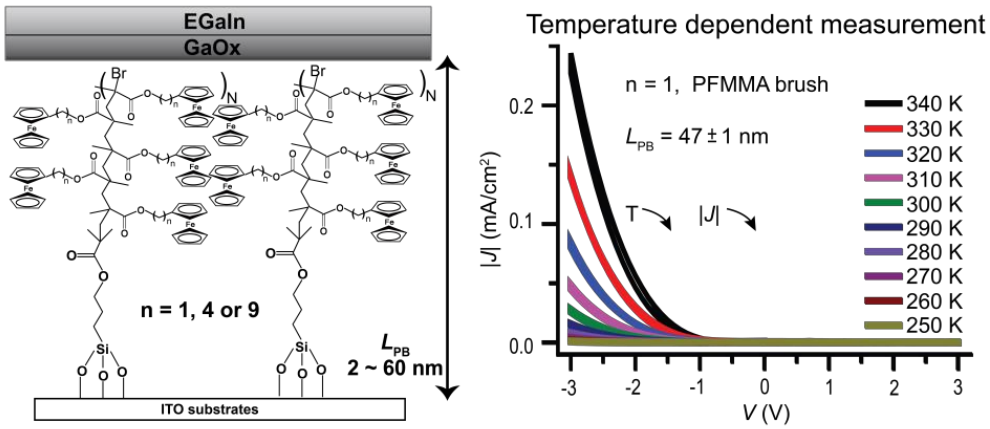

Chapter 5

5.1 Introduction

One of the major goals of molecular electronics is to understand, control and design electronic circuits using organic molecules as components.[1] Numbers of elements such as self-assembled monolayer (SAM) molecules[2-5], conjugated molecular wires (oligomers)[6-10] and polymer materials are widely studied in organic electronics field. As one of the commonly used components for tailoring of surface properties, polymer brush has one end of the chain anchored to a substrate, exhibiting excellent environment robustness and providing good control over surface structures and functionalities different from bulk counterparts.[11]

The applications of polymer brushes in electronics mostly focus on several aspects: (1) They could serve as hole/electron transport later or dielectric elements in organic electronics.[12-16] (2) They could enhance the charge-transport characteristics of normal polymeric films or diodes.[17,18] (3) They could be integrated into memory device.[19,20] (4) They could be explored as electrets to store electrostatic charges.[21] Due to these applications, it is essential to understand how charge transport along polymer brushes. However, charge transport properties across polymers that aligned perpendicularly to the electrode surface instead of paving on the electrode surface have only been rarely studied. Previous studies were focused on charge transport in relatively small molecules such as self-assembled monolayers (SAMs) with simple configuration or conjugated molecular wires (oligomers).

The length dependent of conductance and the rectification properties of molecular diodes are found as the consequences of charge transport mechanism. Frisbie et al. observed that the mechanism of charge transport changed from tunneling to hopping

with increasing molecular length.[10] Rampi et al. studied molecular wires of up to 40nm and reported that hopping was the dominant mechanism of charge transport.[9]

Few examples show polymer brushes have been incorporated in (macro)molecular junctions.[17,18] However systematic studies for charge transport measurements on polymer brushes with varying length scale are lacking. Here we present a detailed transport study on Fc containing polymer brushes with different thickness. Such a study is needed to understand the underlying transport mechanism in these systems and how it changes with the thickness. In our work, ferrocene containing polymer brushes: polyferrocenylmethyl methacrylate (PFMMA), polyferrocenylbutyl methacrylate (PFBMA), and polyferrocenylnonyl methacrylate (PFNMA), are selected as our study targets to study the charge transport through (macro)molecules. All polymer brushes have systematic length scale, ranging from 2 nm to 60 nm (represented by L_{PB}). We applied these 3 different polymer brushes to the same measurements to investigate if the different side chain length would affect the electronic characteristics. Au-S or Ag-S bond of the initiator for polymerization from surface is fragile above 60°C. To evade such issue, we choose ITO as bottom electrode instead, which has good electrical conductivity.

Comparing with SAMs, which are very thin (1 ~ 2 nm), polymer brushes could form thicker film, having a systematic length scale which ranging from several nanometers to several tens of nanometers or even hunderds of nanometers. Comparing with conjugated molecular wire, such polymer brushes are carrying the Fc moieties as functional groups but not conjugated moieties, and they are fixed on the side chain instead of main chain.

Comparing with other polymer thin film, which is a physisorbed film, polymer brush can be more robust and suffer less from the delaminating during device fabrication,

furthermore polymer brush can better control over the size, sequence, conformation and distribution of functional building blocks and the length is variable and controllable.[22-23]

Here we propose a platform based on the Fc containing polymer brushes to investigate their charge transport behaviour by means of the "EGaIn technique". We carried out the EGaIn cone-shape junction studies for Fc-containing polymer brushes with different side chain lengths and thickness to examine if the side chain length or different thickness would affect the charge transport behaviour. With the help of temperature dependent measurements we examined the mechanism of the charge transports in more details.

We applied "cone-tip EGaIn junction" to measure the polymer brush on small substrates, it is non-damaging contact, easy to retrieve the samples and able to obtain statistical data. Cone-shape tips can only be prepared one at a time per "EGaIn-set-up", and it is not applicable for temperature dependent measurement. We further fabricated GaO_x/EGaIn in microfluidic-based PDMS device as electrode to make "microfluidic-device junction". It is easy to control the contact area since the hole size is fixed (~30 μm), the encapsulation of the metal top-electrodes in PDMS eliminates instabilities associated with micromanipulators, and minimizes user-to-user variations in the details of the formation of the top-electrode, resulting in data with high precision and replicability. These features made such EGaIn device possible to study the electrical characteristics of the junctions over a period of time of ten days, and over the range of temperatures of 230 – 340 K. It is applicable for temperature dependent. Based on these charge transport measurements, we found the electronic characteristics were determined by the thickness, while within the full thickness range (2 nm < L_{PB} < 60 nm), such thickness dependent trends show little difference between polymer brushes with different

side chain lengths. The temperature dependent measurements demonstrated that the trap filling space charge limited conduction (TFLSCLC) is the main mechanism for the electron hopping for polymer brush with large thickness (L_{PB} > 20 nm).

Section 5.2 will provide the background of the charge transport mechanism. Section 5.3 mainly displays the results and discussion. The surface characterizations are shown in subsection 5.3.1, followed by statistical junction studies in subsection 5.3.2. The electronic characteristics (rectification ratio and current density as a function of thickness) are shown in subsection 5.3.3. These junctions showed incredible good durability (see subsection 5.3.4). In subsection 5.3.5 – 5.3.8 we discussed the charge transport mechanism. In subsection 5.3.9 we also show the proposed energy diagrams for the charge transport mechanism. Conclusions will be given in section 5.4, followed by section 5.5, experimental section.

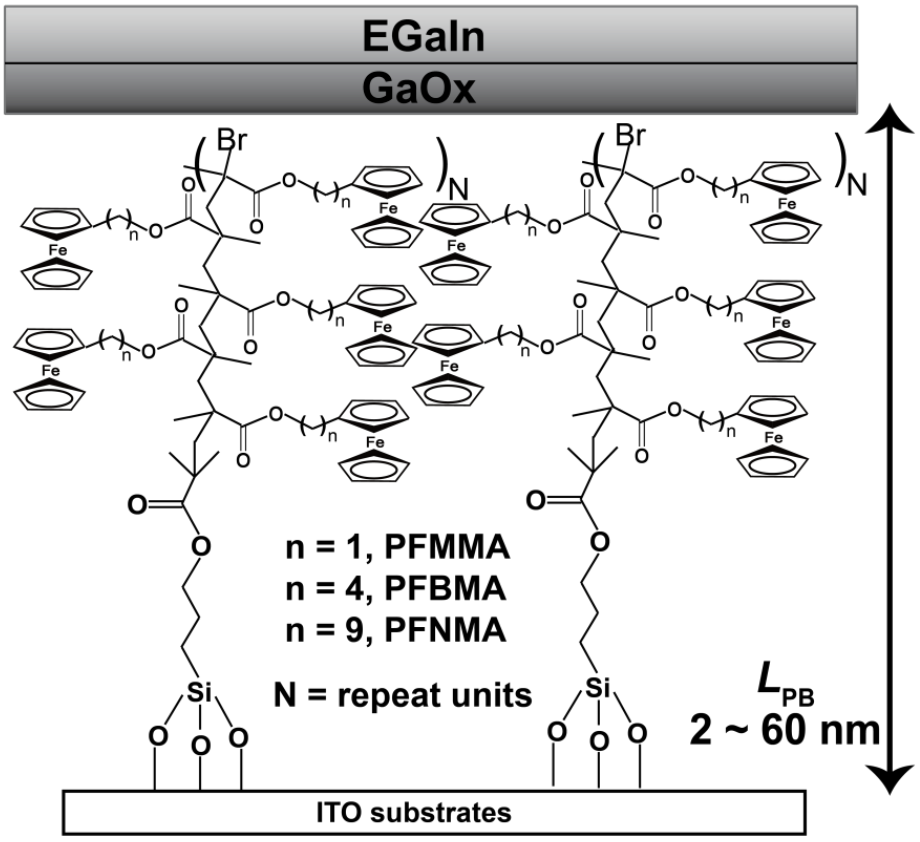

Scheme 5.1 Schematic structure of ITO-Ferrocene-containing Polymer Brushes // GaO_x / EGaIn Junction. PFMMA ≡ polyferrocenylmethyl methacrylate, PFBMA ≡ polyferrocenylbutly methacrylate, PFNMA ≡ polyferrocenylnonyl methacrylate. L_{PB} stands for the brush thickness.

5.2 Background on charge transport mechanism

Charge transports in molecules have several mechanisms, such as coherent tunneling, incoherent tunneling, hopping etc.[24] In the following sections, we introduce some background based on these charge transport mechanisms.

5.2.1 Tunneling

Tunneling dictated by quantum mechanics is based on the probability of an electron traversing a barrier of some thickness and barrier height, and maintains the phase of the electron.[24] The rate of coherent tunneling decreases exponentially with the thickness of barrier. The tunneling equation is shown as eq 5.1.

$$J = J_0 \mathrm{e}^{-\beta d} \qquad (5.1)$$

Where J is current density (A/cm^2), d is the barrier thickness, β is the tunneling decay coefficient.

5.2.2 Electron hopping by space charge limited conduction

In terms of electron hopping, it usually refers to the thermal activated charge transport and it follows a classical Arrhenius equation,[24] which is shown as eq 5.2:

$$J = J_0 e^{(\frac{-E_a}{k_B T})} \qquad (5.2)$$

Where J is current density (A/cm^2), E_a is the activation barrier (eV), k_B is the Boltzmann constant (8.62 ×10^{-5} eV/K) and T is the measured temperature (K). Hopping does not exhibit the exponential distance dependence of coherent tunneling.[24]

The charge transport measurements in metal-polymer-metal sandwich structure have been conducted by many groups to understand the conduction mechanism.[25-29] These transport measurements showed that the charge transport in these organic semiconducting device can be mainly two kinds: injection limited conduction (ILC) and bulk controlled space-charge limited conduction (SCLC).[30,31]

To occur SCLC at least one of the contacts has good injecting properties to provide an inexhaustible carrier reservoir while ILC occurs if the injection barrier is large such that the injection current from the contact into the organic is much less than the SCLC. In the case of metal-polymer interface with large barrier height, the carriers either jump or tunnel to the localized states across the interface, ILC occurs in present of applied electric field. The low barrier Ohmic contact facilitates the presence of a large number of carriers in the sample, at even low bias voltages.

In devices with low mobility, the injected carriers will create a space-charge region near the interface if the injected carriers are larger than intrinsic carriers present in the sample, leading to the SCLC. Once the space-charges are formed, additional injection of carriers are limited by the electrostatic potential of these space charges. One can tune the transport mechanism in organic semiconductor devices by varying the dopant concentration and thickness.[26,32]

Depending on the sample purity, the SCLC mechanism can be either trap-free or trap-filling (trap-filling SCLC, known as TFLSCLC; trap-free SCLC, known as TFSCLC).[33,34] In the case of a perfect insulator without intrinsic carriers and traps[35-37], TFSCLC model obeys Mott-Gurney transport expression[38] as given below:

$$J_{\mathrm{SCLC}} = \frac{9}{8}\varepsilon_{\mathrm{r}}\mu\frac{V^2}{d^3} \qquad (5.3)$$

Where ε_r is the dielectric constant of the material, μ is the mobility, d is the thickness of the film, V is experimental voltage. In the SCLC regime the current varies according to the well-known V^2 law if there are no traps and the mobility is independent of the electric field.

If either trapping or effect of field on mobility is important, the current varies as V^m, where m > 2. This is known as trap-filling SCLC.[25,28,29,39-41] In normal cases, trap sites will be present due to intrinsic disorder in polymeric materials: such as intentionally doping,[26,42] or unintentionally doping, i.e., structure defects and impurities.[43-46]

The current through the device is generally lower in the presence of traps and the quadratic field dependence is retained in the case of a discrete trap level only (or when all traps are filled).Whereas in case of traps which are distributed in energy, the traps get filled gradually with increase in the field and the current will increase faster than quadratic until all traps are filled. In the presence of traps exponentially distributed in energy, the Mott-Gurney expression, eq 5.3, could be rewritten as given below:

$$J = q^{1-l}\mu N_v\left(\frac{2l+1}{l+1}\right)^{l+1}\left(\frac{l}{l+1}\frac{\varepsilon_r\varepsilon_0}{H_t}\right)^l\frac{V^{l+1}}{d^{2l+1}} \qquad (5.4)$$

Where N_v is the carrier density, H_t is the trap density, q is the electron charge, ε_0 is permittivity of vacuum, and l is a parameter defined as $l = T_c / T = E_t / k_B T$, in which E_t is the characteristic trap energy, T is the measurement temperature, k_B is the Boltzman constant. $E_t = k_B \times T_c$, where T_c is a characteristic temperature and determined from the exponent of the power law.[25] E_t can directly be determined by a log-log plot of J(V), however, H_t cannot be determined directly. It is usually treated as a fitting parameter. Normally it can estimate from E_a and E_t by eq 5.5.

$$E_a = \frac{E_t}{k_B}\ln\left(\frac{qH_t d^2}{2\varepsilon_r\varepsilon_0 V}\right) \qquad (5.5)$$

Where d is thickness of polymer brush film (L_{PB}), E_a is an activation barrier which can be obtained from the temperature dependent J(V) data using Arrhenius relation, as given by eq 5.2.

5.3 Results and discussion

5.3.1 Surface characterizations for polymer brushes on ITO

We applied AFM scratch test and ellipsometry to determine the brush thickness (polymer brush on Si/SiO_2 substrate), and the measurement procedures are shown experimental section 5.5.2. Cyclic voltammetry (CV) was conducted in 1.0 M aqueous $HClO_4$ electrolyte at the scan rate 1.00 V/s to estimate the density of Fc groups (polymer brush on ITO substrate). The measurement procedures are shown in experimental section 5.5.3.

Since the polymerization conditions were the same for brush growth on Si/SiO_2 substrates and ITO substrates, the brush thickness is considered to be same in both cases. Here we applied the AFM scratch test on Si/SiO_2 substrate instead of ITO substrate since the Si/SiO_2 surface is much flatter and uniform with roughness (rms) lower than 0.5 nm (commercial bare ITO substrate, rms ~ 3 nm). This advantage allows us simply using a blade to make a clear scratch of polymer brush only, without scratching out any ITO layer. Figure 5.1 displays the morphology images and cross sections of AFM scratch tests for five representative polymer brushes samples which were applied to temperature dependent measurements. Figure 5.2 displays the CV plots for the corresponding samples mentioned in Figure 5.1. The AFM morphology images show clear cross profile for the scratches, providing relatively precise thickness for certain samples. CV plots all show typical broad voltammetric waves with large intensity of current density, indicating that these polymer brushes contain rich Fc groups.

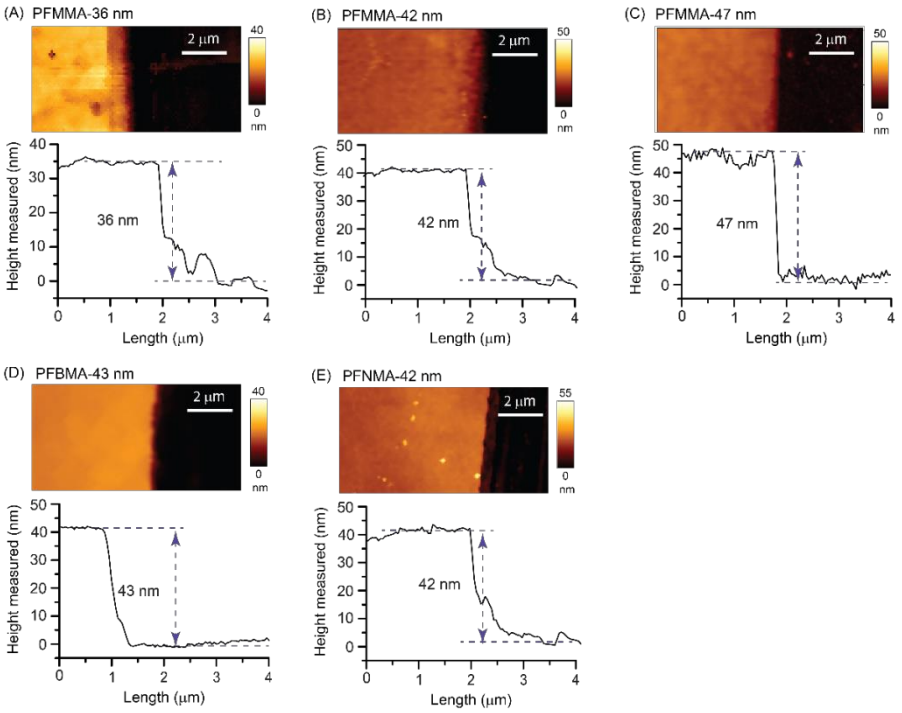

Figure 5.1 AFM scratch tests for five representative samples which was applied to temperature dependent measurements.

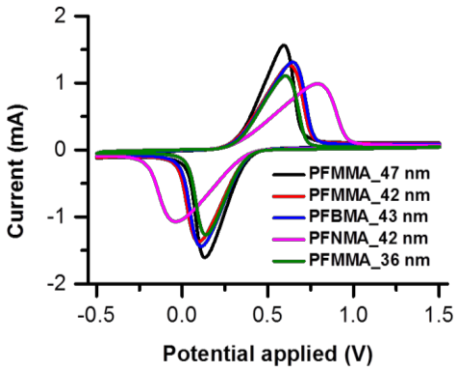

Figure 5.2 CV plots for five representative samples that applied to temperature dependent measurements.

5.3.2 Statistics of ITO – brush // GaO_x / EGaIn junctions

We fabricated junctions of the form ITO – brush // GaO_x / EGaIn junctions with brush thickness ranges from 2 nm to 50 nm to investigate their electronic characteristics as function of carbon number in the linker of monomers. We measured and analysed statistically large numbers of data, following previously reported procedure.[47]

In the J(V) measurements, one trace ≡ 0 V → +1.5 V → 0 V→ -1.5V → 0 V. The log average values of J ($\log_{10}|J|$) for each potential where J was measured were determined and were used to construct the log-average J(V) curves. All log-average J(V) curves, together with the histograms of the values of R (= $|J(-1.5V)|/|J(+1.5V)|$) with a Gaussian fit to these histograms for PFMMA, PFBMA and PFNMA brush with a series of thickness, respectively, are shown in Appendix (Figure A14-A16). Their statistical data are shown in Table 5.1. The Representative $J(V)$ curves and rectification ratios R for two of PFMMA brush samples are shown in Figure 5.3.

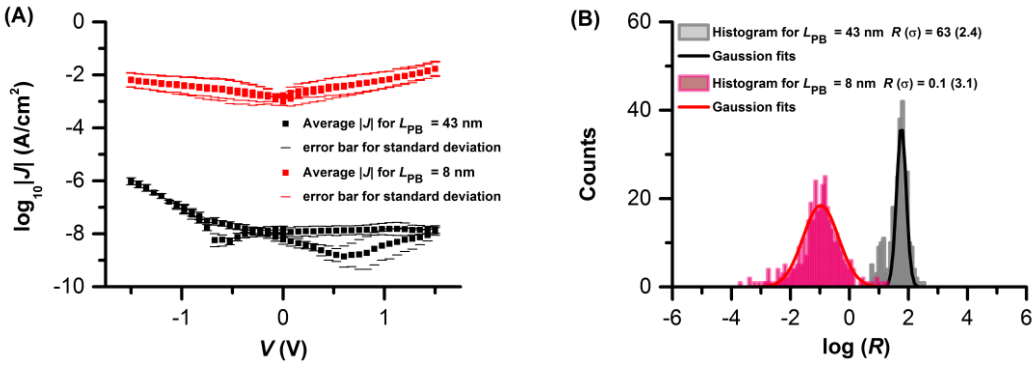

Figure 5.3 (A) Average $|J|(V)$ curves of the ITO–PFMMA brush// GaO_X / EGaIn in semi-log scale for L_{PB} in 8 nm, 43 nm, respectively. (B) Histograms of the rectification ratio log(R), R = $|J(-1.5V)|/|J(+1.5V)|$ shown with Gaussian fits for corresponding samples in (A).

All these statistical data indicate that polymer brushes with small thickness (L_{PB} < 15 nm) always have symmetric $J(V)$ curves while polymer brushes with large thickness (L_{PB} > 20 nm) always rectify the current at negative bias with the rectification ratio (R) about 100 and even higher. Furthermore, such trends show no significant differences among PFMMA, PFBMA, and PFNMA brushes, that is, no side chain effects.

5.3.3 Polymer brush thickness (L_{PB}) *vs.* rectification ratio (R) and polymer brush thickness (L_{PB}) *vs.* current density (J)

For PFMMA, PFBMA, and PFNMA polymer brushes, we can observe similar trends in the relationships for L_{PB} *vs.* R plots and L_{PB} *vs.* J (see Figure 5.4). Figure 5.4 shows the $\log_{10}(R)$ and $\log_{10}(J)$ as the function of thickness (L_{PB}) for PFMMA, PFBMA, and PFNMA polymer brushes, and we make the following observations: i) the directions of the rectification change as a function of L_{PB} for these three polymer brushes, i.e. the $\log_{10}(R) < 0$ with thin brushes ($L_{PB} < 15$ nm) and $\log_{10}(R) > 0$ with thick brushes ($L_{PB} >$ 20 nm); ii) when $L_{PB} > 20$ nm, the values of $\log_{10}$(R) slightly increase with L_{PB} and reach the maximum around 2.5 to 3. These occurrences of the rectification ratios are believed as the consequences of electron hopping processes. For thin polymer brushes ($L_{PB} < 15$ nm), the $\log_{10}(J)$ (at -1.5 V and +1.5 V) decrease exponentially as the thickness increase, indicating that the charge transport through the polymer brushes are dominated by the direct (coherent) tunneling process, which can be described by eq 5.1. For thick polymer brushes ($L_{PB} > 20$ nm), we observed the values of $\log_{10}(J)$ at -1.5 V become independent on the thickness, which is a strong suggestion that the sequential (incoherent) tunneling rate is faster than the direct tunneling and start dominating the charge transport.

The values of L_{PB} at the transition of rectification direction are matchable with that of L_{PB} at the transition of the current density data. This clearly indicated the changes of rectification are caused by the changes of charge transport mechanism over different length.

Table 5.1 Statistics for ITO – PFM(B/N)MA brushes // GaO_x / EGaIn junctions.

Brush	L_{PB} (nm)	Number of junctions	Number of shorts[a]	Number of traces[b]	Non-shorting yield[%][c]	R (σ_{log}[d])
PFMMA	2	14	2	277	86	1.4×10^{-1} (0.54)
	7	14	2	275	86	1.6×10^{-1} (0.38)
	15	14	2	283	86	1.6×10^{-1} (0.48)
	18	15	3	297	80	5.0×10^{-2} (0.43)
	21	16	2	320	88	1.0 (0.30)
	24	15	1	294	93	9.1×10^{1} (0.36)
	29	18	1	355	94	1.2×10^{2} (0.32)
	33	16	1	317	94	6.3×10^{2} (0.28)
	36	16	0	312	100	2.4×10^{2} (0.26)
	41	16	0	317	100	4.4×10^{2} (0.30)
PFBMA	3	15	3	289	80	3.0×10^{-2} (0.53)
	5	15	3	294	80	1.4×10^{-1} (0.49)
	8	14	2	277	86	9.0×10^{-2} (0.48)
	12	14	2	278	86	3.6×10^{-1} (0.48)
	16	16	2	314	88	1.4×10^{1} (0.41)
	20	16	1	317	94	3.8×10^{1} (0.32)
	25	15	1	296	93	1.6×10^{2} (0.28)
	30	14	0	276	100	1.1×10^{2} (0.32)
	33	15	0	291	100	5.0×10^{2} (0.30)
	38	15	0	296	100	3.6×10^{2} (0.38)
PFNMA	3	15	3	289	80	2.2×10^{-1} (0.52)
	6	14	2	271	86	1.8×10^{-1} (0.34)
	8	14	3	273	79	2.2×10^{-1} (0.36)
	13	16	2	311	88	8.7×10^{-1} (0.34)
	16	15	1	298	93	8.7 (0.53)
	20	14	2	275	86	2.8×10^{1} (0.41)
	24	16	1	314	94	3.8×10^{1} (0.32)
	28	15	0	295	100	1.6×10^{2} (0.32)
	33	16	0	312	100	2.0×10^{2} (0.30)
	36	15	0	296	100	1.5×10^{2} (0.36)

[a]A short was defined when the value of J exceeded 100 A/cm^2 while recording J(V) in 20 scans.
[b]The number of J(V) traces of the ITO – brush // GaO_x / EGaIn junctions.
[c]The yield of nonshorting junctions is defined as the number of junctions minus the number of shorts divided by the number of junctions.
[d]The σ_{log} is the log-standard deviation.

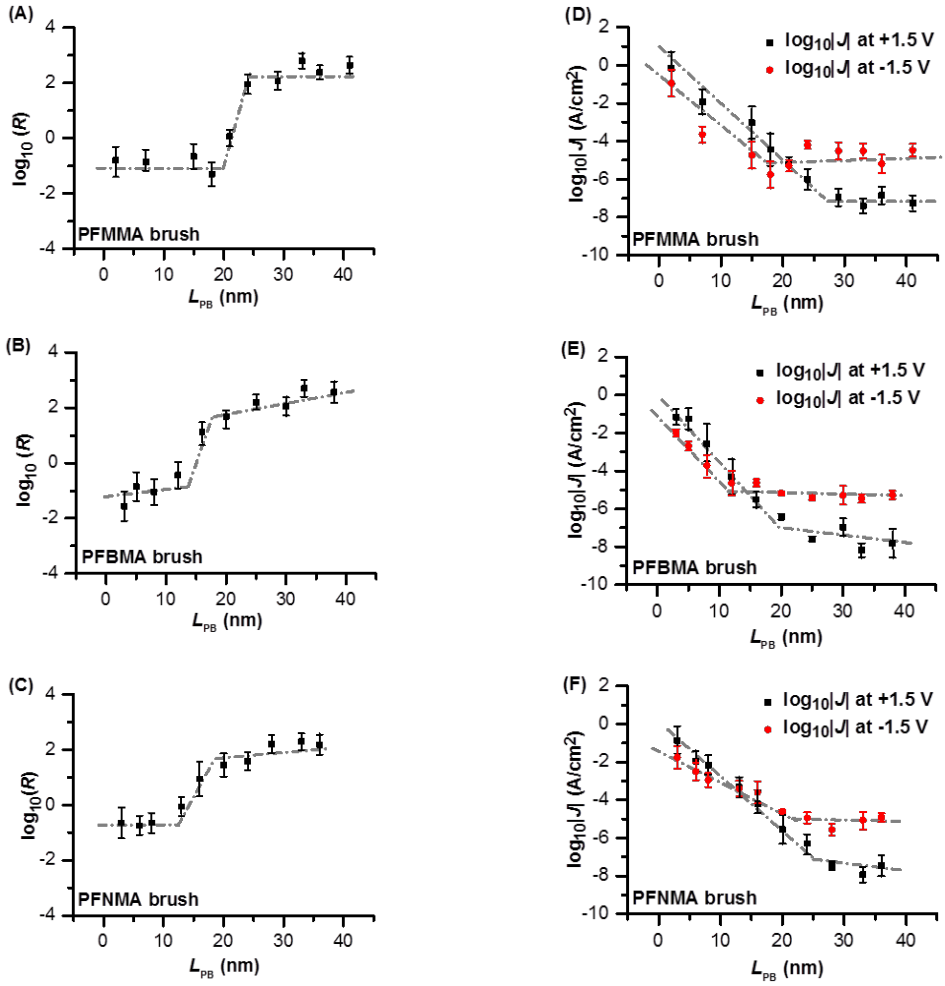

Figure 5.4 The relationships between the thickness of polymer brushes (L_{PB}) and rectification ratios R in log value are shown in (A), (B), and (C), for PFMMA, PFBMA, and PFNMA brushes, respectively. The relationships between the thickness of polymer brushes (L_{PB}) and current density J in log value at +1.5 V and -1.5 V are shown in (D), (E), and (F) for PFMMA, PFBMA, and PFNMA brushes, respectively. Error bars are standard deviations, grey dash lines are served at guide to the eyes.

Before polymer brushes reached 15 nm, all current density (on both positive and negative bias) decrease exponentially as the thickness increase, indicating that the charge transport may be dominated by tunneling mechanism which follows eq 5.1. The rate of coherent tunneling decreases exponentially with the thickness of the barrier, its simplest form is given by eq 5.1. As is shown in Figure 5.6, the transition points for all three polymer brushes are quite similar. As we observed, all the changes on current rectification ratio (R) were based on the thickness (L_{PB}). Hence, we believe there is a

thickness dependent performance in these charge transports, which is carefully discussed in subsection 5.3.5.

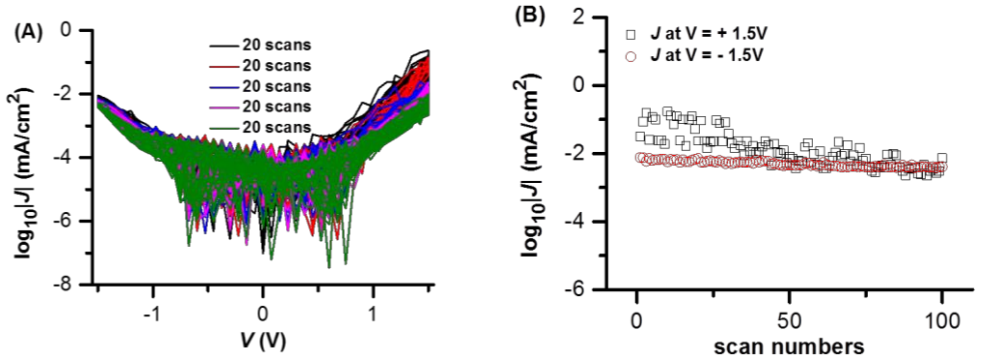

Figure 5.5 Stability test of current density recorded at constant bias of $|V| = 1.5$ V for 100 scans for 8 nm PFMMA brush sample. (A) J(V) curves of cone-shape tip junction measured the same sample on same spot over 100 scans. (B) Current density values on +1.5 and -1.5 bias as the function of scan numbers.

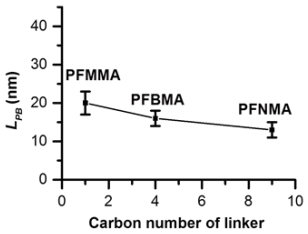

Figure 5.6 Transition points corresponding to PFMMA brush, PFBMA brush and PFNMA brush.

5.3.4 Durability of the polymer brush sample: tested by EGaIn cone-shape tip junction

Some basic tests are required to verify if this test bed is able to be fabricated into device in the future. First of all, durability is one of the important aspects. In order to investigate the stability of these polymer brush samples based on EGaIn cone junction measurements, we conducted time-decay (two time periods: 1.5 months and 4.0 months were chosen) cone junction measurement and compared with the original junction scan (fresh prepared sample measured within 2 days), tracking how the J(V) signals and R values would change in time. We carefully stored these polymer brush samples at -4°C fridge without inert gas protection for long time. Before junction measurements, the

sample was rinsed with DCM and EtOH, followed by drying in a stream of N_2 gas. The average $\log_{10}|J|$ curves (error bars for each curve were omitted in this plot) and histograms of the values of R (= $|J(-1.5V)|$ / $|J(+1.5V)|$) with a Gaussian fit were shown in Figure 5.7. On one hand, we can observe that the rectification ratios were kept same as around 100, while the histograms shows that the 4.0 months sample has the largest distribution, indicating that this junction measurement was not as stable and reproducible as other two, which may attributed by the impurity or moisture adulterated after such long time storage. On the other hand, the average current density for samples stored over 1.5 months has around half order of magnitude decreasing at both bias, as well as the 4.0 months case.

5.3.5 Transport mechanism

In this section, we discuss the charge transport mechanism in polymer brushes with large thickness (L_{PB} > 20 nm), and we applied PFMMA brush as example for data analysis. From the junction measurements with EGaIn cone-shape tip, we assumed that charge transport of polymer brushes with thin polymer brushes (L_{PB} < 15 nm) may be dominated by tunneling, where examined at a given applied voltage, J roughly obeyed a simple approximation of the tunneling equation (eq 5.1), as is shown in Figure 5.4(D)-(F).

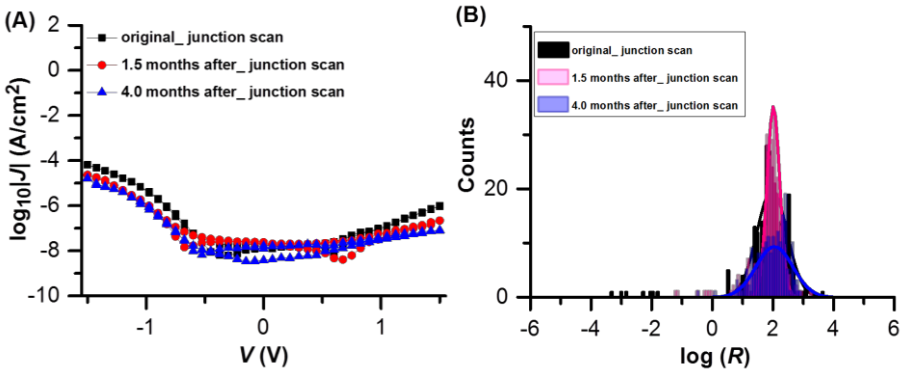

Figure 5.7 (A) The stacked average $\log_{10}|J|$ curves of ITO – PFMMA brush // GaO_x / EGaIn junctions for original (black square), 1.5 months after (red dot), and 4.0 months after (blue triangle) junctions. (B) The stacked histograms of the values of R (= $|J(-1.5V)|/|J(+1.5V)|$) with a Gaussian fit to these histograms for corresponding J(V) curves in panel (A), original (black column), 1.5 months after (pink column), and 4.0 months after (blue column).

While for thick polymer brushes (L_{PB} > 20 nm) tunneling transport may not be possible transport mechanism as the tunnelling probability decreases exponentially with thickness. Activated carrier hopping mechanism may be the possible transport mechanism in these thick polymer brush junctions. To understand more about the transport mechanism we carrier out the temperature dependent measurements on these samples. Current was observed rectifying at negative bias for thicker (L_{PB} > 20 nm) polymer brushes, leading to an asymmetric current-voltage (J(V)) curve. To distinguish if such asymmetric shape is resulted from Schottky barrier by injection limited conduction (ILC) or space charge limited conduction (SCLC), we examined the electronic characteristics for a series of PFMMA brushes in different thickness at room temperature. The room temperature (T =300 K) J(V) characteristics measured by microfluidic EGaIn device of all 6 PFMMA samples with different thickness are shown in Figure 5.8. In the case of ILC, J is independent of thickness but depends on the interface barrier. While we can see from Figure 5.8(A) that J linearly scales with L_{PB} in log-log scales, suggesting that the mechanism is not ILC. Such linear relationship between J and L_{PB} in log-log scales indicates that the transport is dominated by SCLC mechanism. In the case of SCLC with an exponential trap distribution the current at constant field scales with d^{-l} with l > 1. The linear relationship between J and L_{PB} in log-log scales with slope ~ -2.7, indicating that the transport mechanism is SCLC. To understand more about the charge transport mechanism, we analyzed the J(V) data plotted in log-log scales for each sample. For all these samples, J(V) in log-log plots show nonlinear behavior with a linear region at higher voltages at negative bias (1.2 V <

$|V| < 3.0$ V) (an example of J(V) in log-log plot is shown in Figure 5.9), as can be seen in Figure 5.8(B). Here a 47 nm PFMMA brush was measured with microfluidic-device at room temperature. J(V) curves show nonlinear behaviour, having a super linear region at higher voltages, with a slope about 4.19. All other samples in this experiment were fitted in the same method (See Figure A17). According to eq 5.3, slopes for the linear region are all > 2, indicating the presence of traps in our devices. We obtained a slope about 4 ~ 5 and J(V) that follows a power law, $J \propto V^{m}$ with m > 2, indicating it is TFLSCLC with exponential trap distribution.

5.3.6 Key parameters for temperature dependent charge transport measurements: E_t, T_c, H_t and E_a

To determine the activation energy and other transport parameters we carried out the temperature dependent measurements. The temperature dependent measurement on three PFMMA brush samples with different thickness > 40 nm were conducted to examine if the charge transport mechanism has the thickness dependence. In order to find out the effect of side chain we measured the temperature dependent J(V) characteristic of a PFBMA brush sample and a PFNMA brush sample with the same thickness.

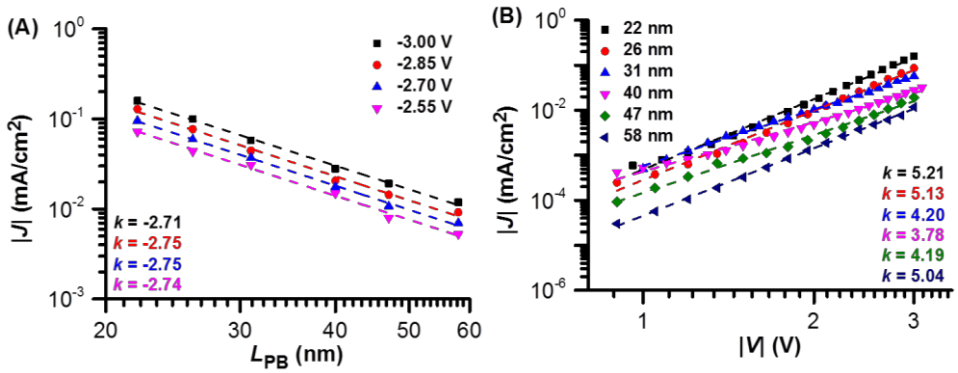

Figure 5.8 (A) Current density J on the dependence of PFMMA brush thickness L_{PB} in log-log plots on negative bias at higher voltages range. (B) Current density J on the dependence of the voltage V on negative bias (1.2 V < $|V|$ < 3.0 V) in log-log scales for PFMMA brush with a group of thickness. Colored dash lines are fitting lines for corresponding plots. Values of slopes (k) are shown.

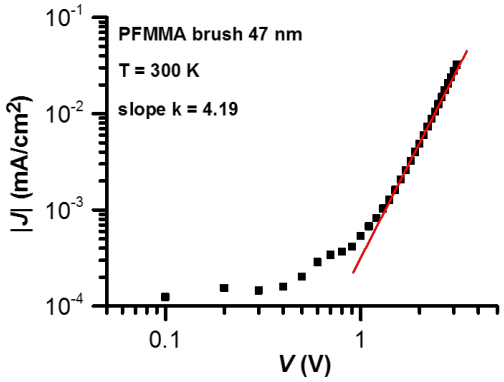

Figure 5.9 *J*(V) in log-log plots on negative bias in full voltage range (0 V < |*V*|< 3.0 V) at 300 K for 47 nm PFMMA brush. The solid line indicates the linear fitting at higher voltage (1.2 V< |*V*|< 3.0 V).

Many influences can contribute to traps forming. It is clear that both physical (e.g., conformational disorder) and chemical defects (e.g., broken bonds and impurities) are present in insulating materials and that both may trap electrons.[43-45] Here we believe Fc moieties act as the trap site.

Temperature dependent measurements assist to identify the nature of traps in these junctions. Figure 5.10(A) shows the *J*(V) curve in linear scale for representative PFMMA brush sample with thickness as 47 nm on the dependence of temperature under the applied voltage |*V*| = 3.0. In a disordered system, transport involves phenomena such as hopping between localized sites wherein the vibrations help to overcome the energy difference between sites. Thick polymer brushes (L_{PB} > 20 nm) show the rectification at negative bias, and the current density *J* are decreasing with the decrease in temperature, indicating the hopping behaviour indeed is important.

Figure 5.10(B) shows the linear region for *J*(V) plots in log-log scales as the function of *T* for 47 nm polymer brush sample at higher voltage on the negative bias (1.9 V < |*V*| < 3.0 V). The slopes of all the linear fitting contribute to the estimation of exponent *l*, which is shown in Figure 5.10(C). T_c as the characteristic temperature could be

determined from the slope of the 1/T *vs. l* plot. This linear relationship traps are in exponential distribution.

Using the value of T_c, the characteristic trap energy, E_t = 0.19 ± 0.01 eV is obtained (see background). The current density J that flows across the junction is described by the Arrhenius relation, as shown in eq 5, from which we can obtain the activation energy E_a. The inset in Figure 5.10(A) shows the values of J measured at -3.0 and +3.0 V as the function of temperature, and Figure 5.10(D) shows the Arrhenius plots of the ITO – PFMMA brushes // GaO_X / EGaIn junctions. The activation energy = 0.45 ± 0.01 eV.

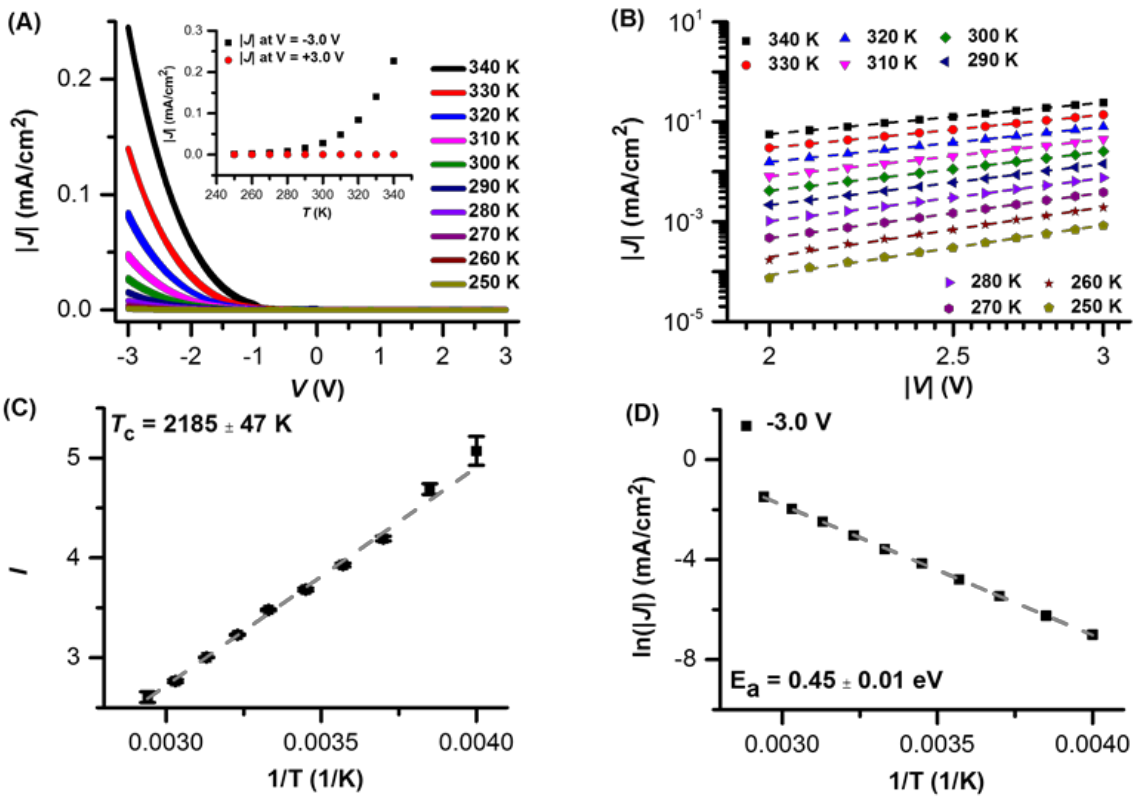

Figure 5.10 Thermally activated charge transport across ITO – PFMMA brush // GaO_X / EGaIn junctions. (A) J(V) linear scale plot as the function of T for 47 nm polymer brush sample at the voltage $|V|$ = 3.0 V. Inset image shows the values of $|J|$ measured at -3.0 and +3.0 V as a function of temperature. (B) J(V) plots in log-log scale at the negative bias (1.9 V < $|V|$ < 3.0 V) as the function of T for 47 nm polymer brush sample. Colored dash lines indicate the linear fitting. (C) Exponent l *vs.* 1/T plots. Black dash line indicates the linear fitting. Error bars for all data points indicate the fitting errors from (B). (D) ln|J| on negative bias at $|V|$ = 3.0 V as the function of 1/T, black dash line indicates the linear fitting.

Plots in Figure 5.10 yield three important pieces of information. For such polymer brush sample with large thickness (L_{PB} > 20 nm) (1) Hopping is only observed on negative bias. (2) The relationship between the current density and voltage in log-log scales as the function of temperature indicates the space charge limited conduction charge transport model.

E_t is the energy required for detrapping the carriers in traps, extra energy (~ 0.26 eV) compared E_a to E_t is the energy used for hopping between sites. With the already-known E_a value (0.45 ± 0.01 eV), we can obtain the rough value of trap density H_t using eq 5.5. The values of ε_r is assumed as 2.8,[48] and we took 3.0 V as experimental voltage for examples. Using the eq 5.5, H_t is estimated as 4.8×10^{18} cm^{-3}. This value is comparable with other reported values.[25] Comparing the value of the trap density with the value of Fc units (~10^{21} cm^{-3}) in the corresponding polymer brush samples that roughly estimated from the surface coverage of PFMMA brush on ITO surface with certain thickness, we can find that these two values are in the comparable range. This observation demonstrates that Fc units contribute to acting as the trap sites.

Table 5.2 The parameters for polymer brush samples in the temperature range 250 – 340 K. [a] All thickness were obtained by AFM scratch tests with the images shown in Figure 5.1. [b] All Fc densities were estimated by wet electrochemistry (CV).

Thickness[a] (nm)	T_c ($\times 10^3$ K)	E_t (eV)	E_a (eV)	H_t ($\times 10^{18}$ cm^{-3})	d_{Fc} ($\times 10^{21}$ cm^{-3})[b]
PFMMA brush					
47 ± 1	2.22 ± 0.05	0.19 ± 0.01	0.45 ± 0.01	4.8	2.0
42 ± 1	2.68 ± 0.12	0.23 ± 0.01	0.46 ± 0.01	3.9	1.9
36 ± 1	3.55 ± 0.19	0.31 ± 0.02	0.45 ± 0.01	3.3	1.5
PFBMA brush					
43 ± 1	2.39 ± 0.05	0.21 ± 0.01	0.43 ± 0.01	4.2	1.9
PFNMA brush					
42 ± 1	2.43 ± 0.76	0.21 ± 0.01	0.43 ± 0.01	4.2	1.9

Several more samples were applied the temperature dependent measurements to examine the trap filling space charge limited conduction model. Their thicknesses were determined by AFM scratch test, whose morphology and cross profile are shown in Figure 5.1.

5.3.7 Thickness dependence and side chain dependence for polymer brushes in temperature dependent measurements

Table 5.2 shows in total 5 polymer brush samples with all parameters obtained from temperature dependent measurements. All the corresponding *J*(V) plots as the function of temperature are shown in Appendix (see Figure A18-A21). As shown in Table 5.2, little difference can be observed among the polymer brushes with different thicknesses (PFMMA brush with 47 nm, 42 nm and 36 nm) and different side chain length (PFBMA brush with 42 nm and 36 nm). Generally speaking, the trap energy (E_t) increased as the increasing thickness, while the activation energy (E_a) are always similar in values. The density of Fc groups (d_{Fc}) increase with the increasing brush thickness, same as the trap density (H_t), indicating that the these two have positive correlation, which is consistent with the statement that Fc groups contribute to the traps in the charge transport processes.

5.3.8 *J*(V) in semi-log plot as the function of temperature to 6 nm polymer brush at the voltage $|V| = 3.0$ V

Figure 5.11(A) shows the *J*(V) curve in semi-log scale for a representative PFMMA brush with thickness of 6 nm as reference. We observe similar electronic characteristics for polymer brush junction bases on microfluidic-device as cone-tip junction: thin brush samples do not rectify. The *J*(V) curves are independent of the temperature. However, the non-overlapping curves may result from the measurement error from instability.

Figure 5.11(B) shows the ln|*J*| values on both bias |*V*| = 3.0 V. Current density shows no correlations to temperature, indicating that such charge transport behaviour does not follow the Arrhenius equation, i.e., hopping mechanism. Based on the temperature dependent measurement, we believe for thinner polymer brush (L_{PB} < 15 nm), the charge transport mechanism may be dominated by tunneling.

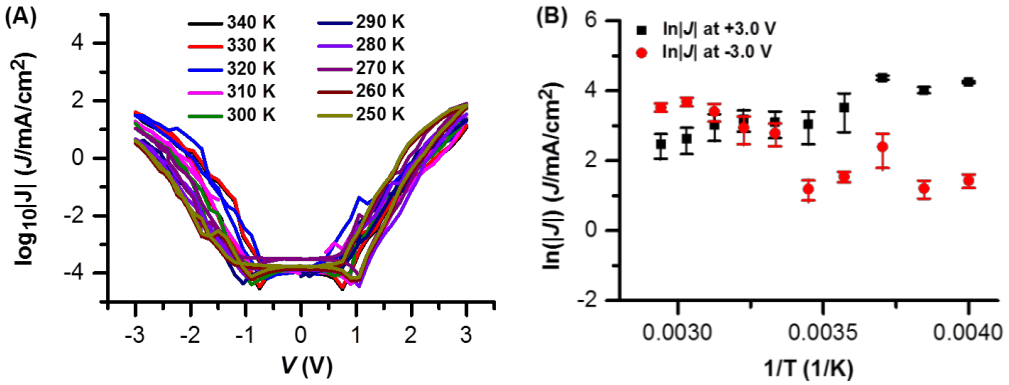

Figure 5.11 (A) *J*(V) in semi-log plot as the function of temperature for 6 nm polymer brush on the bias |*V*| = 3.0 V. (B) ln|*J*| values on bias |*V*| = 3.0 V as the function of temperature.

5.3.9 Energy diagrams for charge transport

The ultraviolet photoelectron spectroscopy (UPS) data is the foundation for developing the energy diagrams. HOMO level was determined of the by UPS and CV, values are shown in Table 5.3, energy level diagrams are shown in Scheme 5.2. Representative UPS are shown below in Figure 5.12. Changes in the surface electronic properties of polymer brushes modified ITO samples were probed using UPS. ITO surface itself has a work function of 4.5-4.7 eV[49-55] according to different fabrication procedures. From the secondary cut-off, we can obtain the work function and the HOMO level. The work function of the analyzer is 4.42eV, and we applied -5.0 eV bias on the sample, so the real work function value is: $\phi_{\text{work function}} = E_{\text{LECO}}\text{-}(5.0\text{-}4.42) = h\nu\text{-}(E_f\text{-}E_{\text{LECO}})$ (eV). For example, bare ITO has E_{LECO} = 5.08 eV, so $\phi_{\text{work function}}$ = 4.50 eV, then we can know the E_f is 21.79 eV, since $h\nu$ = 21.21 eV is known. In terms of the HOMO levels,

use the value of E_f = 21.79 eV to subtract the original values of valance band maximum (VBM), converting the kinetic energy to binding energy (see the inset of Figure 5.12). The inset shows the cutoff of the right hump (~ 20 eV) to make a tangent for HOMO relative to E_f level. HOMO relative to vacuum level = HOMO relative to E_f level + $\phi_{work\ function}$. Since in wet electrochemical measurements, the Fc units exposed to electrolyte solution, while in the junction measurements, the Fc units are in a very different environment. The HOMO levels values may have small deviation (0.1 ~ 0.5 eV)[56] measured by wet electrochemistry comparing to values obtained by UPS (in vaccum).

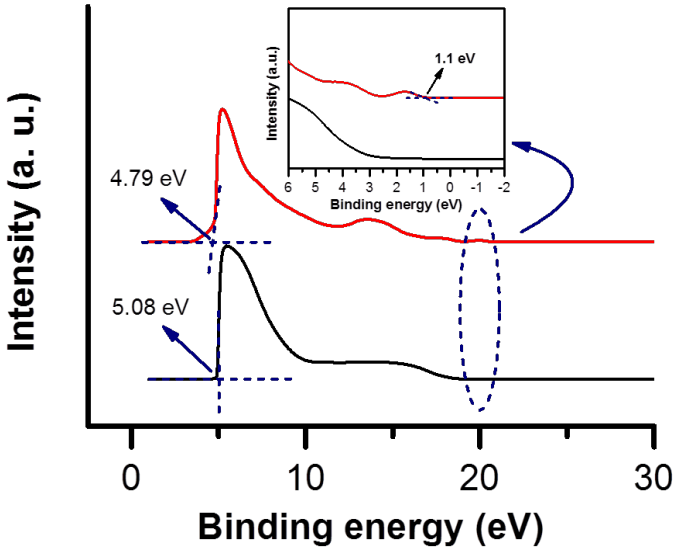

Figure 5.12 The representative ultra-photon spectra of bare ITO and PFMMA polymer brush (L_{PB} = 12 nm) modified ITO. The cut offs on the left side refer to the work function. The inset figure shows the zoom-in spectra for high energy range (~ 20 eV), and the cut-off for the hump refers to the HOMO level relatives to E_f. Blue dash lines are guide lines for eyes.

In Scheme 5.2 (A), the HOMO level of the polymer brushes was -5.3 eV, estimated from the average values measured from UPS shown in Table 5.3. The value of the LUMO level was -2.3 eV, which was calculated from its molecule gap value (2.8 eV) from UV/Vis measurement. Details were discussed in Chapter 3. The Fermi levels of ITO and EGaIn were measured by UPS (the work function value of bare ITO, -4.5 eV) and referred from literature[4,57] (-4.3 eV), respectively. All these values are shown in the case open circuit (OC). The charge transport mechanism changes from thin polymer

brush (L_{PB} < 15 nm) to thick polymer brush (L_{PB} > 20 nm) when applying -1.5 V and + 1.5 V: i) for thin polymer brush, direct tunneling dominated the charge transport that current can flow from top electrode (GaO_X/EGaIn) to bottom electrode (ITO) without involving in the HOMO level of polymer brush. However ii) for thick polymer brush, the distance from top electrode to bottom electrode are too far to allow electrons tunnel through, and temperature dependent measurement demonstrated that the charge transport mechanism is hopping. In this charge transport process, ITO acts as hole injection layer (p-type) and provide holes (GaO_X/EGaIn[58-61] as n-type electrode). The holes are trapped at the layer of polymer brushes and the current can flow only if these holes are detrapped and hop to the top electrode. However, in the whole charge transport process, we only observed hopping current at forward bias (applying - 1.5 V) while at reverse bias (applying + 1.5 V) we could barely detect the current since it is as low as the noise level. Based on this observation, we speculated that in the case of thicker polymer brush, the HOMO level did involve in the charge transport process, as is shown in Scheme 5.2(C). Little current can leak from EGaIn to ITO electrode which results in the current rectifications. To prove our hypothesis about whether HOMO level of Fc involves in the charge transport process, we tested two mores samples of PMMA brush (6 nm and 15 nm) as the comparison, whose $J(V)$ curves are showed in Figure 5.13. Only 10 traces were measured for these two samples for a quick check. From the $J(V)$ traces we can see that both samples show symmetric traces and there is no current rectification occurring, and the current densities decrease as the brush thickness increase, suggesting that there is no such hopping behaviour but only tunneling mechanism dominating. This observation indirectly prove that Fc units are essential for the hopping mechanism and the HOMO level of Fc units should take part in the charge transport process in the case when Fc-containing polymer brush is over 20 nm.

Table 5.3 Summary of work function values and HOMO levels for corresponding samples.

Item	Sample	Work function (eV)	HOMO relative to E_f (eV)	HOMO relative to vacuum level (eV)	Calculated HOMO by CV(eV)
Reference sample	Bare ITO	4.5	N.A.	N.A.	N.A.
PFMMA brush	2 nm	4.2	1.0	5.2	5.1
	7 nm	4.3	1.1	5.4	5.1
	12 nm	4.2	1.1	5.3	5.1
PFBMA brush	3 nm	4.2	1.1	5.3	4.9
	8 nm	4.2	1.2	5.4	4.9
	12 nm	4.1	1.4	5.5	5.0
PFNMA brush	2 nm	4.3	1.0	5.3	4.9
	6 nm	4.2	1.2	5.4	4.9
	10 nm	4.2	1.3	5.5	5.0

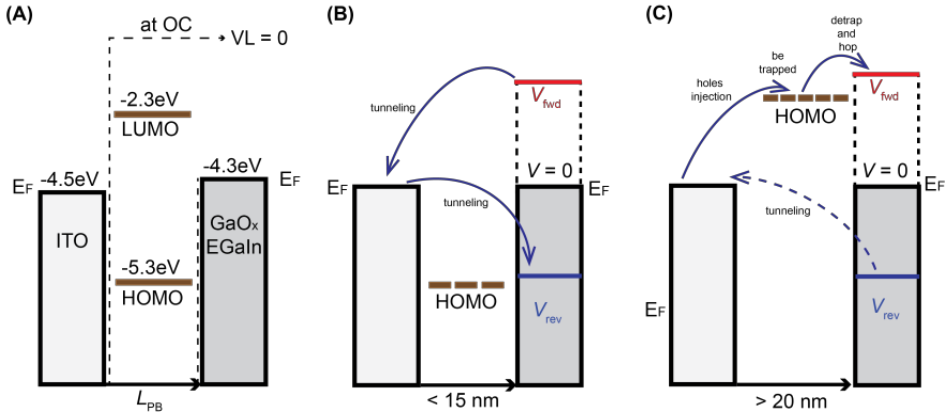

Scheme 5.2 Proposed schematic representation of the energy level diagrams (with respect to vacuum) of ITO – brush // GaO_x / EGaIn junctions: (A) at open circuit (OC), (B) at $V = 0$ V, at $V = -1.5$ V, at $V = +1.5$ V for thin polymer brushes ($L_{PB} < 15$ nm), (C) at $V = 0$ V, at $V = -1.5$ V, at $V = +1.5$ V for thick polymer brushes ($L_{PB} > 20$ nm). Black dashed lines indicate the width and height of the barrier. Blue (solid and dashed) arrows indicate the route and direction of charge transports, the one with the red dashed crosses indicates the forbidden route.

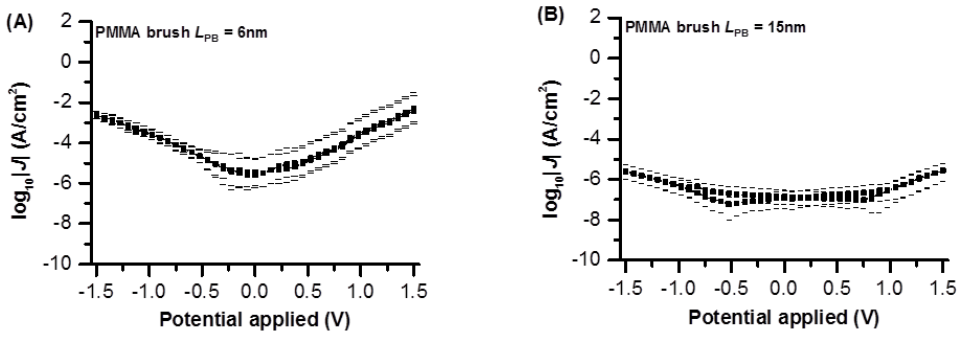

Figure 5.13 $J(V)$ curves averaged from 10 measurement traces for PMMA brushes with two thicknesses: 6 nm and 15 nm.

5.4 Conclusions

A series of Fc-containing polymer brushes with systematic thickness range (2 nm ~ 50 nm) was measured by EGaIn cone tip junction, little difference in electronic characteristics between PFMMA, PFBMA, and PFNMA brush was observed, suggesting that the different side chain lengths may not affect the electronic characteristics.

Temperature dependent measurements for polymer brushes (PFMMA brush as example) with small and large thicknesses (8 nm and 47 nm) were conducted with EGaIn microfluidic-device junctions. Temperature dependent measurements revealed the charge transport mechanism for large thickness polymer brush, $L_{PB} > 20$ nm, is the electron hopping by space charge limited conduction. While for polymer brush with smaller thickness, $L_{PB} < 15$ nm, electron tunneling may dominate the charge transport.

We estimated the characteristic temperature of traps $T_c = 2.22 \pm 0.05$ K, the trap energy $E_t = 0.19 \pm 0.01$ meV, by Mott-Gurney expression, and the activation energy $E_a = 0.45 \pm 0.01$ meV by Arrhenius relation, finally determined the trap density $H_t = 4.8 \times 10^{18}$ cm^{-3}.

5.5 Experimental section

5.5.1 Chemicals and materials

PFMMA, PFBMA, and PFNMA brushes were generated in advance by the method shown in Chapter 3. Methyl methacrylate (MMA, 99%, Aldrich) was used to generate poly (methyl methacrylate) (PMMA) brush with the same SI-ATRP recipe mentioned in Chapter 3. Absolute ethanol (AR EtOH, EMSURE), toluene (95%, EMSURE), deionized water (DI water, obtained from a Millipore-Q water system) were used for substrates cleaning. Indium tin oxide (ITO) (Singapore optics shop, 101×101×1.1 mm, ITO layer

thickness ~ 180nm, sheet resistance ~ 10Ω sq^{-1}) was used as bottom electrode. A home-built "EGaIn-setup" set-up uses the eutectic metal alloy EGaIn (75.5% Ga and 24.5% In by weight, Sigma-Aldrich) with its surface layer of predominantly Ga_2O_3 (0.7 nm thickness).[62]

5.5.2 Determination of the thickness for polymer brush

Atomic force microscopy (AFM) (JPK instrument, tapping mode in air with cantilever from Tap 300Al-G/Budget Sensors with 40N/m force constant), was used to obtain the polymer brush thickness by measuring the height different across the scratches. In addition, variable angle spectroscopic ellipsometry (V.A.S.E., M190-1700, Digipol) was used as the supplementary technique to verify the thickness. The wavelength range is from 600 nm to 1100 nm, fitting model is built on a 3-layers model: 0.5mm Si wafer (fixed), 4.5 nm SiO_2 layer (fixed), unknown Cauchy layer (measured and fitting thickness), Refractive indices *n* of 1.45 was used for initiator layers, 1.60, 1.60, 1.55 were used for FMMA, FBMA and FNMA polymer brush films, respectively. Three degrees of the incident angle (65°, 70°, and 75°). were measured in one measurement. Thickness measurements were taken at least on three spots on each substrate.

5.5.3 Determination the Fc unit density by cyclic voltammetry (CV)

AUTOLAB PGSTAT302N with NOVA 1.10 software was used for measuring the surface coverage of Fc groups. It consists of a custom built electrochemical cell equipped with a platinum counter electrode, a Ag/AgCl reference electrode and the ITO substrates with polymer brushes served as a working electrode, which was placed in a Faraday cage. Cyclic voltammograms were recorded in an aqueous (aq.) solution 1.0 M $HClO_4$, between -0.5 V to 1.5 V at a scan rate of 1.00 V/s.

5.5.4 UPS measurements

UPS (Thermo Scientific Theta Probe UPS with monochromatic Al Kα X-ray, hv = 21.21 eV) is utilized to monitor the changes in the surface electronic properties of polymer brushes modified ITO samples. Sample size was as small as 0.8 × 0.8 cm^2 and was loaded into the vacuum chamber as quick as possible after rinsing by EtOH and drying by N_2 flow. Ultrahigh vacuum was applied for at least 1 ~ 2 hrs before the measurements. Bare ITO sample was cleaned by basic solution and applied to UV/O_3 plasma for further cleaning. Silane ITO was modified by vapour deposition of silanebromo initiator.

5.5.5 Fabrication of junctions by EGaIn cone-shape tip

Scheme 5.3 shows the home-built "EGaIn-setup". This was applied to contact polymer brush electrically and to measure the J(V) characteristics at room temperature. We collected 14 ~ 16 junctions on two substrates for each sample. Every junction contained 15 ~ 20 J(V) traces (0 V → +1.5 V → 0 V→ -1.5V → 0 V) with a 0.075 V step size and 0.2 s delay.

5.5.6 Fabrication of junctions by EGaIn device

Fabrication of "microfluidic-device junction" with GaO_x/EGaIn filled in a micro-size hole and channels as top electrode was described elsewhere.[63] The PDMS device with its implanted microchannels and its schematic cross section are shown in Figure 5.13. Such device was applied to contact polymer brush electrically and to measure the J(V) characteristics at room temperature or under temperature change. We collected 5 ~ 6 traces (0 V → +3.0 V → 0 V→ -3.0V → 0 V) with a 0.15 V step size and 0.2 s delay on 1 junction for each sample. EGaIn filled device was gently put on polymer brushes

modified ITO substrate. One probe contacted with the EGaIn in device, another probe contacted with ITO susbtrates.

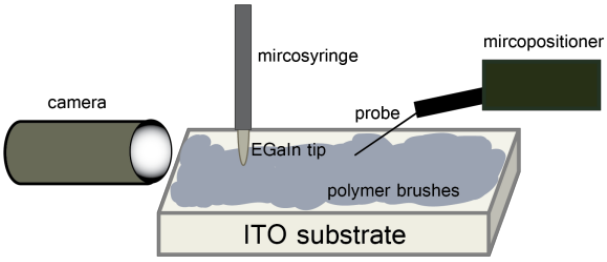

Scheme 5.3 The home-built EGaIn set up with cone-shape tip. Camera was used to magnify the observation scope for the contact. Microsyringe is filled with EGaIn, the probe can be manipulated by mircopositioner.

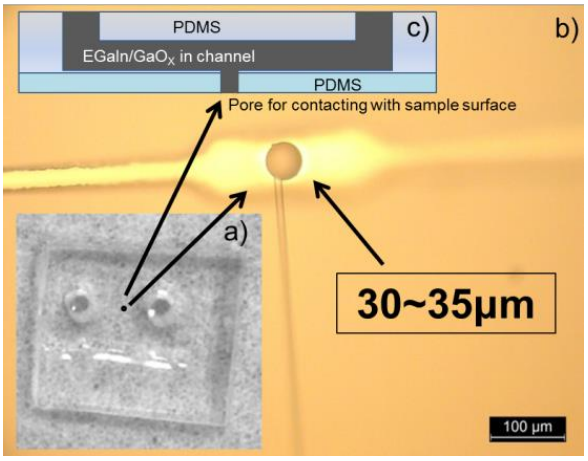

Figure 5.14 a) Top, b) back and c) side views of PDMS device.

5.5.7 Temperature dependent measurements

Based on microfluidic-device, in all of our measurements we biased the GaO_X/EGaIn top electrodes and grounded the ITO bottom electrode. *J* as a function of *V* at different values of temperature on junctions was measured. The temperature dependent measurements (250K – 340K) were conducted with a probe station (model Lakeshore CRX-VF) in vacuum (1×10^{-6} bar). The electrodes were not contacted with the probes during cooling or heating of the devices. At intervals of 10 K we contacted top electrode

and bottom electrode with the probes and recorded one *J*(V) curve while keeping the temperature constant.

5.6 References

1. McCreery, R. L. and Bergren, A. J., *Adv. Mater.* **2009,** *21* (43), 4303-4322.

2. Nerngchamnong, N.; Yuan, L.; Qi, D. C.; Jiang, L.; Thompson, D. and Nijhuis, C. A., *Nat. Nanotechnol.* **2013,** *8* (2), 113-118.

3. Nijhuis, C. A.; Reus, W. F.; Barber, J. R.; Dickey, M. D. and Whitesides, G. M., *Nano Lett.* **2010,** *10* (9), 3611-3619.

4. Nijhuis, C. A.; Reus, W. F. and Whitesides, G. M., *J. Am. Chem. Soc.* **2010,** *132* (51) 18386-18402.

5. Thuo, M. M.; Reus, W. F.; Nijhuis, C. A.; Barber, J. R.; Kim, C.; Schulz, M. D. and Whitesides, G. M., *J. Am. Chem. Soc.* **2011,** *133* (9), 2962-2975.

6. Nitzan, A. and Ratner, M. A., *Science* **2003,** *300* (5624), 1384-1389.

7. Sayed, S. Y.; Fereiro, J. A.; Yan, H.; McCreery, R. L. and Bergren, A. J., *Proc. Natl. Acad. Sci. U. S. A.* **2012,** *109* (29), 11498-11503.

8. Yan, H.; Bergren, A. J.; McCreery, R.; Della Rocca, M. L.; Martin, P.; Lafarge, P. and Lacroix, J. C., *Proc. Natl. Acad. Sci. U. S. A.* **2013,** *110* (14), 5326-5330.

9. Tuccitto, N.; Ferri, V.; Cavazzini, M.; Quici, S.; Zhavnerko, G.; Licciardello, A. and Rampi, M. A., *Nat. Mater.* **2009,** *8* (1), 41-46.

10. Ho Choi, S.; Kim, B. and Frisbie, C. D., *Science* **2008,** *320* (5882), 1482-1486.

11. Orski, S. V.; Fries, K. H.; Sontag, S. K. and Locklin, J., *J. Mater. Chem.* **2011,** *21* (37), 14135-14149.

12. Park, S. H.; Lee, H. S.; Kim, J. D.; Breiby, D. W.; Kim, E.; Park, Y. D.; Ryu, D. Y.; Lee, D. R. and Cho, J. H., *J. Mater. Chem.* **2011,** *21* (39), 15580-15585.

13. Park, K.; Park, S. H.; Kim, E.; Kim, J. D.; An, S. Y.; Lim, H. S.; Lee, H. H.; Kim, D. H.; Ryu, D. Y.; Lee, D. R. and Cho, J. H., *Chem. Mater.* **2010,** *22* (18), 5377-5382.

14. Pinto, J. C.; Whiting, G. L.; Khodabakhsh, S.; Torre, L.; Rodríguez, A.; Dalgliesh, R. M.; Higgins, A. M.; Andreasen, J. W.; Nielsen, M. M.; Geoghegan, M.; Huck, W. T. S. and Sirringhaus, H., *Adv. Funct. Mater.* **2008,** *18* (1), 36-43.

15. Rutenberg, I. M.; Scherman, O. A.; Grubbs, R. H.; Jiang, W.; Garfunkel, E. and Bao, Z., *J. Am. Chem. Soc.* **2004,** *126* (13), 4062-4063.

16. Kim, S. H.; Jang, M.; Yang, H.; Anthony, J. E. and Park, C. E., *Adv. Funct. Mater.* **2011,** *21* (12), 2198-2207.

17. Whiting, G. L.; Snaith, H. J.; Khodabakhsh, S.; Andreasen, J. W.; Breiby, D. W.; Nielsen, M. M.; Greenham, N. C.; Friend, R. H. and Huck, W. T. S., *Nano Lett.* **2006,** *6* (3), 573-578.

18. Snaith, H. J.; Whiting, G. L.; Sun, B.; Greenham, N. C.; Huck, W. T. S. and Friend, R. H., *Nano Lett.* **2005,** *5* (9), 1653-1657.

19. Wei, Y.; Gao, D.; Li, L. and Shang, S., *Polymer* **2011,** *52* (6), 1385-1390.

20. Liu, Y.; Lv, S.; Li, L. and Shang, S., *Synth. Met.* **2012,** *162* (13-14), 1059-1064.

21. Ma, X.; Xie, Z.; Liu, Z.; Liu, X.; Cao, T. and Zheng, Z., *Adv. Funct. Mater.* **2013,** *23* (25), 3239-3246.

22. Azzaroni, O., *J. Polym. Sci., Part A: Polym. Chem.* **2012,** *50* (16), 3225-3258.

23. Caster, K. C., (2005) *Polymer brushes: Synthesis, Characterization, Applications, Chapter 17 Applications of Polymer Brushes and Other Surface-Attached Polymers*. Wiley-VCH Verlag GmbH & Co.; pp 329-370.

24. McCreery, R. L., *Chem. Mater.* **2004,** *16* (20) 4477-4496.

25. Kumar, V.; Jain, S. C.; Kapoor, A. K.; Poortmans, J. and Mertens, R., *J. Appl. Phys.* **2003,** *94* (2), 1283-1285.

26. Anjaneyulu, P.; Sangeeth, C. S. S. and Menon, R., *J. Appl. Phys.* **2010,** *107* (9), 093716.

27. Campbell, A. J.; Bradley, D. D. C. and Lidzey, D. G., *J. Appl. Phys.* **1997,** *82* (12), 6326-6342.

28. Taunk, M. and Chand, S., *J. Appl. Phys.* **2014,** *115* (7), 074507.

29. Diaham, S. and Locatelli, M. L., *Appl. Phys. Lett.* **2012,** *101* (24), 242905.

30. Campbell, A. J.; Weaver, M. S.; Lidzey, D. G. and Bradley, D. D. C., *J. Appl. Phys.* **1998,** *84* (12), 6737-6746.

31. Rose, A., *Phys. Rev.* **1955,** *97* (6), 1538-1544.

32. Valaski, R.; Ayoub, S.; Micaroni, L. and Hümmelgen, I. A., *Thin Solid Films* **2002,** *415* (1–2), 206-210.

33. Weiser, K., *Science* **1970,** *170* (3961), 966-967.

34. Montero, J. M.; Bisquert, J.; Garcia-Belmonte, G.; Barea, E. M. and Bolink, H. J., *Org. Electrons.* **2009,** *10* (2), 305-312.

35. Shao, J. and Wright, G. T., *Solid-State Electron.* **1961,** *3* (3–4), 291-303.

36. Mark, P. and Helfrich, W., *J. Appl. Phys.* **1962,** *33* (1), 205-215.

37. Kao, K. C. and Hwang, W., Philo. Mag. B **1981,** *44* (6), 731-733.

38. Mott, N. F. and Gurney, R. W., *J. Chem. Educ.* **1941**, *18* (5), 249.

39. Jain, S. C.; Geens, W.; Mehra, A.; Kumar, V.; Aernouts, T.; Poortmans, J.; Mertens, R. and Willander, M., *J. Appl. Phys.* **2001,** *89* (7), 3804-3810.

40. Blom, P. W. M.; de Jong, M. J. M. and Vleggaar, J. J. M., *Appl. Phys. Lett.* **1996,** *68* (23), 3308-3310.

41. Jain, S. C.; Kapoor, A. K.; Geens, W.; Poortmans, J.; Mertens, R. and Willander, M., *J. Appl. Phys.* **2002,** *92* (7), 3572-3576.

42. Inganäs, O.; W, Bantikassegn.; *J. Phys. D: Appl. Phys.* **1996,** *29*, 2971.

43.Anta, J. A.; Marcelli, G.; Meunier, M. and Quirke, N., *J. Appl. Phys.* **2002,** *92* (2), 1002-1008.

44. Meunier, M. and Quirke, N., *J. Chem. Phys.* **2000,** *113* (1), 369-376.

45. Meunier, M.; Quirke, N. and Aslanides, A., *J. Chem. Phys.* **2001,** *115* (6), 2876-2881.

46. Lagos, M.; Mahanty, J. and Slusarenko, V., *Surf. Sci.* **1987,** *191* (1–2), 806-812.

47. Reus, W. F.; Nijhuis, C. A.; Barber, J. R.; Thuo, M. M.; Tricard, S. and Whitesides, G. M., *J. Phys. Chem. C* **2012,** *116* (11), 6714-6733.

48. Ahmad, Z., (2012), *Polymer Dielectric Materials. Licensee InTech.*

49. Yan, H.; Huang, Q.; Cui, J.; Veinot, J. G. C.; Kern, M. M. and Marks, T. J., *Adv. Mater.* **2003,** *15* (10), 835-838.

50. Kim, J. S.; Cacialli, F.; Cola, A.; Gigli, G. and Cingolani, R., *Synth. Met.* **2000,** *111–112* (0), 363-367.

51. Hatton, R. A.; Willis, M. R.; Chesters, M. A.; Rutten, F. J. M. and Briggs, D., *J. Mater. Chem.* **2003,** *13* (1), 38-43.

52. Zhu, L.; Tang, H.; Harima, Y.; Yamashita, K.; Aso, Y. and Otsubo, T., *J. Mater. Chem.* **2002,** *12* (8), 2250-2254.

53. Park, Y.; Choong, V.; Gao, Y.; Hsieh, B. R. and Tang, C. W., *Appl. Phys. Lett.* **1996,** *68* (19), 2699-2700.

54. Kugler, T.; Salaneck, W. R.; Rost, H. and Holmes, A. B., *Chem. Phys. Lett.* **1999,** *310* (5–6), 391-396.

55. Kim, J. S.; Lägel, B.; Moons, E.; Johansson, N.; Baikie, I. D.; Salaneck, W. R.; Friend, R. H. and Cacialli, F., *Synth. Met.* **2000,** *111–112* (0), 311-314.

56. Shumate, W. J.; Mattern, D. L.; Jaiswal, A.; Dixon, D. A.; White, T. R.; Burgess, J.; Honciuc, A. and Metzger, R. M., *J. Phys. Chem. B* **2006,** *110* (23), 11146-11159.

57. Chiechi, R. C.; Weiss, E. A.; Dickey, M. D. and Whitesides, G. M., *Angew. Chem.* **2008,** *47* (1), 142-144.

58. Wimbush, K. S.; Fratila, R. M.; Wang, D.; Qi, D.; Liang, C.; Yuan, L.; Yakovlev, N.; Loh, K. P.; Reinhoudt, D. N.; Velders, A. H. and Nijhuis, C. A., *Nanoscale* **2014,** *6* (19), 11246-11258.

59. Fleischer, M. and Meixner, H., *J. Appl. Phys.* **1993,** *74* (1), 300-305.

60. Lorenz, M. R.; Woods, J. F. and Gambino, R. J., *J. Phys. Chem. Solids* **1967,** *28* (3), 403-404.

61. Hosono, H., *Thin Solid Films* **2007,** *515* (15), 6000-6014.

62. Cademartiri, L.; Thuo, M. M.; Nijhuis, C. A.; Reus, W. F.; Tricard, S.; Barber, J. R.; Sodhi, R. N. S.; Brodersen, P.; Kim, C.; Chiechi, R. C. and Whitesides, G. M., *J. Phys. Chem. C* **2012,** *116* (20), 10848-10860.

63. Wan, A.; Jiang, L.; Sangeeth, C. S. S. and Nijhuis, C. A., *Adv. Funct. Mater* **2014,** *24* (28), 4442-4456.

Chapter 6

General Conclusions & Outlook

This Thesis describes the investigation on the mechanism of charge transport across ferrocene-containing polymer brushes, including the generation of polymer brushes with different side chain lengths in a series thickness; the deep electrochemical studies for these polymer brushes; and the electronics characteristics for these polymer brushes.

Chapter 1 gives a short introduction to this Thesis and the Chapter 2 provides a literature overview of the background and applications on functional polymer brushes, and the recent related work on molecular junction research.

In Chapter 3, we described the work on generating Fc-containing polymer brushes with different side chain lengths by SI-ATRP. We simulated the ideal packing model for these polymer brushes followed by estimating the theoretical thickness based the model and surface coverage of Fc groups measured via cyclic voltammetry (CV). Actual thicknesses were verified by two other techniques: ellipsometry and AFM scratch test. Thermal properties for corresponding bulk polymers and mechanical properties for polymer brushes were examined. All the observations indicated that the packing structures were affected by the side chain length, which in turn resulted in different performance on both thermal properties and mechanical properties.

In Chapter 4, we described the work on electrochemistry of Fc-containing polymer brushes with different thickness. By carefully studied the cyclic voltammetry (CV) behaviour of a series polymer brushes, we learned that such polymer brushes are electrochemically stable and the electrochemical process strongly depends on both the

scan rates and the thickness of polymer brushes: the effect of scan rate and polymer brush thickness restricted each other, only at very low scan rates and with small thickness, the electrochemical process showed to reversible behaviour, otherwise, in most of the cases, the electrochemical process was quasi-reversible or irreversible. The kinetic parameters of the electrochemical process for polymer brush show good correlations with brush thickness.

In Chapter 5 we described the work on electronic characteristics for Fc-containing polymer brushes. By applying the polymer brushes with different side chain lengths in a series of thickness to EGaIn junction measurements, we statistically studied the relationship between the brush thickness (L_{PB}) and the rectification ratios (R) and current density (J). We have found that polymer brushes with thinner thicknesses (L_{PB} < 15 nm) did not rectify the current while polymer brushes with larger thicknesses (L_{PB} > 20 nm) did rectify the current at the negative bias. In order to understand this charge transport mechanism, we also conducted temperature dependent J(V) measurements. These measurements allowed us to unravel the mechanism of charge transport: the mechanism of charge transport across this brush is dominated by electrons tunnelling, while that for the thick brush is dominated by electron hopping.

The results presented in this Thesis show the basic understanding on electronic characteristics for Fc-containing polymer brushes either in wet electrochemistry or under EGaIn based junction. Additionally, we simulated the packing of the polymer brushes according to the electrochemistry and proved the effect of different side chain length. This simulation allows us to further understand the relationship between the structure/packing of the polymer brushes and their mechanical properties. One of our major goals is to understand the charge transport properties of the polymer brushes

behaving as electronic components in electronic devices by changing in their chemical structure (side chain length) and thickness. The conclusion we can draw here is that: the side chain length may only affect the polymer brush packing structure but not affect the charge transport properties either in wet electrochemistry or in EGaIn based junction/EGaIn based device. However, the thickness of polymer brush may directly affect the electronic characteristics not only in wet electrochemistry but also in EGaIn based junction/EGaIn based device, and the charge transport mechanism is changing depending on the polymer brushes thickness. This study may promote the investigations on polymer brushes based electronic devices and develop a more efficient and high performance organic devices based on functional, chemical-bonded polymer brushes.

Appendix

1. Monomers and polymers

Monomers, ferrocenylbutly methacrylate (FBMA) and ferrocenylnonyl methacrylate (FNMA) used for ATRP in solution were self-synthesis, whose synthesis routes are shown below. Bulk polymers, polyferrocenylmethyl methacrylate (PFMMA), polyferrocenylbutly methacrylate (PFBMA) and polyferrocenylnonyl methacrylate (PFNMA) generated by ATRP in solution were characterized by ^{1}H NMR. Peak assignments are shown in individual figure.

(1) Synthesis of monomer FBMA

Scheme A1 shows the synthesis route for designed compounds, including the intermediate compounds, (a)-(c). All the synthesis details are described below.

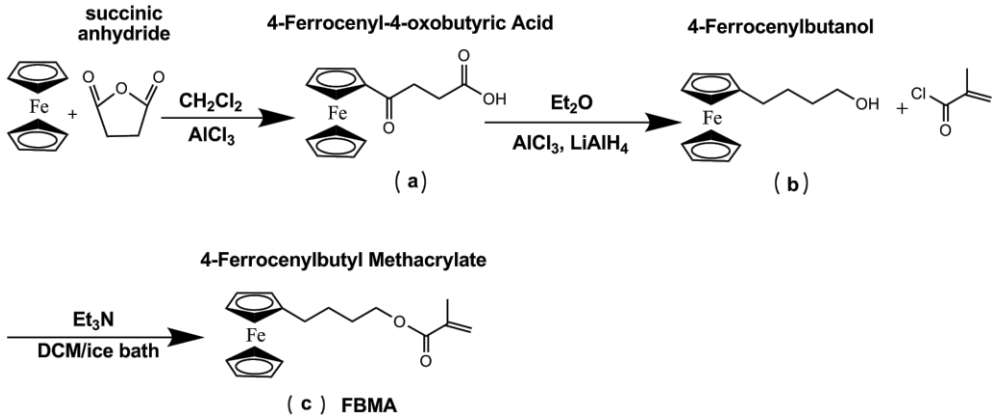

Scheme A1 Synthesis route for monomer FBMA.

Monomer 4-Ferrocenylbutyl methacrylate (FBMA)

4-Ferrocenyl-4-oxobutyric acid (a) 7.44 g (40 mmol) ferrocene was dissolved in 200 mL fresh distilled DCM at room temperature, 2.0 g (20 mmol) succinic anhydride was then added into the solution. 5.8 g (43.5 mmol) anhydrous aluminium chloride ($AlCl_3$)

was dissolve in 50 mL fresh distilled DCM, this suspended solution was then added into the mixture of ferrocene and anhydride solution by pressure equalizing funnel. The mixture changed color from orange to violet upon addition of anhydrous $AlCl_3$ suspension. After sufficiently stirring for 3 h at room temperature, the reaction was quenched by pulling into the ice water. The orange colored organic layer was extracted by anhydrous ether, dried over $MgSO_4$ and concentrated. The desired compound could be isolated by column chromatography over silica gel with DCM/Methanol (98:2) as eluent. The yield was 48% for a reddish brown solid.

^{1}H NMR (300 MHz, $CDCl_3$, 25 ℃): δ 4.82 (t, 2H), 4.53 (t, 2H), 4.24 (s, 5H), 3.10 (t, 2H), 2.76 (t, 2H);

^{13}C NMR (75.5 MHz, DMSO, 25 ℃): δ 201.66 (1C), 173.90 (1C), 78.51 (2C), 71.87 (2C), 69.51 (1C), 68.86 (1C), 33.74 (1C), 27.42 (1C);

MS (ESI): m/z 285 (100%) [M^-]; m/z 287 (100%) [M^+].

4-Ferrocenylbutanol (b) To a suspension of 3.8 g (100 mmol) lithium aluminium hydride ($LiAlH_4$) in 200 mL anhydrous ether was added 8.3 g (62 mmol) anhydrous $AlCl_3$, also suspended in 100 mL anhydrous ether, under nitrogen, at room temperature. 2.86 g (10 mmol) **a** was added into the above suspension and additional 1 g (7.5 mmol) anhydrous $AlCl_3$ was added over a 5 min interval. The reaction mixture was stirred for 30 min at room temperature and refluxed for 3 h. The reaction was quenched by adding ice water and then 6.0 mol/L H_2SO_4 solution to the cooled reaction. The mixture was extracted with anhydrous ether, dried over $MgSO_4$ and solvent removal afforded crude product as a yellowish oil. Desirable compound could be purified by flashing a silica gel column with hexane/ethyl acetate (4:1) as eluent. The isolated yield was 87%.

^{1}H NMR (300 MHz, $CDCl_3$, 25 ℃): δ 4.10 (s, 5H), 4.06 (s, 2H), 4.04 (s, 2H), 3.65 (t, 2H), 2.37 (t, 2H), 1.60, 1.58 (m, 4H);

^{13}C NMR (75.5 MHz, $CDCl_3$, 25 ℃): δ 89.02 (1C), 68.47 (5C), 68.06 (2C), 67.08 (2C), 62.80 (1C), 32.62 (1C), 29.37 (1C), 27.25 (1C);

MS (ESI): m/z 258 (100%) [M^+].

4-Ferrocenylbutyl methacrylate (c) 3.9 g (15 mmol) **b** and 4.0 equiv. of triethylamine (Et_3N) were dissolved in fresh distilled DCM with constant stirring in flask in an ice bath, and 1.3 equiv. of methacryloyl chloride in fresh distilled DCM was added dropwise via a pressure equalizing funnel. After 2 h of stirring at 0 ºC the reaction mixture was filtered and the precipitate was washed with anhydrous ether. The combined ethereal solution was washed with 20% aqueous sodium bicarbonate solution (aq. $NaHCO_3$), 20% sodium chloride solution (aq. NaCl), and DI water, and dried over anhydrous sodium sulfate (Na_2SO_4), then filtered. Filtrate was then concentrated to dryness, the crude product was purified by column chromatography on silica gel using hexane/ethyl acetate (20:1) as eluent. The isolated yield was 54% of orange viscous oil.

^{1}H NMR (300 MHz, $CDCl_3$, 25 ℃): δ 6.10 (s, 1H), 5.55 (s, 1H), 4.16 (t, 2H), 4.10 (s, 5H), 4.07 (s, 2H), 4.06 (s, 2H), 2.36 (t, 2H), 1.95 (s, 3H), 1.71, 1.61 (m, 4H);

^{13}C NMR (75.5 MHz, $CDCl_3$, 25 ℃): δ 167.49 (1C), 136.49 (1C), 125.18 (1C), 88.74 (1C), 68.44 (5C), 68.02 (2C), 67.10 (2C), 64.52 (1C), 29.15 (1C), 28.48 (1C), 27.45 (1C), 18.31 (1C);

MS (ESI): m/z 326 (100%) [M^+], 327 (30%) [M^+].

(2) Synthesis of monomer FNMA

Scheme A2 shows the synthesis route for designed compounds, including the intermediate compounds, (a)-(g). All the synthesis details will be described in the next section.

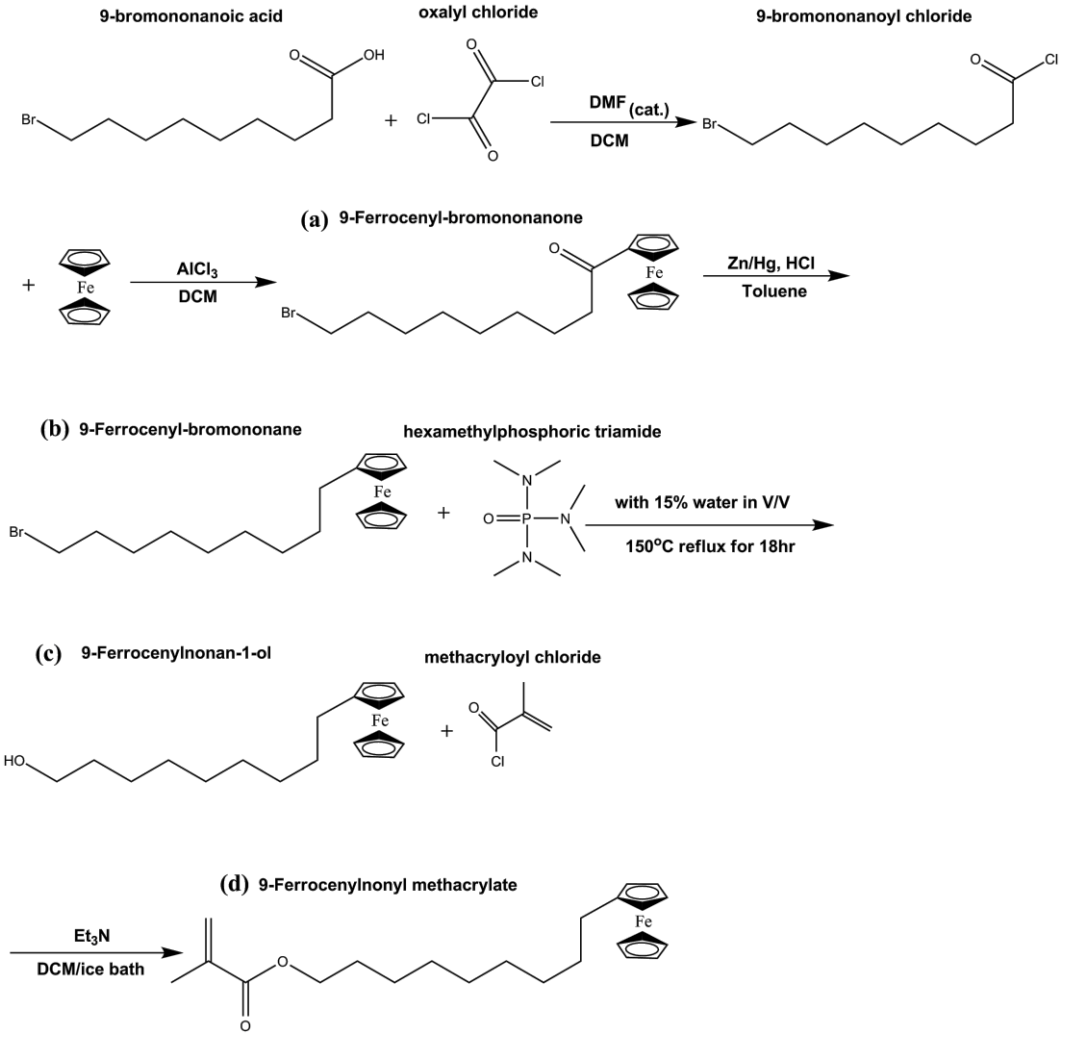

Scheme A2 Synthesis route for monomer FNMA.

Monomer 9-Ferrocenylnonyl methacrylate (FNMA)

9-Ferrocenyl-bromononanone (a) 9-Ferrocenyl-bromononanone was prepared via Friedel-Crafts acylation of ferrocene with 9-bromononanoyl chloride, which, in turn, was prepared in situ from 9-bromononanoic acid. 10 g (42.2 mmol) 9-bromononanoic acid reacted with 13.3 g (105.5 mmol) oxalyl chloride 13.3 g (105.5 mmol) and 0.10 mL (1.34 mmol) in fresh distilled DCM for 40 min at room temperature under Nitrogen atmosphere followed by removal of the volatiles in vacuum. The in situ generated 9-bromononanoyl chloride was used in the next step without further purification. To a solution of 10.8 g (42.2 mmol) 9-bromononanoyl chloride in 500 mL fresh distilled

DCM was added 7.9 g (42.2 mmol) ferrocene and 5.6 g (42.2 mmol) anhydrous $AlCl_3$ under Nitrogen protection. The reaction mixture was stirred for 4 h in ice bath (0°C), followed by quenching with ice water. The dark red organic layer was then extracted from the reaction mixture by anhydrous ether, dried over $MgSO_4$ and concentrated. The desired compound could be isolated by column chromatography over silica gel with hexane/ethyl acetate (8:1) as eluent. The isolated yield was 60%.

^{1}H NMR (300 MHz, $CDCl_3$, 25 ℃): δ 4.78 (t, 2H), 4.49 (t, 2H), 4.19 (s, 5H), 3.41 (t, 2H), 2.69 (t, 2H), 1.88, 1.83 (m, 2H), 1.72, 1.67 (m, 2H), 1.46, 1.36 (m, 8H);

^{13}C NMR (75.5 MHz, $CDCl_3$, 25 ℃): δ 204.61 (1C), 79.16 (1C), 72.09 (2C), 69.72 (5C), 69.31 (2C), 39.68 (1C), 34.02 (1C), 32.77 (1C), 29.41 (1C), 29.31 (1C), 28.62 (1C), 28.11 (1C), 24.52 (1C);

MS (ESI): m/z 406 (100%) [M^+].

9-Ferrocenyl-bromononane (b) Freshly prepared zinc-mercury amalgam was used for the Clemmensen reduction of the carbonyl group. 16.8 g (260 mmol) Zn granules and 1.17 g (40 mmol) mercury (II) chloride ($HgCl_2$) were added to 300 mL toluene followed by the addition of 100 mL water and 12.0 mol/L 50 mL aqueous hydrochloric acid (aq. HCl). Then 7 g (17.3 mmol) **a** was added to this two-phase mixture, and refluxed for overnight (12 h) while the reaction mixture was vigorously stirred. The reaction mixture was allowed to cool down to room temperature, the organic layer was extracted with anhydrous ether, dried over $MgSO_4$. Solvent removal yielded an orange oil. The crude product could be purified by column chromatography over silica gel with hexane/ethyl acetate (100:1) as eluent. The isolated yield was 82%.

^{1}H NMR (300 MHz, $CDCl_3$, 25 ℃): δ 4.10 (s, 5H), 4.06 (s, 2H), 4.04 (s, 2H), 3.41 (t, 2H), 2.31 (t, 2H), 1.87, 1.84 (m, 2H), 1.49, 1.28 (m, 12H);

^{13}C NMR (75.5 MHz, $CDCl_3$, 25 ℃): δ 89.54 (1C), 68.46 (5C), 68.05 (2C), 66.99 (2C), 34.00 (1C), 32.81 (1C), 31.08 (1C), 29.56 (2C), 29.38 (2C), 28.73 (1C), 28.15 (1C);

MS (ESI): m/z 390 (100%) [M^+].

9-Ferrocenylnonan-1-ol (c) 5.60 g (14.3 mmol) **b** was dissolved in 50 mL (244 mmol) hexamethylphosphoric triamide (HMPA) aqueous solution (with 15% water in V/V). The reaction was refluxed at 150 °C for 8 h. After cooling the reaction mixture to room temperature, the orange organic layer was extracted by anhydrous ether and dried over $MgSO_4$. Solvent removal yielded an orange oil. The crude product could be purified by flashing a silica gel column with hexane/ethyl acetate (4:1) as eluent. The isolated yield was 85%.

^{1}H NMR (300 MHz, $CDCl_3$, 25 ℃): δ 4.10 (s, 5H), 4.06 (s, 2H), 4.04 (s, 2H), 3.65, 3.62 (q, 2H), 2.30 (t, 2H), 1.51, 1.30 (m, 14H);

^{13}C NMR (75.5 MHz, $CDCl_3$, 25 ℃): δ 89.66 (1C), 68.52 (5C), 68.11 (2C), 67.04 (2C), 63.06 (1C), 32.78 (1C), 31.09 (1C), 29.56 (3C), 29.44 (2C), 25.72 (1C);

MS (ESI): m/z 328 (100%) [M^+], 329 (20%) [M^+].

9-Ferrocenylnonyl methacrylate (d) 1.7 g (5.2 mmol) **c** and 4.0 equiv. of triethylamine (Et_3N) were dissolved in fresh distilled DCM with constant stirring in flask in an ice bath, and 1.3 equiv. of methacryloyl chloride in fresh distilled DCM was added dropwise via a pressure equalizing funnel. After 2 h of stirring at 0 ºC the reaction mixture was filtered and the precipitate was washed with anhydrous ether. The combined ethereal solution was washed with 20% aqueous sodium bicarbonate solution (aq. $NaHCO_3$), 20% sodium chloride solution (aq. NaCl), and DI water, and dried over anhydrous sodium sulfate (Na_2SO_4), then filtered. Filtrate was then concentrated to dryness, the crude product was purified by column chromatography on silica gel using hexane/ethyl acetate (25:1) as eluent. The isolated yield was 48% of orange viscous oil.

^{1}H NMR (300 MHz, $CDCl_3$, 25 ℃): δ 6.10 (s, 1H), 5.54 (s, 1H), 4.14 (t, 2H), 4.09 (s, 5H), 4.05 (s, 2H), 4.03 (s, 2H), 2.31(t, 2H), 1.95 (s, 3H), 1.68, 1.64 (m, 2H), 1.48, 1.46 (m, 2H), 1.37, 1.30 (m, 10H);

^{13}C NMR (75.5 MHz, $CDCl_3$, 25 ℃): δ 167.55 (1C), 136.56 (1C), 125.11 (1C), 89.55 (1C), 68.45 (5C), 68.05 (2C), 66.98 (2C), 64.81 (1C), 31.11 (1C), 29.59 (2C), 29.46 (2C), 29.23 (1C), 28.60 (1C), 25.97 (1C), 18.33 (1C);

MS (ESI): m/z 396 (100%) [M^+], 397 (28%) [M^+].

(3) ^{1}H NMR of PFMMA

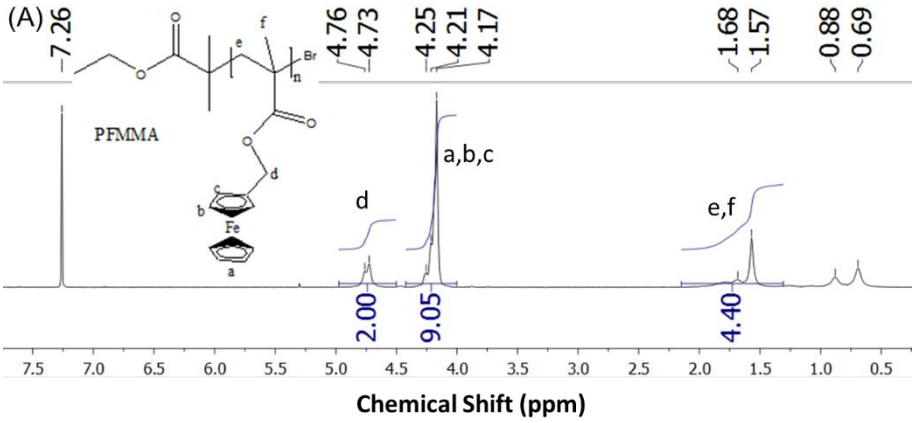

Figure A1 ^{1}H NMR spectrum by $CDCl_3$ for PFMMA bulk polymer.

(4) ^{1}H NMR of PFBMA

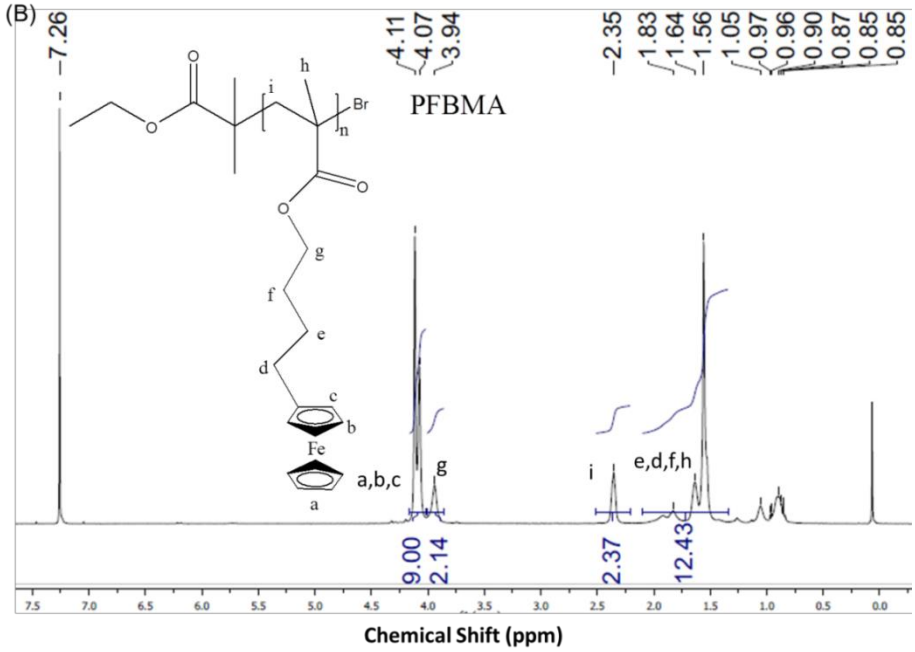

Figure A2 ^{1}H NMR spectrum by $CDCl_3$ for PFBMA bulk polymer.

(5) ^{1}H NMR of PFNMA

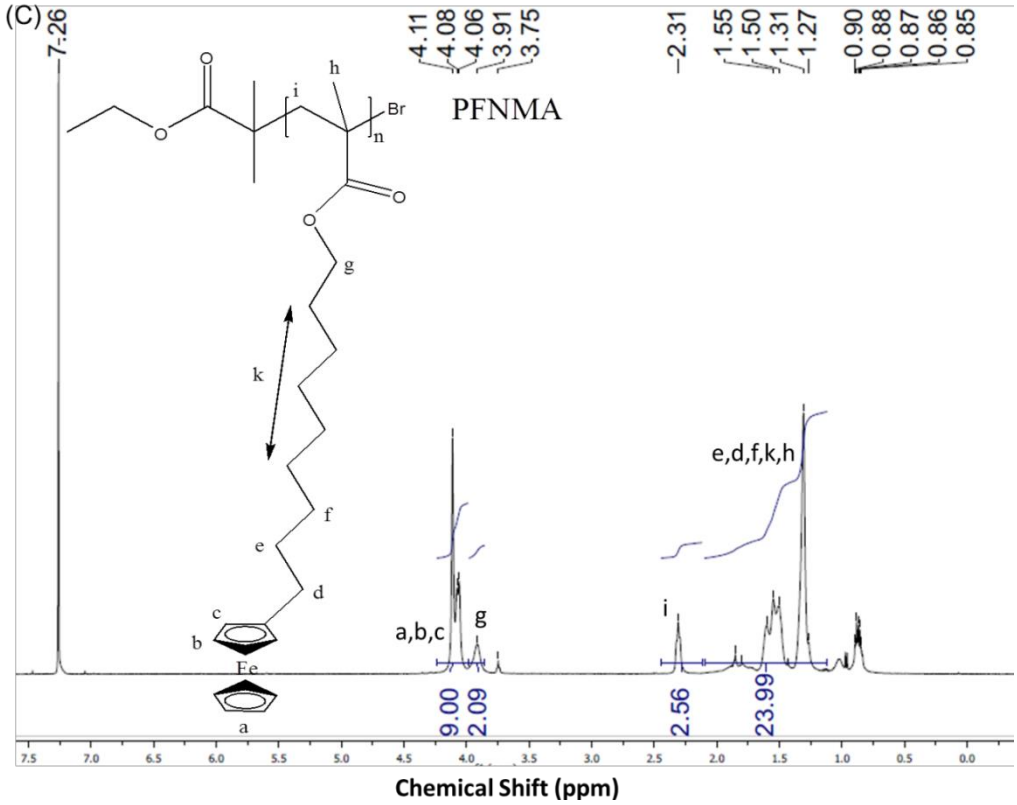

Figure A3 ^{1}H NMR spectrum by $CDCl_3$ for PFNMA bulk polymer.

All isolated bulk polymers were dried in vacuum oven at 40 ºC overnight, yielding yellow solids. We observed the expected characteristic peaks from each species, such as the proton peaks of ferrocene and proton peaks of alkyl side chain. In stoichiometric, absolute pure bulk polymers have the ratios of peak integral are 2 : 5 (peak d *vs* peak e, f in Figure A1), 2 : 2 (peak g *vs* peak i in Figure A2), and 2 : 2 (peak g *vs* peak i in Figure A3) for PFMMA, PFBMA and PFNMA polymers, respectively. Experimentally, the observed ratios are 2.00 : 4.40, 2.14 : 2.37, and 2.09 : 2.56, respectively, indicating that the isolate polymer are about 90% pure.

2. Ellipsometry data related to thickness correlation plots

The wavelength range is from 600 nm to 1100 nm, fitting model is built on a 3-layers model: 0.5mm Si wafer (fixed), 4.5 nm SiO_2 layer (fixed), unknown Cauchy layer (measured and fitting thickness), Refractive indices *n* of 1.45 was used for initiator layers, 1.60, 1.60, 1.55 were used for FMMA, FBMA and FNMA polymer brush films, respectively. Three degrees of the incident angle (65°, 70°, and 75°). were measured in one measurement. Thickness measurements were taken at least on three spots on each substrate.

(1) PFMMA brush with thickness ranges from 2 nm to 40 nm

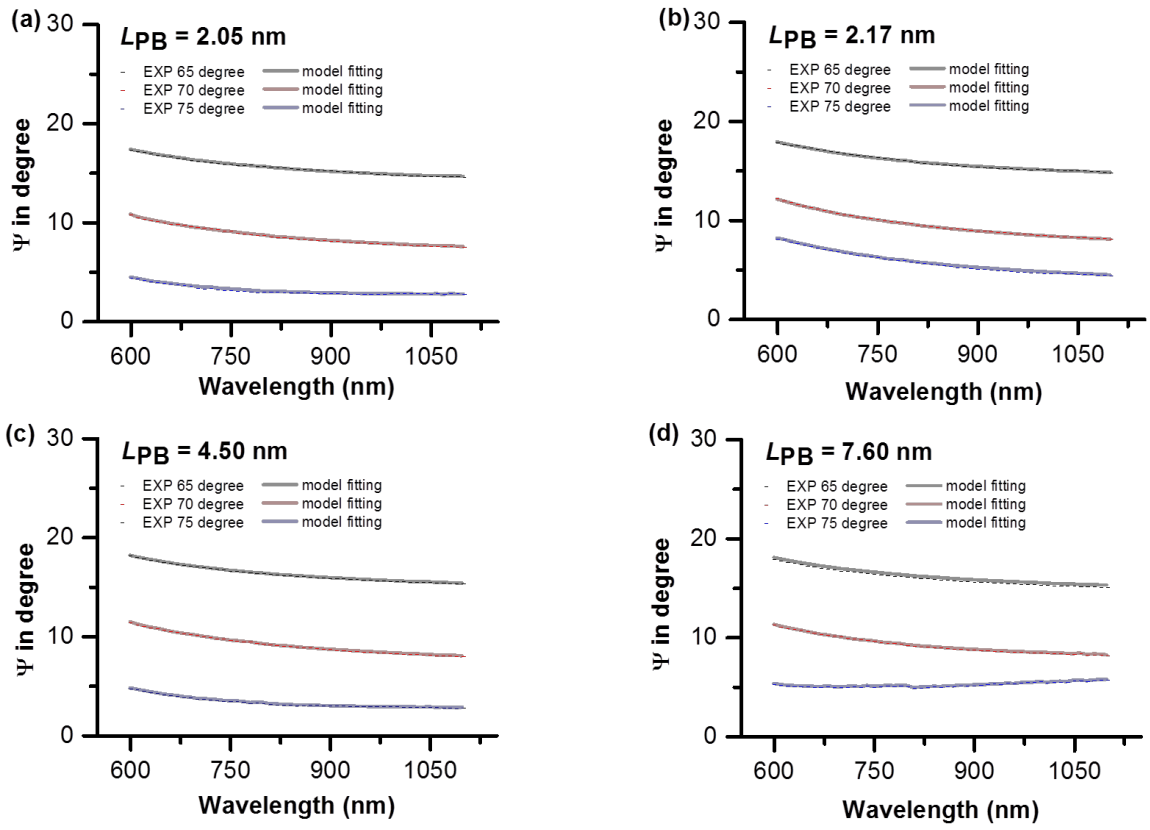

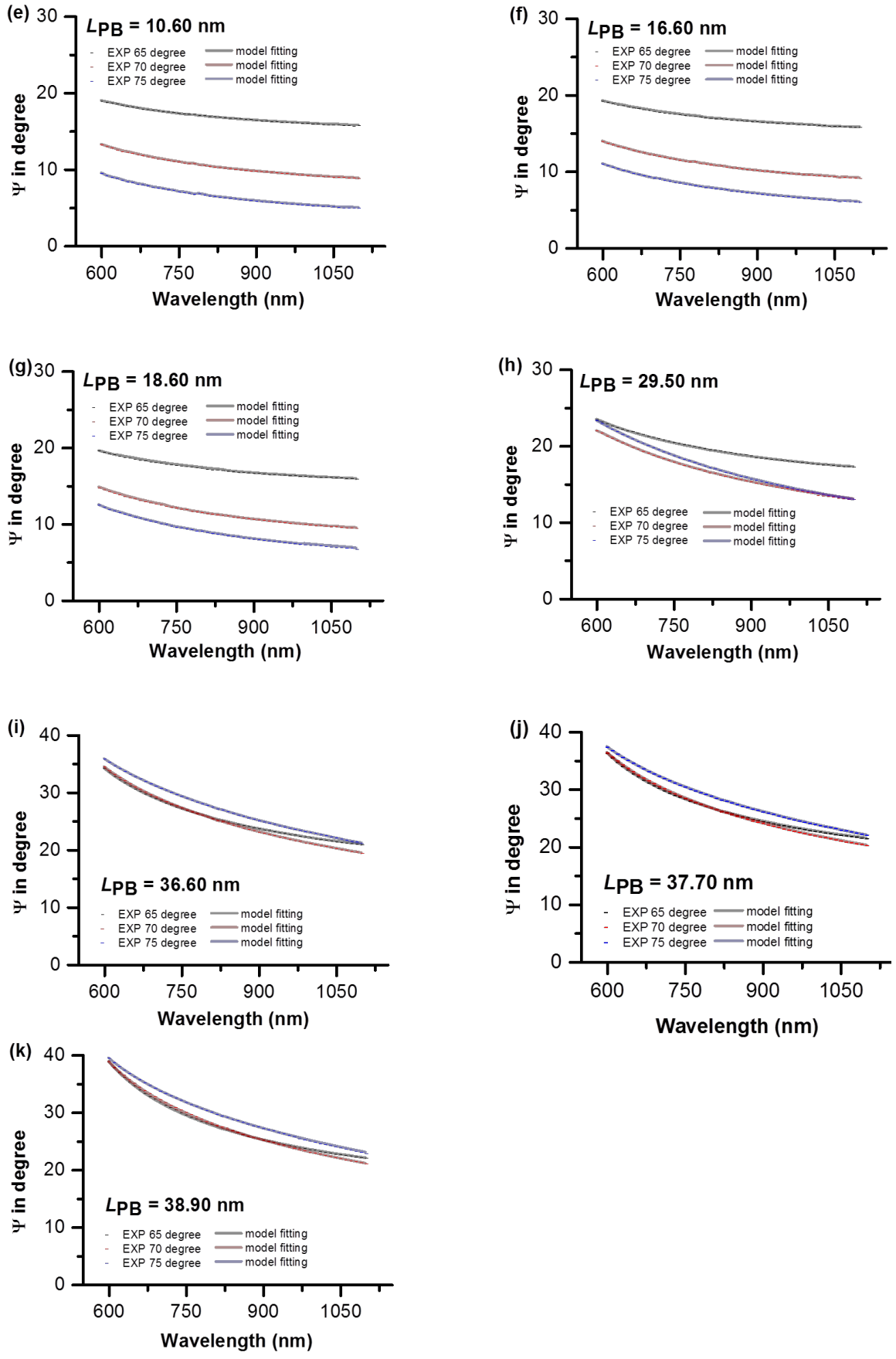

Figure A4 Ellipsometry data for samples shown in Figure 3.15(A).

(2) PFBMA brush with thickness ranges from 4 nm to 32 nm

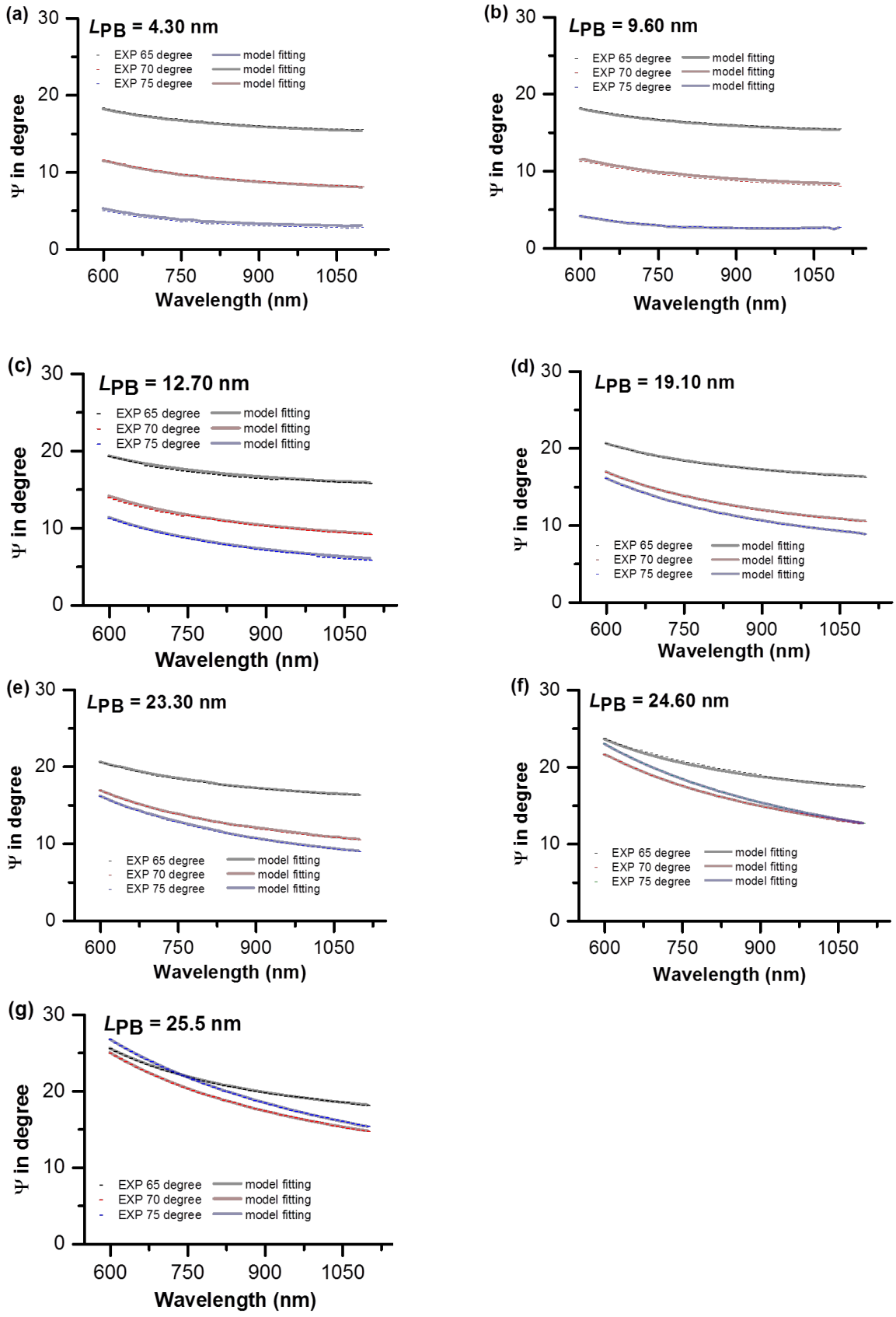

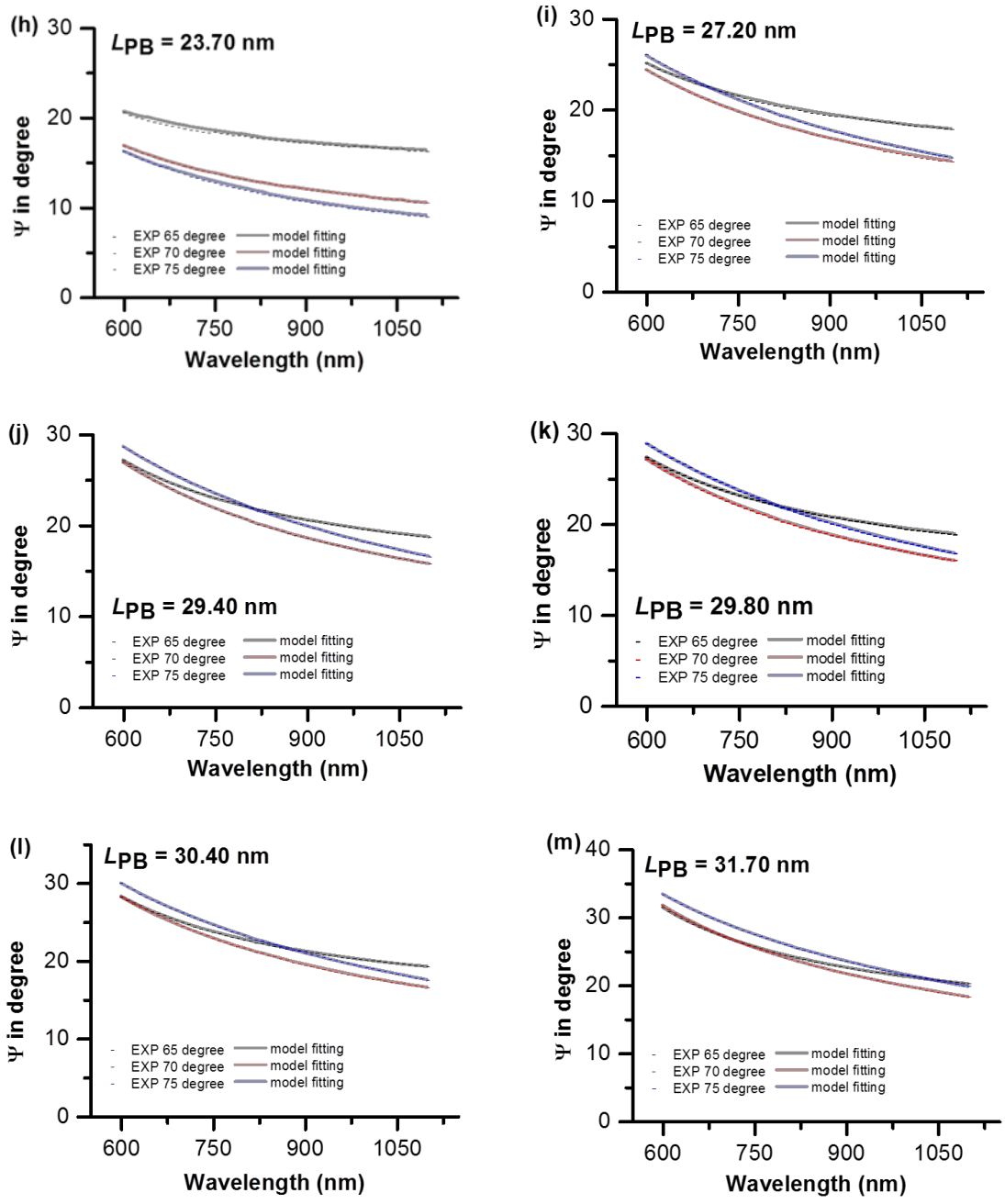

Figure A5 Ellipsometry data for samples shown in Figure 3.15(B).

(3) PFNMA brush with thickness ranges from 4 nm to 31 nm

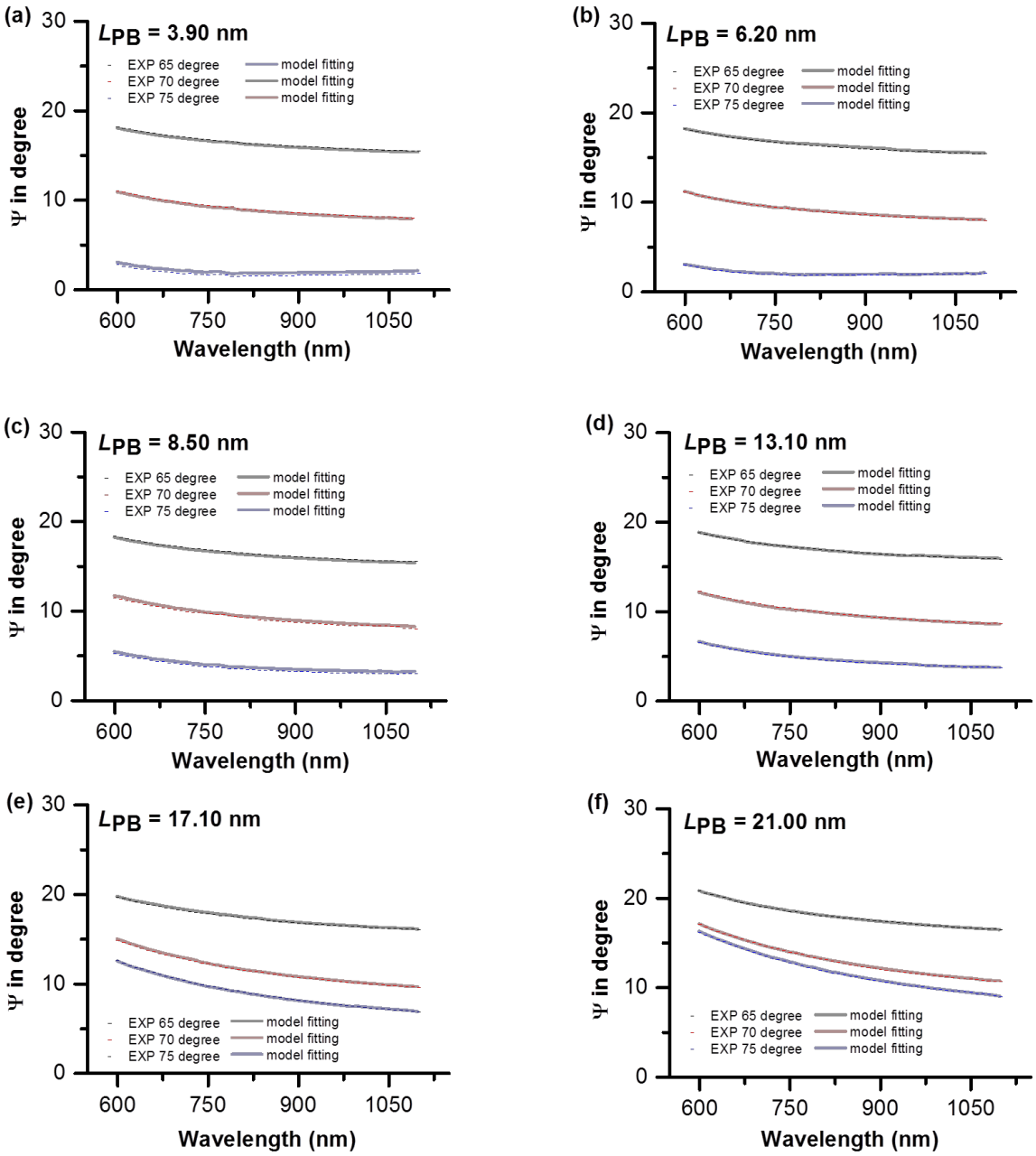

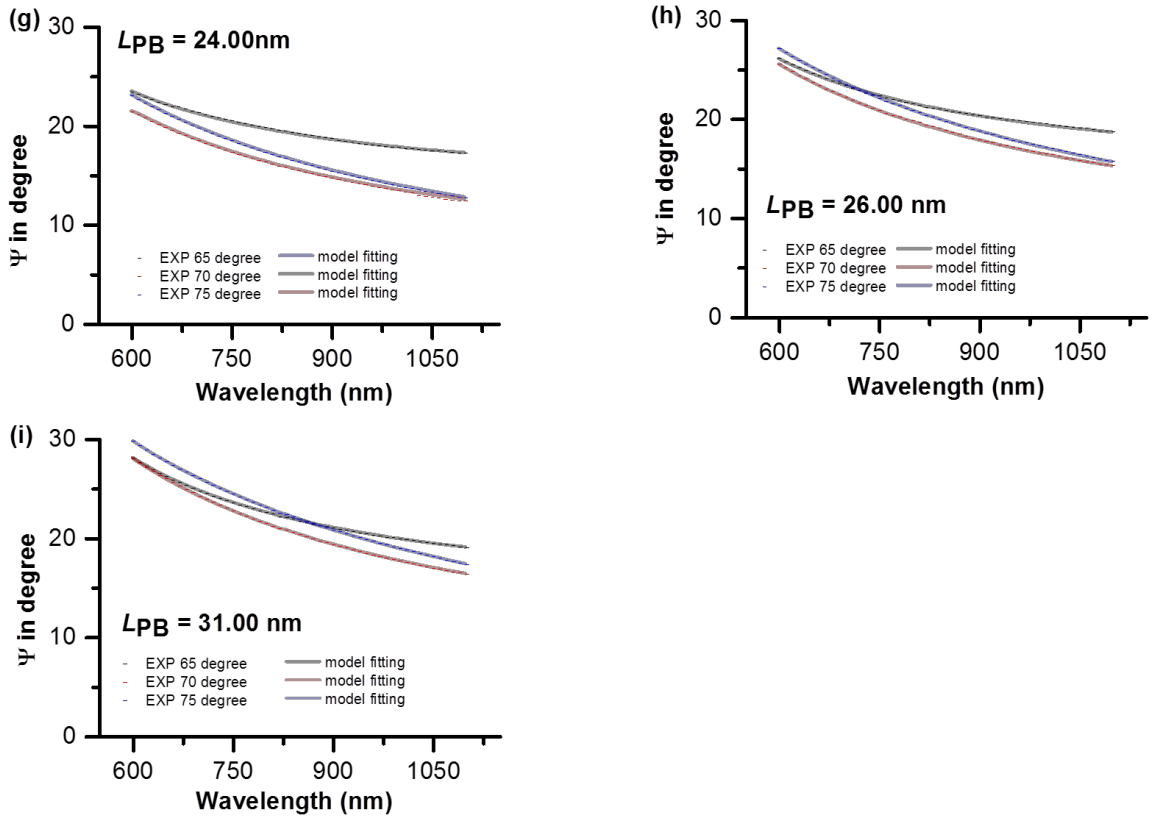

Figure A6 Ellipsometry data for samples shown in Figure 3.15(C).

3. Cyclic voltammograms related to thickness correlation plots

AUTOLAB PGSTAT302N with NOVA 1.10 software was used for measuring the surface coverage of Fc groups by CV, as well as the total number of Fc groups in polymer brush. Furthermore, based on the simple packing model, we were able to estimate the average number of Fc groups per brush chain. These numbers help to build the theoretical thickness plot. Cyclic voltammograms were recorded in an aqueous (aq.) solution 1.0 M $HClO_4$, between -0.5 V to 1.5 V at a scan rate of 1.00 V/s.

(1) PFMMA brush, number of Fc groups per brush increases as the polymerization time, and the maximum value is below 500

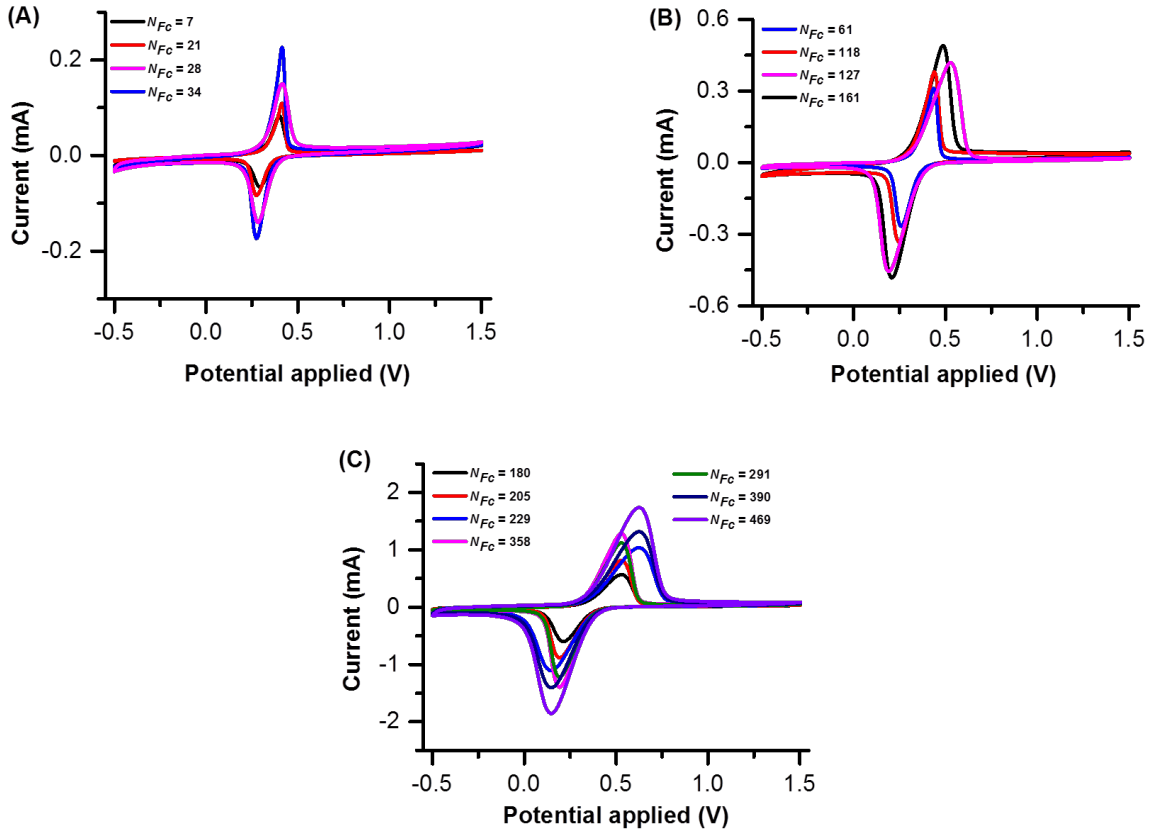

Figure A7 CV data for building theoretical thickness plot shown in Figure 3.15(A).

(2) PFBMA brush, number of Fc groups per brush increases as the polymerization time, and the maximum value is below 500

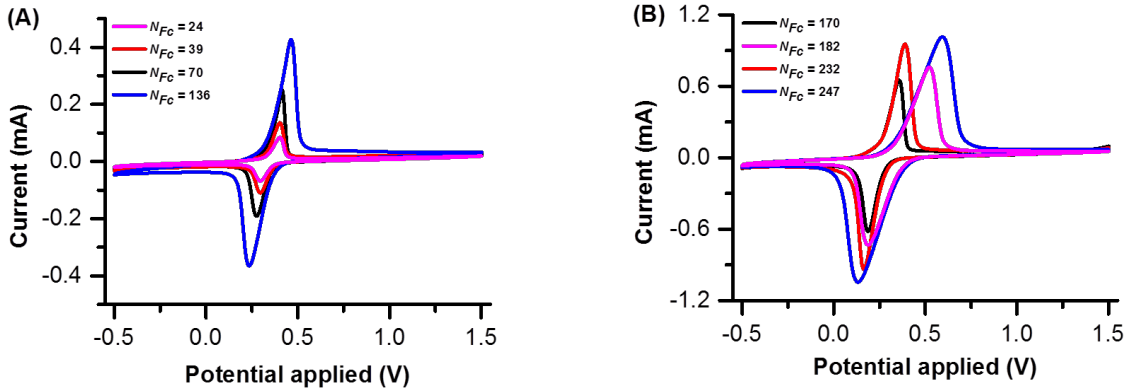

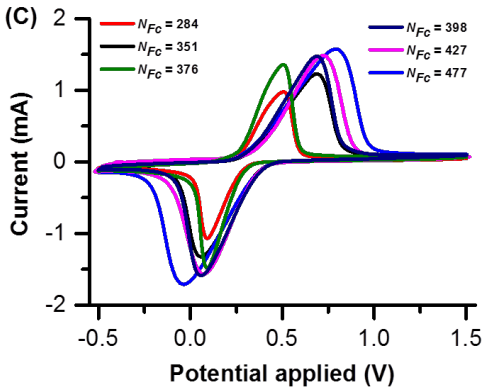

Figure A8 CV data for building theoretical thickness plot shown in Figure 3.15(B).

(3) PFNMA brush, number of Fc groups per brush increases as the polymerization time, and the maximum value is below 500.

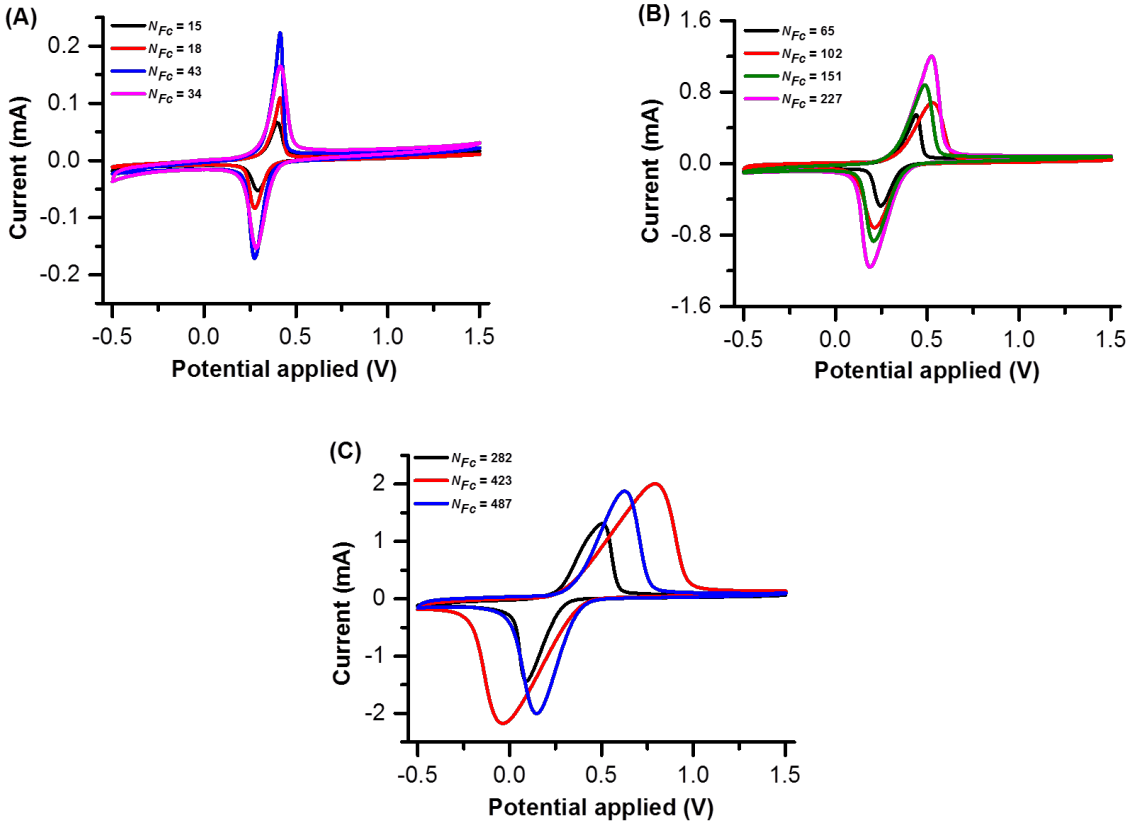

Figure A9 CV data for building theoretical thickness plot shown in Figure 3.15(C).

4. Influence of scan rates in cyclic voltammograms for PFBMA and PFNMA representative polymer brushes

In this section, we studied the scan rates dependent for relatively thicker polymer brush of PFBMA (L_{PB} = 48 nm) and PFNMA (L_{PB} = 40 nm) in 1.0 M $HClO_4$ electrolyte with a series of scan rates. The corresponding CV plots on the dependence of scan rates were presented in Figure A10 and Figure A12. Figure A11 and Figure A13 summarize the voltammetric parameters plotted on the dependence of scan rates.

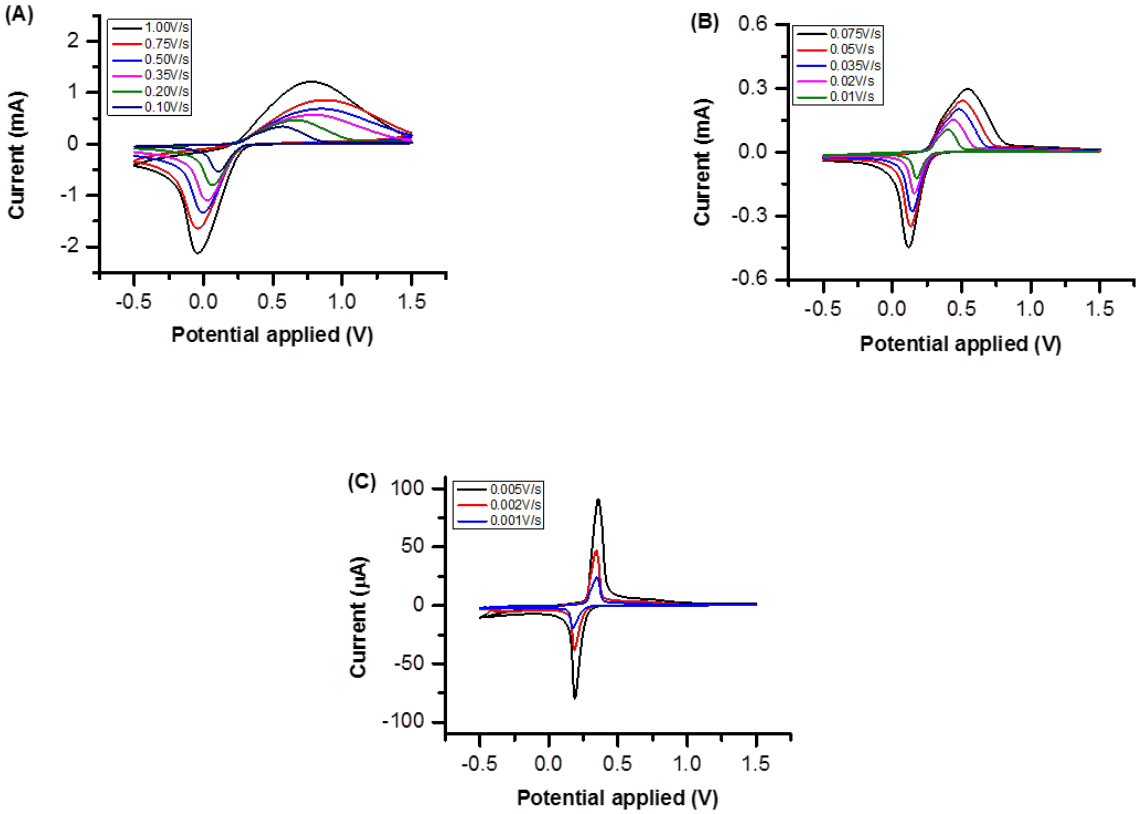

Figure A10 Stacked cyclic voltammograms of a representative PFBMA brush sample with large thickness (~48 nm) as the function of scan rates.

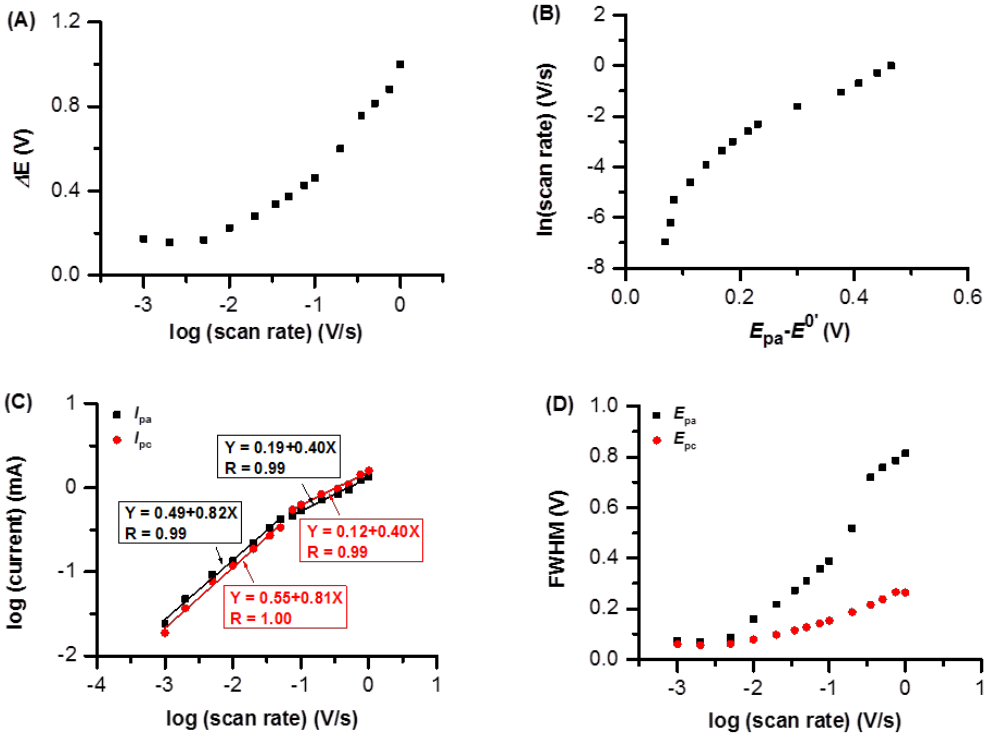

Figure A11 Plots of voltammetric parameters as the function of scan rates. (A) log(scan rates) *vs.* peak-to-peak separation (ΔE). (B) Peak potential (E_{pa}-$E^{0'}$) *vs.* ln(scan rates). (C) log(scan rates) *vs.* log(I_{pa}) and log(I_{pc}). (D) log(scan rate) *vs.* full width at half maximum (FWHM). Solid lines are fitting lines.

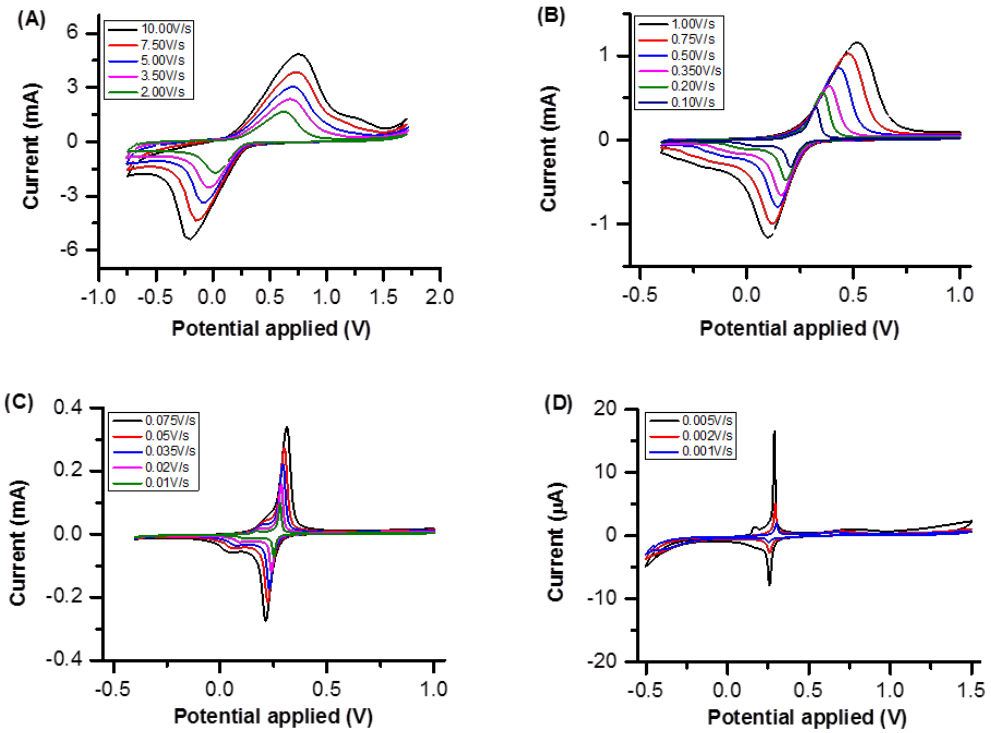

Figure A12 Stacked cyclic voltammograms of a representative PFNMA brush sample with large thickness (~40 nm) as the function of scan rates.

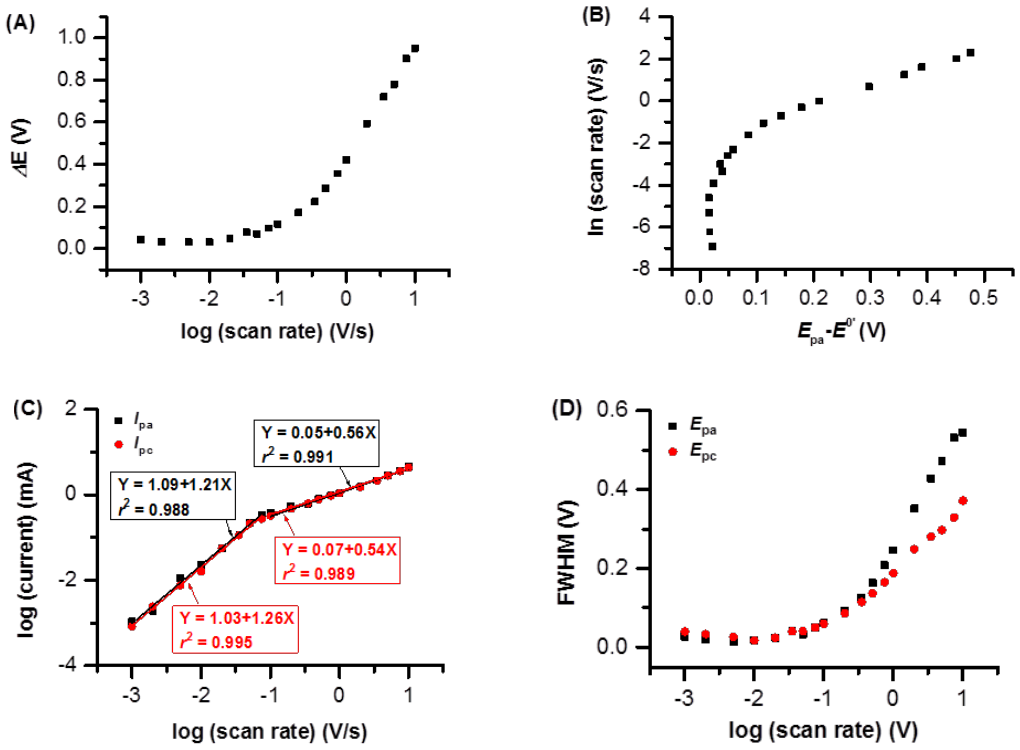

Figure A13 Plots of voltammetric parameters as the function of scan rates. (A) log(scan rates) *vs.* peak-to-peak separation (ΔE). (B) Peak potential (E_{pa}-$E^{0'}$) *vs.* ln(scan rates). (C) log(scan rates) *vs.* log(I_{pa}) and log(I_{pc}). (D) log(scan rate) *vs.* full width at half maximum (FWHM). Solid lines are fitting lines.

5. Statistical junction for PFMMA, PFBMA, and PFNMA brushes with systematic thickness

In the *J*(V) measurements, one trace ≡ 0 V → +1.5 V → 0 V→ -1.5V →0 V. The log average values of *J* for each potential where *J* was measured were determined and were used to construct the log-average *J*(V) curves. Figure A1, A2, and A3 show the log-average *J*(V) curves, together with the histograms of the values of *R* (= |*J*(-1.5V)|/|*J*(+1.5V)|) with a Gaussian fit to these histograms.

(1) PFMMA brushes (2 nm ~ 41 nm)

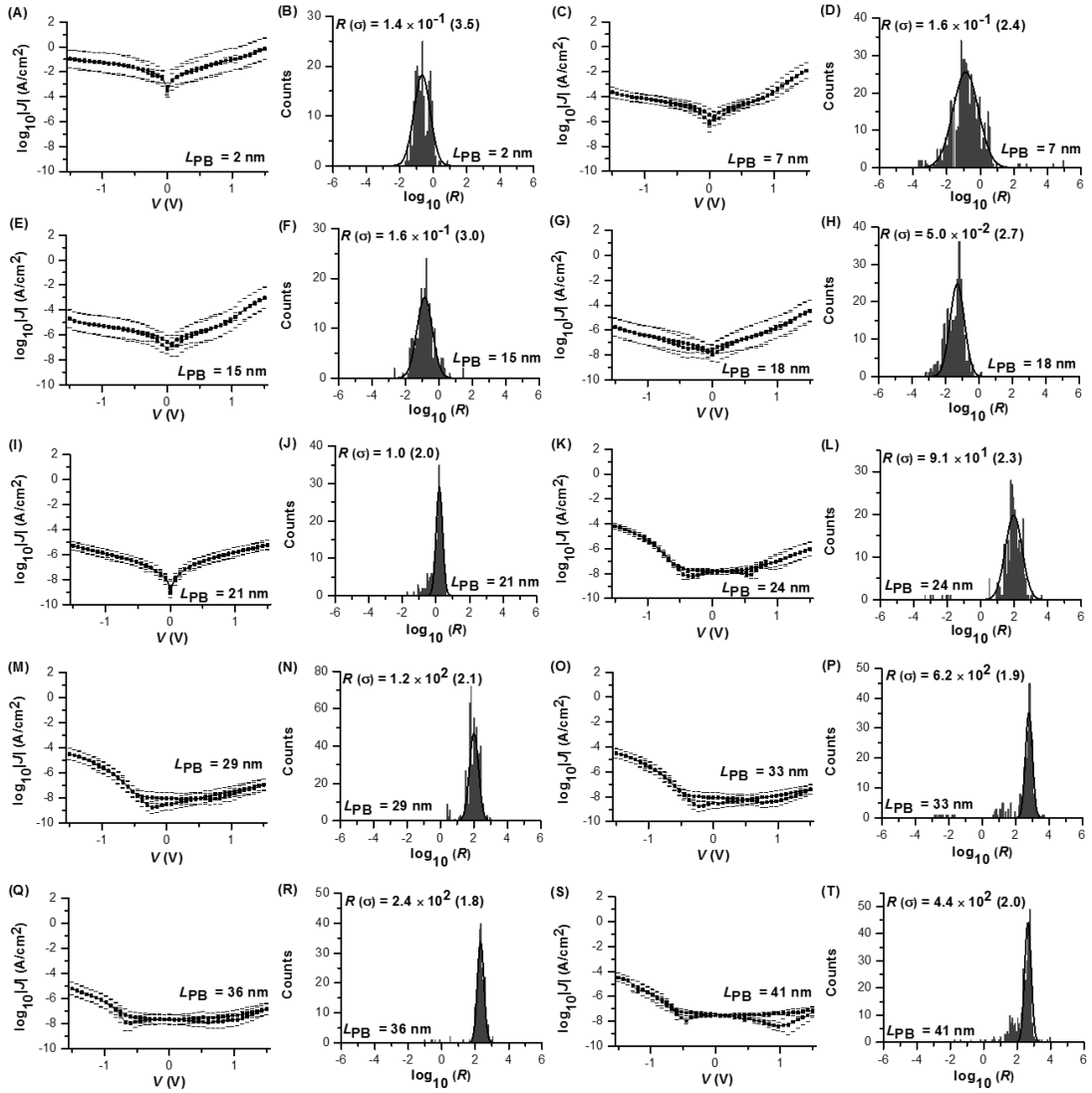

Figure A14 The average $\log_{10}|J|$ curves of ITO – PFMMA brush // GaO_x / EGaIn junctions and histograms of the values of R (= $|J(-1.5V)|/|J(+1.5V)|$) with a Gaussian fit to these histograms. L_{PB} stands for the thickness of PFMMA brush, and σ in parentheses stands for the standard deviation.

(2) PFBMA brushes (2 nm ~ 38 nm)

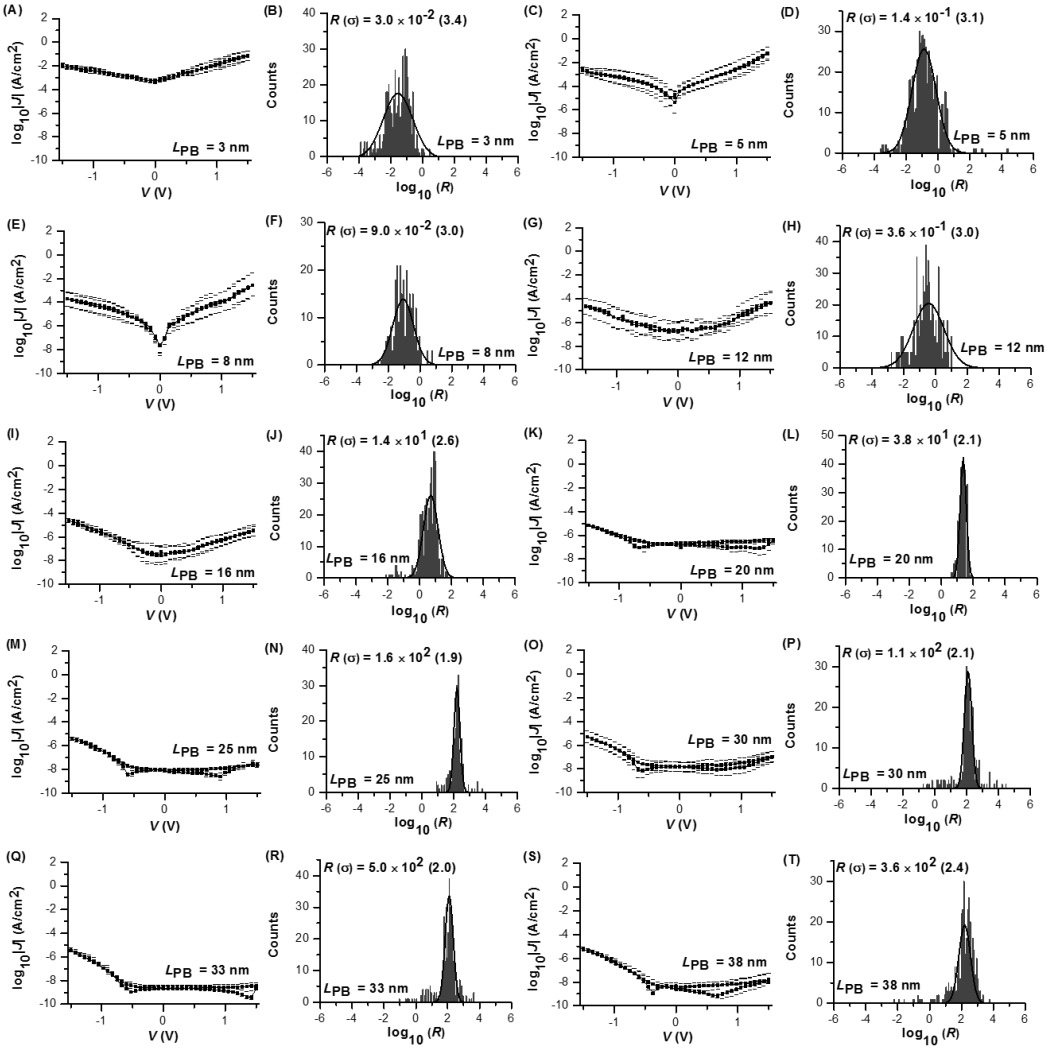

Figure A15 The average $\log_{10}|J|$ curves of ITO – PFBMA brush // GaO_x / EGaIn junctions and histograms of the values of R (= $|J(-1.5V)|/|J(+1.5V)|$) with a Gaussian fit to these histograms. L_{PB} stands for the thickness of PFBMA brush, and σ in parentheses stands for the standard deviation.

(3) PFNMA brushes (2 nm ~ 36 nm)

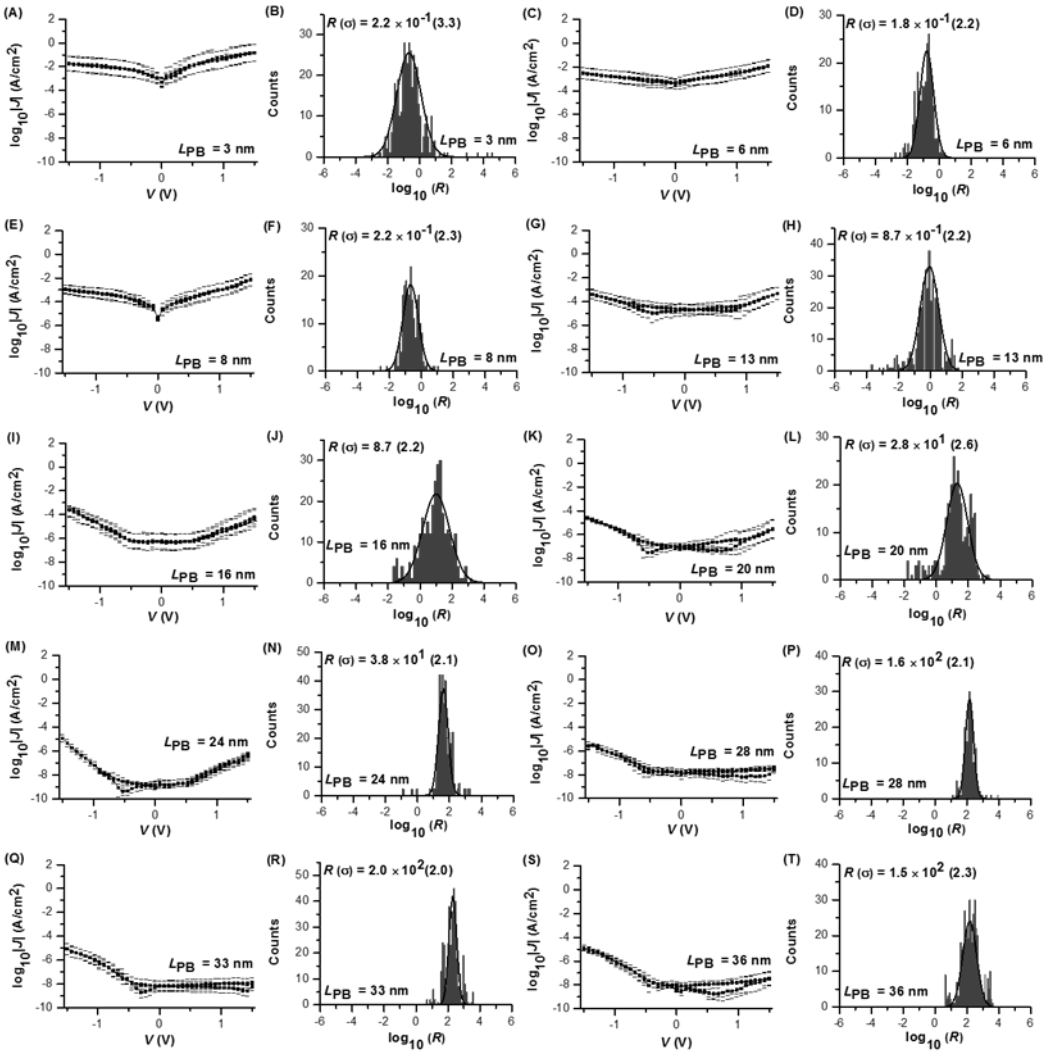

Figure A16 The average $\log_{10}|J|$ curves of ITO – PFNMA brush // GaO_x / EGaIn junctions and histograms of the values of R (= $|J(-1.5V)|/|J(+1.5V)|$) with a Gaussian fit to these histograms. L_{PB} stands for the thickness of PFNMA brush, and σ in parentheses stands for the standard deviation.

6. *J*(V) curves for junctions of PFMMA brush samples measured with microfluidic device on bias |*V*| = 3.0 V at room temperature

To prove that the charge transport behaviour follows the space charge limited conduction model, we examined a serious of samples with different thickness and plotted the current density depends on thickness and voltage in log scales (see Chapter 5 in main text). Here we display the original *J*(V) curves for each sample.

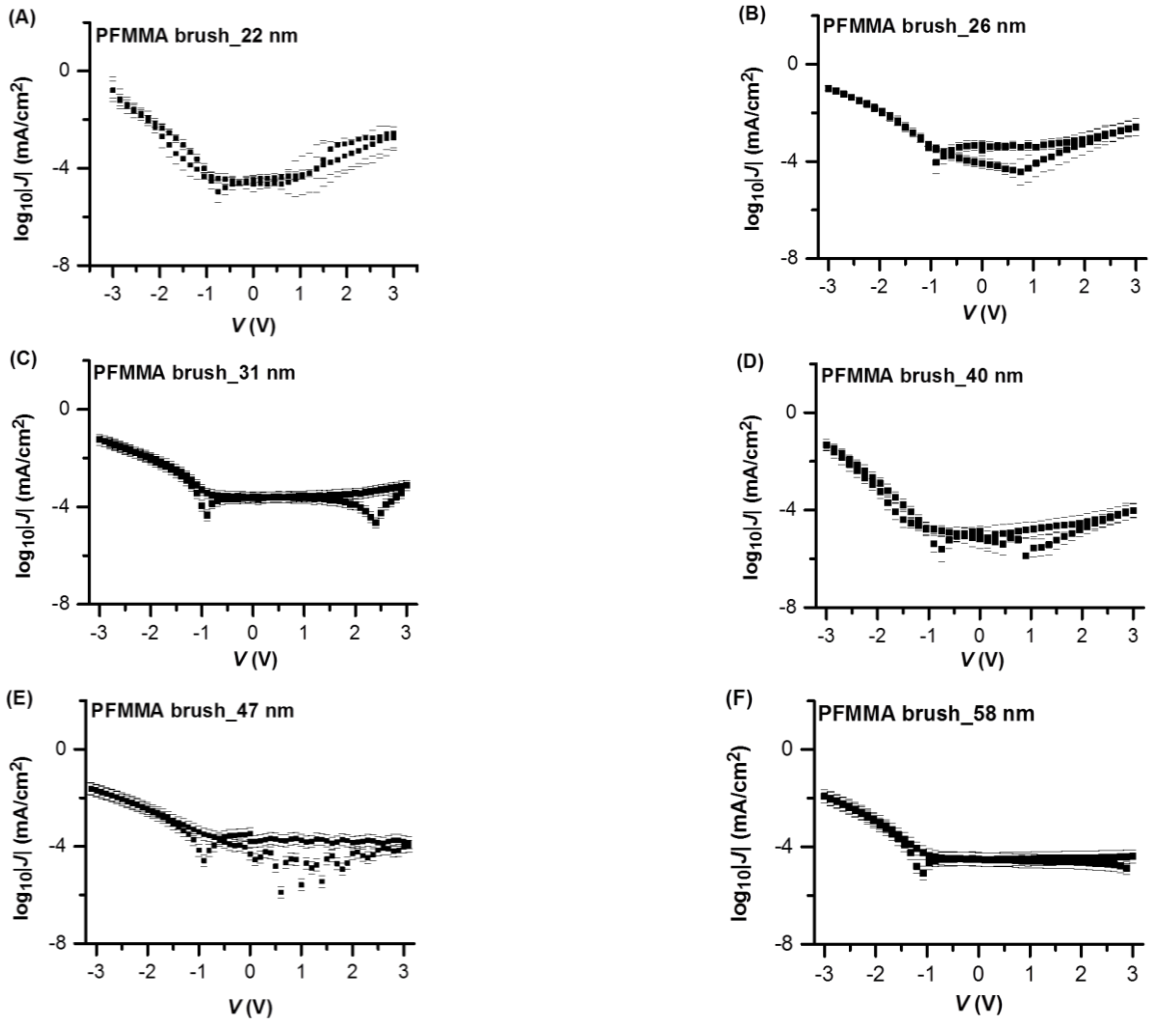

Figure A17 *J*(V) curves measured at room temperature on bias |*V*| = 3.0 V with EGaIn device.

7. *J*(V) plots as the function of T ranges from 340 K to 250K for PFMMA polymer brushes with 42 ± 1 nm

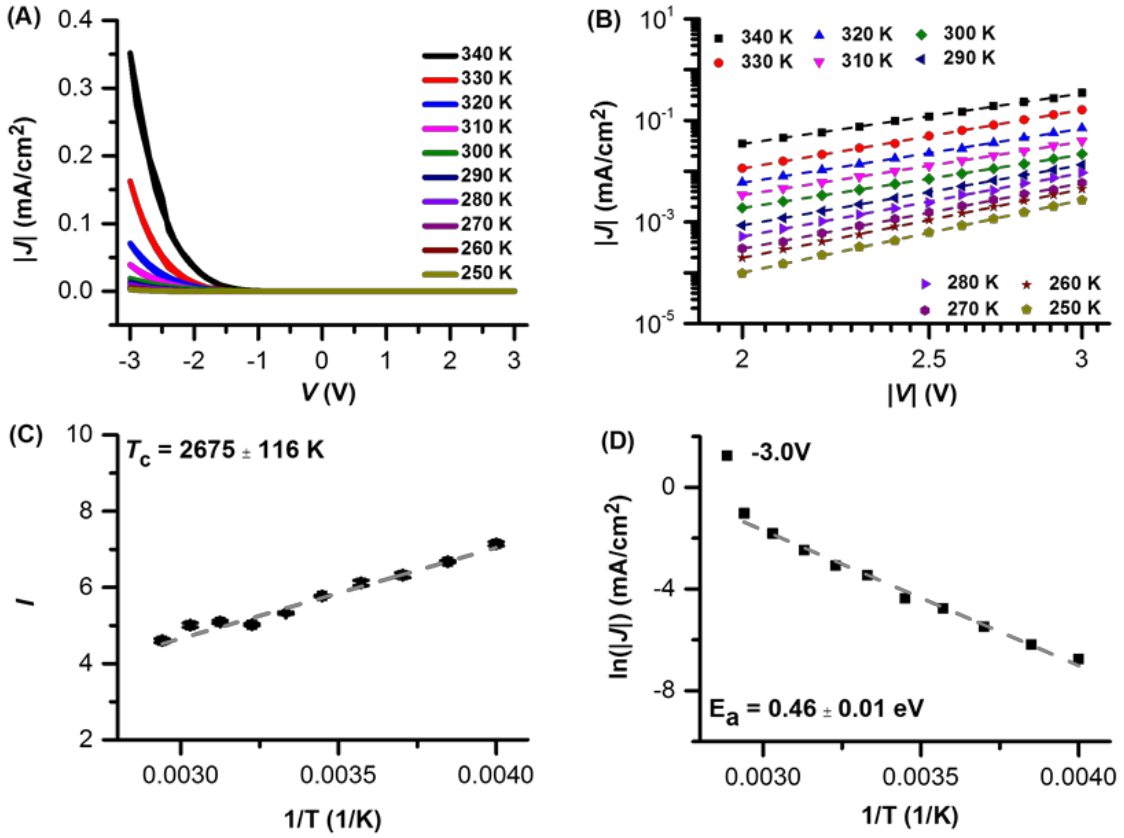

Figure A18 Thermally activated charge transport across ITO – PFMMA brush // GaO_X / EGaIn junctions. (A) *J*(V) linear scale plot as the function of *T* for 42 nm polymer brush sample at the voltage $|V| = 3.0$ V. inset image shows the values of $|J|$ measured at -3.0 and +3.0 V as a function of temperature. (B) *J*(V) plots in log-log scale at the negative bias ($1.9\ V < |V| < 3.0\ V$) as the function of *T* for 42 nm polymer brush sample. Colored dash lines indicate the linear fitting. (C) Exponent *l vs.*1/*T* plots. Black dash line indicates the linear fitting. Error bars for all data points indicate the fitting errors from (B). (D) ln|*J*| on negative bias at $|V| = 3.0$ V as the function of 1/*T*, grey dash lines indicate the linear fitting.

8. *J*(V) plots as the function of T ranges from 340 K to 250K for PFMMA polymer brushes with 36 ± 1 nm

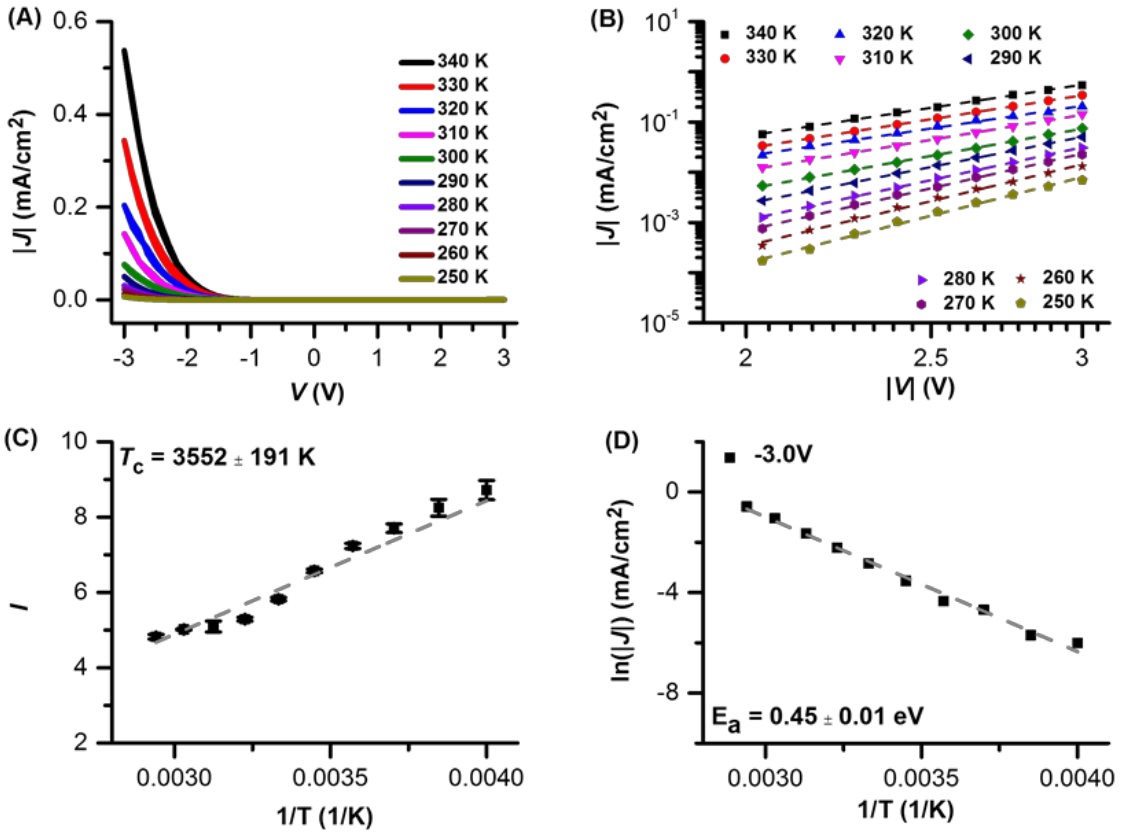

Figure A19 Thermally activated charge transport across ITO – PFMMA brush // GaO_X / EGaIn junctions. (A) *J*(V) linear scale plot as the function of *T* for 36 nm polymer brush sample at the voltage $|V| = 3.0$ V. inset image shows the values of $|J|$ measured at -3.0 and +3.0 V as a function of temperature. (B) *J*(V) plots in log-log scale at the negative bias ($1.9\ V < |V| < 3.0\ V$) as the function of *T* for 36 nm polymer brush sample. Colored dash lines indicate the linear fitting. (C) Exponent *l vs.* $1/T$ plots. Black dash line indicates the linear fitting. Error bars for all data points indicate the fitting errors from (B). (D) $\ln|J|$ on negative bias at $|V| = 3.0$ V as the function of $1/T$, grey dash lines indicate the linear fitting.

9. *J*(V) plots as the function of T ranges from 340 K to 250K for PFBMA polymer brushes with 43 ± 1 nm

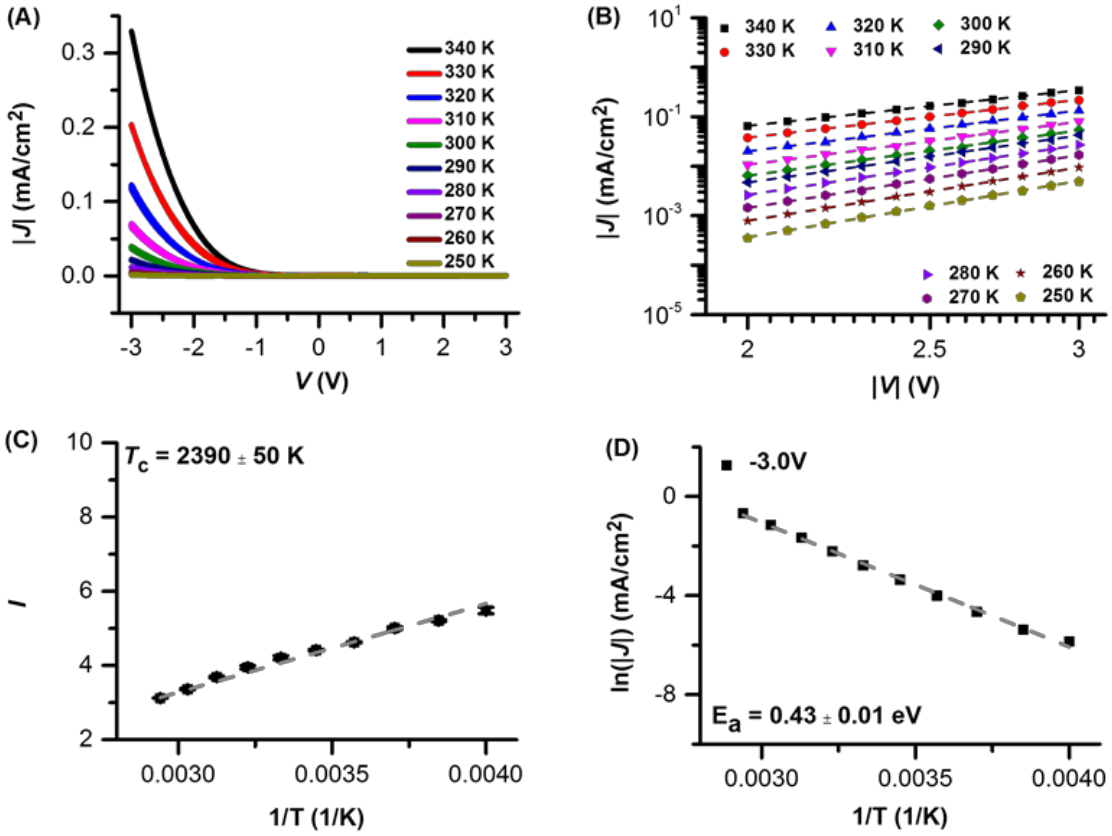

Figure A20 Thermally activated charge transport across ITO – PFBMA brush // GaO_X / EGaIn junctions. (A) *J*(V) linear scale plot as the function of *T* for 43 nm polymer brush sample at the voltage $|V| = 3.0$ V. inset image shows the values of $|J|$ measured at -3.0 and +3.0 V as a function of temperature. (B) *J*(V) plots in log-log scale at the negative bias ($1.9\ V < |V| < 3.0\ V$) as the function of *T* for 43 nm polymer brush sample. Colored dash lines indicate the linear fitting. (C) Exponent *l vs.* $1/T$ plots. Black dash line indicates the linear fitting. Error bars for all data points indicate the fitting errors from (B). (D) $\ln|J|$ on negative bias at $|V| = 3.0$ V as the function of $1/T$, grey dash lines indicate the linear fitting.

10. *J*(V) plots as the function of T ranges from 340 K to 250K for PFNMA polymer brushes with 42 ± 1 nm

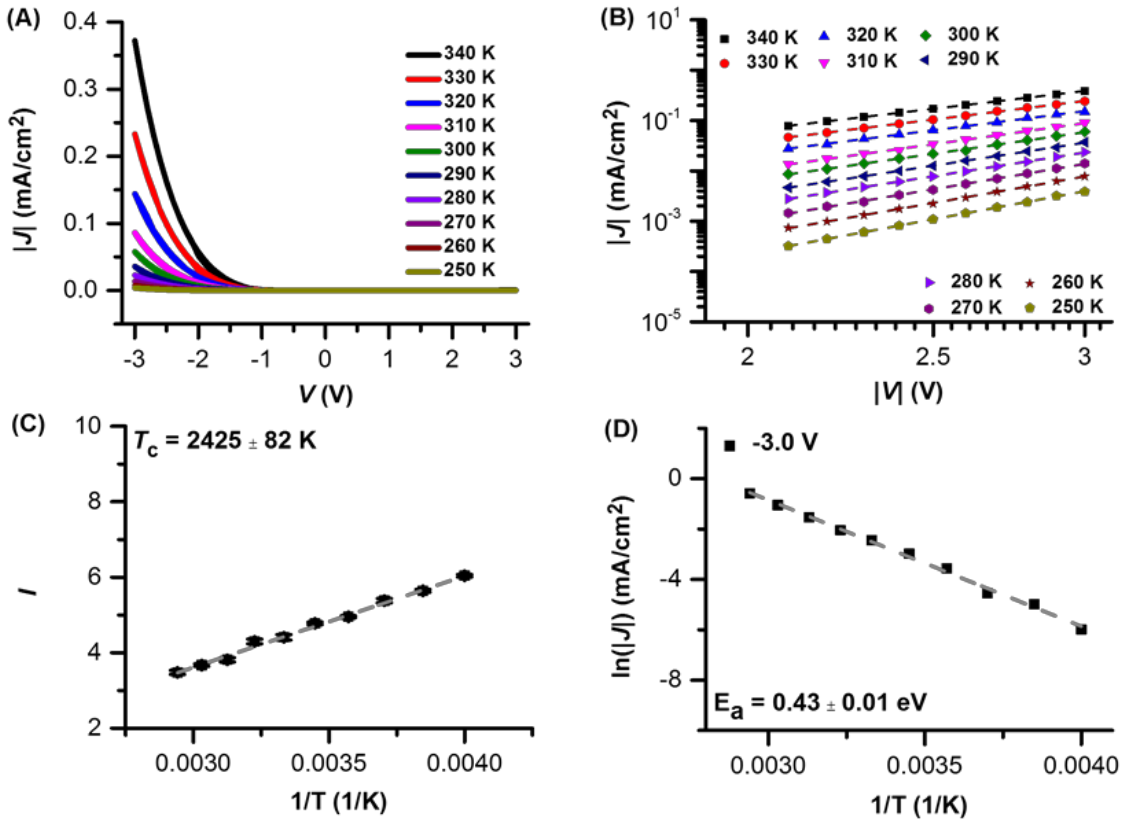

Figure A21 Thermally activated charge transport across ITO – PFNMA brush // GaO_X / EGaIn junctions. (A) *J*(V) linear scale plot as the function of *T* for 42 nm polymer brush sample at the voltage $|V| = 3.0$ V. inset image shows the values of $|J|$ measured at -3.0 and +3.0 V as a function of temperature. (B) *J*(V) plots in log-log scale at the negative bias ($1.9 \text{ V} < |V| < 3.0 \text{ V}$) as the function of *T* for 42 nm polymer brush sample. Colored dash lines indicate the linear fitting. (C) Exponent *l vs.* $1/T$ plots. Black dash line indicates the linear fitting. Error bars for all data points indicate the fitting errors from (B). (D) $\ln|J|$ on negative bias at $|V| = 3.0$ V as the function of $1/T$, grey dash lines indicate the linear fitting.

Publication list:

1. Side Chain Effects in the Packing Structure and Stiffness of Redox-Responsive Ferrocene-Containing Polymer Brushes
   Authors: Lu Gan, Jing Song, Shifeng Guo, Dominik Jańczewski, and Christian A. Nijhuis
   submitted to special issue “REDOX Responsive Polymers and Biopolymers” of European Polymer Journal (in review)
2. Tuning the Charge Transport across ITO-Ferrocene-containing Polymer Brushes // GaOX / EGaIn Junction by Controlled the Brush Thickness (manuscript in process)